UNIVERSITY OF SOUTHAMPTON

FACULTY OF SCIENCE

DEPARTMENT OF CHEMISTRY

ANODIC OXIDE FILMS ON TITANIUM IN ACIDIC MEDIA

by Daniel John Blackwood

A thesis submitted in partial fulfillment
of the requirements for the Degree of
Doctor of Philosophy

September, 1986

UNIVERSITY OF SOUTHAMPTON

ABSTRACT

FACULTY OF SCIENCE

CHEMISTRY

Doctor of Philosophy

ANODIC OXIDE FILMS ON TITANIUM IN ACIDIC MEDIA.

by Daniel John Blackwood

The properties of thin (less than 10 nm) anodic oxide films formed on titanium have been investigated. Particular attention was paid in this study to the spontaneous open-circuit passive-active transition that the oxide films are known to undergo in acidic media. The mechanism leading to this breakdown was found to involve uniform dissolution of the film. The rate of the dissolution process was found to be proportional to the initial growth rate of the oxide film and to the open-circuit temperatute. In addition the nature and concentration of both the cation and anion species in the open-circuit media were found to have a pronounced effect on the thinning rate of the anodic oxide films.

Photocurrent spectroscopy and capacitance measurements were used to show that slowly formed oxide films are more crystalline than their rapidly grown counterparts. These tehcniques were also used to obtain the absorption coefficient spectrum, over the wavelength range 250 - 400 nm, for the titanium anodic oxide films.

Ellipsometry revealed that the anodic oxide films formed on titanium have a structure similar to the anatase form of TiO_2, and that a suboxide layer forms between the metal and the dioxide when the original growth field is reduced.

ACKNOWLEDGEMENTS

I wish to express my sincere gratitude to my supervisor, Dr. Laurence Peter, for his guidance and constant encouragement over these last three years.

I would like to thank Dr. David Williams, of AERE Harwell, my CASE supervisor, for his many helpful ideas throughout this project.

My thanks are also due to Jeff, Li, Baruch, Steve, Ivor, Ariel and Maria for being such good companions in the lab, and especially to Bob Peat for his ever helpful advice.

My thanks are extended to Dr. Bob Greef, Colin Norman, Paul Harvey and Pete Pearson for their help in obtaining and interpreting the ellipsometric data. Also to Paul Chalker of AERE Harwell, for operating the SIMS and SEM spectrometers.

I owe a debt to the glassblowers, Mike, Clive and Jeremy who cheerfully repaired my all too frequent breakages, and to Alistair Clark for the daily use of his "Mirror".

My sincere thanks to Sandra Wilkins for deciphering my handwriting and typing this thesis.

Finally, I would like to acknowledge the financial support of both the Science and Engineering Research Council and AERE Harwell.

To my Parents.

La culture, c'est ce

qui demeure dans l'homme,

lorsqu'il a tout oublié.

E. Henriot.

CONTENTS

CHAPTER 1

INTRODUCTION

Introduction

Titanium is a relatively abundant metal, making up 0.6% of the Earth's crust, with the most common ores being the rutile form of the dioxide and a mixed oxide of composition $FeTiO_3$, known as ilmenite.

Although the metal was discovered in 1791 by W. Gregor, it was not readily available until 1949, when the Kroll process (1) was introduced. This method converts the ore into the liquid tetrachloride, which is purified by distillation and then reduced to the metal in a furnace with magnesium. However, the main commercial process for titanium production is now an electrolytic method.

Below 882°C titanium has a hexagonal close packed structure (α-phase) and has good mechanical properties for a low density (4.5 g cm^{-3}) metal (2). Above 882°C, titanium undergoes a crystal transformation to a body centre cubic structure (β-phase) (3).

Although titanium is intrinsically very reactive, a thin protective oxide film is formed rapidly on exposure to oxygen in the presence of trace amounts of water, preventing any further reaction. However, in the complete absence of moisture, no protective film is formed and oxidation occurs in depth (3). When a natural protective film is formed, titanium is found to be corrosion resistant in a wide range of chemical environments (3). This has led to titanium becoming an important industrial material (4-7), for example in copper electrowinning, where titanium is used as a cathode on which the copper can be deposited with a finely balanced adhesion, which makes it easy to remove at a later stage.

In chemical environments such as concentrated sulphuric acid, where titanium is not particularly corrosion resistant, anodic protection can be used to improve its performance. This method involves raising the electrode potential of the titanium so that a passivating anodic oxide film is formed. Once formed, the passivity of the film can be maintained if a small anodic current is applied, typically 8×10^{-4} A m^{-2} in 67% H_2SO_4 (8). Anodic passivation has made possible widespread

industrial application of titanium, for example for heat exchangers handling sulphuric acid in the viscose rayon process (9), as heating and cooling coils and support anodes in the electroplating industry (10,11) and in the field of nuclear energy where titanium has been used in the processing of fuel elements with nitric acid or aqua-regia (12,13).

The behaviour of passive films on metals has been studied by a wide range of techniques in addition to the well established steady state (14-16) and non-steady state (17,18) electrochemical methods. In recent years, optical techniques have played an increasing role, with ellipsometry (19-21), reflectance (22), electroreflectance (23,24) and photocurrent spectroscopy (25,26) leading the way. There is also a range of structural techniques available for the study of thicker films (>10 nm), such as electron diffraction (27,28) and X-ray diffraction (29,30). The final catalogue of techniques presently being used to study oxide films also includes high vacuum surface analytical techniques, such as X-ray photoelectron spectroscopy (31,32), Auger electron spectroscopy (31-33), secondary ion mass spectroscopy (34) and scanning electron microscopy(35).

Despite the availability of this impressive array of techniques, the exact nature of the protective oxide film formed on titanium by anodisation, is still open to debate. At high voltages (> 50 V), evidence from structural techniques for both rutile (27) and anatase (28) has been presented. For the thin films formed at low voltages (< 10 V), there is even more uncertainty, with reports (27,28,36-42) suggesting that all three naturally occurring oxides; rutile, anatase and brookite; as well as a series of lower oxides, are present in the film.

The growth of the oxide film during anodic oxidation takes place by the migration of titanium interstitial ions or oxygen vacancies from the metal oxide interface (43,44), although some authors (45,46) have reported evidence of growth via oxygen migration. It has been shown that anodic oxide growth obeys the inverse log law (47).

The literature concerning the anodic oxidation of titanium was reviewed by Aladjem (48) in 1972, and more recently the general electrochemistry of the metal has been reviewed by Kelly (49).

Although the anodic oxide film stabilises titanium in many corrosive environments, it is known to undergo a spontaneous breakdown (50) in various acidic media, leading to the active dissolution of the metal, if it is not anodically protected. Although this phenomenon has been studied frequently (14,15, 50-61), the mechanism of the breakdown has remained uncertain.

The time taken for a titanium electrode, passivated initially by an anodic oxide film, to become active after it is switched to open-circuit, is defined as the breakdown period, τ_b. It has been shown (60-62) that τ_b decreases with increasing temperature, film growth rate and acid concentration, but increases with increasing film thickness and Ti^{3+} concentration in solution. In addition, it has been demonstrated that τ_b is uneffected by scratching of the oxide film after growth; the oxide film in this case is believed to regrow to a thickness determined by the anodising ratio (40,44) and the open circuit potential (50).

It has been suggested by Armstrong et al. (55) that the breakdown in passivity of titanium anodic oxide films is caused by the nucleation and growth of two dimensional holes. This mechanism was later modified by Harrison and Williams (15), on the basis of impedance data from the breakdown of very thin (< 20 nm) anodic oxide films which suggested that nucleation and growth of patches of a porous reduced oxide occurred. Harrison and Williams (15) proposed that the reduction of the TiO_2 film may be a consequence of the reduction of hydrogen ions at sites within the oxide leading to the formation of TiOOH. Indeed in an earlier paper, Dyer (63) explained the electrolytic rectifaction behaviour of titanium electrodes as a consequence of the reaction,

$$TiO_2 + H^+ \rightleftharpoons TiOOH + e^- \qquad 1.1$$

Two further possible causes of the loss of passivity were considered in the present work. The first possibility is that the dioxide is reduced at the metal/oxide interface via a disproportionation reaction,

$$3TiO_2 + Ti \longrightarrow 2Ti_2O_3 \qquad 1.2$$

The alternative mechanism is that the oxide simply dissolves slowly in the acid at a rate that depends on both the open-circuit environment of the oxide film and on the conditions under which it was grown. The results presented in this thesis show clearly that the second mechanism is responsible for the open-circuit breakdown in passivity of anodic oxide films grown on titanium and the effect on the dissolution rate of temperature, film thickness, growth rate of the film and the electrolyte composition has been characterised in detail in terms of the dissolution mechanism.

The effect of alloying on the performance of titanium in corrosive environments has been studied in detail by other authors (64-71). It has been reported that small amounts of molybdenium, zirconium, nickel, tungsten and niobium stabilize the passive film. Radocivi et al (65) have reported the following trend in passivity of titanium alloys;

$$Pd > Ni > Mo > MnAl > VAl \qquad 1.3$$

In addition to studying the passive-active transition of anodic oxide films on titanium, the present work involved investigation of the semiconductor properties of these films using a range of techniques including photocurrent spectroscopy (25-26) and electroreflectance (23,24,72).

McAleer and Peter (26) have already used photocurrent spectroscopy to show that above about 1.5 V vs S.C.E., anodic oxide films on titanium are essentially pure TiO_2 with an amorphous structure. The spectral dependence of the photocurrent of thin films has been investigated by McAleer (44), and the photocurrent onset was found to be at 420 nm

(3.06 eV), which is close to the indirect band gap of rutile single crystals (73). Evidence is put forward in this thesis, from photocurrent measurements, that shows that the crystallinity of the oxide films increases as either the temperature is increased, or the growth rate is decreased. In addition, the spectral dependence of the absorption coefficient of these films is derived.

The properties of the oxide films were also studied by electroreflectance. Frova et al. (23) have indicated previously that when electroreflectance measurements are performed on thin absorbing films, reflection from the back surface must be taken into account, and that this may lead to electroabsorption effects dominating the spectra obtained. More recently, Blondeau et al. (74) have proposed that this phenomenon leads to interference effects. Both these ideas were considered in the interpretation of the results obtained for this thesis.

References

1. KROLL, W.J.; Trans. Electrochem. Soc. 78 (1940) 35.
2. KROLL, W.J. and SCHLECHTEN, A.W.; Met. Ind. 69 (1946) 319.
3. SHREIR, L.L.; (ed.) "Corrosion", Vol. 1, "Metal Environment Reactions" Chapter 5.4 Newnes-Butterworth, London (1979).
4. ERBIN, E.F.; J. Metals, 15 (1963) 192.
5. FEIGE, N.G. and KANE, R.L.; Desalination 7 (1969) 17.
6. O'BRIG, H. and EHLE, J.C.; Chem. Process. Engrg. 50, (1969) Sept. 95.
7. HARPUR, N.F.; Metal. Mater. Technol. 13 (1981) 259.
8. Reference 3, Vol. 2,"Corrosion Control" Chapter 11.8.
9. COTTON, J.B.; Chem. Eng. Prog. 66, (1970) 57.
10. SIBERT, M.E. and STEINBERG, M.A.; Material, 46 (1957) 132.
11. SIMONS, C.S.; Corrosion 15 (1959) 95.
12. SAVOLAINEN, J.E. and DLANCO, R.E.; Chem. Eng. Prog. 53 (1957) 78F.
13. PETERSON, C.L., MILLER, P.D., WHITE, E.L. and WALTER, E.C.; Industr. Engng. Chem. 51 (1959) 32.
14. THOMAS, N.T. and NOBE, K.; J. Electrochem. Soc. 116 (1969) 1748.
15. HARRISON, J.A. and WILLIAMS, D.E.; Electrochim. Acta, 27 (1982) 891.
16. ARMSTRONG, R.D. and FIRMAN, R.E.; J. Electroanal. Chem. 34 (1972) 391.
17. HUNTER, M.S. and FOWLE, P.; J. Electrochem. Soc. 101 (1954) 482.
18. JOUVE, G. and DERRADJI, N.E.; J. Less-Common Met. 86 (1982) 161.
19. HAYFIELD, P.C.S.; Surf. Sci. 56 (1976) 488.
20. KRUGER, J.; J. Phys. (Paris) Colloq. 5 (1977) 129.
21. GREEF, R. and NORMAN, C.F.F.W.; J. Electrochem. Soc. 132 (1985) 2362.
22. BLONDEAU, G., FROELICHER, M., FROMENT, M. and HUGOT-LE GOFF, A.; Thin Solid Films 38 (1976), 261.
23. FROVA, A., BODDY, P.J. and CHEN, Y.S.; Phys. Rev. 157 (1967) 700.
24. PAATSCH, W.; Surf. Sci. 37 (1973) 59.

25. PETER, L.M.; in PLETCHER, D. (Ed.) "Electrochemistry", Vol. 9. A Specialist Periodical Report, Royal Society of Chemistry, London, 1984.

26. McALEER, J.F. and PETER, L.M.; Far. Disc. Chem.Soc. 70 (1980), 67.

27. JOUVE, G., POLITI, A., SERVANT, C. and SEVERAC, C.; J. Microsc. Spectrosc. Electron. 3 (1978) 513.

28. BLONDEAU, G., FROELICHER, M., FROMENT, M., HUGOT-LE GOFF, A., BRIEU, M., CALSOU, R. and LARROQUE, P.; J. Microsc. Spectrosc. Electron. 2 (1977), 27.

29. ANDERSSON, S., COLLEN, B., KUYLENSTIERNA, U. and MAGNEL, A., Acta. Chem. Scand. 11 (1957) 1641.

30. FLEISCHMANN, M., GRAVES, P., HILL, I.R., OLIVER, A. and ROBINSON, J.; J. Electroanal. Chem. 150 (1983) 33.

31. ARMSTRONG, N.R. and QUINN, R.K.; Surf. Sci. 67 (1977) 451.

32. ARMSTRONG, N.R. and QUINN, R.K.; J. Electrochem. Soc. 125 (1978) 1790.

33. MATHIEU, J.B., MATHIEU, H.J. and LANDOLDT, D.; J. Electrochem Soc. 125 (1978) 1039.

34. HUNT, C.P. and SEAH, M.P.; Surface and Interface Analysis 5, (1983) 199.

35. HAYFIELD, P.C.S.; "Titanium Science and Technology" vol. 4, p.2 405 "Proceedings of the 2nd International Conference on Titanium", Massachusetts, 1972, Edited by Jaffee, R.I. and Burte, H.M., Plenum Publishing Corporation, New York, 1973.

36. MORIOKA, S. and UMEZONO, A.; Nippon Kinzoku Gakkaishi 20 (1956) 403.

37. PASCAL, P.; Nouveau Trate de Chimie Minerale, 14; (Masson et Cie, Paris, 1963).

38. SIBERT, M.; J. Electrochem. Soc. 110 (1963) 65.

39. HUBER, F., J. Electrochem. Soc. 115 (1968) 203.

40. BLONDEAU, G., FROELICHER, M., FROMENT, M. and HUGOT-LE GOFF, A., J. Less-Common Met. 56 (1977) 215.

41. AKIMOV, A.G.; Zasch. Metallova, 5 (1969) 217.

42. PESANT, J.C. and VENNEREAU,P.; J.Less-Common Met. 69 (1980), 63.

43. KOVER, F. and MUSSELIN, M.; Thin Solid Films 2, (1968), 211.

44. McALEER, J.F.; University of Southampton, Ph.D. Thesis (1980).

45. TYLECOTE, R.; CNRS Symp. No. 122 (1963) Publ. Paris (1965) 241.

46. DORNELAS, W.; University of Paris, Ph.D. Thesis (1967).

47. ASHOK, K.V.; "Electrochemistry of Metals and Semiconductors" Decker, New York (1973).

48. ALADJEM, A.; J. Mater. Sci. 8 (1973), 688.

49. KELLY, E.J.; Mod. Aspects Electrochem. 14 (1982) 319. Eidted by Brockeris, J. O'M., Conway, B.E. and White, R.E.

50. COTTON, J.B.; Werkst and Korrosion, 11 (1960) 152.

51. PEKSHEVA, N.P. and VORONTSOV, E.S.; Mater. Naucho-Tekh. Konf. Varonezh. Politekh Inst. 1972, p. 95.

52. GURINA, T.V. and ANASHKIN, R.D., Elektrokhim.15 (1979) 234.

53. GURINA, T.V. and OUCHARENKO, V.I.; Elektrokhim. 11 (1975) 1449.

54. DYER, C.K. and LEACH, J.S.L.; J. Electrochem.Soc. 125 (1978) 1032.

55. ARMSTRONG, R.D., HARRISON, J.A., THIRSK, R. and WHITFIELD, R.; J. Electrochem. Soc. 117 (1970) 1003.

56. AMMAR, I.A. and KAMAL, I.; Electrochim. Acta, 16 (1971) 1540.

57. De PAULI, C.P., GIORDANO, M.C. and ZEBINO, J.O.; Electrochim. Acta. 12 (1983) 1781.

58. ARSOV, Lj. D.; Electrochim. Acta, 30 (1985) 1645.

59. LEVY, M; Corrosion, 23 (1967), 236.

60. FRANCIS, K.F.; University of Southampton, M.Sc. Thesis, (1982).

61. CLARK, D.; University of Southampton, M.Sc. Thesis (1983).

62. BARTLETT, D., ASHWORTH, V., BOWDEN, F.L. and GILBERT, J.R.B.; "Titanium '80" Vol. 4. p. 2639. "Proceedings of the 4th International Conference on Titanium", Kyoto, Japan, May 1980, Edited by Kimura, H. and Izumi, O.; Metallurgical Society AIME, Warrendal, Philadelphia, 1980.

63. DYER, C.K.; Electrocomp. Sci. Tech. 1 (1974) 121.

64. FEIGE, N.G. and MURPHY, T.J.: Corrosion 22 (1966) 320.

65. RADOVICI, D. and POPA, M.V.; Rev. Coroz. 1 (1971). 9.

66. GREISS, J.C.;Jr. Corrosion, 24 (1968) 24.

67. GLASS, R.S.; Corrosion-N.A.C.E., 41 (1985), 89.

68. GLASS, R.S.; Electrochim Acta, 28 (1983), 1507.

69. GLASS, R.S.; Electrochim. Acta, 29 (1984), 1465.

70. McKAY, P.; International Congress on Metallic Corrosion. Toronto, Canada, 1984. Proceedings. Vol. 3, p. 288.

71. KOSSYL, G.G., TRUSOV, G.N., GONCHARENHO, B.A. and MIKHEEV, V.S.; Zashch. Met. 14 (1974) 662.

72. PAATSCH, W.; Ber. Bunsenges, Phys. Chem. 79 (1975) 922.

73. MORRISON, S.R. "Electrochemistry at Semiconductor and Oxidised Metal Electrodes", Plenum, New York, 1980.

74. BLONDEAU, G., FROELICHER, M., JOVANCICEVIC, V. and HUGOT-LE GOFF, A.; Surf. Sci. 80 (1979) 151.

CHAPTER 2

THEORY

2.1 Passivation and Oxide Growth

2.1.1 Passivation

Many metals, including titanium, can form protective films which slow down the rate of corrosion in natural environments. Whether it is thermodynamically possible for these films to be formed depends on the potential of the metal and the pH of its surroundings. If only water and the metal are considered, this information can be obtained from the Pourbaix diagram (1) for the metal.

In the case of titanium, oxidation of the metal by water is spontaneous, up to the Ti(IV) oxidation state;

$$Ti + 2H_2O \xrightarrow[-3e-]{E^{\ominus}_{Ti/TI^{3+}}} Ti^{3+} + 2H_2O \xrightarrow[-e-]{E^{\ominus}_{Ti^{3+}/TiO_2}} TiO_2 + 4H^+ \qquad 2.1$$

$E^{\ominus}_{Ti/T^{3+}} = -1.209V$

$E^{\ominus}_{Ti^{3+}/TiO_2} = -0.666V.$

This means that titanium is not in a true state of equilibrium when it is in aqueous media, hence its standard potentials cannot be measured accurately. Therefore, experimental verification of the Pourbaix diagram (Fig. 2.1) calculated from thermochemical data, is difficult.

The most recent review of the standard potentials of titanium, by James et al (1985) (2), showed only one major alteration, that was to move the Ti^{3+}/Ti^{2+} standard potential down from -0.368V to -2.3V suggesting that the former experimentally determined value was due to a mixed potential, with the oxidation of Ti(iii), not Ti(ii), being the positive side and the reduction of H^+ the negative side.

The steady state current vs potential curve for a passivating metal is shown schematically in figure 2.2.

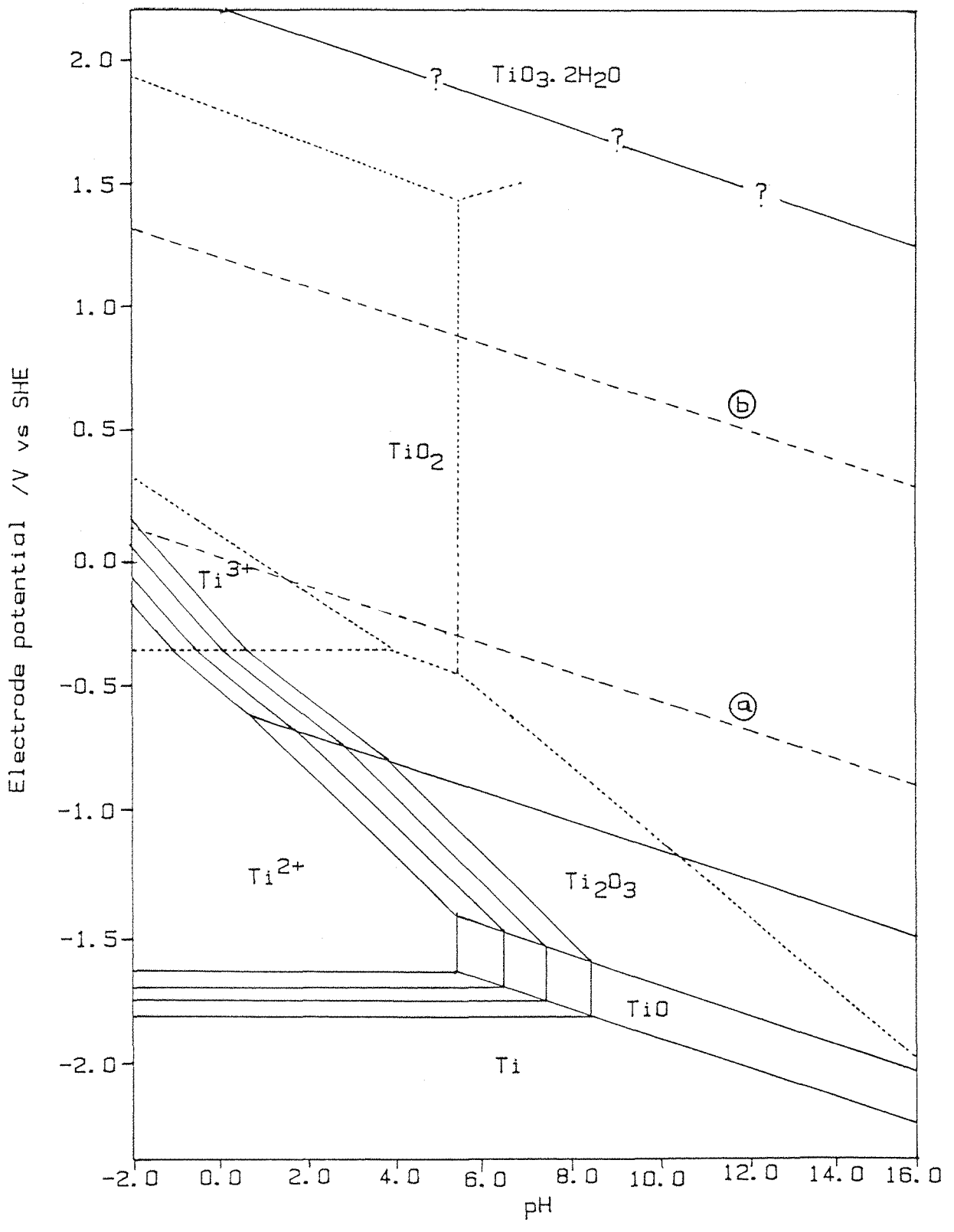

Fig. 2.1. Potential-pH equilibrium diagram for the titanium-water system, at 25°C. The anhydrous oxide of Ti_2O_3 and TiO_2 (rutile) have been considered (1).

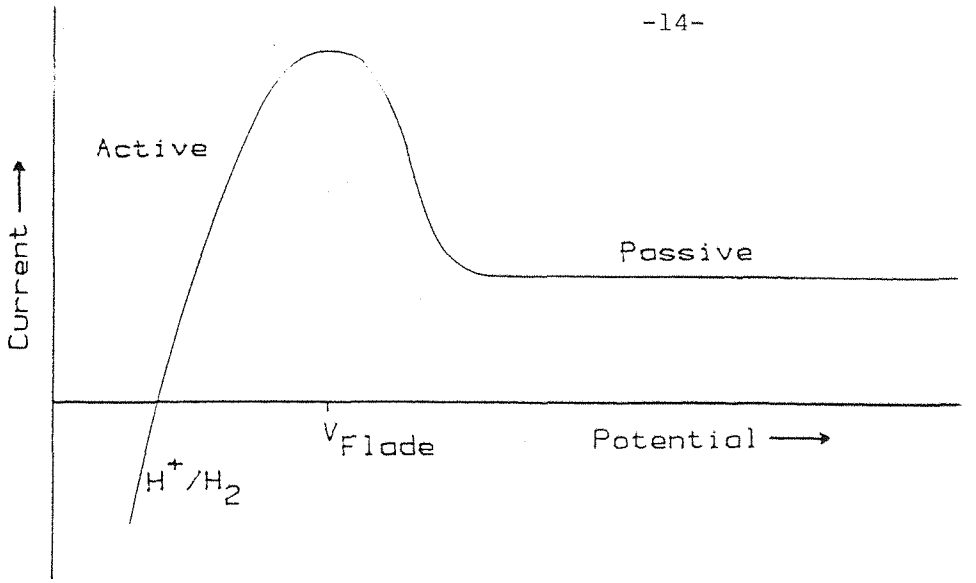

Fig 2.2 Steady state current-potential curve for a passivating metal.

As the potential is made more positive, the current is seen to rise steeply at first due to the active dissolution of the metal. However, as the potential becomes still more positive, the current begins to fall, and this has been interpreted as the point at which either oxygen is adsorbed on the metal surface, or the oxide film starts to form, inhibiting dissolution of the metal. The potential at which this occurs is often referred to as the Flade potential (3). Two different types of behaviour are observed when the potential is made still more positive. In the case of the so-called 'valve metals', the oxide film thickens and the dissolution rate falls to zero. In other cases, e.g. chromium, the metal may undergo a further oxidation and become transpassive if the higher valence state is soluble.

In the case of titanium, the Flade potential is in the region of -0.32V vs. SHE (-0.96 vs $Hg(Hg_2SO_4)$, at pH 0, and a pH dependence of 60 mV per decade has been reported (4).

The first step in oxide film formation is in some doubt. Armstrong (5) has suggested that it is related to the adsorption of oxygen, whilst Evans (6) has proposed that a monolayer of bulk oxide is formed in the first stage of growth. Depsite the uncertainty about the initial steps in the mechanism of oxide formation, it is believed (7), that an oxide layer is always present, even immediately after polishing. It has even been suggested that this layer is not removed by cathodic polarisation, but is undermined instead by a layer of

titanium hydride (8). This view has been challenged recently by Arsov (9), who has presented ellipsometric data that appear to show that bare titanium is exposed after holding the potential in the region of -0.36V to -0.66V vs SHE for a period of minutes in sulphuric acid.

2.1.2 Growth Laws

Although titanium is in some ways similar to many transpassive metals (Fe, Co, Ni, Cr, etc.), in that the metal spontaneously activates in acidic deoxygenated aqueous chloride or sulfate solutions (10), the anodic film growth characteristics of titanium in the passive state are very similar to those of the typical valve metals (Zr, Hf, Ta, etc.) (11). Anodic oxide films formed on valve metals tend to have insulating properties, and large fields are required for oxide growths by ionic conduction to occur, so oxide growth on titanium is expected to follow the inverse logarithmic law (12), which is the high field limiting form of both the Cabrera-Mott (13) and the Verwey (14) theories. These theories consider the flux of ions over a potential barrier. The Cabrera-Mott theory considers the largest energy barrier to be located at the metal/oxide interface (Fig. 2.3a), whereas in the Verwey theory the rate controlling activation energy barrier is assumed to be within the bulk oxide (Fig. 2.3b).

The barrier is effectively lowered as the available electric field is increased so that more ions are able to cross, resulting in oxide growth. For any particular ion, the probability of crossing the barrier is given by;

$$P = E\exp\left[-(\Delta G - Zea E_{ox})/kT\right] \qquad 2.2$$

where ΔG is the barrier height, Ze is the charge on the ion, a is the half-width of the barrier and E_{ox} is the electric field across the oxide. In earlier theories of oxide growth (13,14) the field has simply been defined as

$$E = \frac{V_{tot}}{L_f} \qquad 2.3$$

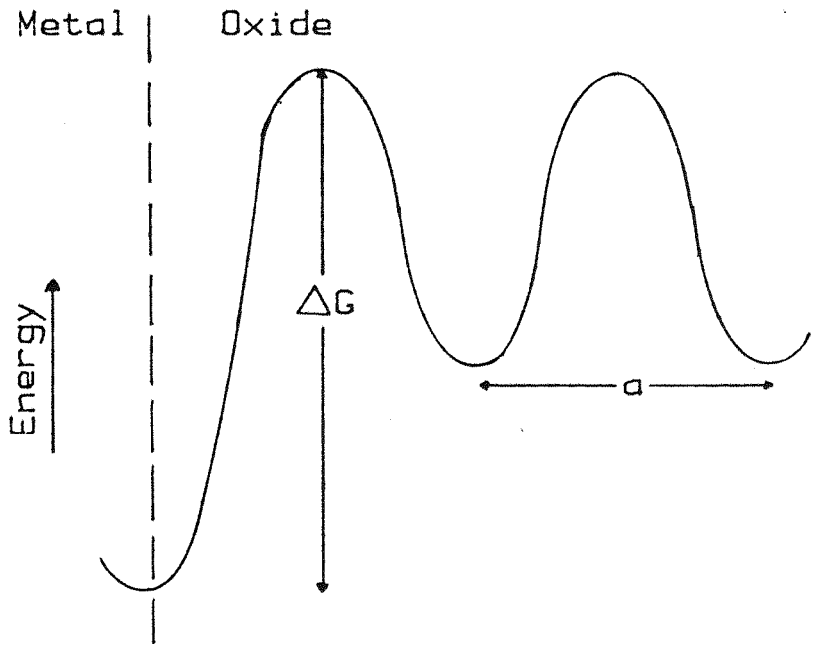

a) Cabrera-Mott theory.

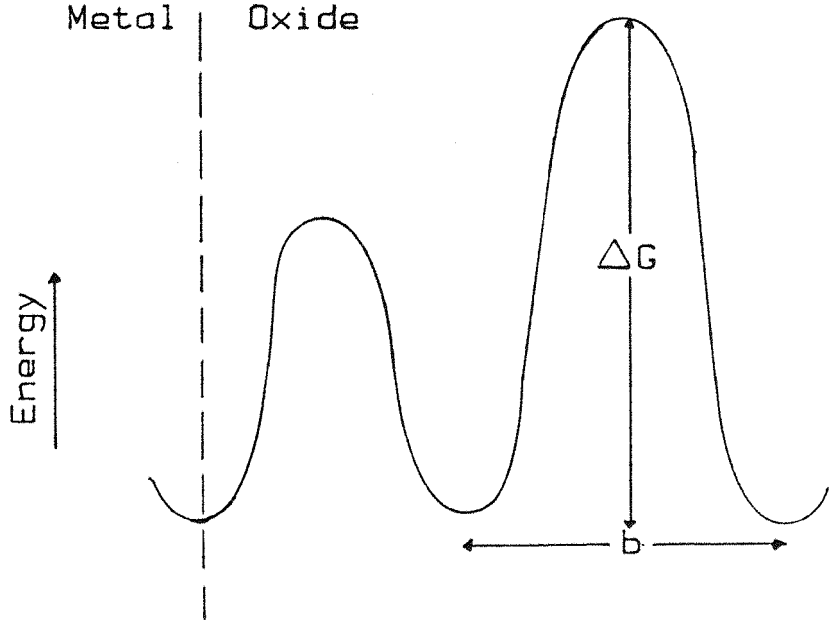

b) Verwey theory.

Fig. 2.3 Schematic potential-energy profiles for ion transport across an oxide film on a metal (zero field), showing the limiting cases corresponding to (a) the Cabera-Mott theory, (b) the Verwey theory.

where V_{tot} is the total potential drop between the electrode and the solution and L_f is the oxide films thickness. For the very thin films grown in the work for this thesis account should be taken of the potential drop across the Helmholtz layer.

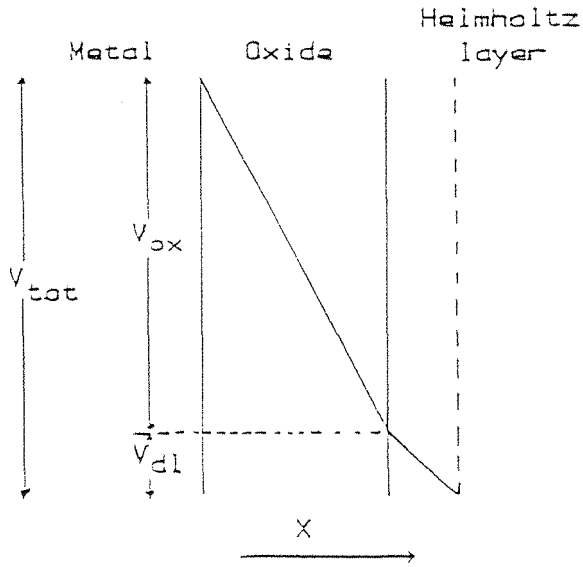

Fig. 2.4 Schematic representation of the total potential drop across the electrode/ electolyte interface.

Figure 2.4 shows that V_{tot} is made up of two parts

$$V_{tot} = V_{ox} + V_{dl} \qquad 2.4$$

The oxide and double layer can also be represented as two capacitors in series, so that the fraction of the total potential drop which occurs across the oxide can be expressed as

$$\frac{V_{ox}}{V_{tot}} = \frac{L_f}{L_f + \frac{\varepsilon_{ox}\varepsilon_o}{C_{dl}}} \qquad 2.5$$

$$= \frac{L_f}{L_f + \frac{\varepsilon_{ox}}{\varepsilon_H} L_H} \qquad 2.6$$

where ε_{ox} and ε_H are the relative premittivities of the oxide film and the Helmholtz layer respectively, C_{dl} is the double layer capacitance

and L_H is its width. The field across the oxide is given by,

$$E_{ox} = \frac{V_{ox}}{L_f} = \frac{V_{tot}}{L_f \frac{\varepsilon_{ox}\,\varepsilon_o}{C_{dl}}} \qquad 2.7$$

If a surface density of mobile ions at the major potential barrier of $N cm^{-2}$, with a characteristic frequency of ν, is considered, it follows from equation 2.2 that the current density in the direction of the field is

$$\vec{j} = N\nu\, Ze\, Exp\, [-(\Delta G - Zea\, E_{ox})/kT] \qquad 2.8$$

The reverse current density is

$$\overleftarrow{j} = N\nu\, Ze\, Exp\, [-(\Delta G + Zea\, E_{ox})/kT] \qquad 2.9$$

Hence the net current density flowing is

$$j_{net} = \vec{j} + \overleftarrow{j} \qquad 2.10$$

$$= N\nu Ze\, Exp\, -(\Delta G/kT)\, \sinh\, (Zea\, E_{ox}/kT) \qquad 2.11$$

In the high field limit, $E_{ox} > 10^6 V\, cm^{-1}$, the reverse current can be neglected so that equation 2.11 becomes

$$j = j_o\, Exp\, (Zea\, E_{ox}/kT)$$

$$= j_o\, Exp\, \beta E_{ox} \qquad 2.12$$

where j_o is the exchange current density and β is often referred to as the "Tafel slope". Substitution of equation 2.7 and 2.13 into equation 2.12 gives equation 2.14.

$$j = \frac{4F}{V_m} \times \frac{dL_f}{dt} \qquad 2.13$$

$$\frac{dL_f}{d} = \frac{V_m j_o}{4F} \text{Exp}\left(\frac{V_{tot}}{L_f + \frac{\varepsilon_{ox}\varepsilon_o}{C_{dl}}}\right) \qquad 2.14$$

where V_m is the molar volume of the oxide. Integration of equation 2.14, neglecting terms L_f^3 and above gives

$$t = \frac{4F\left(L_f + \frac{\varepsilon_{ox}\varepsilon_o}{C_{dl}}\right)^2}{V_m j_o \beta V_{tot}} \text{Exp}\left[-\beta V_{tot}/\left(L_f + \frac{\varepsilon_{ox}\varepsilon_o}{C_{dl}}\right)\right] \qquad 2.15$$

For small changes in L_f

$$\left(L_{f2} + \frac{\varepsilon_{ox}\varepsilon_o}{C_{dl}}\right)^2 / \left(L_{f1} + \frac{\varepsilon_{ox}\varepsilon_o}{C_{dl}}\right)^2 << \text{Exp}\left[-\beta V\left\{\frac{L_{f1} - L_{f2}}{\left(L_{f1} + \frac{\varepsilon\varepsilon_o}{C_{dl}}\right)\left(L_{f2} + \frac{\varepsilon\varepsilon_o}{C_{dl}}\right)}\right\}\right] \qquad 2.16$$

Therefore for small changes in the film thickness,

$$t \cong A \text{ Exp}\left[-\beta V/\left(L_f + \frac{\varepsilon_{ox}\varepsilon_o}{C_{dl}}\right)\right] \qquad 2.17$$

$$-\text{Ln}t = \left(\frac{\beta V_{tot}}{L_f + \frac{\varepsilon_{ox}\varepsilon_o}{C_{dl}}}\right) - \text{Ln}A \qquad 2.18$$

where A is a constant.

The inverse log law states that the film thickness is inversely proportional to the natural log of time, but equation 2.18 shows that this will only hold if the volume of C_{dl} tends to infinity.

Computer calculations (Fig. 2.5) using the complete Cabrera-Mott (13) equation (equ. 2.11), show that plots of Int vs $^{1}/L_f$ will be curved for smaller values of C_{dl}, although in practice detection of this non-linearity would involve measuring charge-time transients over several decades of time.

The effect of this Helmholtz layer on the results expected from linear sweep voltametry (section 3.2.2) was generated by a numerical method (Fig. 2.6). It was found that the Helmholtz layer was equivalent to an initial oxide film $\frac{\varepsilon_{ox}}{\varepsilon_H} L_H$ thick and therefore moved the apparent onset potential for film growth in the anodic direction, but the magnitude of the plateau current was not affected. However, as the Helmholtz layer will always be present, there is no experimental way of measuring the onset potential for film growth in its absence. In addition, there is likely to be a natural oxide layer on the electrode's surface, so that the potential shift due to the Helmholtz layer above is not accessible to measurement.

2.1.3 The effect of the space charge on anodic oxide growth

Dewald (15) and later Fromhold (16) have considered the effect on the growth field of the space charge due to ions in transit. This charge will cause the size of the field acting on the ions migrating through the film to be position dependent, with the average field $\bar{E}$ given by (15)

$$\bar{E} = E_{ox} + {}^{1}/\beta_b [(1 + {}^{1}/\delta) \text{ Ln } (1 + \delta) - 1] \qquad 2.19$$

where E_{ox} is the space charge free value of the field, the subscript b refers to a bulk oxide barrier as in the Verwey theory (14) and

$$\delta = \frac{4\pi\beta_b Z_b \, e \, N(O) L_f}{\varepsilon\varepsilon_o} \qquad 2.20$$

where N(O) is the ion concentration at the metal/oxide interface.

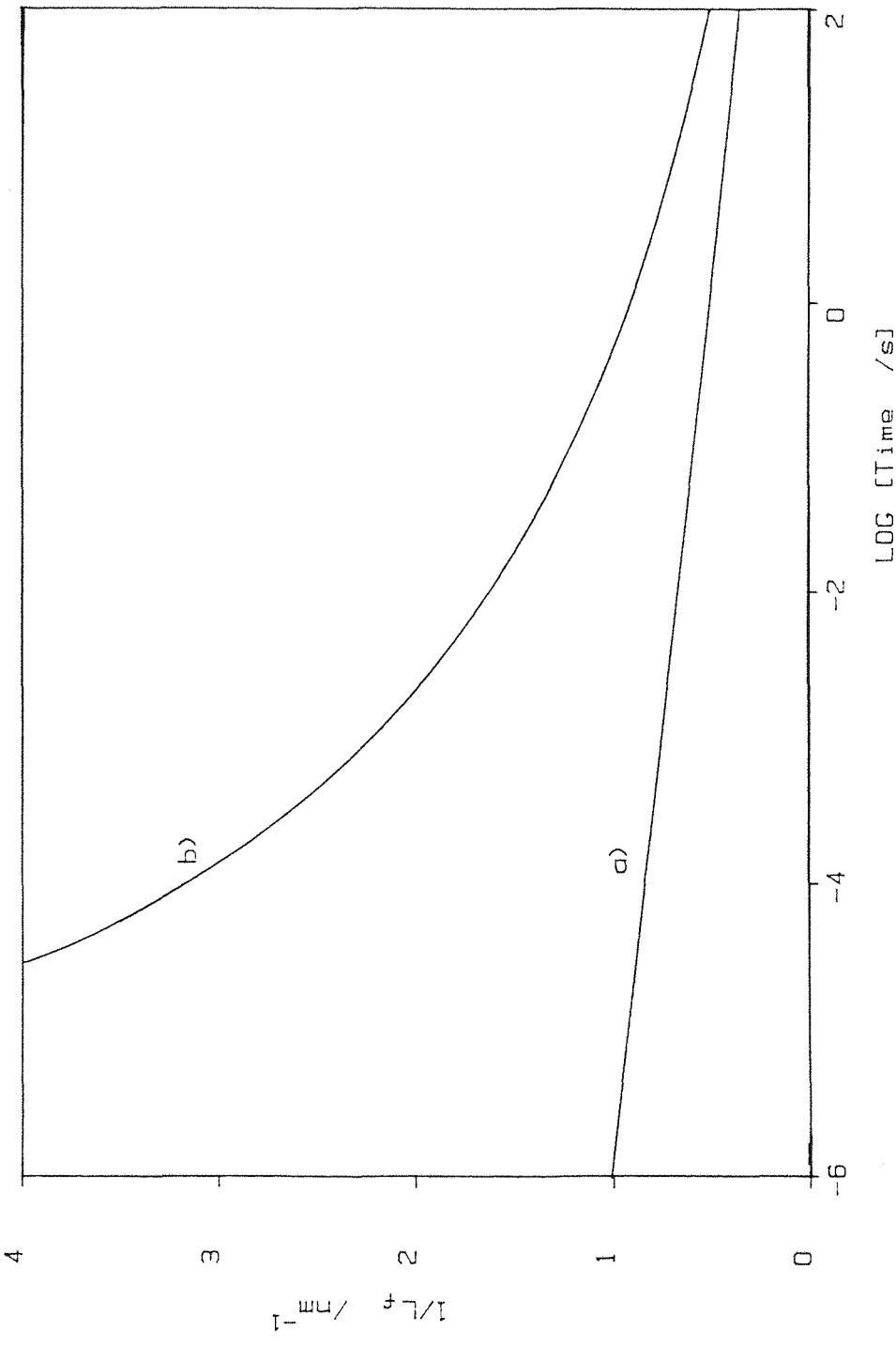

Fig. 2.5. Computer calculated theoretical plots of Log t vs $^{1}/_{L_f}$ showing the effect of the Helmholtz layer on the inverse log law. Applied potential = 1V, $j_o = 10^{-8}$ A cm^{-2}, curve a) no Helmholtz layer, curve b) with Helmholtz layer using $\varepsilon_{ox} = 40$, $C_{HL} = 40$ μF cm^{-2}.

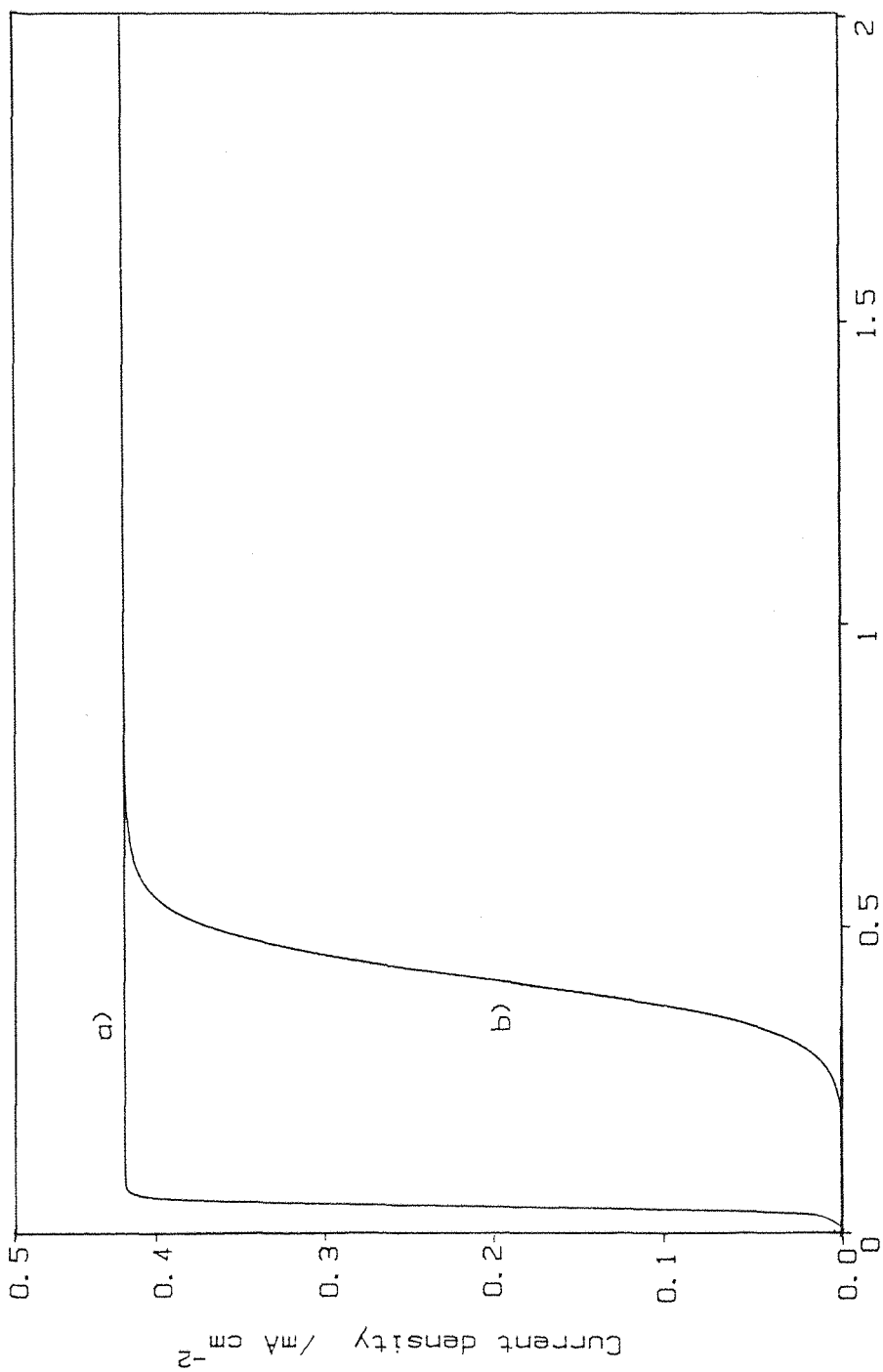

Fig. 2.6. Theoretical cyclic voltammograms generated by a numerical method, showing the effect of Helmholtz layer. Theoretical growth conditions; j_o = 10^{-8} A cm^{-2}, ν = 100 mVs^{-1}. initial film thickness = 0.1 nm, curve a) no Helmholtz layer, curve b) with Helmholtz layer using ε_{ox} = 40, C_{dl} = 40 μF cm^{-2}.

In the limit that $\delta << 1$, equation 2.19 tends to the Cabrera-Mott theory (equ . 2.12), on the other hand when $\delta > 10$ the space charge becomes all important,

$$\bar{E} \cong {}^{1}/_{\beta_b} \text{Ln}\ \delta$$

$$= {}^{1}/_{\beta_b} \text{Ln} \left(\frac{4\pi\beta_b Z_b\ e\ N_{(O)} L_f}{\varepsilon\ \varepsilon_o} \right) \qquad 2.21$$

In the high field limit, it can be shown that $N_{(O)}$ is related to the current density by the Dewald expression (15).

$$N_{(O)} = j^{(1-\gamma)} \frac{\left(N_s \nu_s Z_s e\right)^{\gamma}}{Z_b \nu_b e} \text{Exp}\left[(\Delta G_b - \gamma \Delta G_s)/kT\right] \qquad 2.22$$

where γ is the ratio of the half jump distance of the barrier in the bulk oxide to its counterpart at the metal/oxide interface and the subscript s refers to parameters at the metal/oxide interface barrier. Hence both equations 2.12 and 2.21 predict currents which depend exponentially on the average field, and it is therefore difficult to distinguish between the two mechanisms experimentally.

2.1.4 The anodising ratio

When an appropriate potential is applied to a titanium electrode, the oxide will grow by ion migration. Kover et al. (18) have reported that this migration involves metal cations moving through a sublattice of oxide anions. As the oxide thickens, the effective field is reduced, which in turn slows down the growth rate until it eventually becomes insignificant.

From equation 2.23 it can be shown that the film thickness, at any specific value of residual current is directly proportional to the applied potential;

$$j = j_o\ \text{Exp}\left(\frac{V_{tot}}{L_f + \frac{\varepsilon_{ox}\varepsilon_o}{C_{dl}}} \right) \qquad 2.23$$

rearrangement gives

$$L_f = \beta V_{tot} \, Ln\left(\frac{j_o}{j}\right) - \frac{\varepsilon_{ox}\varepsilon_o}{C_{dl}} \, Ln\left(\frac{j_o}{j}\right) \qquad 2.24$$

When C_{dl} tends to infinity, equation 2.24 shows that the ratio $L_{f/V_{tot}}$ will be constant. This is then known as the Anodising Ratio (A.R.) (17).

The A.R. is sometimes (19) defined as the ratio of the film thickness to the applied potential after a specified length of time, rather than a residual current. However, it can be shown from equation 2.26 that the value of $L_{f/V_{tot}}$ at constant t is not independent of V_{tot}, even when C_{dl} equals infinity;

$$t = \frac{4F \, L_f^{\,2}}{V_m j_o \beta V_{tot}} \; Exp\left(\frac{-\beta V_{tot}}{L_f}\right) \qquad 2.25$$

Rarrangement gives

$$\frac{L_f}{V_{tot}} = \frac{\beta V_m j_o t}{4F \, L_f} \; Exp\left(\frac{\beta V_{tot}}{L_f}\right) \qquad 2.26$$

If it is assumed growth starts at the Flade potential (3), the thickness of any film at a given potential can be estimated if the anodising ratio is known. As this is simply the inverse of the field it can be calculated using equations 2.12 and 2.13.

$$A.R. = {}^{1}/_{E_{ox}} = \frac{L_f + \left(\varepsilon_{ox}\varepsilon_o/C_{dl}\right)}{V_{tot}}$$

$$= \frac{\varepsilon_{ox}\varepsilon_o}{V_{tot} C_{dl}} + {}^{1}/_{V_{tot}} \int_o^t \frac{V_m j}{4F} \, dt$$

$$A.R. = \frac{\varepsilon_{ox}\varepsilon_o}{V_{tot} C_{dl}} + \left[\left(\frac{q}{4F}\right) \times \left(\frac{V_m}{Ar}\right)\right] \qquad 2.27$$

where q is the charge passed, A is the geometric area of the oxide, with r being a roughness factor.

For titanium the anodising ratio has been found generally to be in the range of 1.4 - 3.0 nm V^{-1} (17,19,20) for film grown to less than 25 nm.

2.2 Properties of Anodic Oxide Films

2.2.1 Origin of film capacitance

The formation of an oxide film separates the charges on the metal from those of the Helmholtz layer. The system can be thought of as a parallel plate capacitor, with a capacitance given by

$$C = \varepsilon\varepsilon_o r/L_f \qquad 2.28$$

where ε_o is the permittivity of free space and ε is the relative permittivity of the oxide.

Since the limiting thickness of the film $L_{f(lim)}$, is linearly dependent on the applied field (section 2.1.4) a plot of the reciprocal capacitance of the film versus the applied potential should be a straight line, with a slope proportional to ε.

When a sinusoidal perturbation in the field is applied across the oxide film, a polarization is produced that lags behind the applied perturbation by a frequency dependent angle θ (Appendix 1). The response can therefore be resolved into an inphase and a quadrature component. The phase shift arises from the complex permittivity of the oxide,

$$\varepsilon = \varepsilon_1 + i\varepsilon_2 \qquad 2.29$$

Several different polarization processes contribute to the permittivity of the oxide films. These include lattice vibrations

and electronic polarization, and each process will contribute fully to ε_1 only well below a characteristic critical frequency, ω_c and to ε_2 only near this frequency (near in this context means within one or two decades of frequency). This arises because when $\omega >> \omega_c$ the polarizaion process will not respond at all; when $\omega \cong \omega_c$ a response is obtained but it lags behind in phase; when $\omega << \omega_c$ the time lag of the response becomes negligible so that it is essentially in phase with the applied perturbation.

For an ideal capacitor the phase angle, θ, between the voltage and the current is 90°, but if the case of an anodic oxide film is considered the dielectric propoerties of the oxide will cause θ, to deviate by an amount known as the loss angle δ,

$$\delta = (90° - \theta) \qquad 2.30$$

$\tan\delta$ is called the "loss tangent" and is given by

$$\tan\delta = {}^{1}/_{\tan\theta} = {}^{\varepsilon_2}/_{\varepsilon_1} \qquad 2.31$$

Anodic oxide films on valve metals characteristically have a constant value of $\tan\delta$ for frequencies between 10 Hz and 10 kHz (21). This feature has been explained (22,23) in terms of ionic relaxation processes with a wide range of relaxation times, so that ε_2 effectively remains constant and ε_1 only varies slightly. The relaxation processes are believe (24) to involve the movement of interstitial ions and are therefore related to ionic conductivity.

Anodic oxide films are not perfect capacitors as flaws allow leakage current to flow. They can therefore be described in terms of a resistor R_{ox} and a non-ideal capacitor C_{ox} in a parallel circiut (Appendix 2). Since

$$\tan\theta = \frac{Im(Z)}{Re(Z)} \qquad 2.32$$

where Z is the impedance of the circuit, it is easy to show for this circuit that,

$$\tan\delta = \varepsilon_2/\varepsilon_1 = 1/\omega R_{ox} C_{ox} \qquad 2.33$$

A frequency dispersion in the measured value of the capacitance of an anodic oxide should be observed in the region where $\tan\delta$ = constant (25,26).

2.2.2 Band Theory

The electrons associated with an atom in the gaseous phase occupy discrete energy levels, but when the electrons are in a many atom solid, these discrete levels overlap to form continuous bands. These energy bands are often separated by forbidden regions, of width E_g, called band gaps (27), where there are no solutions to the Schrödinger equation.

For systems in their ground state, energy levels or bands, will be filled in order of increasing energy. The band with the highest occupied states is called the valence band, while the band with the lowest unoccupied states is called the conduction band. The Pauli exclusion principle implies that only two electrons can occupy the same energy state, therefore each band can hold two electrons for every atom in the structure. Hence, for odd-valent elements, such as the group 1 metals, only half the states in the outer band are filled (Fig. 2.8a). This means that if a field is applied, an electron can easily move up to a higher energy level, to increase its energy and consequently its velocity in the direction of the field. Hence these elements conduct electricity readily, and they are often referred to as true metals.

For even-valent elements in the ground state, the valence band will be completely full and the conductivity will depend on which of the three possible situations occurs;

i) the energy levels of the conduction and valence bands overlap, (Fig. 2.7b), producing a conducting material, sometimes referred to as a semimetal.

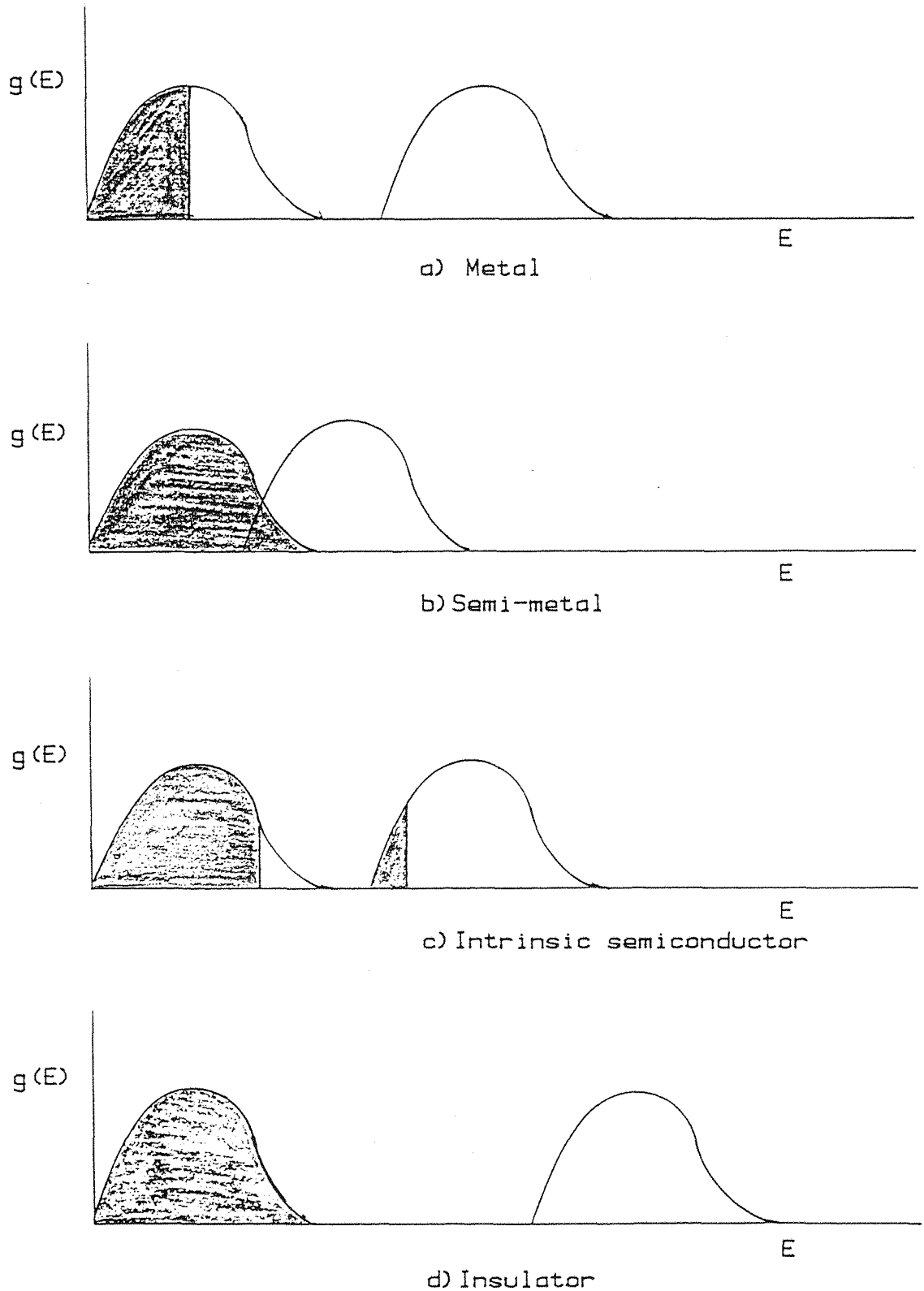

Fig. 2.7 Density of states as a function of energy for different classes of solid.

ii) the energy levels of the conduction and valence bands are separated by a small energy gap (Fig. 2.7c) across which thermal excitation of electrons can occur fairly readily. This is the situation for intrinsic semiconductors.

iii) the energy levels of the conduction and valence bands are separated by a large energy gap (Fig. 2.7d), which greatly reduces the probability that an electron can be excited to the conduction band at room temperatures. This is the case for insulators.

2.2.3 The Fermi energy level

The probability that an electronic energy level is occupied, is given by the Fermi distribution function

$$P = \frac{1}{1 + \mathrm{Exp}\,[(\mathbf{E} - \mathbf{E}_F)/kT]} \qquad 2.34$$

where $\mathbf{E}_F$, the Fermi energy is effectively the level where the probability of occupation by an electron is exactly 0.5.

For simple metals, the Fermi energy level is located in the middle of the partially occupied band. In the case of intrinsic semiconductors and insulators in their ground state at absolute zero temperature, the Fermi energy level will lie exactly half way between the valence and conduction bands (Fig. 2.8a). This is because the probability of finding an electron in the valence band, under these conditions, is exactly one, while that for finding an electron in the conduction band is exactly zero.

If the system leaves the ground state, its Fermi energy level will move and will be given by, (28)

$$\mathbf{E}_F = \frac{\mathbf{E}_c + \mathbf{E}_v}{2} + \frac{kT}{2}\ \mathrm{Ln}\ \frac{N_v}{N_c} \qquad 2.35$$

where E_c and E_v are the energy levels of the upper edge of the valence band and the lower edge of the conduction band respectively, while N_v and N_c are the densities of states in the two bands.

2.2.4 Intrinsic and doped semiconductors

Intrinsic semiconductors, are highly pure perfect crystals, whereas in doped, or extrinsic, semiconductors some lattice atoms have been replaced by impurity atoms with more (donor) or fewer (acceptor) electrons than the original lattice atoms. Structures with an excess of donor atoms are referred to as n-type and those with an excess of acceptor atoms are called p-type semiconductors.

n-Type doping gives rise to an excess of electrons, some of which are thermalised from the donor energy level into the nearby conduction band. Hence the probability of finding an electron in the conduction band is increased, and as a reuslt the Fermi energy level moves up towards the conduction band (Fig. 2.8b). In the case of p-type doping, the acceptor states are able to extract electrons from the valence band, thereby reducing the probability of finding an electron in the valence band, so that the Fermi energy level moves downwards (Fig. 2.8c).

At high doping levels, the Fermi energy level moves out of the forbidden region into either the conduction or valence bands and the material becomes a degenerate semiconductor. The concentration of free carriers must be calculated in this case form the Fermi-Dirac distributions, as the Boltzmann approximation will no longer apply (28).

If a crystal structure is not perfect but contains vacancy or interstitial defects, these can act as electron acceptors or donors, producing the same effect as doping with foreign atoms. In undoped imperfect crystals therefore, the stoichiometry determines the semi-conducting properties. In the case of oxides, the number of defects in a crystal can be influenced by the partial pressure of oxygen (P_{O_2}) in the surrounding gas phase (29). However, at room temperature, the

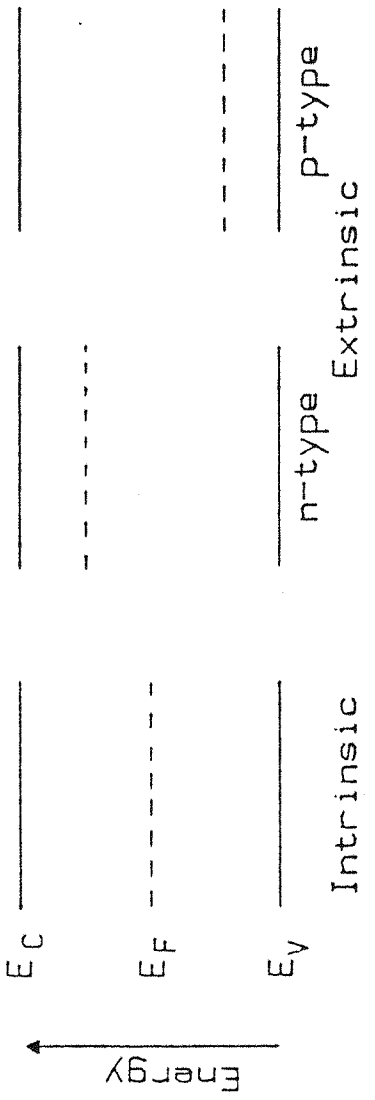

Fig. 2.8. Schematic representation of the energy band structure of intrinsic and extrinsic semiconductors.

motion of the defects in the crystal is slow, so only a surface equilbrium can be established. At high P_{O_2}, some of the oxygen for the surrounding gas phase can become incorporated into the crystal, altering the defect concentrations in such a way as to induce p-type behaviour.

In the case of rutile, strong n-type behaviour can be obtained by reducing the crystal in a hydrogen atmosphere. The donor states have been reported to be interstitial titanium ions (30,31).

In addition to controlling the type of semiconductor behaviour, cyrstal imperfections result in local stresses that can destroy lattice periodicity so that the energy levels and band gaps become dependent on position. This effect is referred to as band tailing (32), and it is expected to occur in the amorphous and polycrystalline structures which are formed in anodic oxide films.

2.2.5 Semiconductor/solution interfaces

A redox reaction at a metal electrode's surface may be represented as

$$O_{sol} + e^-_m \rightleftharpoons R_{sol} \qquad 2.36$$

where O_{sol} and R_{sol} refer to the oxidised and reduced solution species respectively and e_m refers to the electron in the metal phase. Equation 2.36 can be rewritten in terms of the electrochemical potentials

$$\bar{\mu}_o + \bar{\mu}_e = \bar{\mu}_R \qquad 2.37$$

or

$$\bar{\mu}_e + \bar{\mu}_R - \bar{\mu}_o \qquad 2.38$$

Since the electrochemical potential of the electron, $\bar{\mu}_e$, can be thought of as the chemist's definition of the electronic Fermi level, it follows that $\bar{\mu}_R - \bar{\mu}_e$ must be formally equivalent to a "redox

Fermi level" in the solution, although of course there are no de-localised energy levels in the solution and O and R are still discrete ionic species.

If an n-type semiconductor comes into contact with a solution, the two Fermi levels present at the interface will tend to the same energy. This equilibration is achieved by charge transfer (C.T.). Because this is a rapid process compared to the motion of the solution species, the Frank-Condon principle applies and as a result C.T. will only occur between quantum states of the same energy. C.T. can therefore be represented as a horizontal line on the energy diagram shown in figure 2.9. In addition, the localised energy levels of any particular solution species taking part in the C.T. will fluctuate with time in response to polarization changes in the solution. The energy levels of the O and R species have therefore been represented as a normal distribution about the most probable energy in figure 2.9.

In the case where the semiconductor's original Fermi energy level was higher than the final level, a net loss of electrons will have occurred from this phase, leaving a depleted positive layer called the space-charge. The positive charge is localised on the immobile donors. The depth to which the space charge penetrates the semiconductor is called the Schottky length, L_s, which is given by

$$L_s = \left[\frac{2\varepsilon\varepsilon_2\Delta\phi}{eN}\right]^{\frac{1}{2}} \qquad 2.39$$

where N is the density of ionised donors and $\Delta\phi$ is the potential across the depletion layer, which corresponds to the band bending, $e\Delta\phi$, (fig. 2.9), that arises from the space charge.

The space charge capacity, C_{sc}, is defined as,

$$C_{sc} = -dQ_{sc}/d\Delta\phi_{sc} \qquad 2.40$$

where Q_{sc} is the space charge.

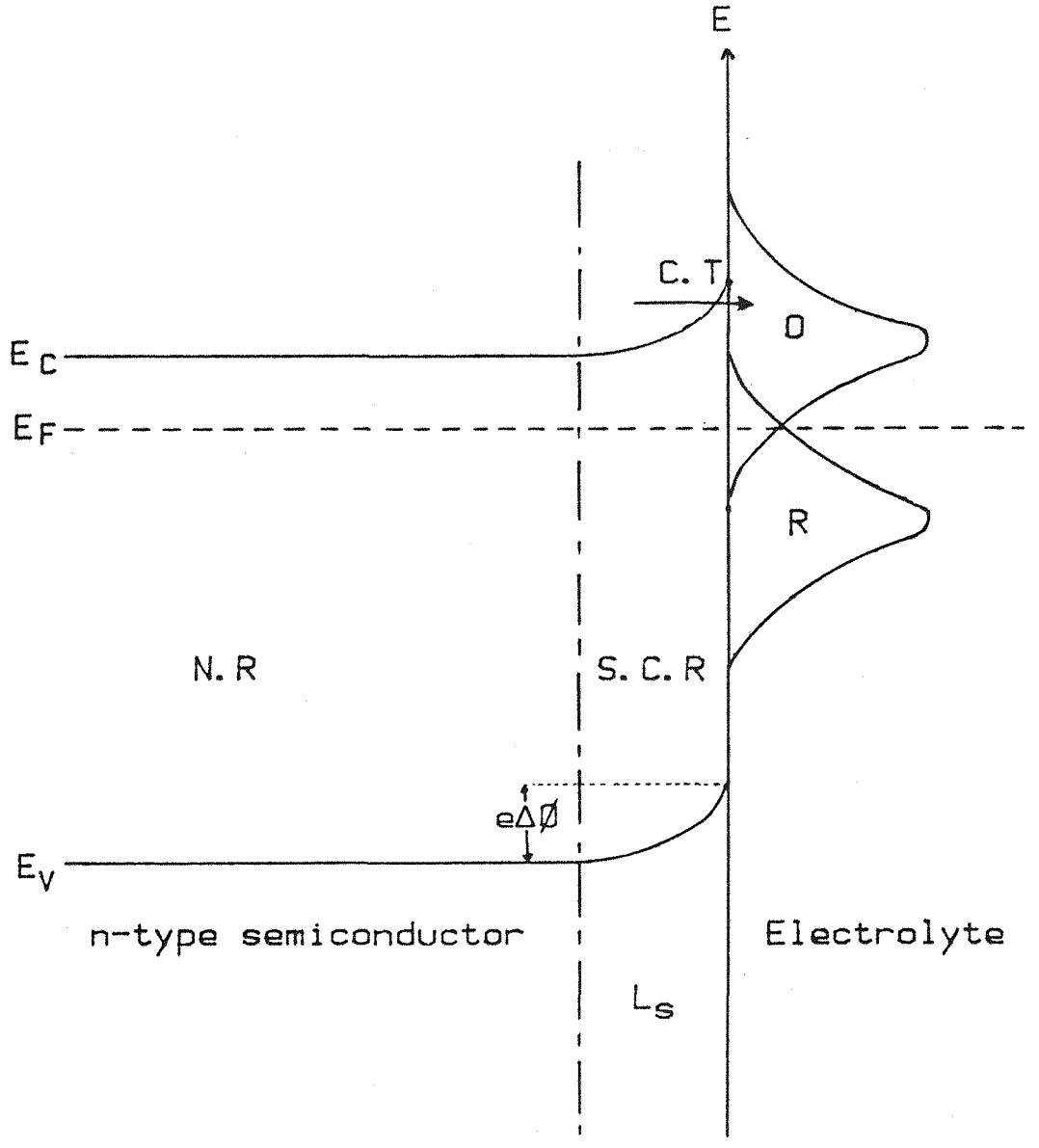

Fig. 2.9. Band-bending and distribution of energy states for an n-type semiconductor in contact with a redox electrolyte O/R couple in the absence of an applied field. N.R. = neutral region; S.C.R. = space-charge region; C.T. = charge transfer reaction.

Dewald (33) has used the Poisson-Boltzmann distribution function to produce a general expression for the space charge capacitance of a wide (> 3 eV) bandgap n-type semiconductor, in contact with an electrolyte,

$$C_{sc} = \frac{-dQ_{sc}}{d\Delta\phi_{sc}} = \left(\frac{q^2 N_D \varepsilon\varepsilon_o}{2kT}\right)^{\frac{1}{2}} \frac{\left|f\, e^{Y} - 1/\{1+(1/f-1)e^{Y}\}\right|}{[f(e^{Y}-1)-Y-\mathrm{Ln}\,\{f+(1-f)d^{Y}\}]^{\frac{1}{2}}} \qquad 2.41$$

where f is the fraction of donors which are ionised in the bulk of the semiconductor, N_D is the total density of donors and Y is the value of the surface potential in units of $^{kT}/_{e}$;

$$Y = -e\Delta\phi/kT \qquad 2.42$$

If all the donors are ionised (f = 1), equation 2.27 becomes

$$C_{sc} = \left(\frac{q^2 N_D \varepsilon\varepsilon_o}{2kT}\right)^{\frac{1}{2}} \frac{|e^{Y}-1|}{(e^{Y}-Y-1)^{\frac{1}{2}}} \qquad 2.43$$

In the limit of large negative Y equation 2.43 can be rearranged into the Mott-Schottky equation (34,35),

$$^{1}/_{C_{sc}^2} = \frac{2}{e\varepsilon\varepsilon_o N_D}\left(\Delta\phi - {}^{kT}/_{q}\right) \qquad 2.44$$

which was first derived for the metal/semiconductor junction. Equation 2.29 will be obtained regardless of the value of f, as long as

$$\mathrm{Exp}\,(-e\Delta\phi/kT) = \mathrm{Exp}\,(Y) << 1 \qquad 2.45$$

and

$$Y >> (f - \mathrm{Ln}f) \qquad 2.46$$

Equation 2.44 shows that a plot of $^{1}/_{C_{sc}^2}$ against $\Delta\phi$, should be linear with a slope depending on the total donor density and an intercept at a point $^{kT}/_{e}$ away from the flat-band potential. However, any experimental measurement of the capacitance, at a solution/semi-

conductor interface, will have to be corrected for the Helmholtz layer capacitance, which appears in series with the space charge capacitance, so that,

$$1/C_{meas} = 1/C_{sc} + 1/C_H \qquad 2.47$$

The resultant correction term for the flat-band potential has been determined by Pettinger et al. (36) as,

$$\Delta V = e \varepsilon N_s L_H^2 / 2\varepsilon_H^2 \varepsilon_o \qquad 2.48$$

where ε_H and L_H are the relative premittivity and width of the Helmholtz layer respectively.

For thin anodic films, the width of the depletion layer can easily be greater than the film thickness. In this case some additional counter charge is required on the metal (Fig. 2.10).

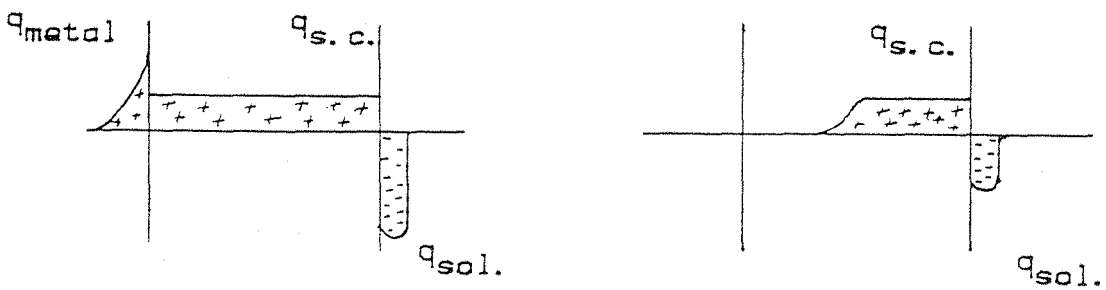

Fig. 2.10 Schematic representations of the charge distribution within an anodic oxide film/electrolyte interface. a) At high voltage and b) at low potentials.

For anodic oxide films, with typical values of L_f = 10 nm, $N = 10^{20}$ cm^{-3} and $\varepsilon = 30$, equation 2.39 can be used to show that the Schottky length will be greater than the film thickness for values of $\Delta\phi$ greater than $\sim$ 3.0 V. Above this value the potential drop will be across the whole semiconductor. Hence the space charge

will not be modulated by the applied field, resulting in the measurement of the geometric capacitance. Thus an ideal Mott-Schottky plot for a thin anodic film should tend to a limiting value (Fig. 2.11).

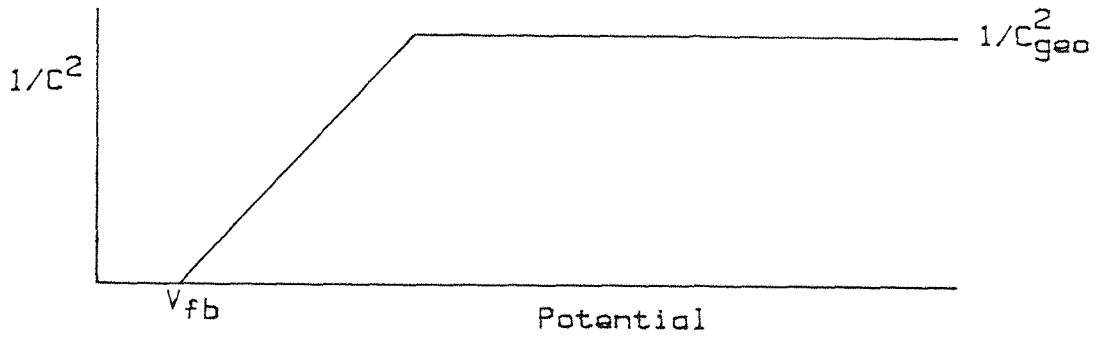

Fig. 2.11. Theoretical Mott-Schottky slot for an anodic oxide film.

2.2.6 The effect of a distribution of donor levels

The above theory only applies if there is only one type of donor level, which is completley ionised at room temperature. This may be the case for a single crystal, but is unlikely in a polycrystalline anodic oxide film. A more realistic model involves additional donor levels, which are not ionised until the Fermi energy passes through them at higher band bending. The effect of various donor level distributions has been considered by McAleer (17).

The simplest of the cases considered by McAleer (197), based on work by Myamlin (28), involves a single deep donor level in addition to the completely ionised one. At low potentials the space charge capacitance is given by (assuming $\Delta\phi >> {}^{kT}/_{e}$)

$$C_{sc} = \left(\frac{\epsilon \varepsilon_o \, eN_s}{2 \Delta \phi} \right)^{\frac{1}{2}} \qquad 2.49$$

where N_s is the density of shallow donors, which are completely ionised at room temperature, without the application of a field.

At higher potentials, the Fermi energy level will move through the deep donor level, so that the space charge capacitance becomes

$$C_{sc} = \left(\frac{\epsilon \varepsilon_o \, e(N_s + N_t)}{2 \Delta \phi} \right)^{\frac{1}{2}} \qquad 2.50$$

where N_t is the density of deep donors.

The Mott-Schottky plot for this model (Fig. 2.12) exhibits a discontinuity at $\Delta\phi^*$, the potential at which the Fermi energy level moves through the deep donor level.

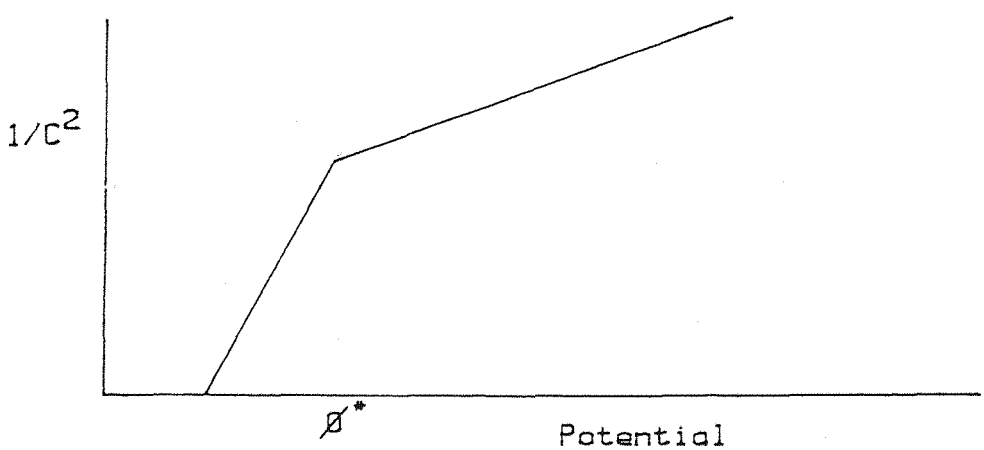

Fig. 2.12. Theoretical Mott-Schottky plot for a semiconductor with a single deep donor level in addition to the completely ionised one. ϕ^* represents the potential at which the Fermi level moves through the deep donor level.

The slope where $\Delta\phi < \Delta\phi^*$ will be inversely proportional to N_s, whereas that when $\Delta\phi > \Delta\phi^*$ will be inversely proportional to $(N_s + N_t)$.

It is possible to see from this model, that a curved Mott-Schottky plot could arise as a result of a continuous donor level distribution.

2.3 The Effect of Light on Semiconducting Films

2.3.1 Optical Transitions

Electrons from the valence band can be promoted across the forbidden bandgap to the conduction band if photons of sufficient energy, ($h\upsilon > Eg$), are absorbed.

The photon absorption process is subject to moment conservation. In the case of a direct transition (Fig. 2.13a), no change in the promoted electron's wave vector, k, occurs. If, however, the transition involves the absorption or emission of a quantised lattice vibration, or a phonon, it is referred to as indirect (Fig. 2.13b). In general, the oscillator strength of an indirect transition is two to three orders of magnitude lower than a direct transition, as it only comes about by a second order perturbation.

The crystal symmetry of the semiconductor, described by the crystallographic space group of the crystal, gives rise to a further selection rule for optical transitions (37). As a result, some transitions are allowed for all values of k and others are only allowed at $k \neq 0$. The latter are called forbidden transitions and are of a much lower oscillation strength.

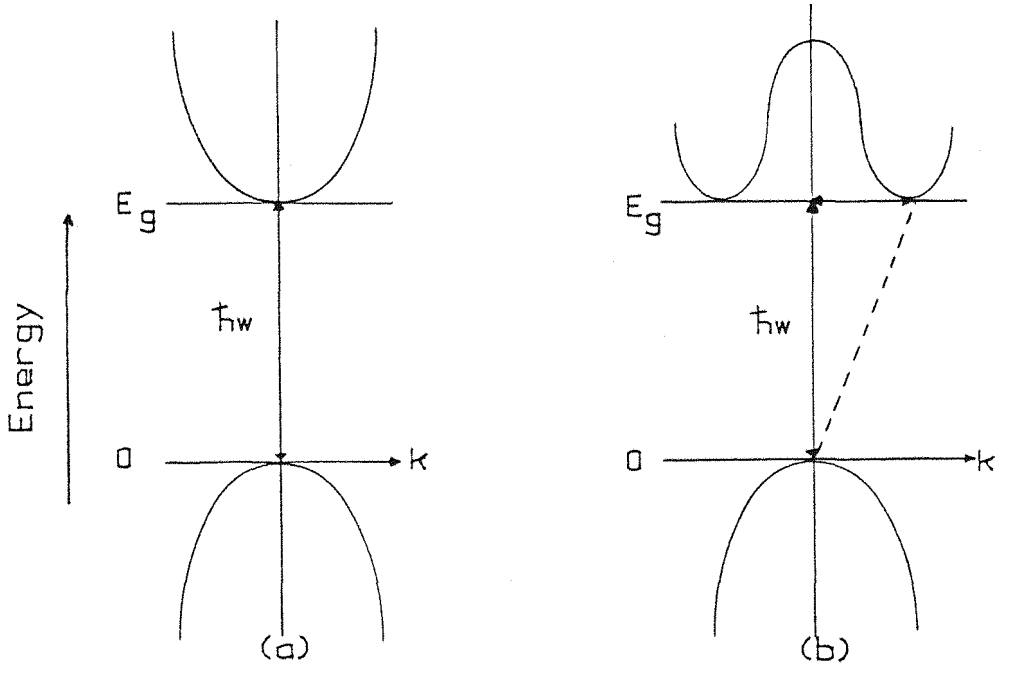

Fig. 2.13 Schematic representations of a) a direct and b) an indirect transition.

The amount of light absorbed by a material is given by the Beer-Lambert Law,

$$I_t = I_o \text{ Exp } [-\alpha(\lambda)d] \qquad 2.51$$

where I_o is the incident light, which has been corrected for reflection, I_t is the transmitted light, $\alpha(\lambda)$ is the absorption coefficient at wavelength λ and d is the path length through the material.

If parabolic energy bands are assumed, the absorption coefficient can be shown (38) to be related to the incoming photons' energy by

$$\alpha = \frac{\beta_n (h\nu - Eg)^n}{h\nu} \qquad 2.52$$

Where β_n is a constant and the value of n depends on the kind of transition.

i) $n = {}^1/_2$ corresponds to a direct allowed transition. The value of α rises rapidly from threshold and may reach values of 10^6 cm^{-1}.

ii) $n = {}^3/_2$ corresponds to a direct forbidden transition.

iii) n = 2 corresponds to an indirect allowed transition. The value of α rises only slowly from threshold.

iv) $n = {}^1/_3$ corresponds to an indirect forbidden transition.

Values of α for chemical vapour depositioned TiO_2 films on SnO_2 coated quartz have been presented by Memming et al. (39).

2.3.2 Production of Photocurrents

The mechanism of photocurrent generation at a semiconductor/electrolyte interface has been studied (40-43) extensively, and several quantitiative treatments are available (44).

Consider the case of an n-type semiconductor in contact with an electrolyte. In the dark, the number of holes in the valence band will be extremely small, but on exposure to light of the appropriate energy, this value will increase greatly as electrons are excited to the conduction band. A photocurrent will only arise, however, if the excited electrons and the remaining holes are separated. This can be achieved by the application of an electric field, so that the conduction band electrons migrate towards the back contact and the holes in the valence band migrate towards the semiconductor/electrolyte surface, where they can oxidise solution species (Fig. 2.14).

$$h^+ + R \longrightarrow O \qquad 2.53$$

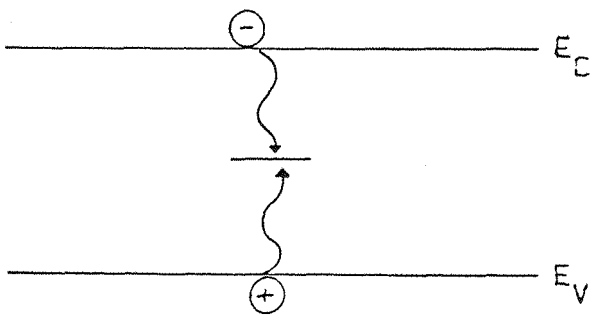

Fig. 2.15 Schematic representation of electron-hole recombination occurring via a recombination centre.

Photoelectrolysis, in which the speices undergoing oxidation and reduction is water, has received particular attention due to its potential as a means of energy conversion and storage (45-47).

It has been suggested (48) that charge transfer reaction at semiconductors are two step processes. The first involves charge transfer from the electrolyte to some state at the semiconductor surface, and the second the capture, by this intermediate, of a hole from the valence band.

2.3.2 The Gartner Theory (40)

Although originally developed to explain the photocurrent-voltage behaviour at a semiconductor/metal junction, the Gartner model has been adapted by Butler (41) for semiconductor/electrolyte systems.

The total minority carrier flux, J_p, through the depletion layer is given by

$$J_p = J_{SCR} + J_{LS} \qquad 2.54$$

where J_{SCR} is the flux due to the minority carriers generated within the depletion layer and J_{LS} is the diffusion flux of minority carriers generated in the bulk, but diffusing into the depletion layer. In the absence of recombination, the total flux of minority carriers at the semiconductor/electrolyte surface can be shown (40,41,44,49,50) to be,

$$J_{p(x=0)} = I_o \left(1 - \frac{\text{Exp}\,(-\alpha L_s)}{1+\alpha L_p} \right) \qquad 2.56$$

the current density is therefore

$$j = eI_o \left(1 - \frac{\text{Exp}(-\alpha L_s)}{1 + \alpha L_p} \right) \qquad 2.57$$

where L_p is the diffusion length of minority carriers.

The absolute photocurrent conversion efficiency is defined as,

$$\Phi = \frac{\text{photo-induced interfacial electron transfer flux}}{\text{incident photon flux}} \qquad 2.57a$$

so from equation 2.57,

$$\Phi = 1 - \frac{\text{Exp}(-\alpha L_s)}{1+\alpha L_p} \qquad 2.58$$

The limiting form of equation 2.58 when $L_p \longrightarrow 0$ and $L_s \longrightarrow L_f$, is

$$\Phi = 1 - \text{Exp}(-\alpha L_f) \qquad 2.59$$

this is identical to the Beer-Lambert Law, if Φ is replaced by the fraction of the light incident on the electrodes surface that is absorbed by the film I_a/I_o.

2.3.4 Recombination Processes

2.3.4.1 Bulk recombination

If the electron-hole pair created by illumination is not separated by an electric field, recombination will occur via a radiative or a non-radiative route. The radiative mechanism is similar to absorption, in that it depends on the densities of the occupied initial states and unoccupied final states. By contrast, the non-radiative recombination route uses deep energy levels or recombination centres (51), which may be present in the bandgap. These recombination centres are associated with imperfections in the structure of the semiconductor and capture carriers readily from either band. Recombination centres are normally fully occupied by majority carriers, so the centre first captures a minority carrier before being reoccupied by the majority carrier, thus the electron hole pair are recombined and the excited electron is returned to the valence band (Fig. 2.15).

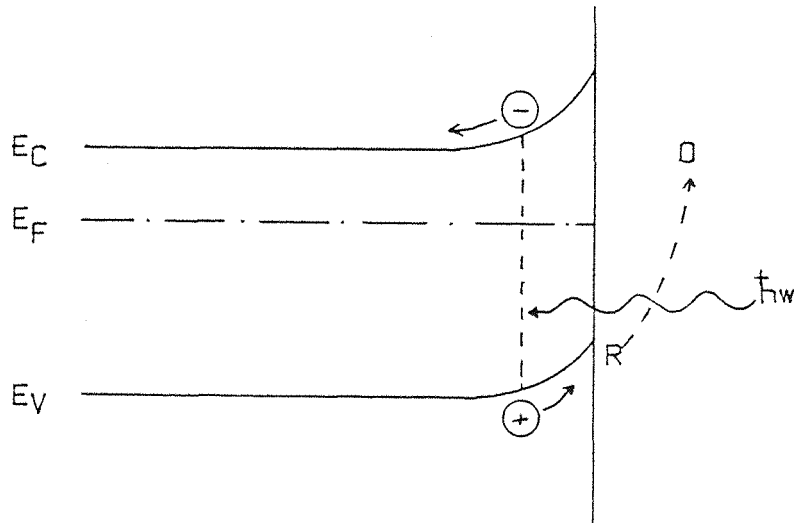

Fig. 2.14. An n-type semiconductor/electrolyte contact under illumination.

As the probability of energy emission in successive steps is considerably higher than emission by one large single step (28), the non-radiative process is more likely.

A third route by which bulk recombination can occur (32), is for an electron in the conduction band to be caught by a vibrationally-excited interband state, before cascading through a series of low lying states, emitting a phonon for each step. Finally it is possible for recombination to take place via localised defects, which may provide a continuum of states right across the bandgap. This last route is likely to be particularly important in polycrystalline anodic oxide films, where there will be substantial long-range disorder, as well as a high probability of incorporation of impurities from the metal substrate or from the electrolyte.

2.3.4.2 Surface recombination effects on the photocurrent

At a surface, there is a strong singularity in the crystal lattice that gives rise to a large number of "dangling-bonds" which can easily absorb impurities. A high concentration of interband levels is therefore available to act as recombination sites, increasing the probability that electrons and holes created within a diffusion length will combine.

It has been suggested by Wilson (52) that the surface bound intermediates believed to be involved in charge transfer reactions can also act as recombination centres. The flux of holes to the surface which results in a photocurrent, J_p, will therefore be given by

$$J_p = J_h - J_e = J_h - J_r \qquad 2.60$$

where J_h is the total flux of holes to the surface and J_e is the flux of electrons to the surface which then recombine with holes, thus J_e is equivalent to being a recombination flux of holes, J_r.

Peter et al. (49,53,54) have produced a mathematical model to show the influence of surface recombination and recombination in the space charge region on the photocurrent-voltage characteristic curves for semiconductors.

Figure 2.16 shows the theoretical photocurrent-voltage responses for a semiconductor with a single surface level and with an exponential distribution of levels. Clearly the energy distribution of surface recombination centres has a pronounced effect near the photocurrent onset potential.

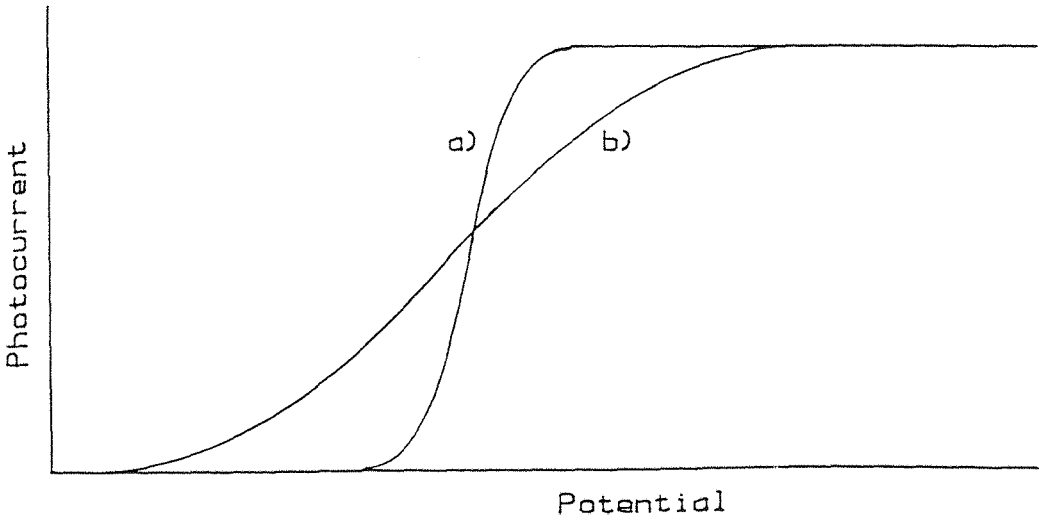

Fig. 2.16. Theoretical photocurrent-voltage responses for a semiconductor with a) a single surface level and b) an exponential distribution of levles according to the model of Wilson (48).

Analysis of photocurrent-voltage curves, of n-type semiconductors has been carried out by Laser (55) who considered three possible modes of hole injection from the electrode into the electrolyte.

i) Via a surface state, which is also a recombination centre.
ii) Via the valence band, in the presence of surface recombination.
iii) With a varying rate constant.

The third mode of charge transfer was first suggested by Gerischer (56), who pointed out that hole injection could not take place unless the quasi Fermi level of the holes in the semiconductor surface was equal or below the energetic locations (57) of the hole acceptor. Thus the value of the formal rate constant, k_ω for the injection of non-equilibrium holes into levels in the electrolyte which are energetically located above the quasi Fermi level of the holes at the semiconductor surface, should be smaller than the value of k_ω for more matched levels. Since the position of the quasi-Fermi level depends on the surface potential, the value of k_ω for a given hole acceptor will vary according to the applied electric field.

Each of the three above models predicts a quenching of the photocurrent near the flat band potential and it is difficult to distinguish between them from steady state measurements, although recently developed time resolved techniques promise to be more successful (53,54).

2.3.5 A simple model for the generation of photocurrent in thin anodic films in the absence of surface recombination

For thin films, < 10 nm, it is likely that the penetration depth of the incident light will be greater than the thickness of the film (58). The light will therefore be reflected at the metal substrate, passing through the film a second time. (Fig. 2.17).

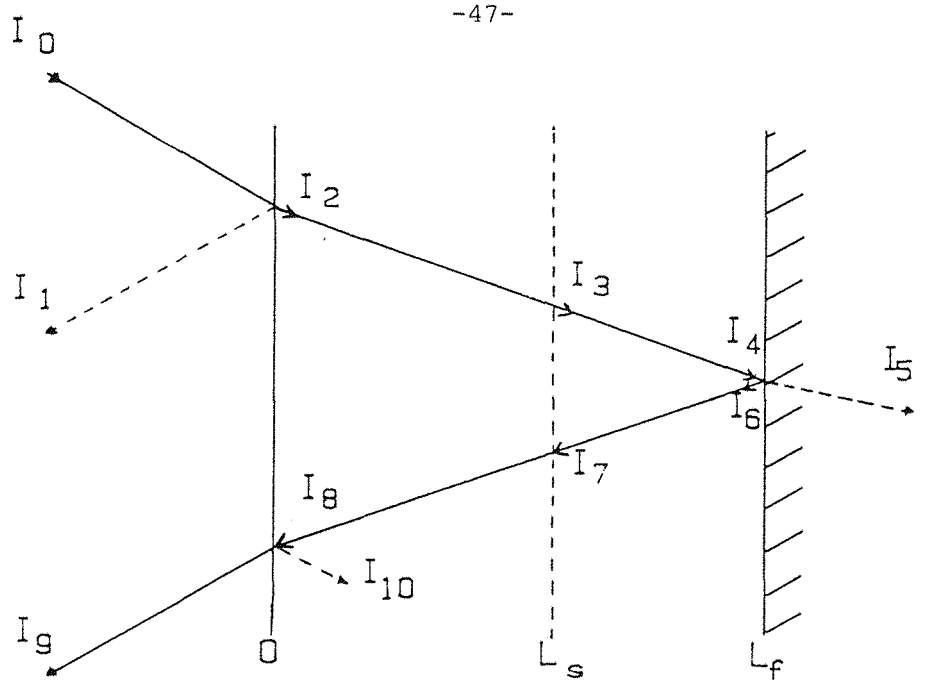

Fig. 2.17. Schematic representation of the trajectory for light incident on the surface of a thin anodic oxide film.

If the anodic oxide film obeys the Cabrera-Mott theory during growth, a substantial field will be required at the metal/oxide interface. This can only be achieved if the Schottky length is greater than the film thickness. Under this condition, the electric field extends throughout the film, increasing the probability of charge carrier separation, so that the entire film is capable of contributing towards the photocurrent. Therefore, if reflection at the metal/oxide interface is 100% and no reflection occurs at the oxide/electrolyte interface, equation 2.58 becomes

$$\Phi = 1 - \mathrm{Exp}\ (-2\ \alpha L_f) \qquad 2.61$$

This relationship has been used to characterise the growth of the oxide film on titanium (59).

For oxide films with high donor densities ($> \sim 10^{19}$ cm^{-3}), the Schottky length may become shorter than the film thickness, if the field is reduced after growth. Since electron-hole pairs created more than one diffusion length outside the space charge region will no longer be separated, rapid recombination will occur. As a consequence, most of the light absorbed outside the depletion layer will not contribute towards the photcurrent. Equation 2.58 then becomes (60)

$$\Phi \cong 1 - \frac{\mathrm{Exp}(-2\alpha L_s)}{1 + 2\alpha L_p} \qquad 2.62$$

Using equation 2.39 to substitute for L_s gives,

$$\text{Ln } (1-\Phi) = \left(\frac{8\alpha^2 \varepsilon \varepsilon_o}{eN}\right)^{\frac{1}{2}} \Delta\phi^{\frac{1}{2}} - \text{Ln}(1 + 2\,\alpha L_p) \qquad 2.63$$

Hence of plot of $\text{Ln}(1-\Phi)$ vs $\Delta\phi^{\frac{1}{2}}$ should be a straight line with a slope proportional to ε/N, allowing a comparison with the values of εN obtained from Mott-Schottky plots.

McAleer and Peter (59) have used equation 2.63 to show that anodic oxide films on titanium appear to grow by high-field migration until the space charge in the film reduces the field at the metal/oxide interface to zero ($L_s = L_f$). As a consequence, the growth limit of the film, at a constant potential is determined by the donor density and a true steady-state thickness may be defined.

2.3.6 Effect of reflection on photocurrents

If the diffusion length of minority carriers is sufficiently small, most of the photocurrent will arise from the absorption of light in the space-charge region. Figure 2.17 shows that the photocurrent conversion efficiency under these conditions can be expressed as,

$$\Phi = \frac{I_2 - I_3}{I_o} + \frac{I_7 - I_8}{I_o}$$

$$= (A + Be^{\alpha L_s})\ (1 - e^{-\alpha L_s}) \qquad 2.64$$

where

$$A = (1 - R_{12}) \qquad 6.25$$

$$B = (1 - R_{12})R_{23}\ e^{-2\alpha L_f} \qquad 2.66$$

and R_{12} and R_{23} are the coefficients of reflection at the electrolyte/oxide and the metal/oxide interfaces respectively.

Multiplication of both sides of equation 2.64 by $e^{\alpha L_s}$ and rearrangement produces a quadratic expression, with roots given by

$$e^{\alpha L_s} = \frac{-(A-B-\Phi) \pm \sqrt{(A-B-\Phi)^2 + 4AB}}{2B} \qquad 2.67$$

The boundary condition that $\Phi = 0$ when $L_s = 0$ restricts the solution to the positive root. If the right hand side of equation 2.67 is written as Λ and L_s is substituted using equation 2.39, then the following is obtained.

$$\alpha\left(\frac{2\varepsilon\varepsilon_o}{eN}\right)^{\frac{1}{2}} \Delta\phi^{\frac{1}{2}} = Ln\Lambda \qquad 2.68$$

Unfortunately $\Delta\phi$ is difficult to determine exactly and the donor density in the film may be inhomogeneous, resulting in the value of N varying with the size of the applied electric field. However, the Schottky length is also related to the space charge capacitance by

$$C_{sc} = {}^{\varepsilon\varepsilon_o r}/_{L_s} \qquad 2.69$$

assuming ${}^{kT}/_{e} << \Delta\phi$. By combining equations 2.51 and 2.53 a relationship independent of both $\Delta\phi$ and N can be derived,

$$(\alpha\varepsilon\varepsilon_o r)/C_{sc} = Ln\Lambda \qquad 2.70$$

A plot of $Ln\Lambda$ against ${}^{1}/_{C}$ should yield a straight line which passes through the origin and has a slope proportional to α. However, in practice the measured capacitance is given by

$${}^{1}/_{C_{meas}} = {}^{1}/_{C_{sc}} + {}^{1}/_{C_H} \qquad 2.47$$

hence the above plot will not pass through the origin, but instead it will have an intercept at ${}^{1}/_{C_H}$.

2.4 Reflection of Light from Surface Oxides

2.4.1 Optical principles (61)

The electric vector associated with a light wave oscillates in a plane orthogonal to the direction of propagation and the intensity of the light is proportional to the square of the electric field. Many light sources produce unpolarised light, where the planes of oscillation of the electric vector are randomized with respect to the direction of propagation. When light is transmitted through, or reflected from, a surface, the process is usually more efficient for waves with certain orientations of the electric vector with respect to the physical surface involved. These will dominate the resultant beam coming from the surface giving rise to partially polarised light. If all the electric vectors, in the resultant beam have the same angle of orientation to the axis of propagation, then the beam is referred to as linearly, or plane, polarised.

For reflection experiments, the state of polarisation is always referred to the plane of incidence; if the polarisation of the wave is parallel to this plane then it is referred to as p-polarised, whereas if it is perpendicular it is called s-polarised light (Fig. 2.18). Any other angle of polarisation can be resolved into p and s components.

2.4.2 Elliptically polarised light

If a linearly polarised light beam is reflected from a surface, it is likely that the p and s components will undergo different changes in their respective amplitudes and phases. As a result, the tip of the electric vector traces out the shape of an ellipse, as a function of time, in a given plane (Fig. 2.19). The light is said to be elliptically polarised.

Elliptically polarised light can be described by two parameters, Δ and ψ, where Δ is the phase difference between the p and s components and $\tan\psi$ is the ratio of their amplitudes.

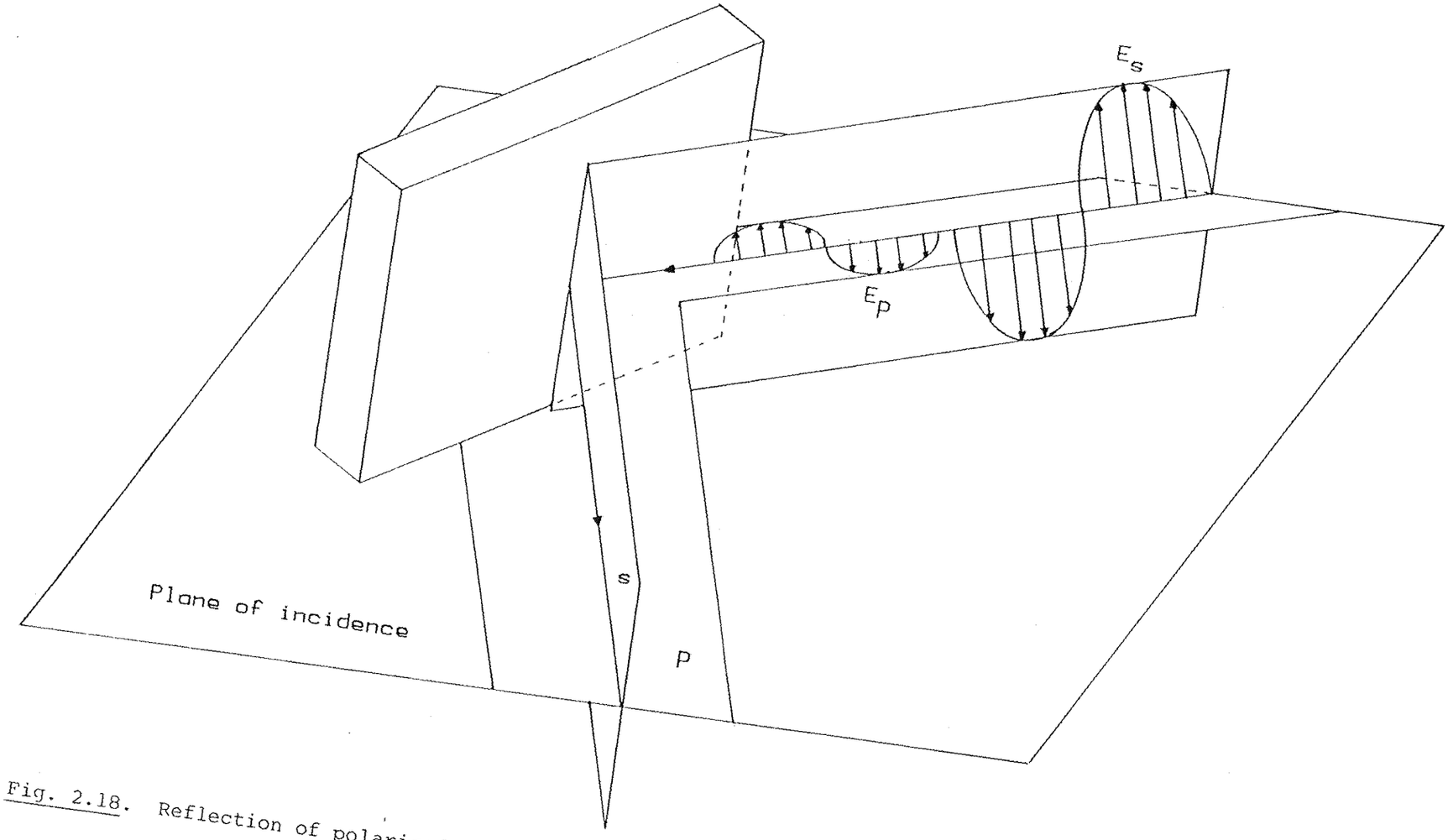

Fig. 2.18. Reflection of polarized light from a surface showing p and s polarizations.

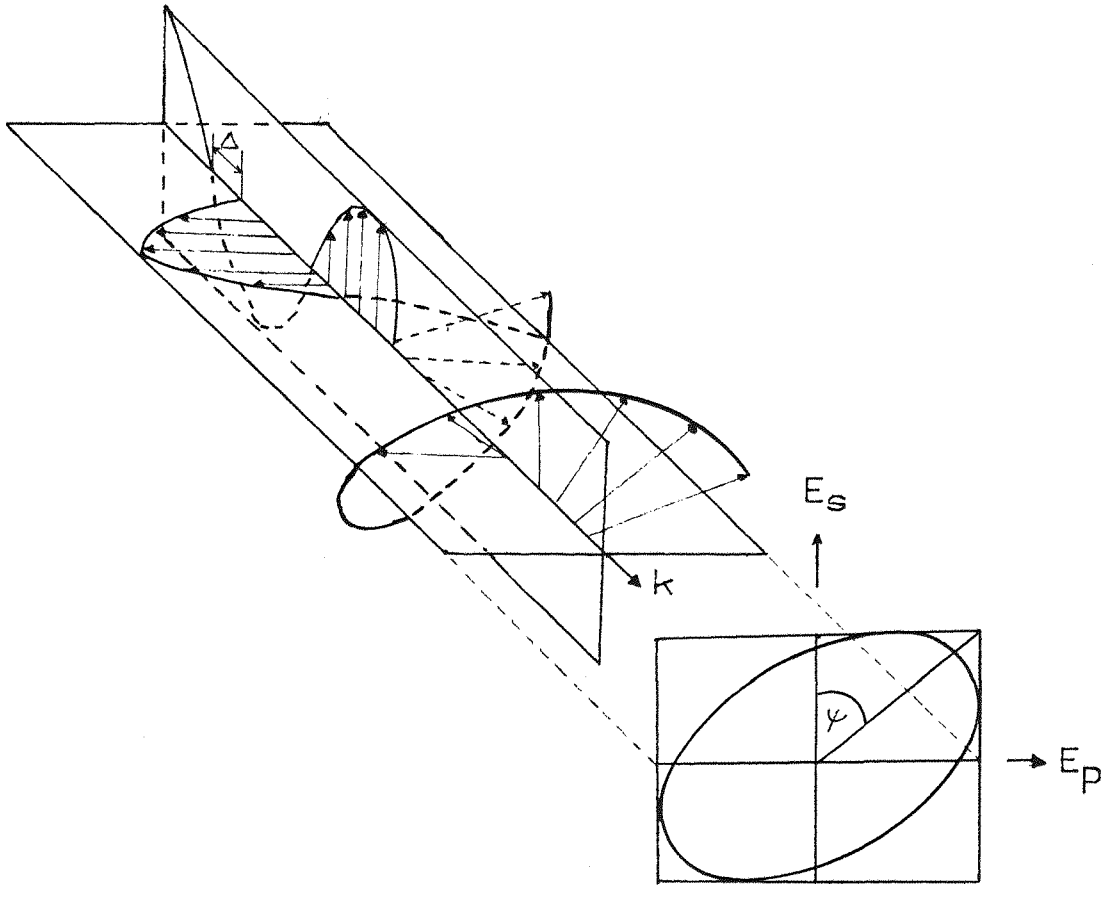

Fig. 2.19. Schematic representation of elliptically polarized light resulting from a phase shift, Δ, occurring between p and s components.

$$\Delta = \delta_p - \delta_s \quad 0 < \Delta < 360 \qquad 2.71$$

$$\tan\psi = \left|\frac{E_p}{E_s}\right| \quad 0 < \psi < 90 \qquad 2.72$$

where δ_x is the time-independent phase and $|E|$ is the real amplitude of the electric field. δ_x and $|E|$ are related by

$$E_x = |E| \, e^{i\delta_x} \qquad 2.73$$

where E_x is the time-dependent complex amplitude.

A special case arises when the two amplitudes are equal ($\tan\psi = 1$) and the phase shift is 90°, as this causes the electric vector to trace a circle with time. Consequently, this condition is known as circular polarisation.

2.4.3 Optical properties of materials

The optical characteristics of a material depend on its optical constants. The first of these is the absolute index of refraction, n, which is defined as the velocity of light in a vacuum, c, divided by the velocity of light in the material under investigation, v; it should be noted that this definition refers to plane waves (62) where at any instant in time the rate of propagation of the wave is a constant over all three spatial planes. The other optical constants are the optical-frequency dielectric constant, ε, the magnetic permeability μ, the extinction coefficient k and the absorption coefficient α. These constants are related in the following way (62),

$$n = (c/v) = (\varepsilon\mu)^{\frac{1}{2}} \qquad 2.74$$

$$\alpha = 4\pi k/\lambda \qquad 2.75$$

It is often convenient to use the complex refractive index $\hat{n}$.

$$\hat{n} = n - ik \qquad 2.76$$

where $i = \sqrt{-1}$. By analogy, there is a complex optical frequency dielectric constant, $\hat{\varepsilon}$,

$$\hat{\varepsilon} = \varepsilon' - i\varepsilon'' \qquad 2.77$$

since

$$\hat{n} = (\mu\,\hat{\varepsilon})^{\frac{1}{2}} \qquad 2.78$$

it follows that

$$\varepsilon' = \frac{n^2 - k^2}{\mu} \qquad 2.79$$

$$\varepsilon'' = \frac{2nk}{\mu} \qquad 2.80$$

For nearly all materials, μ is essentially unity for most optical frequencies.

2.4.4 Optical reflection

2.4.4.1 Reflection from a dielectric surface

The reflection of light from a non-absorbing dielectric interface can be described by the Fresnel amplitude reflection coefficients r_x. These give the ratio of the reflected to the incident electric field amplitudes for both the p and s components.

$$r_{p1,2} = E'_p/E_p \qquad 2.81$$

$$r_{s1,2} = E'_s/E_s \qquad 2.82$$

Primed variables denote reflected waves and unprimed denote incident waves.

These coefficients were used by Fresnel to relate angles of incidence θ_1 and refraction θ_2, to refractive indices (Fig. 2.20). Although Fresnel's original derivation is no longer accepted, the Fresnel relationships have been verified experimentally and are the same as those deduced from modern electromagnetic theory.

$$r_{p1,2} = \frac{n_1\cos\theta_2 - n_2\cos\theta_1}{n_1\cos\theta_2 + n_2\cos\theta_1} = \frac{\tan(\theta_1 - \theta_2)}{\tan(\theta_1 + \theta_2)} \qquad 2.83$$

$$r_{s1,2} = \frac{n_1\cos\theta_1 - n_2\cos\theta_2}{n_1\cos\theta_1 + n_2\cos\theta_2} = \frac{\sin(\theta_1 - \theta_2)}{\sin(\theta_1 + \theta_2)} \qquad 2.84$$

The angles of refraction may be calculated from Snell's Law.

$$n_{2/n_1} = \frac{\sin\theta_1}{\sin\theta_2} \qquad 2.85$$

As $0° < \theta_1 < 90°$, when $n_2 > n_1$ it follows from Snell's Law that $\theta_1 > \theta_2$. Therefore equation 2.75 will always result in r_s being negative, whilst equation 2.74 will give a positive value of r_p at $\theta_1 = 0°$, but as θ_1 increases, r_p will be found to decrease being zero when the sum of $\theta_1 + \theta_2 = 90°$, since $\tan\pi/2$ is infinite. The angle of incidence at which $r_p = 0$ is referred to as the Brewster or polarising angle, θ_p. As θ_1 increases beyond θ_p, r_p will become negative.

$$r_s < 0 \quad \text{for all } \theta_1 \qquad 2.86$$

$$r_p > 0 \quad \text{for } \theta_1 < \theta_p \qquad 2.87$$

$$r_p = 0 \quad \text{for } \theta_1 = \theta_p \qquad 2.88$$

$$r_p < 0 \quad \text{for } \theta_1 > \theta_p \qquad 2.89$$

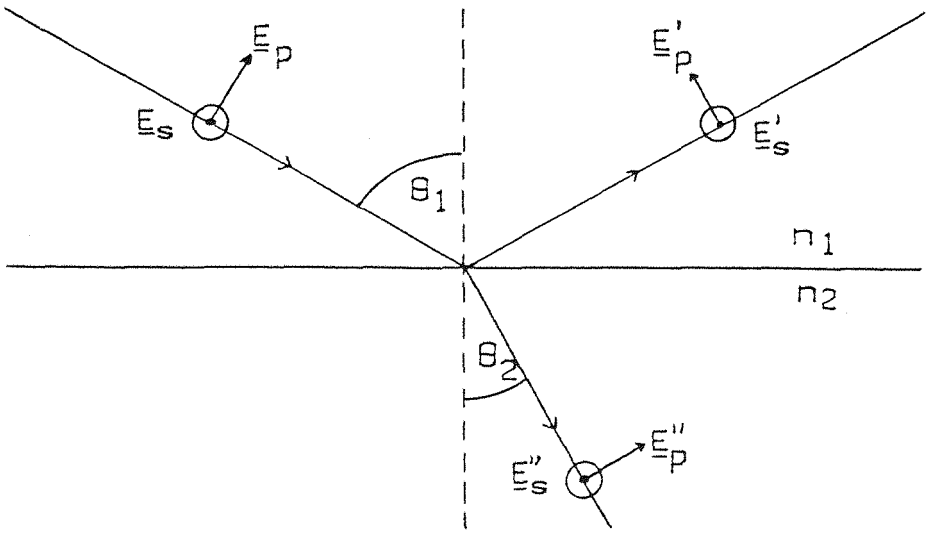

Figure 2.20. Reflection and refraction at a dielectric surface. The vectors $\underline{E}_s$ are normal to the phase of incidence and have been denoted by the symbol ⊙.

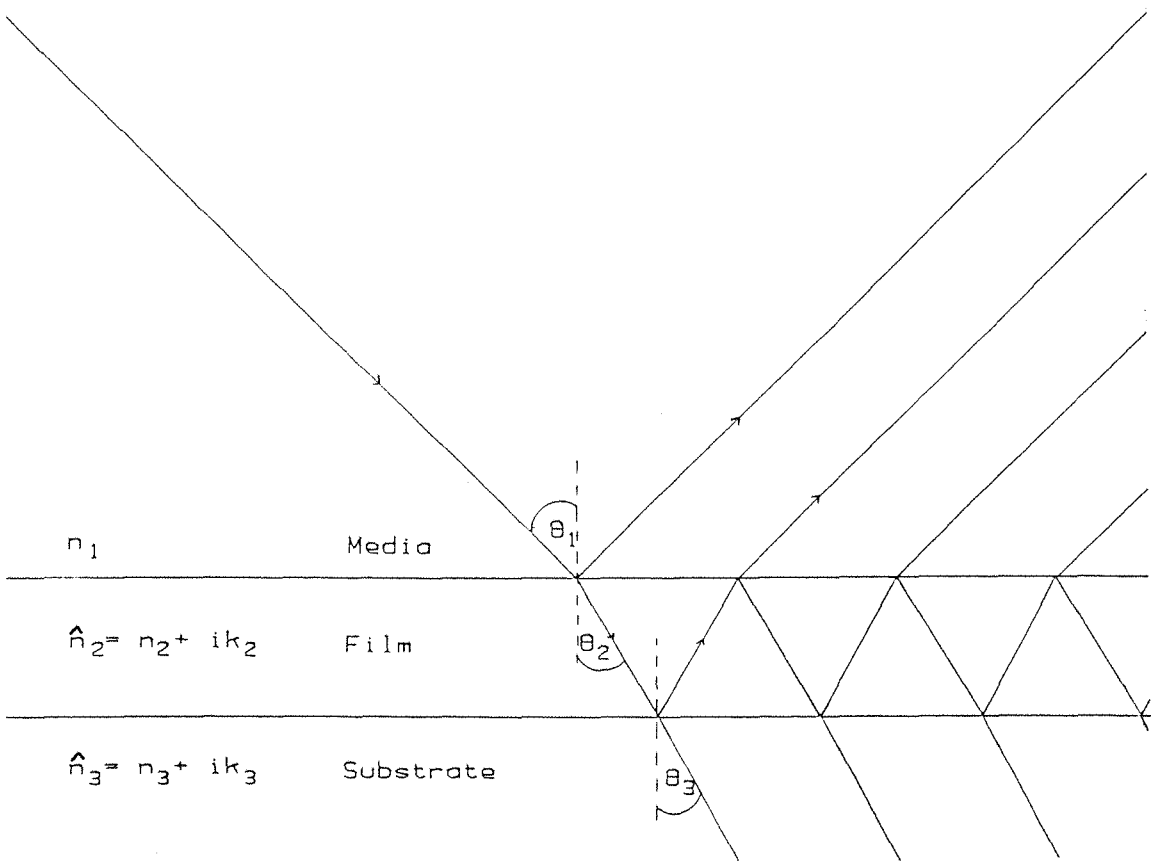

Figure 2.21. Reflection and refraction at a film covered surface.

The negative sign linked with the reflection coefficients indicates a phase shift of 180°C or π radius. Thus r_s is always out of phase by 180°, but r_p is only out of phase with respect to the incident beam of $\theta_1 > \theta_p$.

2.4.4.2 Reflection from a metal surface

Metals contain delocalised free electrons which are able to move under the influence of an electric field. An incident electromagnetic wave will cause these electrons to enter into oscillations that are damped by collisions with the thermally agitated lattice or by lattice imperfections. As a consequence, the size of the electric vector is reduced and the phases of both the p and s components are shifted.

The description of reflection from a metal surface requires the introduction of the complex refractive index (equ. 2.76) into both the Fresnel equations and Snell's Law. This approach gives rise to complex angles of refraction due to the fact that for obliquely incident polarised light, the planes of equal amplitude and the planes of equal phase are not coincident for light propagating through an absorbing media (63). The Fresnel coefficients are now also complex and have the form

$$\hat{r}_p = \frac{|E'_p|}{|E_p|} \text{ Exp } [i\ (\delta'_p - \delta_p)] \qquad 2.90$$

$$\hat{r}_s = \frac{|E'_s|}{|E_s|} \text{ Exp } [i\ (\delta'_s - \delta_s)] \qquad 2.91$$

where δ_x is the phase of the oscillation related to a reference. If $|r|$ represents the modulus of the attenuation of the amplitude and Δ the phase change due to reflection, the Fresnel equations can be recast in the form

$$\hat{r}_p = |r_p| \text{ Exp } i\ \Delta_p \qquad 2.92$$

$$\hat{r}_s = |r_s| \text{ Exp } i\ \Delta_s \qquad 2.93$$

Ellipsometers are used to find the ratio of the complex reflections for the p and s components

$$\rho = \hat{r}_p/\hat{r}_s \qquad 2.94$$

The complex reflection coefficients can then be related to the angles of incidence and refraction and to the refractive indices using equation 2.83 and 2.84.

2.4.4.3 Reflection from a film covered surface (Three layer model)

Drude, (1889) derived the relationship between the complex amplitudes of the reflected and transmitted waves and that of the plane polarised light incident on the interphase, by summing the Fresnal reflection and transmission coefficients associated with a multiple reflection(Fig. 2.21). If the film is assumed to be isotropic, parallel sided and semi-infinite in extent, with a uniform dielectric constant and a thickness d, then summation of the multiple reflected and transmitted waves to infinity, produce the expression

$$\hat{R} = \frac{\hat{r}_{12} + \hat{r}_{12}\ \mathrm{Exp}\ (-2i\beta_\omega)}{1 + \hat{r}_{12}\ \hat{r}_{23}\ \mathrm{Exp}\ (-2i\beta_\omega)} \qquad 2.95$$

where $\hat{R}$ is the total complex reflection coefficient and β_ω is the phase change produced by a single crossing of the film by the wave.

$$\beta_\omega = 2\pi\ d\ \cos\theta_2/\lambda \qquad 2.96$$

The complex Fresnel reflection coefficients are related to the angles of incidence and refraction and the optical constants for each of the phases involved by

$$\hat{r}_{p1,2} = \frac{n_1\cos\theta_1 - n_1\cos\theta_2}{n_2\cos\theta_1 + n_1\cos\theta_2} \qquad 2.97$$

$$\hat{r}_{p2,3} = \frac{n_3\cos\theta_2 - n_2\cos\theta_3}{n_3\cos\theta_2 + n_2\cos\theta_3} \qquad 2.98$$

$$\hat{r}_{s1,2} = \frac{n_1\cos\theta_1 - n_2\cos\theta_2}{n_1\cos\theta_1 + n_2\cos\theta_2} \qquad 2.99$$

$$\hat{r}_{s2,3} = \frac{n_2\cos\theta_2 - n_3\cos\theta_3}{n_2\cos\theta_2 + n_3\cos\theta_3} \qquad 2.100$$

The angles involved are still related by Snell's Law;

$$n_1\sin\theta_1 = n_2\sin\theta_2 = n_3\sin\theta_3 \qquad 2.101$$

An ellipsometer will now measure the ratio of the total complex reflection coefficients for the p and s components

$$\rho = \hat{R}_p/\hat{R}_s \qquad 2.102$$

Substitution of equations 2.90 and 2.91 into equation 2.86, on rearrangement gives

$$\rho = \frac{|E_p'|/|E_s'|}{|E_p|/|E_s|} \text{ Exp } i\,[(\delta_p' - \delta_s') - (\delta_p - \delta_s)] \qquad 2.103$$

insertion of equations 2.71 and 2.72 gives

$$\rho = \frac{\tan\psi'}{\tan\psi} \text{ Exp } [i(\Delta' - \Delta)] \qquad 2.104$$

This last equation is often given in a more simplified form as

$$\rho = \tan\psi \text{ Exp } (i\,\Delta) \qquad 2.105$$

The Drude equation relating the optical properties of the three phase system to the ellipsometrically determine values of Δ and ψ is obtained by substitution for R_p and R_s from equations 2.97 to 2.100 into equation 2.102

$$\rho = \frac{[\hat{r}_{p1,2} + \hat{r}_{p2,3}\ \mathrm{Exp}(-2i\beta_\omega)][1 + \hat{r}_{s1,2}\ \hat{r}_{s2,3}\ \mathrm{Exp}(-2i\beta_\omega)]}{[\hat{r}_{a1,2} + \hat{r}_{s2,3}\ \mathrm{Exp}(-2i\beta_\omega)][1 + \hat{r}_{p1,2}\ \hat{r}_{p2,3}\ \mathrm{Exp}(-2i\beta_\omega)]} \qquad 2.106$$

Reflection from a multilayer surface can be treated by an approach similar to the three layer model, using computer programs developed by McClackin (64).

2.4.5 Modulated electroreflectance (65)

Modulation of the applied electric field, E, will result in changes in the dielectric properties of the unperturbed solid. This can be described as a change of $\Delta\hat{\varepsilon}(E)$ in the complex dielectric function $\hat{\varepsilon}$, both $\Delta\hat{\varepsilon}(E)$ and $\hat{\varepsilon}$ being second rank tensors (Appendix 3). The quantity $\Delta\hat{\varepsilon}(E)$ may be obtained by adding a perturbation term, H', to the Hamiltonian, H_o, of the unperturbed system, then either calculating $\hat{\varepsilon}(E)$ exactly in which case $\Delta\hat{\varepsilon} = \hat{\varepsilon}(E) - \hat{\varepsilon}$, or calculating $\Delta\hat{\varepsilon}(E)$ approximately from first-order perturbation theory.

For a uniform electric field, the perturbation term of the Hamilton will be given by,

$$H' = eE.r \qquad 2.107$$

This term is not lattice periodic, since it represents an accelerating force on the electron, which destroys the Hamiltonian's translational invariance in the direction of the field. The electrolyte electroreflectance (EER) spectra obtained for suitably low fields appear to be closely related to the third derivative of the unperturbed dielectric function (66).

A simple physical model which shows the important effect of the loss of translational invariance has been put forward by Aspnes (67). First a free electron is considered, for which the Hamiltonian

$$H_o = P^2/2m \qquad 2.108$$

is invariant to translation in any direction, because the electron's momentum, P, must be rigorously conserved. Since the free electron's momentum is given by

$$P = \hbar k \qquad 2.109$$

the energy band structure for this system will be a parabola of the form

$$\mathbf{E} = \hbar^2 k^2/2m \qquad 2.110$$

The momentum of any incoming photon will be negligibly small, but if its energy, $\mathbf{E} = \hbar\omega$, is absorbed by the electron, it will cause a relatively large change in the momentum of the system. Thus it is impossible for a first-order optical transition to occur in which both energy and momentum are conserved. It follows from this that the sum of all the allowed transitions for any finite photon energy that is to say ε'', must be zero for the free electron.

However, if an electron is in a crystal, its Hamiltonian becomes

$$H_o = P^2/2m + V(r) \qquad 2.111$$

which is invariant only to translations that take the crystal into itself. This results in a relaxation in the need for the conservation of momentum, which is now only a good quantum number within a reciprocal lattice vector. The energy band structure breaks down from the free electron parabola into a series of discrete bands. First-order optical

transitions can now occur by making use of the reciprocal lattice vector to conserve momentum and they appear as vertical lines on an energy band diagram (Fig. 2.22a). A parabolic density of states distribution will now give rise to a square-root threshold shape in the imaginary part of the dielectric function (Fig. 2.22b).

Perturbation of the crystal, will convert the Hamiltonian into

$$H_o = {}^{p^2}/_{2m} + V(r) + H' \qquad 2.112$$

and will generally result in a lowering of the symmetry of the system. If the applied perturbation retains periodicity, as is the case for thermoreflectance, for example, (68) then momentum will remain a good quantum number within a reciprocal lattice vector so that optical transitions will remain vertical (Fig. 2.22a). Consequently, the dominant changes appear as small shifts in the energy bandgaps. Thus the effects on ε'' will be first order producing a first derivative lineshape (Fig. 2.22b).

In the case of electroreflectance, it is the applied electric field which is perturbed. The field accelerates the electron so that periodicity is lost and momentum is no longer a good quantum number in the field direction. The Bloch functions (69) of the unperturbed crystal become mixed and consequently optical transition will no longer be vertical, but instead spread out over a finite range of initial and final momenta (Fig. 2.23a). For small fields, the mixing will occur amongst wavefunctions close to the original vertical transition. The effect of this will be to smear out the dielectric function, ε'', resulting in a difference spectrum, (Fig. 2.23b), which can be approximated by higher derivatives of the unperturbed dielectric function. A line-shape with two zero crossings is characteristic of a third derivative spectrum.

The energy of the direct bandgap, as well as information about optical constants can be obtained via a Kramer-Kronig analysis of the EER spectra (70) (Appendix 4).

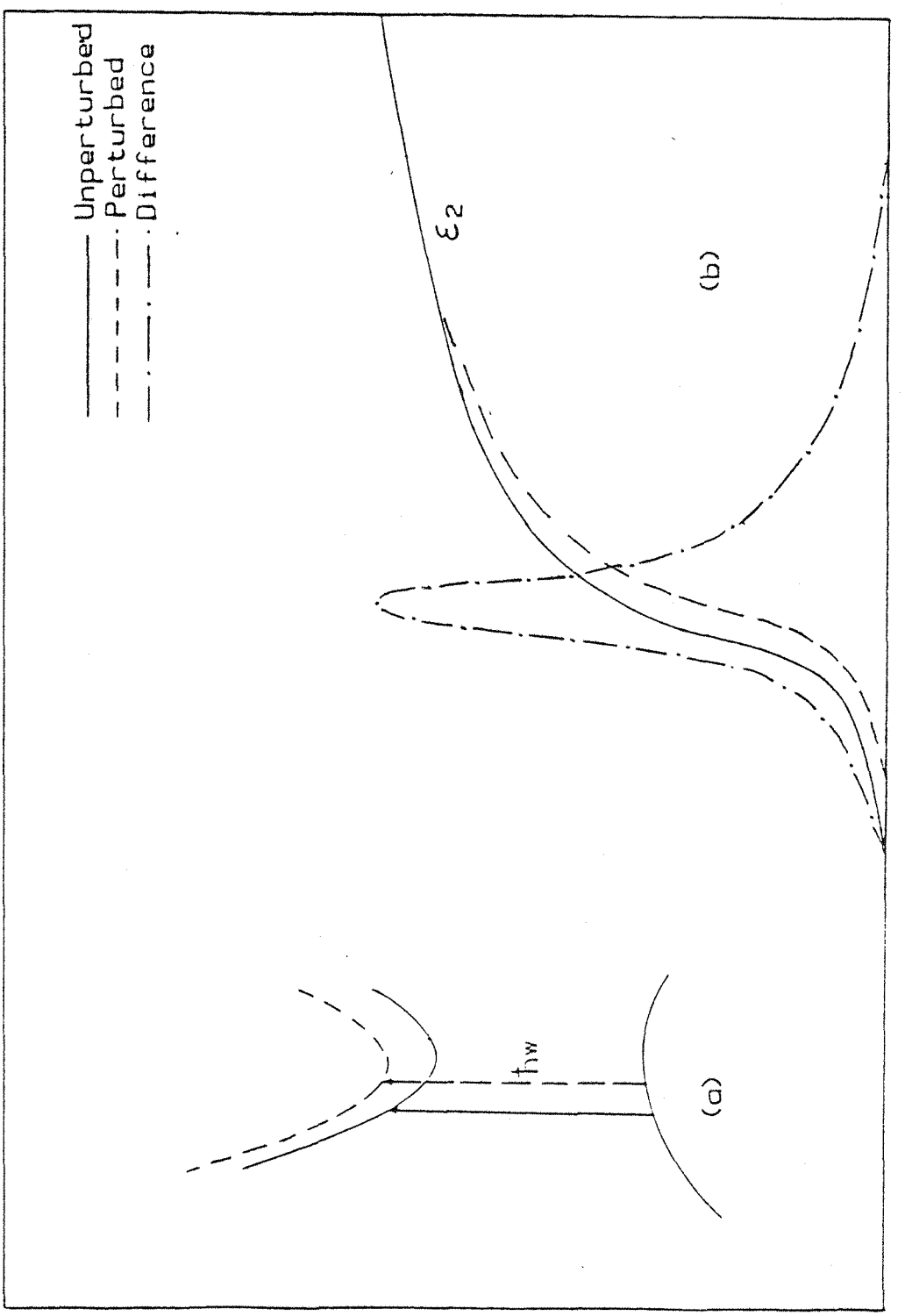

Figure 2.22 Schematic representation of a) optical absorption and b) the change in the imaginary part of the dielectric function expected for the case where lattice periodicity is preserved.

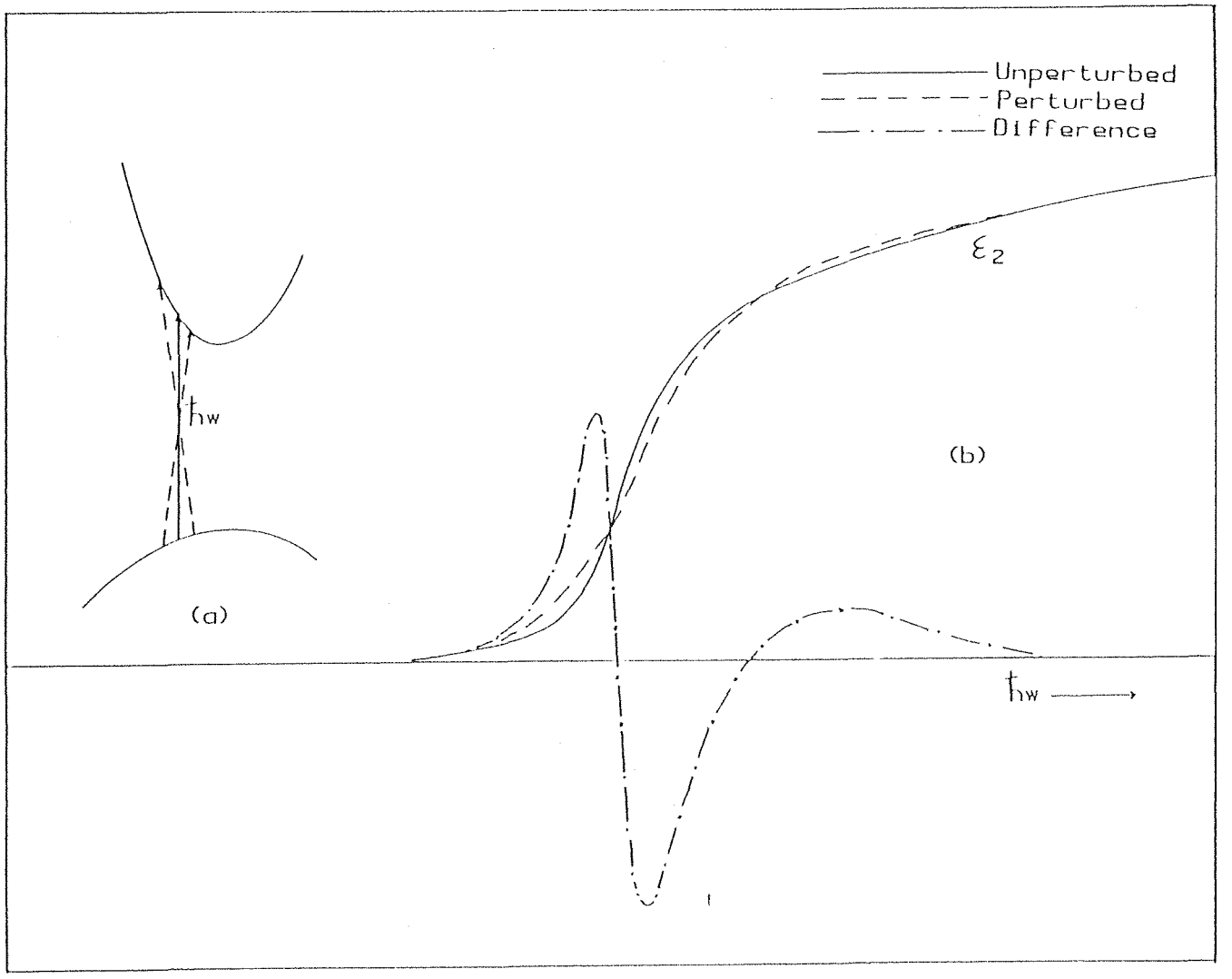

Fig. 2.23. Schematic representations of the effect of an applied perturbation on a) optical absorption and b) the imaginary part of the dielectric function for the case where lattice periodicity is not preserved.

References

1. POURBAIX, M., SCHMETS, J. & VAN MUYLDER, J; in "Atlas of Electrochemical Equilibria." Edited by Pourbaix, M; Pergamon press, Oxford (1966).
2. JAMES, W.J. & JOHNSON, J.W.; in "Standard Potentials in Aqueous Solutions", Edited by Bard, A.J., Parsons, R. & Jordan, J.; Marcel Dekker, New York, 1985.
3. VETTER, K.J.; "Electrochemical Kinetics - Theoretical and Experimental Aspects", Academic Press, New York, (1967).
4. THOMAS, N.T. & NOBE, K.; J. Electrochem. Soc. 117 (1970), 622.
5. ARMSTRONG, R.D.; J. Electroanal. Chem. 34, (1972) 387.
6. EVANS, V.R.; Z. Elektrochem. 62, (1958), 619.
7. LASER, D., YANIV, M. & GOTTESFELD, S.; J. Electrochem. Soc. 125, (1978), 358.
8. SUKHOTIN, A., & TUNGUSOVA, L.; Zasch. Metallova, 4 (1968),8.
9. ARSOV, LJ. D.; Electronchim. Acta, 30, (1985), 1645.
10. AMMAR, I.A. & KAMAL, I.; Electrochim. Acta, 16 (1971), 1540.
11. GUNTHERSCHULZE, A. & BETZ, H.; "Elektrolytkondensatoren" Krayn, Berlin (1937).
12. ASHOK, K.V.; "Electrochemistray of Metals and Semiconductors", Decker, New York. (1973).
13. CABRERA, N. & MOTT, N.F.; Rep. Prog. Phys. 12, (1949), 163.
14. VERWEY, E.J.W.; Physica, 2 (1935), 1059.
15. DEWALD, J.F.; J. Electrochem. Soc. 102 (1955) 1.
16. FROMHOLD, JNR. A.T.; "Oxide and Oxide Films" Vol. III. Ed. J.W. Diggle & A. K. Vijh. Marcel Decker Inc., New York (1976).
17. McALEER, J.F.; University of Southampton, PhD. Thesis (1980).
18. KOVER, F. & MUSSELIN, M.; Thin Solid Films, 2 (1968) 211.
19. BLONDEAU, G., FROELICHER, M., FORMENT, M. & HUGOT-LE GOFF, A.; J. Less-Common Met. 56, (1977) 215.
20. DYER, C.K. & LEACH, J.S.L.; J. Electrochem. Soc. 125 (1978) 1032.

21. YOUNG, L.; "Anodic Oxide Films", Academic Press, New York, 1961.

22. WINKEL, P. & DEGROOT, D.G.; Philips. Res. Rep. 13, (1958) 489.

23. YOUNG, L.; Trans. Faraday Soc. 55, (1959), 842.

24. GARTON, G.C.; Trans Faraday Soc. 42A, (1946) 56.

25. DUTOIT, E.C., VAN MEIRHAEGHE, R.L., CARDON, F. & GOMES, W.P.; Ber. Bunsenges. Phys. Chem. 79 (1975), 1206.

26. MADOU, M.J. & KINOSHITA, K.; Electrochim.Acta.29, (1984), 411

27. MORRISON, S.R.; "Electrochemistry at Semiconductor and Oxidized Metal Electrodes", Plenum Press, New York, 1980.

28. MYAMLIN, V.A. & PLESKOV, Y.V.; "Electrochemistry of Semiconductors" Plenum Press, New York (1967).

29. JARZEBSKI, Z.M.; "Oxide Semiconductors" Plenum Press, Oxford, 1973.

30. KINGSBURY JNR., P.I., OHLSEN, W.O. AND JOHNSON, O.W.; Phys. Rev. 175 (1968), 1091.

31. BUTLER, M.A.; J. Electrochem. Soc. 126 (1979), 338.

32. PANKOVE, J.I.; "Optical Processes in Semiconductors", Prentice-Hall, Inc., New Jersey, (1971).

33. DEWALD, J.F.; The Bell Tech. Jnl. 39, (1960), 615.

34. MOTT, N.F.; Proc. Royal Soc. A171 (1939) 27.

35. SCHOTTKY, W.; Z. Physik, 118 (1942), 539.

36. PETTINGER, B., SCHOPPEL, H.R. AND GERISCHER, H.; Ber. Bunsenges. Phys. Chem. 78, (1947), 450.

37. HARBEKE, G.; in "Optical Properties of Solids", Edited by Abeles, F.; North-Holland, Amsterdam, 1972.

38. JOHNSON, E.J.; "Semiconductors and Semimetals", Edited by Willardson, R.K. & Beer, A.C., Vol. 3, Academic Press, New York, 1977.

39. MEMMING, R., MOLLERS, F. & TOLLE, H.J.; J. Electrochem. Soc. 121, (1974), 116.

40. GARTNER, W.W., Phys. Rev. 116 (1959), 84.

41. BUTLER, M.A.; J. Appl. Phys., 48 (1977), 1914.

42. REICHMANN, J.; Appl. Phys. Lett. 36 (1980), 574

43. ALBERY, W.J., BARTLETT, P.N., HAMNETT, A. & DARE-EDWARDS, M.P.; J. Electrochem. Soc. 128 (1981) 1492.

44. PETER, L.M. in Pletcher, D. (Ed.), "Electrochemistry", Vol. 9, Specialist Periodical Report, Royal Society of Chemistry, London.

45. GHOSH, A.K. & MARUSKA, H.P.; J. Electrochem. Soc. 124, (1977) 1516.

46. BARD, A.; J. Photochem. 10 (1979) 59.

47. CARDON, F., DUTOIT, E.C., GOMES, W.P. and VANDEN KERCHOVE, F.; J. Appl. Electrochem. 8 (1978) 247.

48. WILSON, R.H.; Extended Abstracts - Electrochem. Soc. Meeting, 78-1; (1978) 1036, Princeton, New Jersey.

49. LI, J.; University of Southampton, Ph.D. Thesis, (1984).

50. BUCHANAN, J.S.; University of Southampton, Ph.D. Thesis (1985).

51. SCHOCKLEY, W. & READ, T.; Phys. Rev. 87 (1952), 835.

52. WILSON, R.H.; J. Appl. Phys. 48 (1977) 4292.

53. PETER, L.M., LI, J. & PEAT, R.; J. Electroanal. Chem. 165 (1984) 29.

54. PETER, L.M.and LI, J.; J. Electroanal. Chem. 193 (1985) 27.

55. LASER, D.; J. Electrochem. Soc. 126, (1979), 1011.

56. GERISCHER, H.; J. Electroanal. Chem. 82 (1977) 133.

57. GERISCHER, H.; Photochem. Photobiol. 16 (1972) 143.

58. PETER, L.M.; J. Electroanal. Chem. 98 (1979) 49.

59. MCALEER, J.F. & PETER, L.M.; Far. Disc. Chem. Soc. 70, (1980) 67.

60. ROTENBERG, Z.A., DZHAVRISHVILI, T.V., PLESKOV, Y.V. & ASATIANI, A.L.; Elektrokhimiya. 13, (1977) 1803.

61. JENKINS, F.A. & WHITE, H.E.; "Fundamentals of Optics", 4th ed. McGraw-Hill, New York, 1976.

62. BORN, M. & WOLF, E.; "Principles of Optics", Pergamon Press Inc., New York, 1959.

63. KNITTL, Z.; "Optics of Thin Films", Wiley, New York, 1976.

64. McCRACKIN, F.L.; "A Fortran Program for Analysis of Ellipsometer Measurements", Natl. Bur. Stand.; Tech. Note 479, U.S. Govt. Printing Office, Washington, D.C. 1969.

65. SERAPHIN, B.O.; in "Semiconductors and Semimetals, Vol. 9. Modulation Techniques", Ed. Willardson, R.K. & Beer, A.C., Academic Press, New York, 1972.

66. ASPNES, D.E.; Phys. Rev. Lett. 28 (1972), 168.

67. ASPNES, D.E.; Surf. Sci. 37 (1973), 418.

68. SERAPHIN, B.O.; in Reference 37.

69. EISBERG, R, & RESNICK, R. "Qnatum Physics of Atoms, Molecules, Solids, Nuclei and Particles", 2nd Ed. Wiley, New York, 1985.

70. STERN, F.; Solid State Phys. 15, (1963) 299.

CHAPTER 3

EXPERIMENTAL

3.1 Apparatus

3.1.1 Electrochemical Cells

A conventional three compartment cell design was used for most of the electrochemical experiments (Fig. 3.1). A water jacket was placedaround the cell in order to allow the temperature of the electrolyte to be controlled, and a quartz window was inserted into the base to enable photocurrent measurements to be carried out. During impedance measurements, the resistence of the closed tap was bypassed by placing a 1 μF capacitor between the reference electrode and a small platinum flag electrode on the other side of the tap.

A cell was designed for the electroreflectance measurements with two quartz windows to allow light to strike the electrode at 45° incidence and to collect the reflected light from the electrode surface (Fig. 3.2). For ellipsometry a cell was used which allowed an angle of incidence of 70° (Fig. 3.3).

As the electrolyte for most of the experiment was sulphuric acid, a $Hg/Hg_2SO_{4(s)}/K_2SO_{4(sat)}$ reference electrode was used. This electrode has a reference potential of -0.64 V vs. S.H.E. and all potentials quoted in this thesis are referred to the $Hg/HgSO_4$ electrode. The liquid junction potential, calculated from the Henderson equation (1) to be $|E_L| < 30$ mV, was neglected. Whenever possible, the reference electrode was separated from the working electrode compartment by a closed wetted tape to prevent mercurous sulphate from leaking into the electrolyte.

The counter electrodes were flags constructed from platinum foil, or in the case of impedance measurements, platinum gauze. The working electrodes were made from either specpure rod (Johnson Matthey), IMI 130 commercial purity or Marz grade (Materials Research) titanium. The main impurities in these grades are shown in table 3.1.

A simple button design of electrode was used for the early work at room temperature (Fig. 3.4). Here the titanium was sealed with a

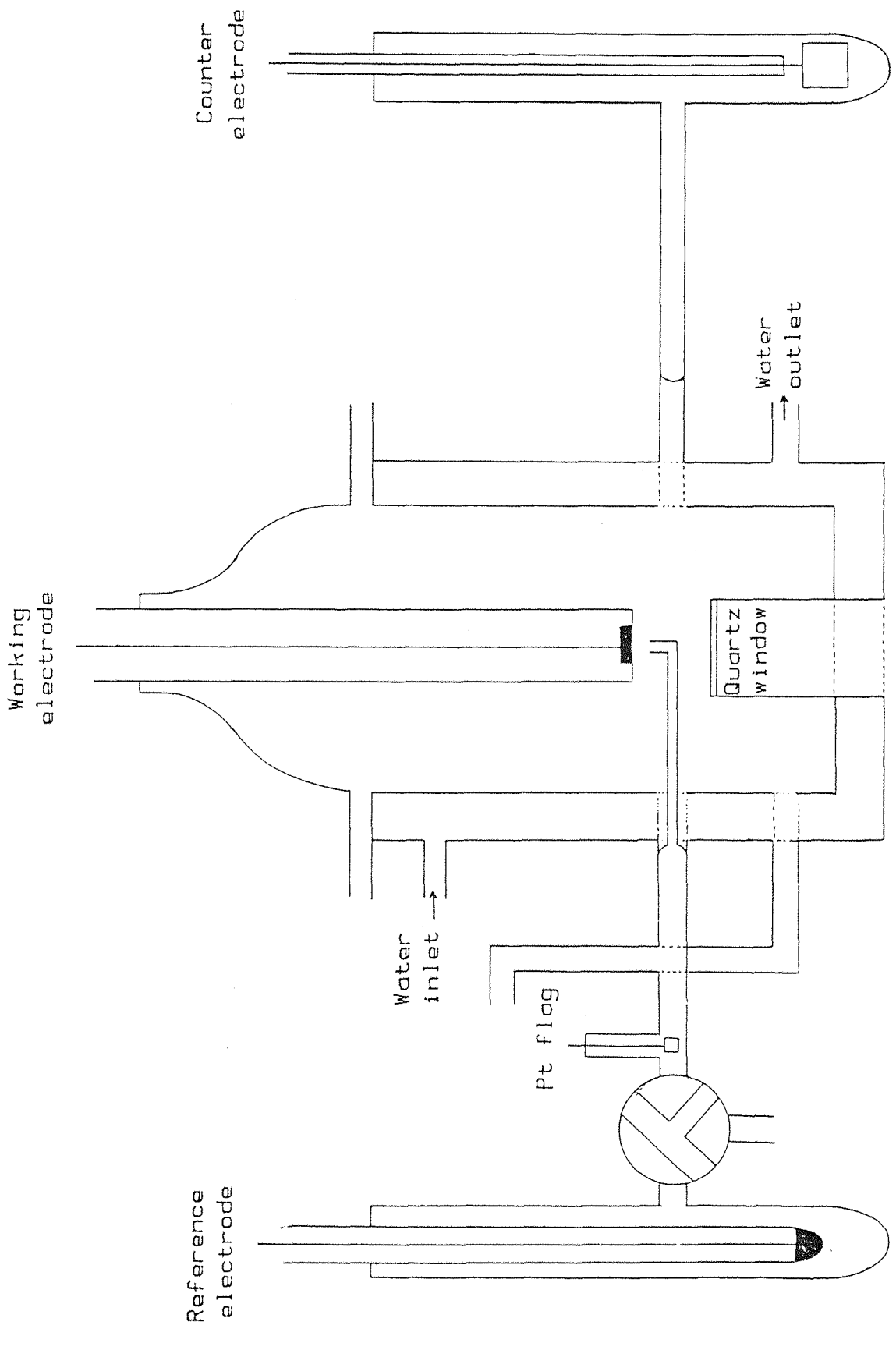

Fig. 3.1 Thermostatted electrochemical cell

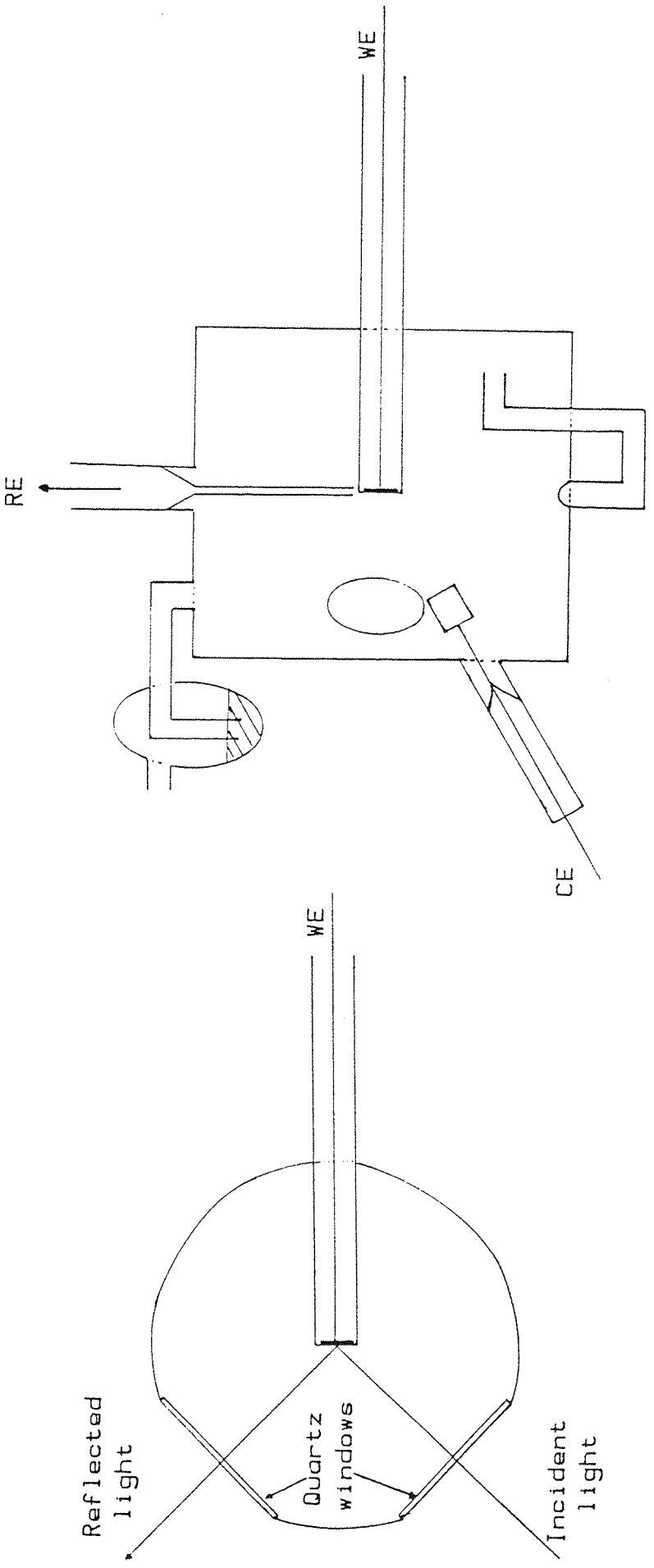

Fig. 3.2 Top and side views of the cell used in electroreflectance measurements.

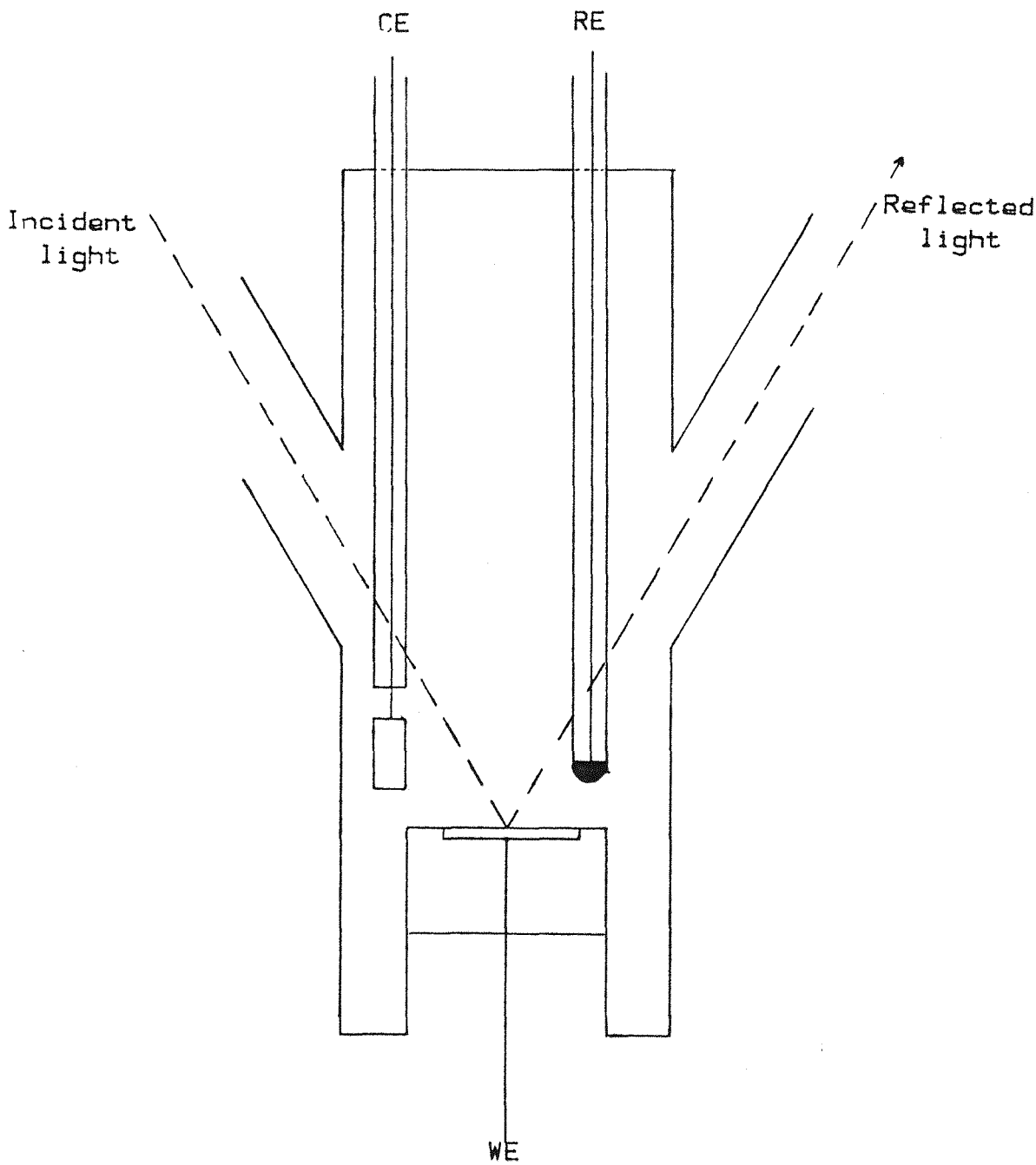

Fig. 3.3 Schematic representation of an electrochemical cell suitable for ellipsometry.

Table 3.1

The major impurities in the grades of titanium used in this work, in ppm are shown below.

	Marz	Specpure	IMI 130
Aluminium	10	10	500
Chromium	35	50	10
Copper	0.3	10	200
Iron	55	300	700
Magnesium	1	3	20
Manganese	15	50	50
Nickel	5	20	15
Carbon	2	-	200
Nitrogen	44	-	-
Oxygen	370	-	1800

No carbon, oxygen or nitrogen contents were quoted for the Specpure grade, but since this material was prepared under vacuum, these elements are likely to be present only in very minor quantities.

potting epoxy resin and contacted with silver loaded epoxy resin. In strong acids and at high temperatures the epoxy resin was attacked and leakage occurred. Various electrode designs were tried in an attempt to overcome this problem, and the design shown in Figure 3.5 was eventually derived. Diallyl phthalate powder was compressed around a length of titanium rod in a mounting press, and the electrode was then machined down to the required diameter. The titanium rod was tapped in the back and the brass contact rod was then screwed directly into it.

In order to eliminate leakage at the joint between the diallyl phthalate and the Teflon rod caused by condensation of the acid electolyte, a piece of Universal indicator paper was wrapped around the joint, followed by Teflon tape. This was then sprayed with a water repellant silicon spray, and finally a piece of heat-shrunk tubing (polyvinylidene fluoride, Radio Spares) was shrunk around the joint. An electrode made in this way was usable for about a month at the higher temperatures (338 K) before the indicator paper turned red, showing that leakage was occurring.

For ellipsometry, a simple silver epoxy/wire contact was made to the back of the diallyl phthalate electrodes (Fig. 3.6), and the contacts were then covered by ordinary epoxy resin. The design of the ellipsometric cell (Fig. 3.3) prevented contact of the epoxy resin with the acid electrolyte.

Electrodes for the electroreflectance measurements (Fig. 3.7) were based on a glass syringe barrel, through the middle of which the titanium rod was placed. Epoxy resin was drawn up between the titanium and the glass by a water vacuum pump to provide an insulating seal.

All working electrodes were polished using successively finer grades of alumina from 60 μm down to 0.05 μm lubricated with distilled water. The electrodes were polished on a 0.05 μm finishing powder prior to each experiment to remove the anodic oxide film formed in the previous experiment.

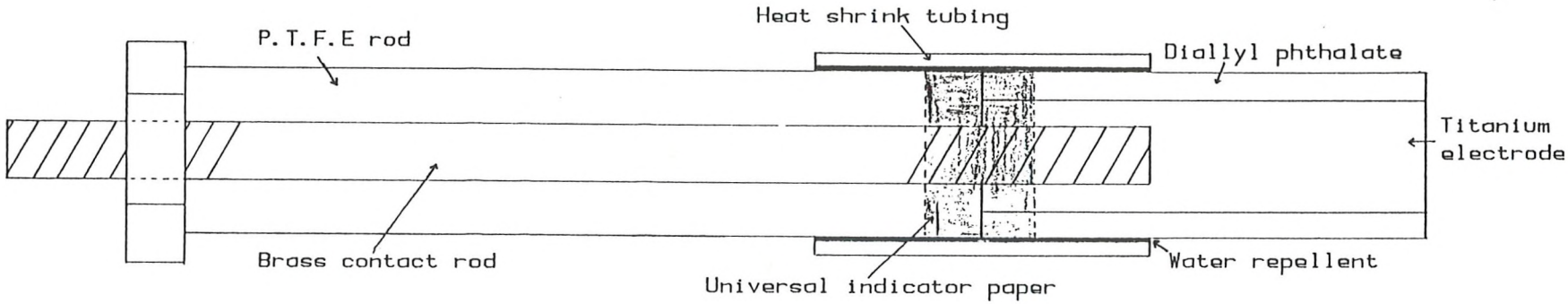

Fig. 3.5 Design of the electrodues used at elevated temperatures.

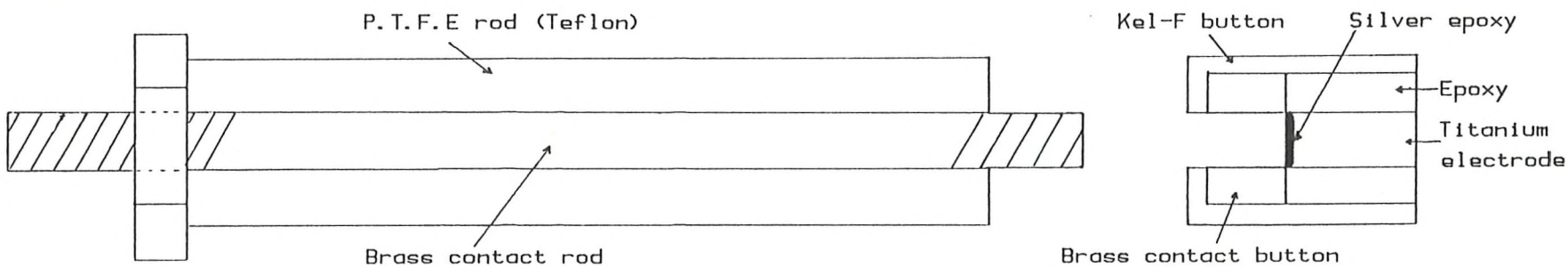

Fig. 3.4 The simple 'button' electrode design suitable for experiments at room temperature.

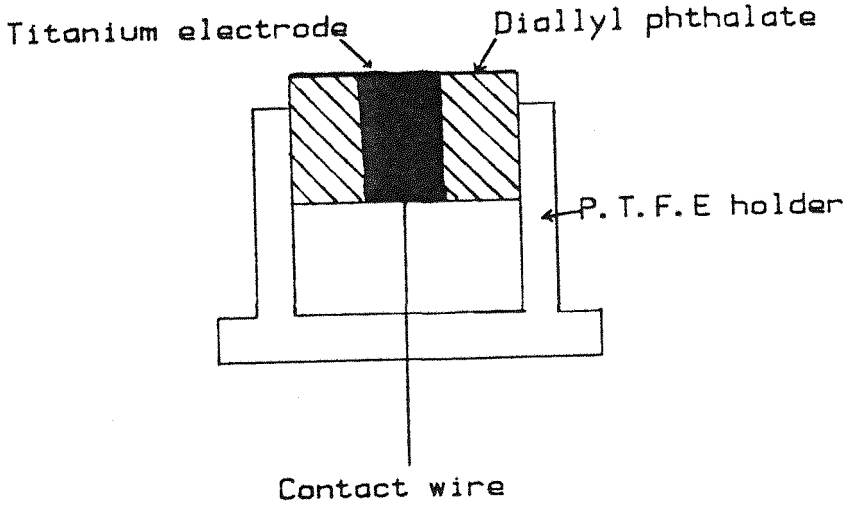

Fig. 3.6 Design of the electrodes used for ellipsometric experiments.

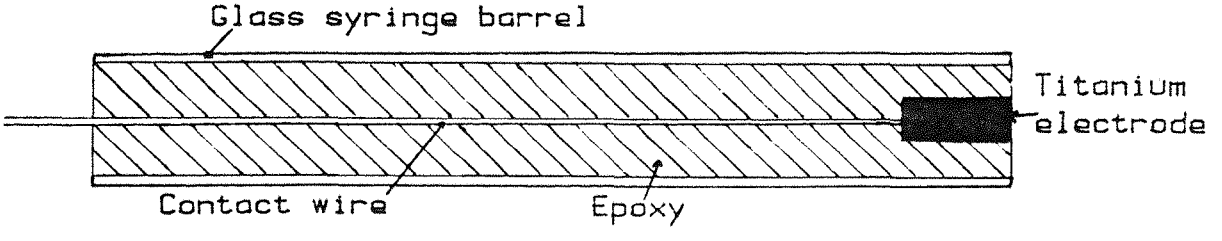

Fig. 3.7 Design of the electrode used during electroreflectance measurements.

3.1.2 Reagents

All chemicals used were of AnalaR grade and all solutions were made up using triply distilled water. Before any experiments were carried out, the electolyte was deoxygenated with OFN grade nitrogen, which was passed through a vanadyl sulphate/zinc metal trap to remove any residual oxygen.

3.2 Experimental Techniques

3.2.1 Steady state measurements

The steady state currents at a titanium electrode were measured at a range of potentials between -1.3 V and -0.6 V vs Hg/Hg_2SO_4 by holding the electrode at the required potential for a period of several minutes until the output current had reached an almost constant value. The apparatus used for this experiment and for cyclic voltammetry is shown in figure 3.8.

3.2.2 Cyclic voltammetry

The growth of titanium anodic oxide films was investigated using cyclic voltammetry. The effects of varying the sweep rate, pH, temperature and electrolyte composition on the size and shape of the cyclic voltammograms were examined.

3.2.3 A.C. impedence techniques

A.c. techniques have been reviewed recently by the Southampton Electrochemistry Group (2). These techniques involve the application of a small alternating perturbation to the system under study. The response is then characterised in terms of its inphase and quadrature components.

The a.c. impedence response of titanium oxide films was recorded under both potential control and open-circuit conditions using either the intrumentation shown in figure 3.9a or that in figure 3.10.

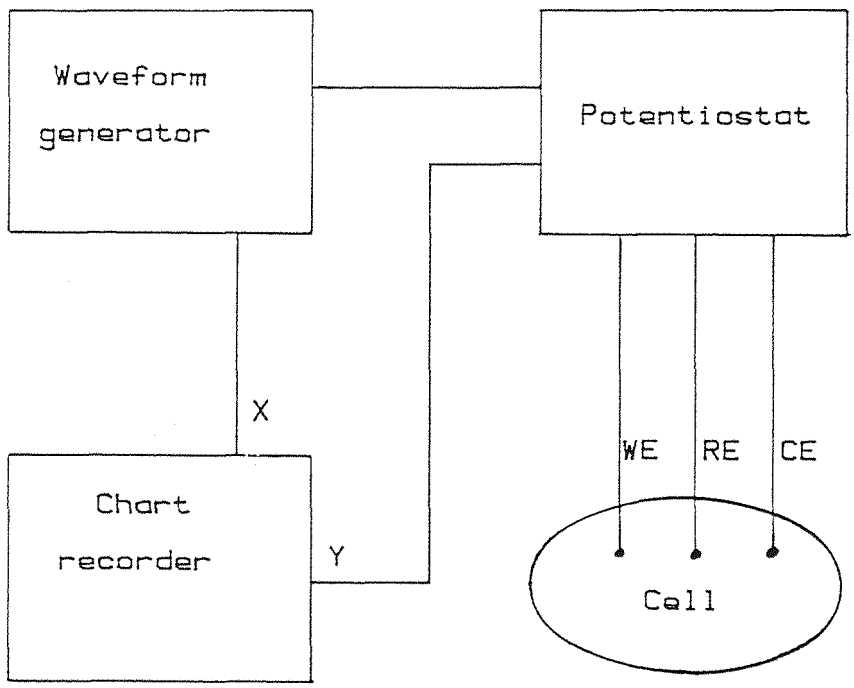

Fig. 3.8 Schematic representation of the apparatus used for steady stage and cyclic voltammetry experiments.

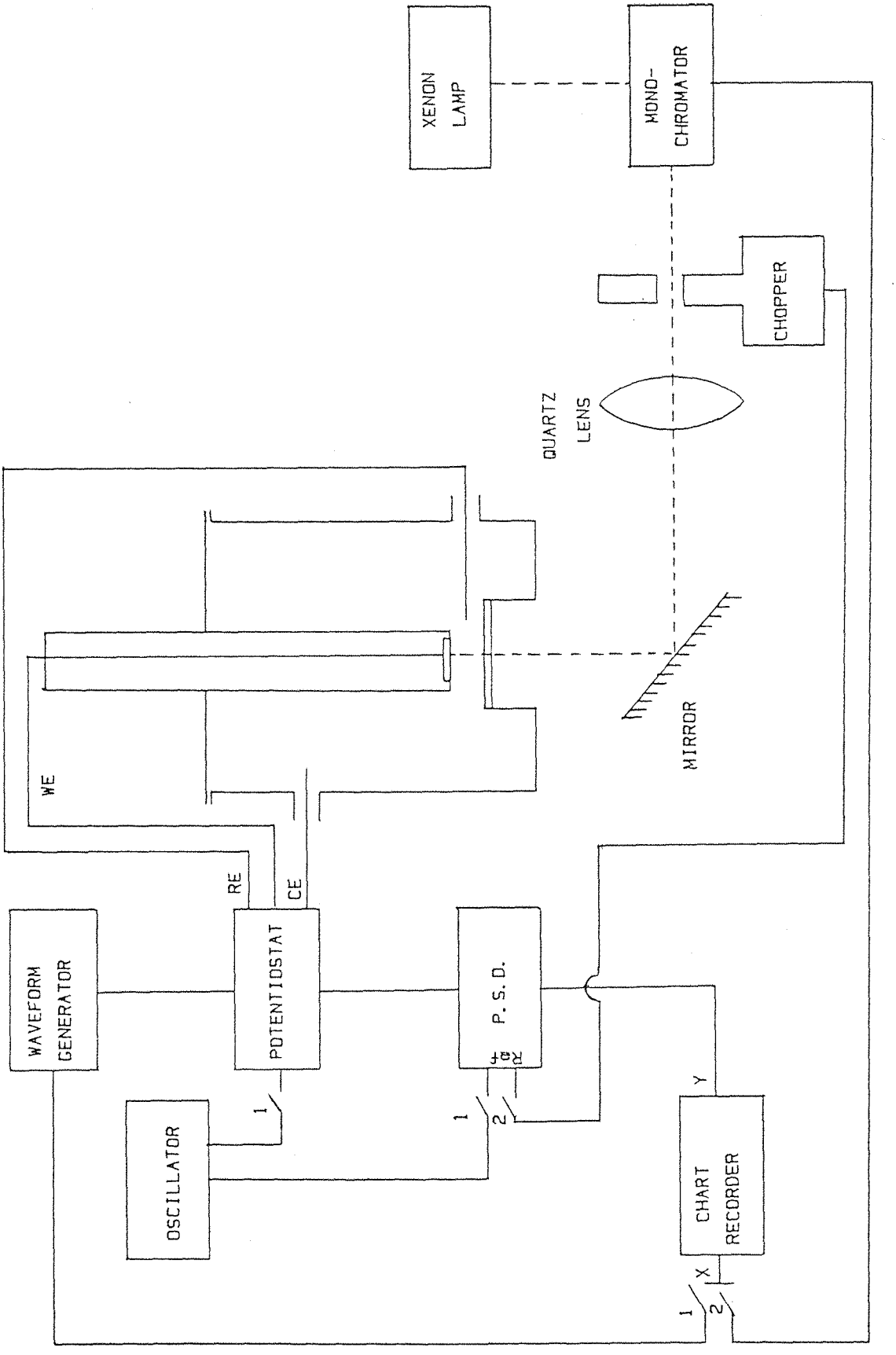

Fig. 3.9 Schematic representation of the instrumentation used for impedance and photocurrent measurements. a) Swtiches 1 closed for impedance measurements and b) switches 2 closed for photocurrent measurements.

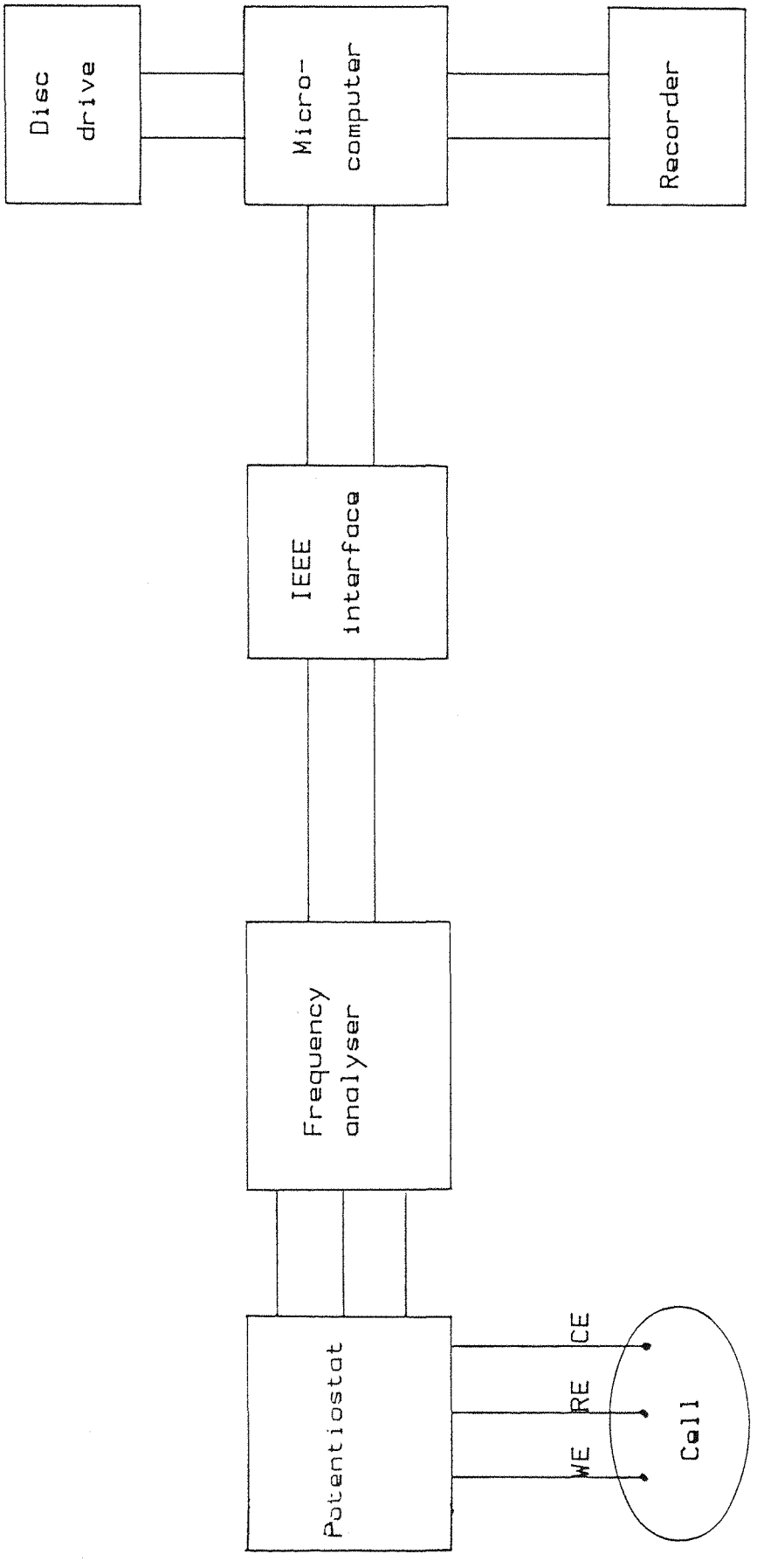

Fig. 3.10 Schematic representation of the instrumentation used to observe the frequency dependence of the impedance of the oxide films.

A flow diagram of the computer program written to control the frequency analyser is shown in appendix 5 and a simple method of data analysis is given in appendix 2.

3.2.4 Photocurrent measurements

Photocurrents from anodic oxide films on titanium were recorded during potential cycling with the instumentation shown in figure 3.9b. the phase sensitive detector (P.S.D.) was employed and the incident light chopped so that the photocurrent could be measured in the presence of a relatively large background current.

In order to determine the absolute photocurrent conversion efficiency of the oxide films, it was necessary to measure the output power, at any given wavelength of the arc lamp/monochrometer combination, using a calibrated R.C.A. 935 photodiode. The calibration was carried out before and after every set of experiments. The calibration curve for the R.C.A. 935 photodiode is shown in figure 3.11, from which its photocurrent conversion efficiency, Φ_e, can be calculated using,

$$\Phi_e = \frac{i_{pd}}{P_L} \times \frac{hC}{\lambda e} \qquad 3.1$$

where i_{pd} is the photocurrent obtained from the photodiode and P_L is the power of the incident radiation. A typical spectrum for Φ_e is also shown in figure 3.11.

The photocurrent conversion efficiency of the oxide film, Φ, can be found from,

$$\Phi = \frac{i_{po}}{i_{pd}} \times \Phi_e \qquad 3.2$$

where i_{po} is the photocurrent observed from the oxide.

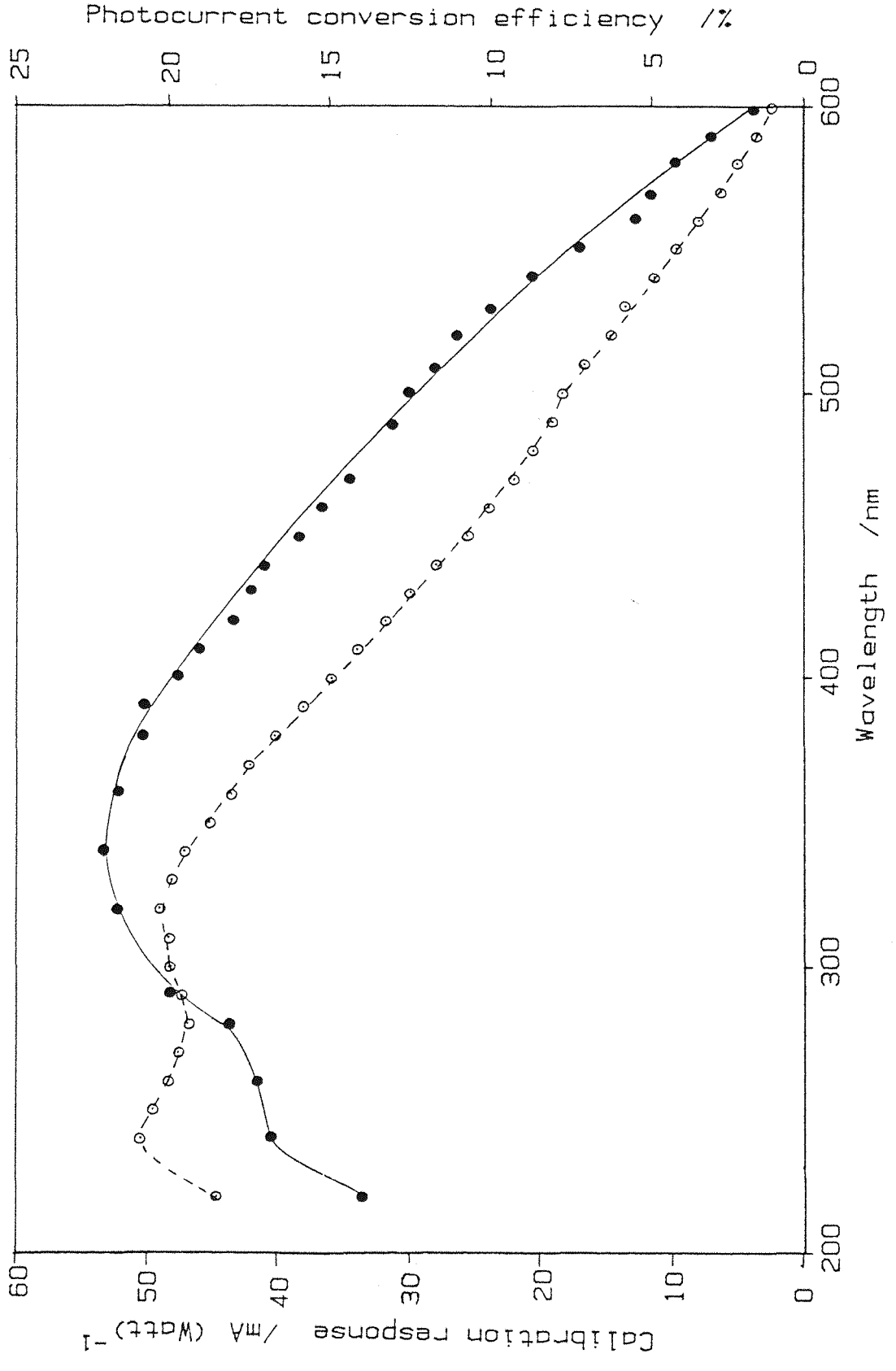

Fig. 3.11 Calibration curve for the RCA 935 photodiode, ●, and a plot of its photocurrent conversion efficiency ⊙.

3.2.5 Open-circuit and reformation experiments

Oxide films were grown in the same way as for cyclic voltammetry, except that the potentiostat was disconnected after the anodic limit had been reached, leaving the system at open-circuit. The open-circuit potential between the working and reference electrodes was then recorded as a function of time, via a high impedance buffered voltage follower.

For open-circuit experiments, the time taken for the electrode to become active was recorded, whereas in the reformation experiments the system was switched back to potential control after a period of time and the cyclic voltammogram was recorded, allowing the relationship between the time spent at open-circuit and the charge needed to repair the film to be determined.

Since it has been reported that Ti^{3+} and Ti^{4+} ions in solution stabilize the passive film (3,4) the electrolyte was renewed regularly during these experiments. In addition, the platinum counter electrode was removed whenever the system was under open-circuit conditions, in order to prevent leakage currents.

The effects of varying growth rate, temperature, pH and film thickness on these experiments were studied in detail. In addition, some experiments were carried out in which small cathodic current, $< 10\ \mu A\ cm^{-2}$, were passed galvanostatically through the oxide films instead of switching them to open-circuit conditions, as this was found to increase the rate of destruction of the anodic films.

3.2.6 Ellipsometry

This technique involves measuring the changes in polarisation state of an obliquely incident light beam upon reflection at a surface. A computer controlled self-nulling ellipsometer was used in this research, for which full details of the instrumentatation and examples of controlling programmes have been given by Pearson (5). A schematic representation of the instrument is shown in figure 3.12.

It was stated in section 2.4.2 that the p and s components of a linearly polarised light beam, are likely to undergo different changes on reflection at a surface, resulting in an elliptically polarised beam. It is therefore intuitively obvious that an elliptically polarised beam, with the current values of Δ and ψ, results in a linearly polarised beam upon reflection. The nulling ellipsometer varies the values of Δ and ψ of an incident elliptical beam, until a linearly polarised reflected beam is obtained. The null point is detected by passing the reflected beam through crossed polarisers.

The changes in the polarisation parameters, Δ and ψ, for reflection from anodic oxide films on titanium, were recorded both during the growth of the films and during the open-circuit passive-active transition. Curve fitting computer programs (6,7) based on the three layer model, (Section 2.4.4.3), were used to obtain information about the complex optical constants of the film and to derive its thickness during the open-circuit passive-active transition.

The major practical difficulty encountered was the need to prepare reproducible optically flat surfaces from the electrode polishing procedure. In addition it proved difficult to obtain the optical constants of the base substrate, since it appears that titanium always has a thin oxide layer on its surface (8). If this final oxide layer is removed the metal dissolves rapidly into the acid electrolyte, causing surface roughness and therefore a scattering of the incident beam.

3.2.7 Electroreflectance spectroscopy

This technique involves modulating the electrode potential, whilst a monochromatic polarised light beam is reflected from the electrode's surface. The apparatus used is shown schematically in figure 3.13.

The phase sensitive detector was used to measure the change in reflectance, ΔR, caused by small changes in the electrode's dielectric constant induced by the modulating potential. The steady

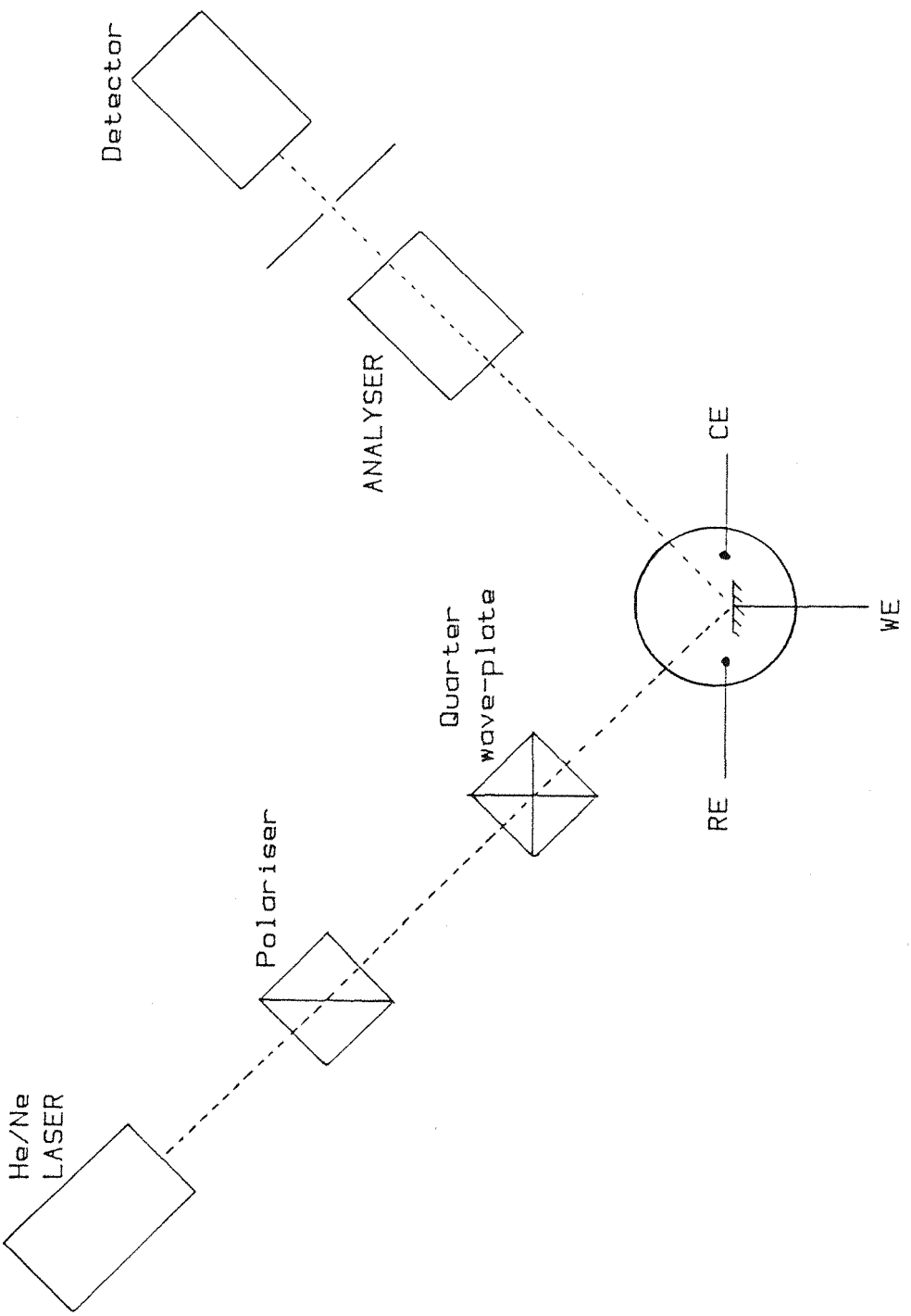

Fig. 3.12 Schematic diagram of an ellipsometer

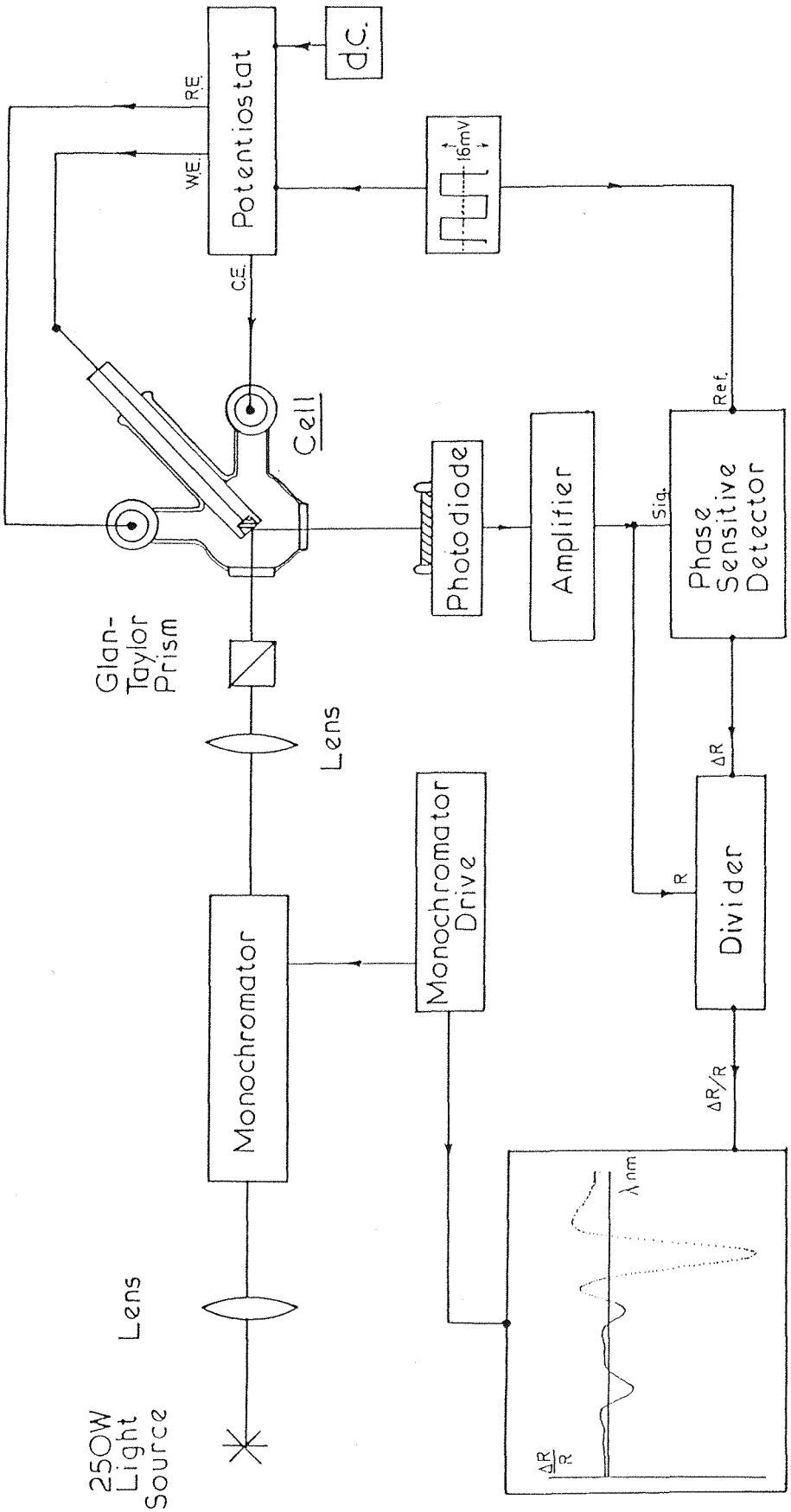

Fig. 3.13 Schematic representation of the apparatus used for electroreflectance experiments.

state reflectivity, R, was measured directly by the photomultiplier, with the signal being passed through a d.c. coupled preamplifier, this enabled the data to be produced in a normalised form of $\Delta R/R$.

3.2.8 High vacuum surface analysis

Two high vacuum techniques, scanning electron microscopy (S.E.M.) and secondary ion mass spectroscopy (S.I.M.S.) were used to analyse the surface of the titanium electrodes used for the work presented in this thesis. The experimental details and theory of these techniques, which are beyond the scope of this thesis, have been reviewed by Allen and Wild (9).

References

1. KORYATA, J., DVORAK, J. and BOHACKOVA, V; "Electrochemistry", Methuen, London, 1970.
2. SOUTHAMPTON ELECTROCHEMISTRY GROUP; "Instrumental Methods in Electrochemistry", Ellis Horwood, Chichester, 1985.
3. BARTLETT, D.L., ASHWORTH, V., BOWDEN, E.L. and GILBERT, J.R.B.; "Titanium '80", Vol. 4, p. 2639, "Proceedings of the 4th International Conference on Titanium", Kyoto, Japan, May 1980. Edited by Kimura, H. and Izumi, O.; Metallurgical Society AIME, Warrendal, Philadelphia, 1980.
4. CLARK, D.; University of Southampton, M.Sc. Thesis (1983)
5. PEARSON, P.J.; University of Southampton, Ph.D. Thesis (1983)
6. NORMAN, C.F.W.; Univeristy of Southampton, Ph.D.Thesis, Submitted 1986.
7. McCRACKIN, F.L.; "A Fortran Program for Analysis of Ellipsometer Measurements", Natl. Bur. Stand.; Tech. Note 479, U.S. Govt. Printing Office, Washington D.C., 1969.
8. LASER, D., YANIV, M. and GOTTESFELD, S.; J. Electrochem. Soc. 125, (1978) 358.
9. ALLEN, G.C. and WILD, R.K., CEGB Res. 11, (1981) 12.

CHAPTER 4

RESULTS

4.1 Steady State Measurements

The steady state current at a titanium electrode in 1 mol dm^{-3} H_2SO_4 at 65°C was measured over the potential range -1.3 V to -0.6 V vs Hg/Hg_2SO_4, and a Tafel plot was constructed (Fig. 4.1). The hydrogen evolution reaction on titanium was found to have a Tafel slope of $(137\ mV)^{-1}$ at the experimental temperature, which is equivalent to $(121\ mV)^{-1}$ at 298 K, and this is in good agreement with literature values (1-3).

The corrosion potention (E_{corr}), defined as the potential at which no net current was found to flow, was determined to be -1.16 V, and extrapolation of the hydrogen evolution line to this potential yielded a corrosion current density (j_{corr}) of 4.5×10^{-4} A cm^{-2}. Further extrapolation of the hydrogen evolution line to -0.64 V (0.0 V vs S.H.E.) enabled an estimation of the exchange current density for this reaction ($j_{O.H.}$) at 65°C to be made. The value of 6.7×10^{-8} A cm^{-2} obtained in this way can be compared with the room temperature value of 6.3×10^{-9} A cm^{-2} quoted by Trasatti (4) for the same electrolyte.

The anodic current was observed to go through a maximum of 9×10^{-4} A cm^{-2} (j_m) at a potential of -0.96 V (E_m), and this value was taken as the Flade potential (section 2.1) representing the onset of passivation of the metal's surface. Kelly (5) indicated that the value of E_m should be corrected for the effect of the hydrogen evolution reaction, before it represents the Flade potential, but at the experimental temperature of 65°C this effect was found to be insignificant.

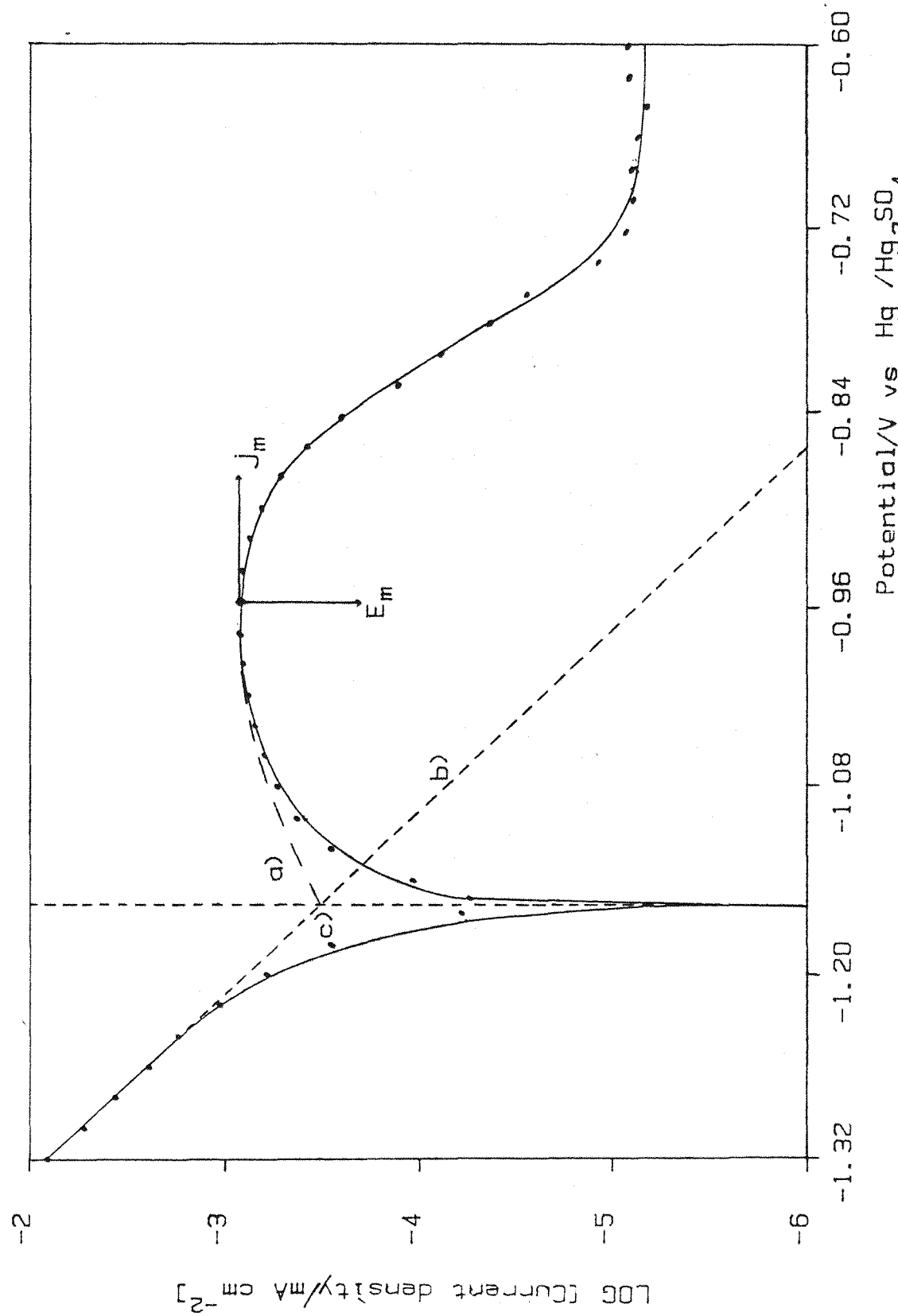

Fig. 4.1 Tafel plot for a titanium electrode in 3 mol dm^{-3} H_2SO_4, at 65°C. Curve (a) Ti^{3+} dissolution corrected for hydrogen evolution, curve (b) hydrogen evolution line, point (c) corrosion current.

4.2 Cyclic Voltammetry

A typical cyclic voltammogram for titanium in 3 mol dm^{-3} H_2SO_4 is shown in figure 4.2. Initially the current is negative due to hydrogen evolution, but as the potential is swept positive, the current changes sign due to the active dissolution of titanium as Ti^{3+}. The anodic peak in the current results from the onset of the formation of a stable oxide film, which reduced the rate of Ti^{3+} dissolution. The slight minimum which occurs after the peak is due to hydrogen evolution still occurring on the oxide film's surface, and the final current plateau corresponds to thickening of the oxide film.

If the potential had been stopped at the anodic limit the oxide film would have continued to grow in accordance with the inverse log law (section 2.1.2). However, in the present case, on the reverse potential cycle the growth field is reduced, and therefore the current falls to zero as the oxide film already present acts as a barrier to any further unassisted growth. At more negative potentials, on the reverse sweep hydrogen evolution is observed. All subsequent cycles produced only a small constant anodic current when the potential was swept in the positive direciton until the potential approached the anodic limit where the current began to rise slightly due to the growth field being large enough to support further film growth. The origin of the small constant current is not clear, but it appears to be related to the incorporation and subsequent oxidation of hydrogen atoms into the film, as it was observed that it was greatly reduced if the direction of the potential scan was reversed before the hydrogen evolution region was entered.

The effect on the size and shape of this cyclic voltammogram of varying the growth conditionswas investigated.

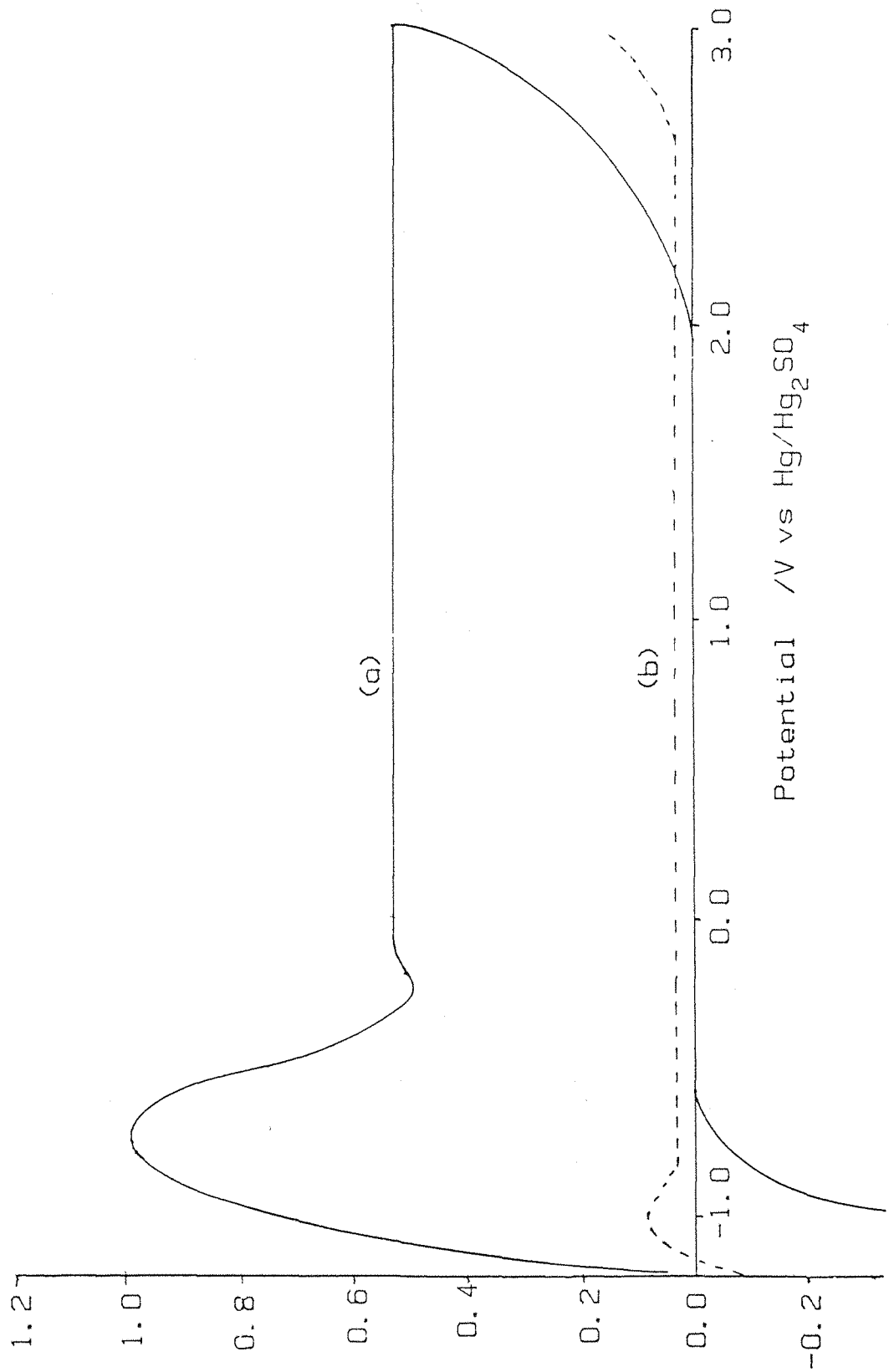

Fig. 4.2 Typical cyclic voltammogram for titanium in 3 mol dm^{-3} H_2SO_4, at room temperature. Scan rate = 100 mV s^{-1}. Curve a) = 1st cycle, curve b) = 2nd cycle.

4.2.1 Effect of varying the sweep rate

Williams and Wright (6) have shown that when no space-charge is present, the field can be expressed as

$$\mathcal{E} = \frac{dV}{dL} = \frac{dV}{dt} \times \frac{dt}{dL}$$

$$= \frac{\nu}{j} \times \frac{4F}{V_m} \qquad 4.1$$

and the high field growth law becomes

$$Ln(j) = Ln(j_o) + (\frac{4FZae}{V_mKT} \times \frac{\nu}{j}) \qquad 4.2$$

where ν is the potential sweep rate. Thus a plot of Ln(j) vs $(\frac{\nu}{j})$ should be linear. Although Williams and Wright neglected the effect of the Helmholtz layer, computer calculations (section 2.12) showed that as long as the value of j was taken from the plateau region of the relative cyclic voltammogram, equation 4.2 was still closely obeyed for the thin films used in this present work.

Figure 4.3 shows a plot of Ln(j) vs $(\frac{\nu}{j})$ for a series of oxide films grown on titanium with sweep rates between 10 mVs^{-1} and 10 Vs^{-1} at room temperature in 3 mol dm^{-3} H_2SO_4. From the slope of this plot, the value for Za was calculated to be 0.63 nm and from the intercept j_o was calculated to be 9.5×10^{-8} A cm^{-2}. These results are in reasonable agreement with values reported earlier (7,8), although the value of j_o should be treated with caution as it has been obtained from a rather long extrapolation.

Some of the cyclic voltammograms used to construct figure 4.3 were also used to calculated anodising ratios for the various sweep

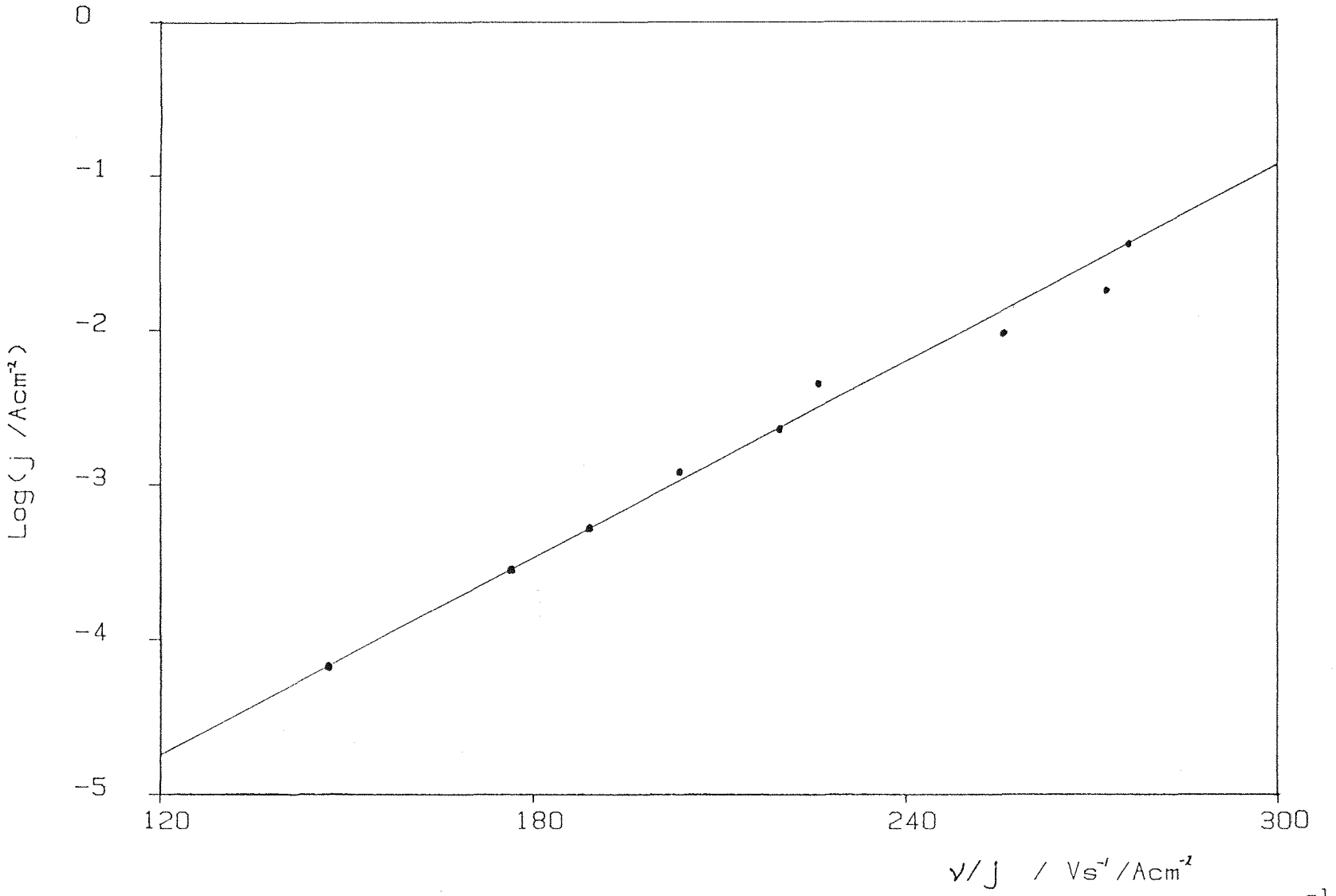

Fig. 4.3 Williams and Wright plot (6) for titanium oxide films grown at scan rates between 10 mVs^{-1} and 10 Vs^{-1} in 3 mol dm^{-3} H_2SO_4, at room temperature.

rates. (The density of anatase, 3.84 g cm^{-3}, was assumed (9)). Table 4.1 shows these anodising ratios with r being a roughness factor for the electrodes. (r is usually assumed to lie in the range between 1.0 and 2.0). Clearly the slower the growth rate, the thicker the film will be at the moment the final potential is reached. However, if the anodic potential limit is maintained, all the films should, in principle at least, eventually approach the same limiting thickness as determined by the inverse log law (section 2.12).

Table 4.1 Sweep rate dependence of the anodising ratio, determined from the plateau currents of the cyclic voltammograms.

Sweep rate/mVs^{-1}	(Anodising ratio x r) $nm\ V^{-1}$
10	36.7
50	30.6
100	28.6
500	24.6
1000	23.9

4.2.2 Influence of pH and anion character

Anodic oxide films were grown on titanium at 100 mVs^{-1} in different electrolytes, and the plateau currents obtained are tabulated in table 4.2.

Although in general the plateau current increased with increasing pH, the nature of the anion species in the electrolyte was also found to have an important influence. The cause of this dependence on electrolyte is not clear, but it possibly involves a change in the structure of the oxide and therefore a change in $\overrightarrow{\Delta G}^{\neq}$ or the barrier half-jump distance, a.

Rotating disc experiments revealed no rotation speed dependence of the plateau current, indicating that there is no contribution to this current by diffusion controlled solution reactions.

Table 4.2 The influence of the electrolyte on the plateau current density of cyclic voltammograms. Scan rate = 100 mVs^{-1}, at 298 K.

Electrolyte	Concentration/mol dm^{-3}	Plateau current density mA cm^{-2}
H_2SO_4	3.0	0.54
"	2.0	0.52
"	1.0	0.49
"	0.5	0.48
"	0.1	0.45
$HClO_4$	1.0	0.46
H_3PO_4	1.0	0.43
Na_2SO_4	1.0	0.36

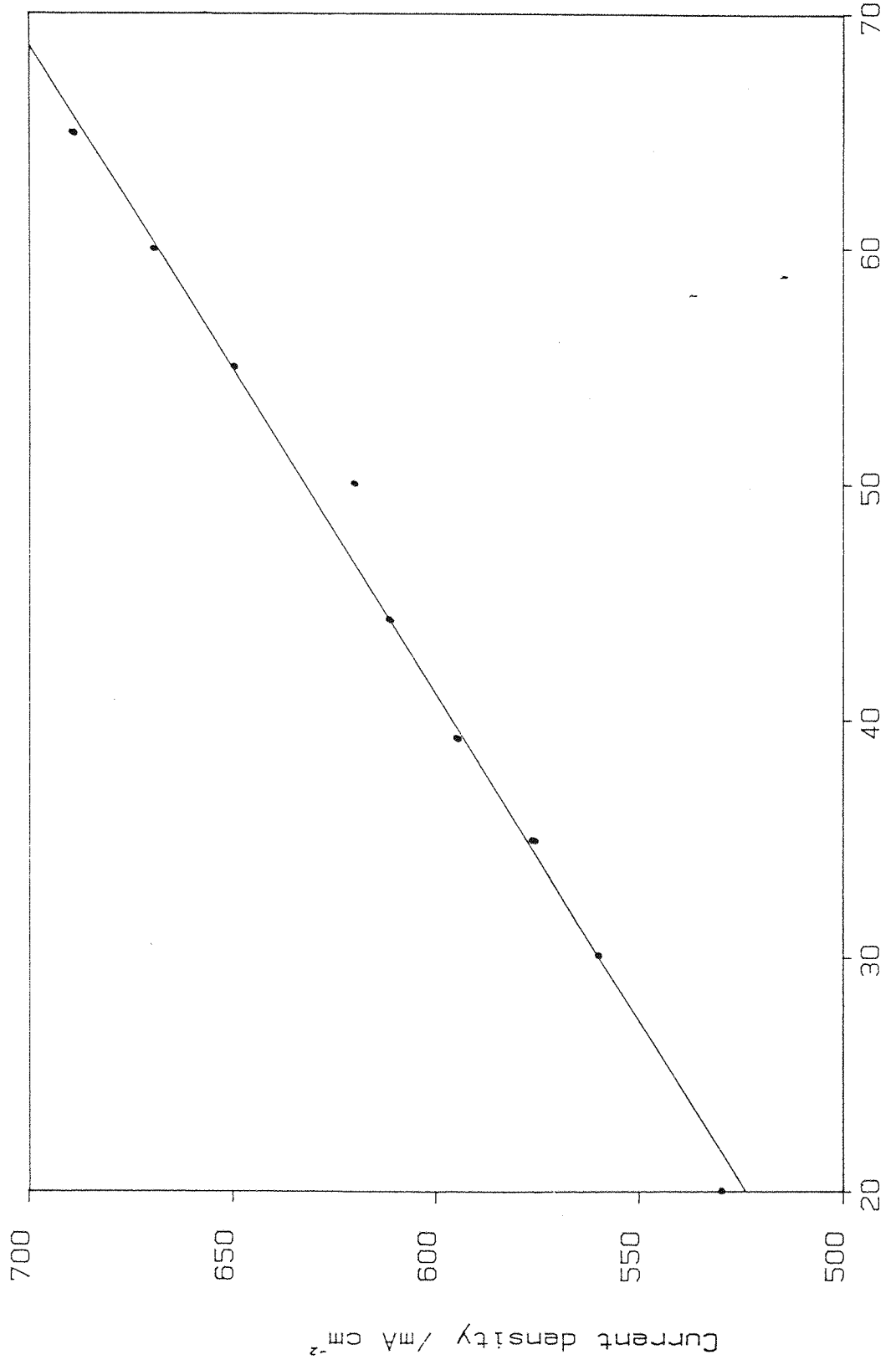

Fig. 4.4 Temperature dependence of the plateau current of titanium oxide films grown at 100 mVs^{-1} in 3 mol dm^{-3} H_2SO_4.

4.2.3 Effect of temperature variation

The temperature of the electrolyte in which the oxide films were grown was varied between 20°C and 65°C. Figure 4.4 shows that this 45°C rise in temperature resulted in an approximately 30% rise in the size of the plateau current for films grown at 100 mV s^{-1} in 3 mol dm^{-3} H_2SO_4.

4.3 Potential Controlled Impedance Measurements

4.3.1 Capacitance during potential cycling

The capacitance of the titanium electrode was recorded during anodic oxide film growth and subsequent potential cycles. A cyclic voltammogram was recorded at the same time in order to determine the anodising ratio. A typical reciprocal capacitance plot is shown in figure 4.5. The slope of this plot yields a value for εr^2 of 62, which compares well with the values quoted by McAleer (8). The product εr^2 arises because the surface roughness enters into both the calculation of the film thickness and into the measured capacitance. As a result, it is difficult to obtain reliable values of the relative permittivity of the anodic oxide since an independent method of determining r is not readily available.

The film capacity measured during the reverse sweep was used to construct a Mott-Schottky plot (Fig. 4.6). This was found to be curved, suggesting that deep donor levels may be present in the oxide film (section 2.2.6). Alternatively, if a spatial distribution of donors is assumed, then the slope at any point will represent the donor density at the edge of the space charge region. For low potentials the foot of the Mott-Schottky plot yielded a donor density of 5.7×10^{19} cm^{-3}, whilst at the anodic potential limit a donor density of 3.9×10^{20} cm^{-3} was determined. These values are independent of r since the surface roughness term in the measured capacitance is cancelled out by using the εr^2 value determined above.

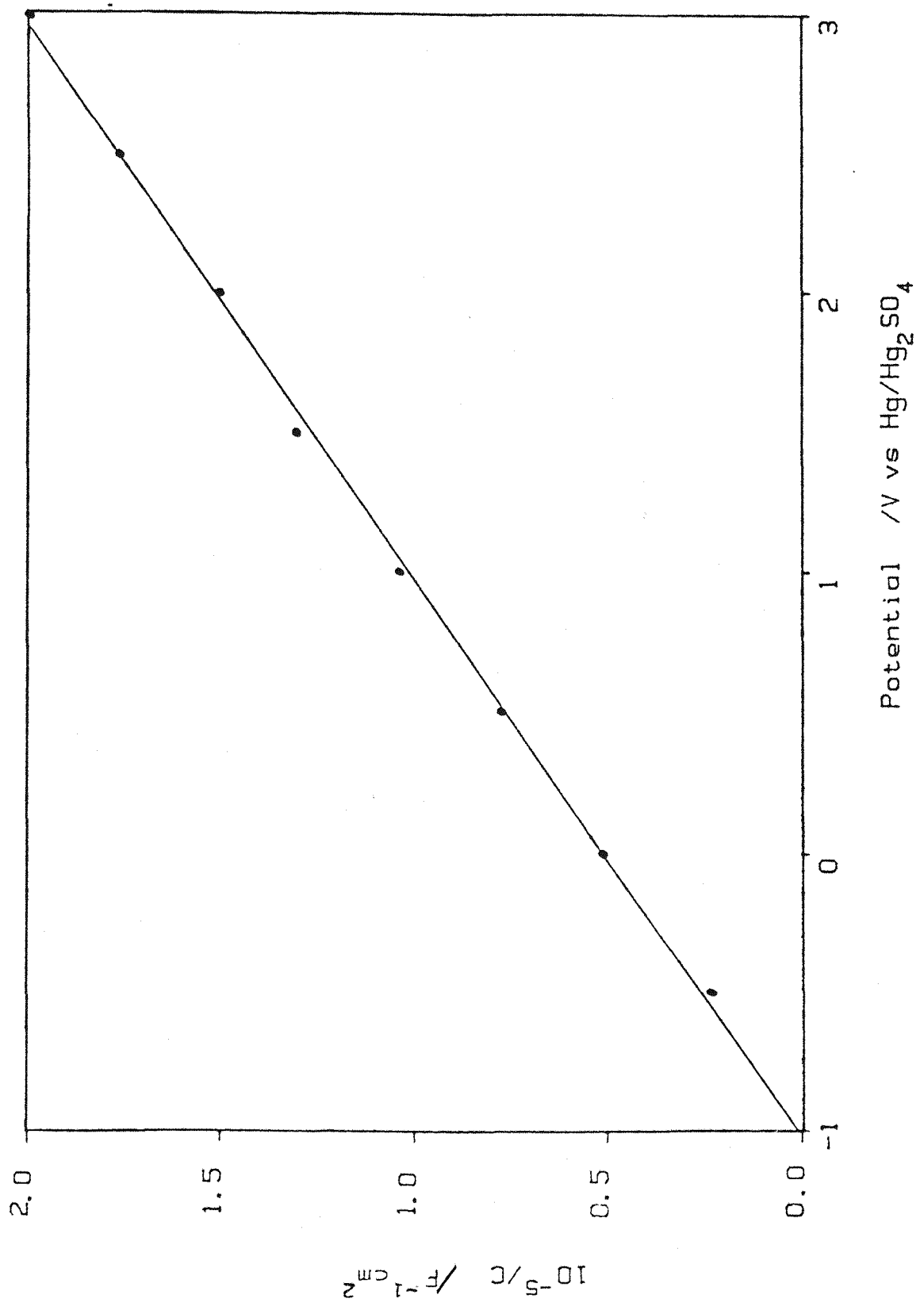

Fig. 4.5 Reciprocal capacitance plot for a titanium oxide film grown at 100 mVs^{-1} in 3 mol dm^{-3} H_2SO_4, at room temperature, 10 mV peak - peak perturbation signal at 340 Hz.

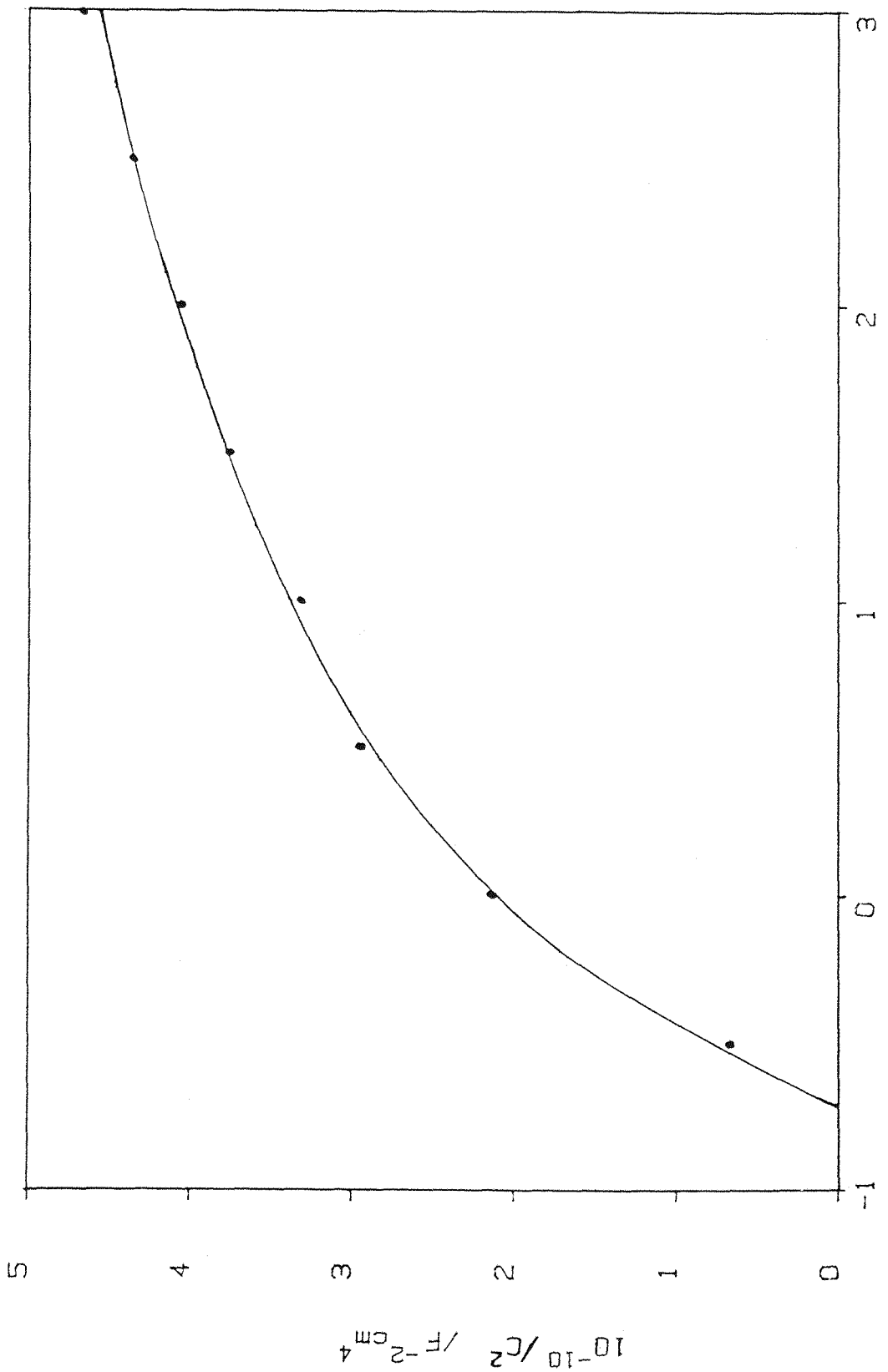

Fig. 4.6 Mott-Schottky plot for the oxide film grown for figure 4.5. Reverse scan rate 10 mVs^{-1}.

The flat band potential of the oxide film was obtained from the intercept on the Mott-Schottky plot. This value of -0.75 V vs Hg/Hg_2SO_4 was corrected for the Helmholtz layer using the equation derived by Pettinger et al. (10).

$$\Delta V = e\varepsilon N_s L_H^2/2\varepsilon_H^2\varepsilon_o \qquad 4.3$$

where $\varepsilon_H = 6$ and $L_H \simeq 0.3$nm are the relative premittivity and the width of the Helmholtz layer respectively. Using $N_s = 5.7 \times 10^{19}$ cm^{-3} and $\varepsilon = 62$, the potential shift was found to be 80 mV making the corrected flat band potential -0.67V vs Hg/Hg_2SO_4, which compares well with published values (7,11,12).

When the electrode potential was cycled continually the film capacitance was seen to go through a hysteresis loop (Fig. 4.7). This was thought to be due to the incorporation of hydrogen atoms into the oxide film, as no hysteresis was observed if the negative limit was kept well above the hydrogen evolution potential of -0.64V vs Hg/Hg_2SO_4. Evidence of a mobile proton space charge in TiO_2 films has been presented previously by Dyer and Leach (13) and by Yaniv and Laser (12).

4.3.2 Growth rate dependence of the film capacitance

4.3.2.1 The geometric capacitance

Reciprocal capacitance plots were constructed for growth rates between 1 mVs^{-1} and 100mVs^{-1}. The slow growth rates were found to give a discontinuity in the plots of $^1/_C$ vs V (Fig. 4.8a). However, when $^1/_C$ was plotted against the charge passed to form the oxide, q, the discontinuity was found to disappear (Fig. 4.8b).

Table 4.3 shows the values of εr^2 obtained for films grown to 3.0V vs Hg/Hg_2SO_4.

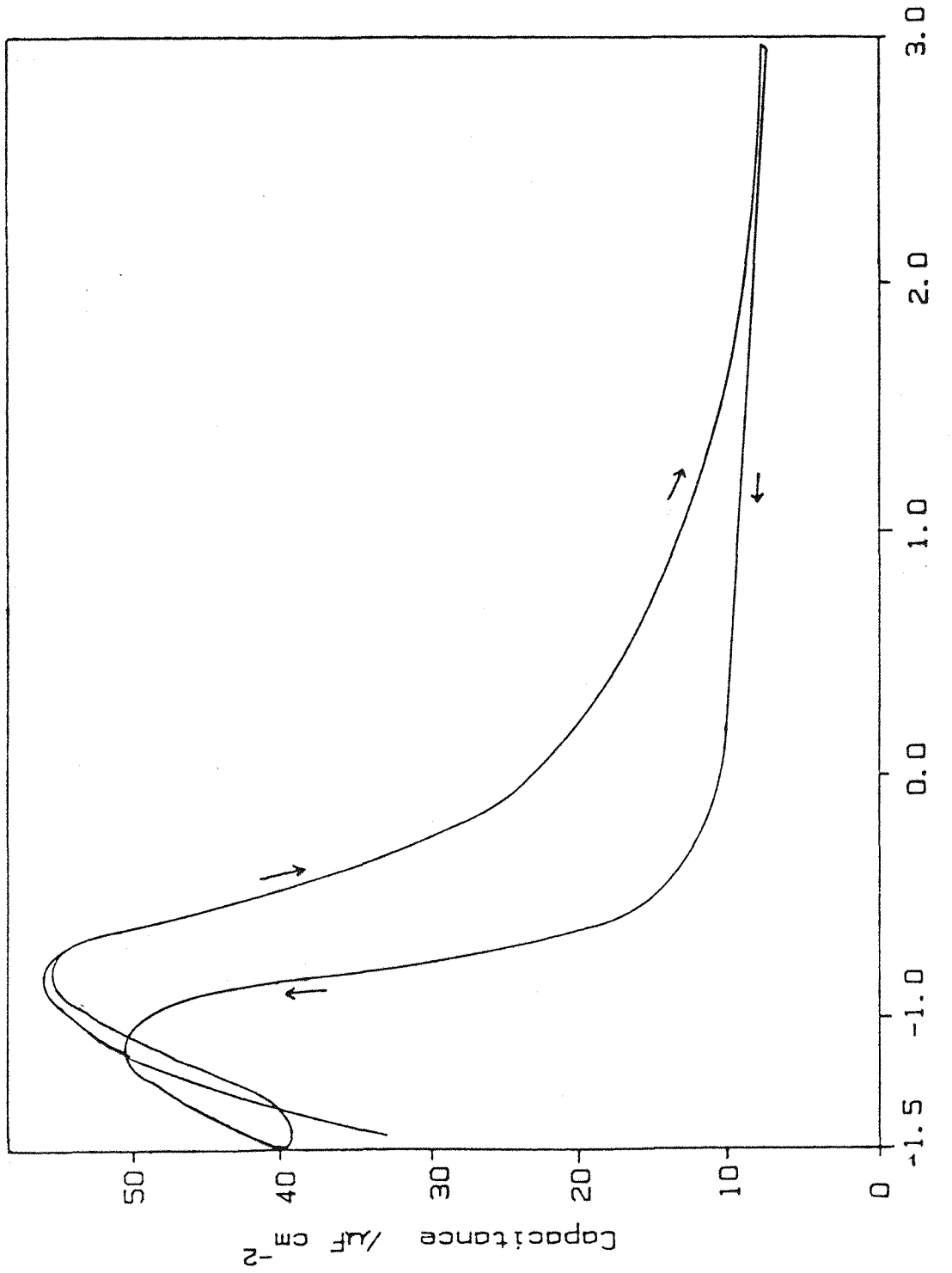

Fig. 4.7 Hysteresis loop in the capacity of an oxide film on continued potential cycling at 10 mVs^{-1}. 340 Hz. (The capacity during the first potential cycle is not shown).

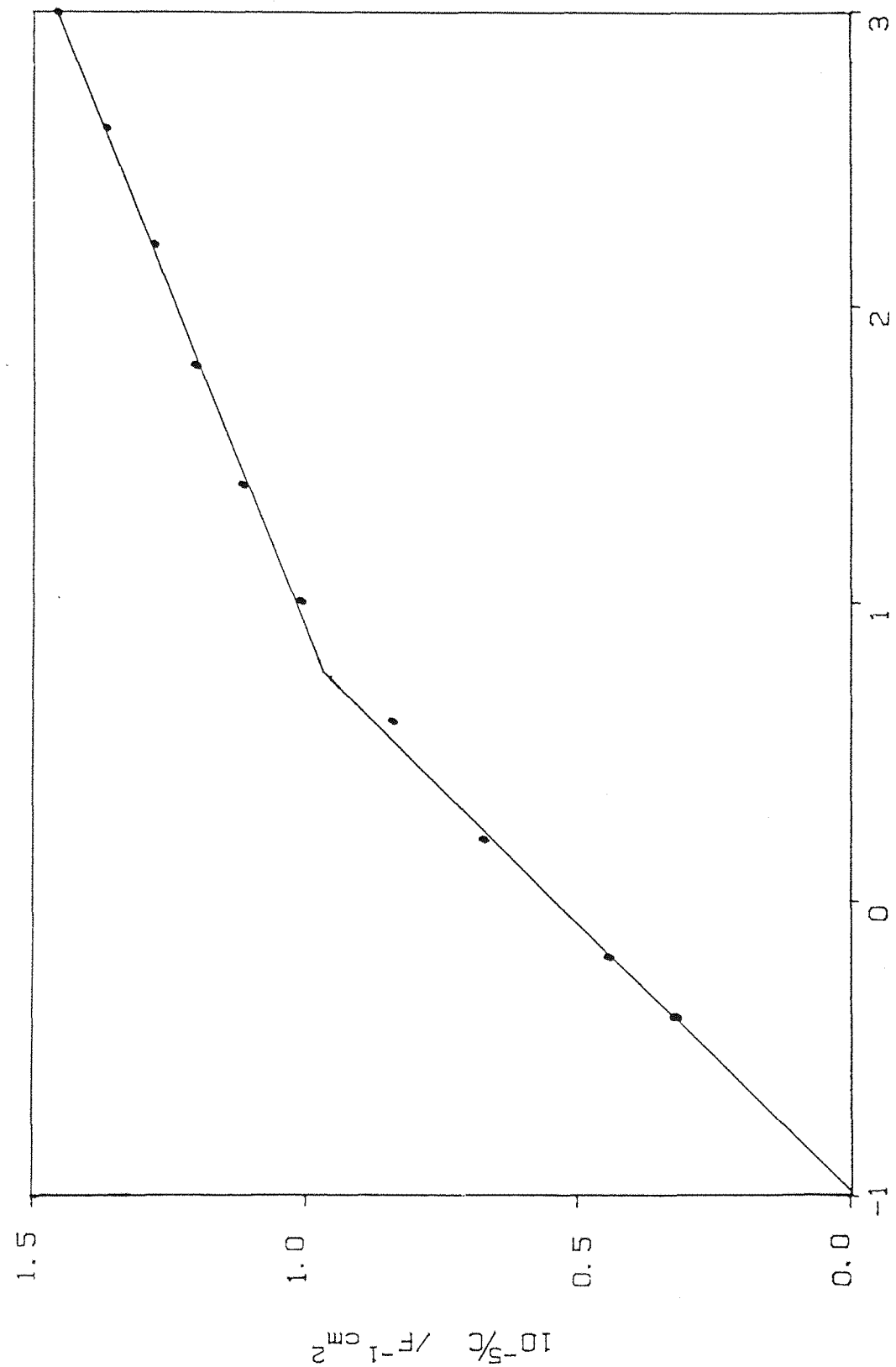

Fig. 4.8a Plot of the reciprocal capacitance of a titanium oxide film against potential (forward sweep). Scan rate = 1 mVs^{-1}, 3 mol dm^{-3} H_2SO_4, room temperature, 340 Hz.

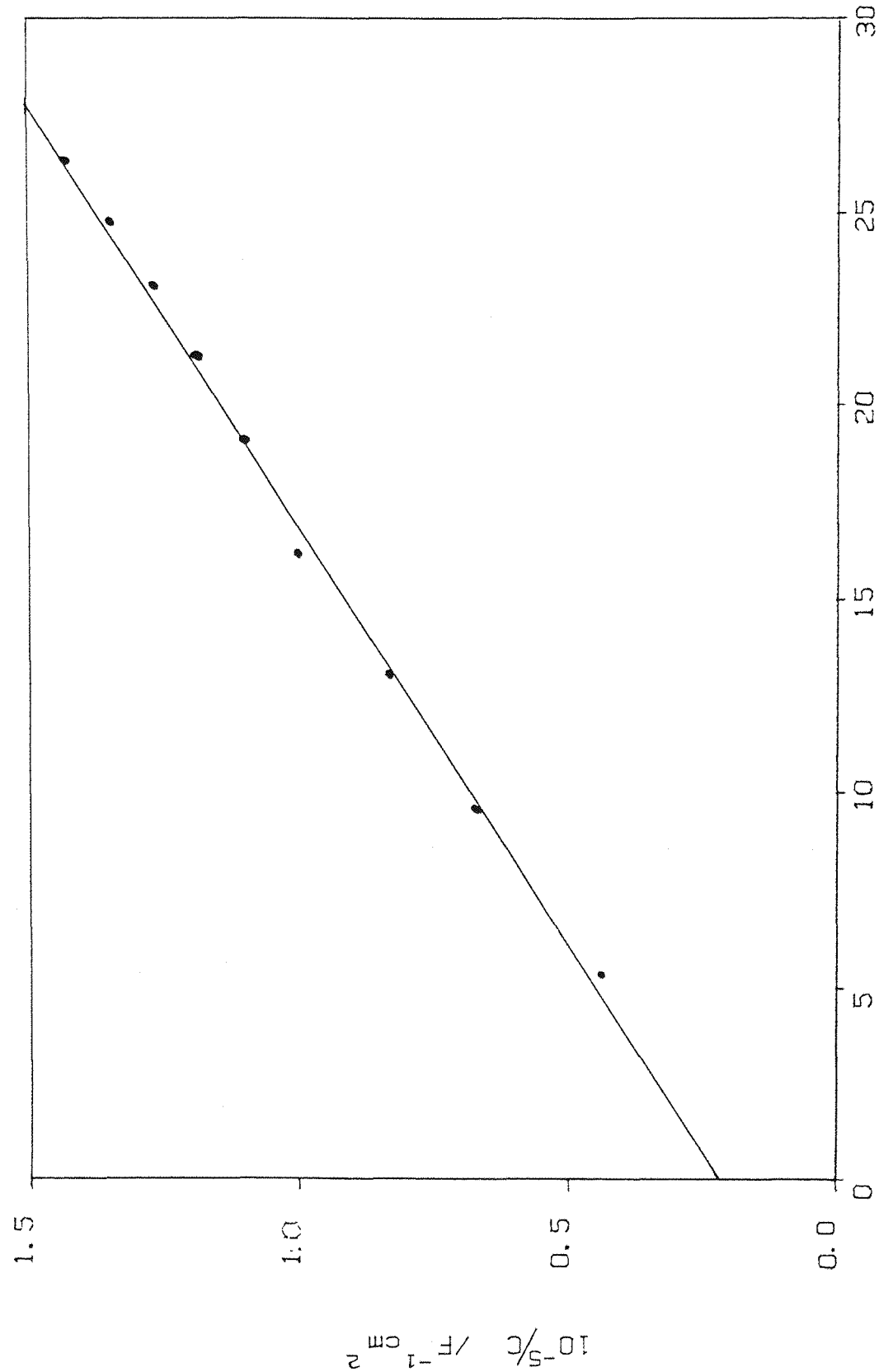

Fig. 4.8b Plot of reciprocal capacitance against growth charge (forward sweep) for the same oxide film used to construct figure 4.8a.

Table 4.3 Growth rate dependance of εr^2 for films grown in 3 mol dm^{-3} H_2SO_4, with a 340 Hz perturbation signal.

Growth rate/mVs^{-1}	εr^2	Capacitance at 3.0V/μFcm^{-2}
1	134	6.8
10	85	6.0
50	72	5.4
100	62	5.0
1000	58	4.6

Clearly as the growth rate is reduced, the dielectric constant, or the roughness, increases. Since an increase in the dielectric constant can be attributed to an increase in the crystallinity of the film, table 4.3 suggests that the structure of the films formed depends on their growth rate.

Further evidence of a difference in film structure has been presented by McAleer (8), who held a film grown at 100 mVs^{-1} at its formation potential and observed its geometric capacitance as a function of time, over a period of 4½ hours. At first, the geometric capacitance was observed to fall as the film continued to thicken, but then it increased towards the value of the capacitance of films formed at a much slower rate, suggesting that a restructuring process was occurring.

4.3.2.2 The space-charge capacitance

Mott-Schottky plots were constructed for films grown over a range of sweep rates between 1 mVs^{-1} and 1 Vs^{-1} (Fig. 4.9). Table 4.4 is a summary of the results obtained, with N_s and N_t being the donor densities determined at low and high potentials respectively.

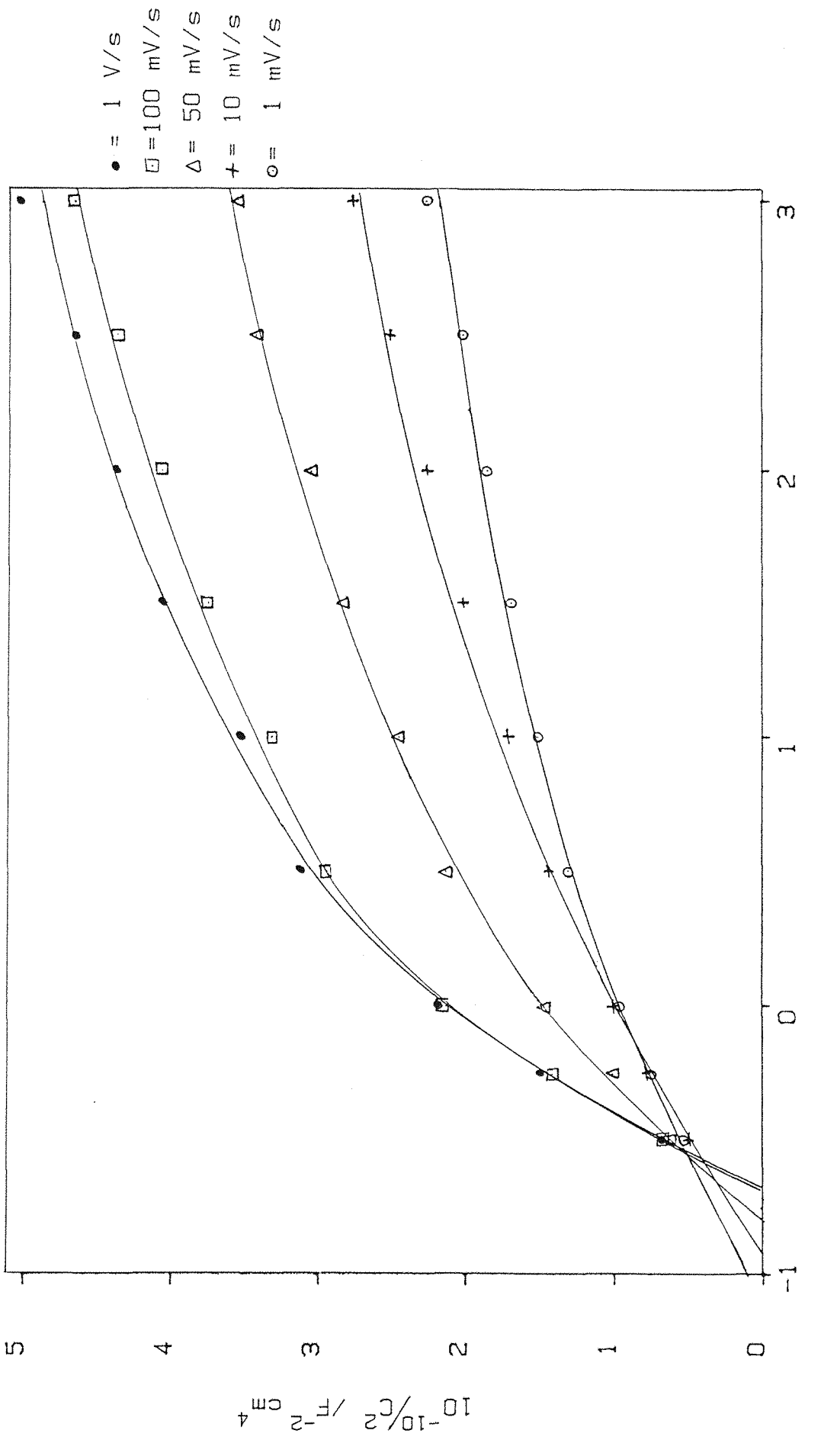

Fig. 4.9 Mott-Schottky plots (reverse sweep) for titanium oxide films grown at various sweep rates to 3.0 V vs Hg/Hg_2SO_4 in 3 mol dm^{-3} H_2SO_4, at room temperature. All reverse scan rates = 10 mVs^{-1}, 340 Hz.

Table 4.4 Growth rate dependence of results obtained from Mott-Schottky plots, for films grown to 3.0 V vs Hg/Hg_2SO_4 in 3 mol dm^{-3} H_2SO_4 at 298K. All reverse sweeps at 10 mVs^{-1}, with a 340 Hz perturbation signal.

Growth rate/mVs^{-1}	$N_s/10^{19}$ cm^{-3}	$N_t/10^{19}$ cm^{-3}	Intercept/V	V_{FB}/V
1	15.0	31.0	-1.13	-0.68
10	11.0	45.6	-0.90	-0.69
50	8.0	51.1	-0.80	-0.67
100	5.7	57.6	-0.71	-0.62
1000	5.0	59.3	-0.70	-0.62

Although the intercepts of the Mott-Schottky plots vary considerably with growth rate, on correcting for the Helmholtz layer using the donor densities obtained at low potentials, the corrected flat-bond potentials are found to vary by only 70 mV, with an average value of -0.66 V vs. Hg/Hg_2SO_4.

As the growth rate was decreased, the density of shallow donors, N_s, was found to increase, whereas the total donor density, N_t, was observed to decrease. (Assuming the roughness factor is the same for all growth rates). This observation could perhaps be explained if the donors are assumed to be titanium ions, in transit to the oxide/electrolyte interface during growth which became trapped in interstitial sites when the growth field was reduced. In a slowly grown film it could be envisaged that these titanium interstitials would be spread fairly evenly throughout the whole film, whereas in a rapidly grown film many of them would not have travelled far from the metal surface before the field was removed giving a much lower shallow donor concentration.

4.3.3 Frequency dependence of film capacitance

A frequency response analyser was used to monitor the overall impedance and the phase angle for titanium oxide films, over a large range of frequencies. Figure 4.10 shows a typical response. The phase angle was found to be mainly in the region of 80°, while the slope of the log (impedance) vs log (frequency) plot was about -0.92. These results suggest that the oxide film behaves essentially as a capacitor over the frequency range studied. The decrease in the modulus of the phase angle, at the higher frequencies, was due to the solution resistance becoming an important term. This response is typical of the anodic oxide films formed on valve metals (section 2.2.1) (14), since tanδ is approximately constant over the frequency range studied. It was found that the impedance of the oxide film on titanium could not be simulated using a simple three component circuit, unless both the resistance and the capacitance of the oxide were allowed to vary with frequency.

The impedance of an anodic oxide film on titanium was measured over a range of fixed potentials, both during film growth and on the reverse cycle, the potential being held constant during each individual measurement to avoid any distortion of the signal at low frequencies.

Figures 4.11 and 4.12 show that there is a clear frequency dispersion in both the reciprocal capacitance and Mott-Schottky plots if the impedance data is interpreted in terms of the three component equivalent circuit shown in appendix 2. This frequency dispersion has been explained in the past in terms of dielectric relaxation phenomena (14,15), current inhomogeneity (16) and doping inhomogeneity (17). In the inhomogeneous doping model, the applied potential perturbation is considered to be sufficient to push the Fermi level through a deep donor energy level at the extremity of its oscillation. If it takes a finite time for the deep donors to be ionised, then the concentration of donors which undergo ionisation should be proportional to the length of time that the Fermi level is above their ionization energy level. Therefore, the lower the frequency the higher

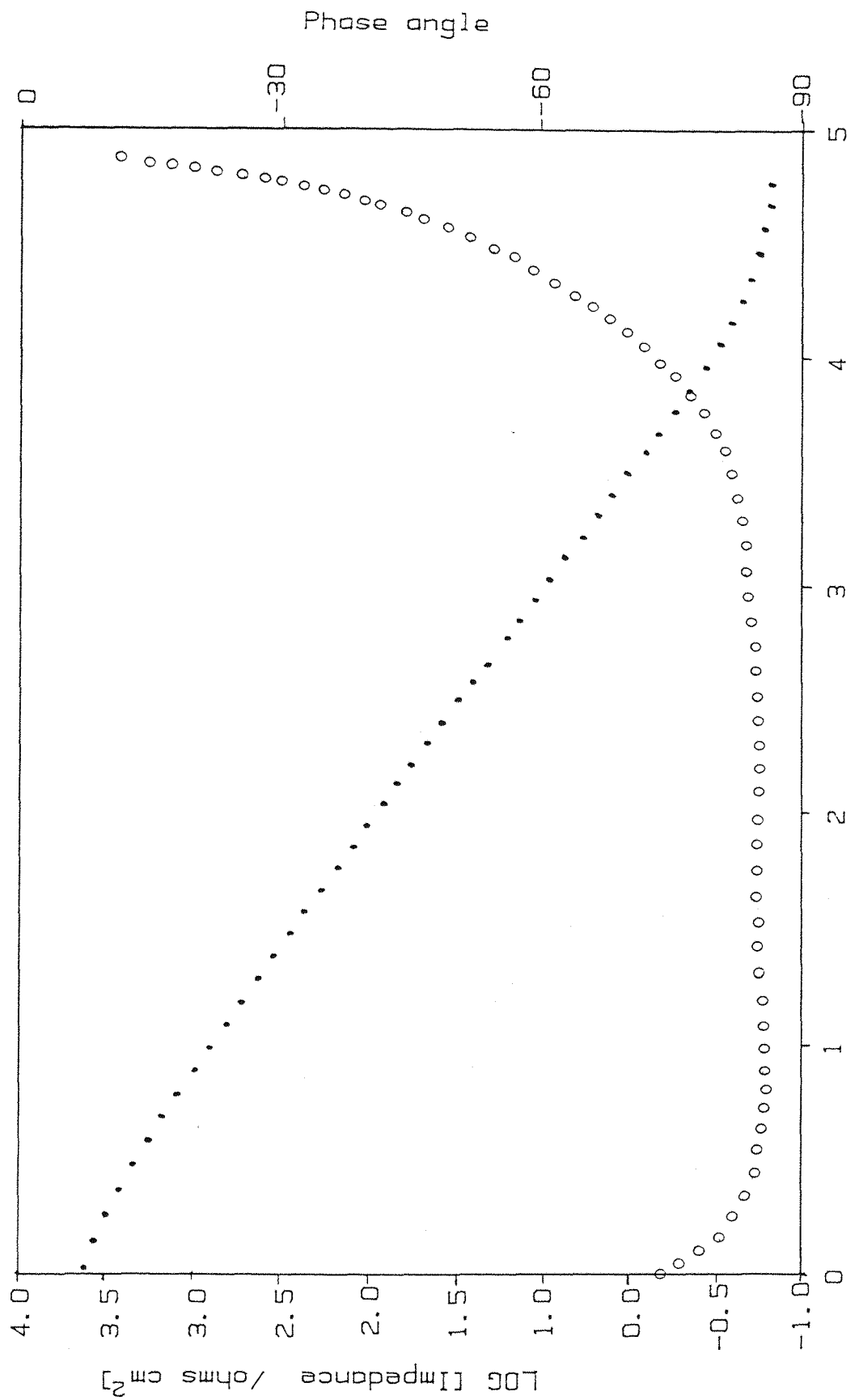

Fig. 4.10 Bode plot of Log(Impedance), •, and the phase angle, o, against Log (Frequency), for a titanium oxide film grown at 100 mVs-1 to 2.0 V vs Hg/Hg_2SO_4 in 3 mol dm^{-3} at room temperature, and held at its formation potential.

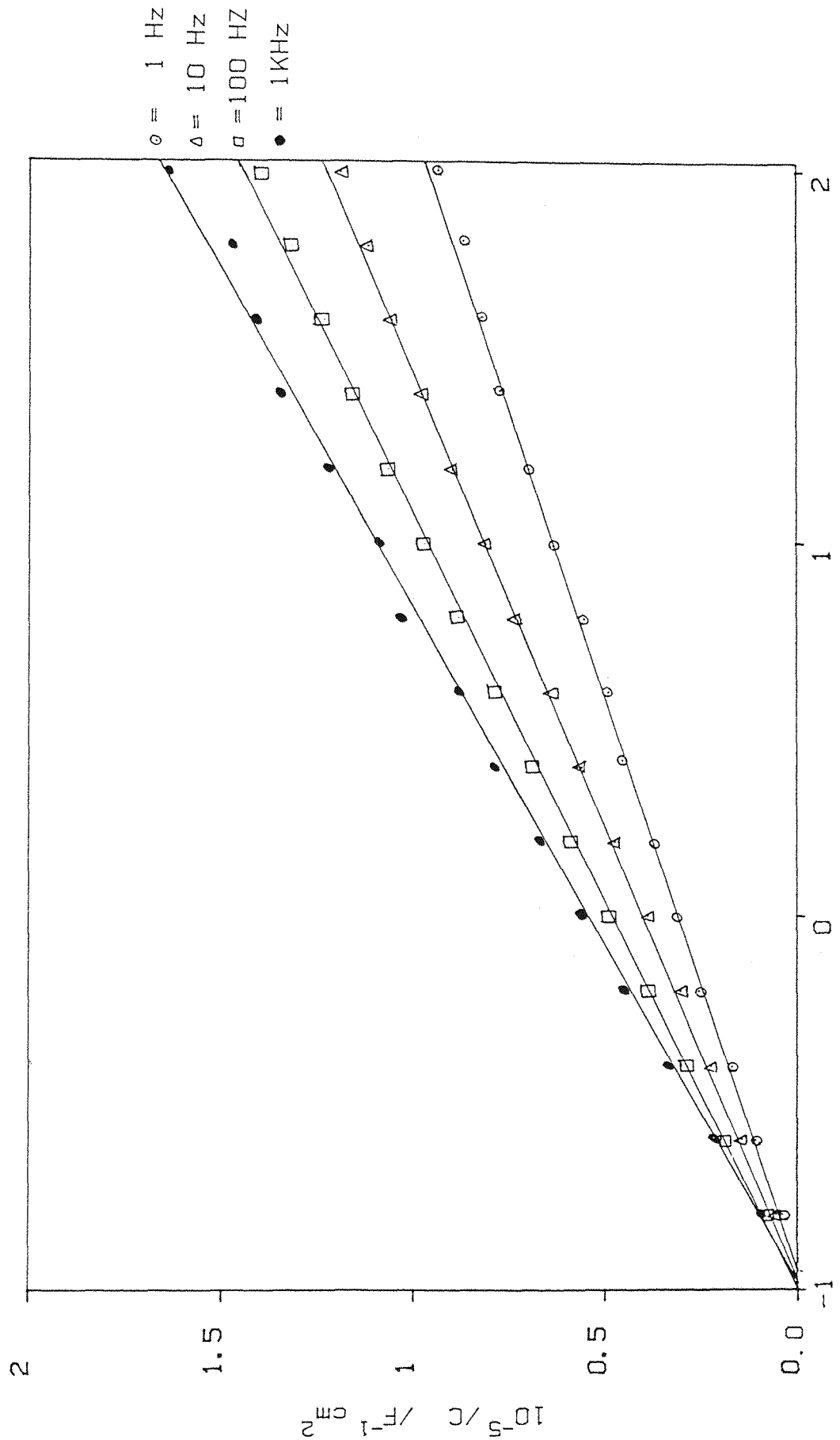

Fig. 4.11 Reciprocal capacitance measurements during the growth of a titanium oxide film, showing the frequency dispersion. Scan rate = 100 mVs-1 to 2.0 V vs Hg/Hg_2SO_4 in 3 mol dm^{-3} at room temperature.

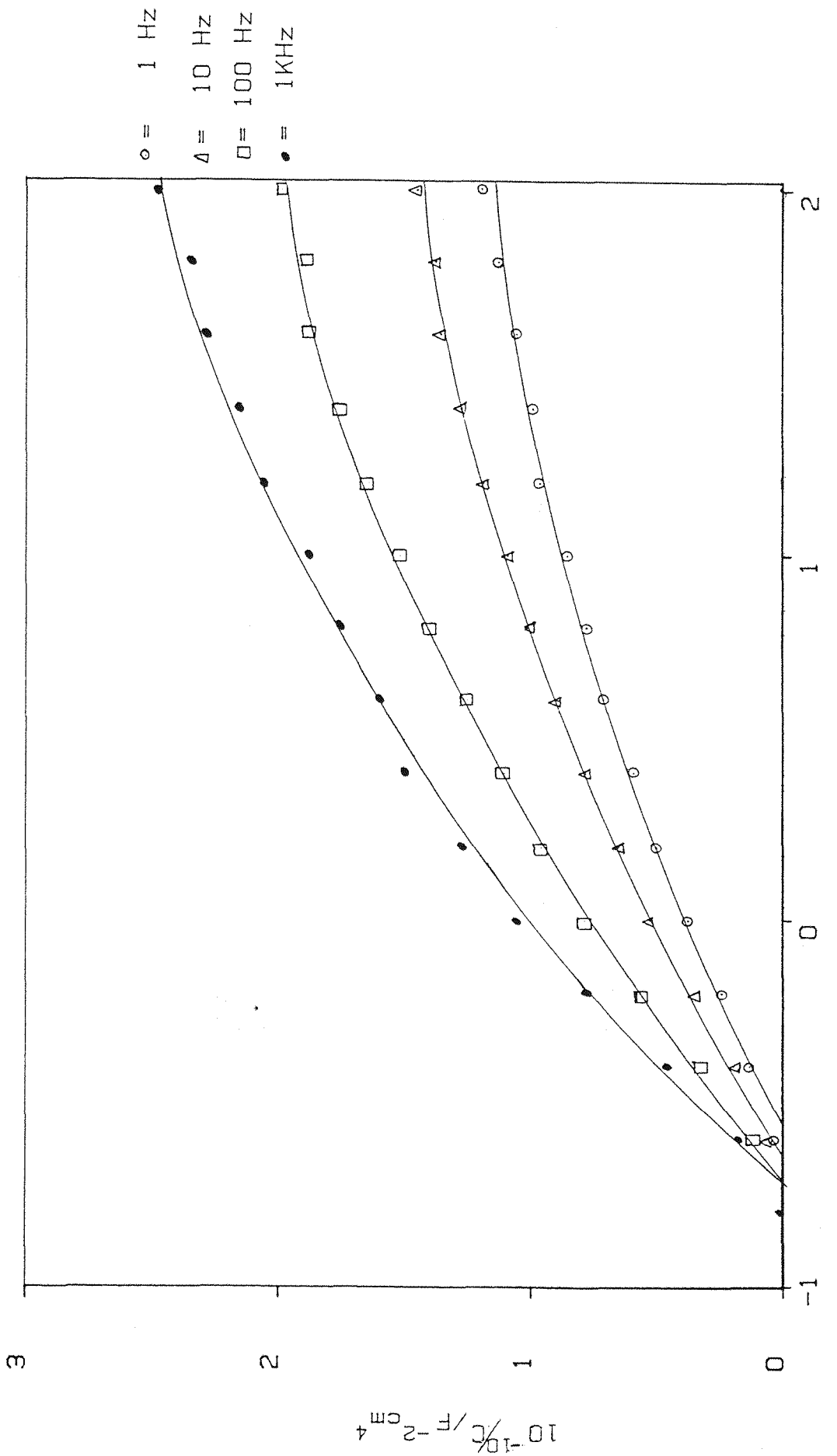

Fig. 4.12 Frequency dependence of the Mott-Schottky plot obtained from the anodic oxide film grown for figure 4.11

the concentration of ionised donors, and thus the higher the size of the space-charge capacitance. This means that the inhomogeneous doping model can successfully explain the trend in the frequency dependence of the space-charge capacitance shown in figure 4.12. However, it does not explain frequency dependence of the geometric capacitance shown in figure 4.11, as in this case all the donors should be ionised.

Table 4.5 summarises the results obtained from reciprocal capacitance and Mott-Schottky plots constructed from the impedance data.

It has been reported by Young (14) that $\tan\delta$ for valve metal oxides is inversely proportional to the formation voltage of the film thickness, indicating that thick films should approach more closely ideal capacitance behaviour ($\tan\delta \longrightarrow 0$). Figure 4.13 shows that this relationship holds for the thin films with which this thesis has largely been concerned. A plot of $^{1}/_{L_f}$ vs $\tan\delta$ was not constructed, as this requires the anodising ratio to be precisely known. Also a plot of this kind would be dominated by the very thin films.

Table 4.5 Frequency dependence of the data obtained from reciprocal capacitance and Mott-Schottky plots. Films grown in 3 mol dm^{-3} H_2SO_4 to 2.0 V vs Hg/Hg_2SO_4 at room temperature (N_s = donor density at lower potentials, N_t = donor density at the anodic potential limit).

Growth rate/ mVs^{-1}	Frequency/ Hz	εr^2	N_s $/10^{19} cm^{-3}$	N_t $/10^{19} cm^{-3}$	V_{Fb}/V vs Hg/Hg_2SO_4
1	1	140	20.0	35.0	-0.53
1	10	135	16.0	32.2	-0.58
1	100	150	13.0	29.0	-0.60
1	1000	135	11.0	27.5	-0.61
10	1	89	15.8	60.1	-0.52
10	10	79	13.5	57.8	-0.55
10	100	77	10.6	56.6	-0.57
10	1000	72	8.3	55.2	-0.61
100	1	106	14.5	87.6	-0.47
100	10	77	11.0	87.3	-0.60
100	100	67	5.7	69.3	-0.66
100	1000	60	4.6	70.6	-0.67

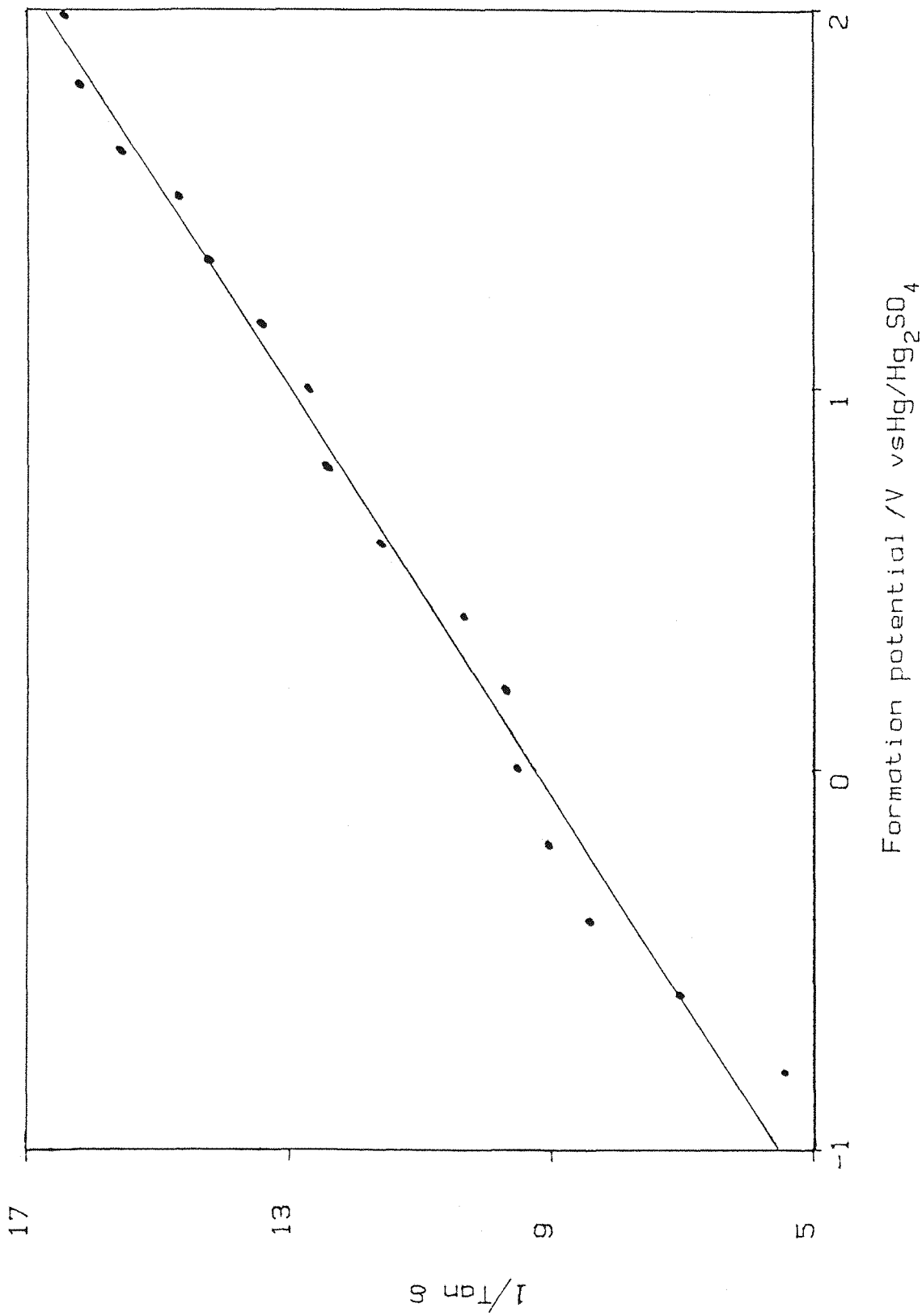

Fig. 4.13 Plot of $1/\tan\delta$ against formation potential for a titanium oxide film grown at 100 mVs^{-1} in 3 mol dm^{-3}, at room temperature, 100 Hz.

4.4 Photocurrent Spectroscopy

4.4.1 Spectrtal distribution of the photocurrent

The uncorrected spectral response of a titanium oxide film measured at its formation potential of 3.0 V vs Hg/Hg_2SO_4 was recorded (Fig. 4.14). From this the corrected spectral response (Fig. 4.15) was calcualted with the aid of a vacuum photodiode (Fig. 3.11). The photocurrent rises sharply at approximately 400 nm, which indicates a band gap of 3.1 eV. This is between the absorption edges of rutile 3.02 eV, 410 nm, and anatase 3.22 eV, 385 nm (18). The small photocurrent observed above 400 nm was probably due to band tailing.

No direct evidence of surface states was identified in the spectra, as no photocurrent was observed for wavelengths greater than 420 nm. This does not rule out the existence of surface states in the anodic films, as it may be necessary to use a dual beam experiment to detect them. This method, which uses band gap radiation to create the states and sub-band gap radiation to detect them, was employed by Laser and Gottesfeld (19) to find active band gap sites on thermally produced titanium oxide films.

The corrected spectrum for a rutile single crystal is shown in figure 4.16. Comparison with figure 4.15 indicates that the conversion efficiency rises at approxiamtely twice the rate on the crystal compared with the anodic film. A possible explanation of this result is that indirect transitions between band tails are occurring in the anodic oxide. These tails are caused by imperfections in the structure of the solid, and therefore they are more likely to occur in the polycrystalline anodic oxide film than in the single crystal.

4.4.2 Potential dependence of the photocurrent

The uncorrected spectral response (Fig. 4.14), shows a maximum photocurrent at 310 nm, so this wavelength was used for most of the photocurrent measurements taken during potential cycling. Wavelengths shorter than 310 nm gave a reduced photocurrent response due largely to the restricted intensity output of the xenon lamp.

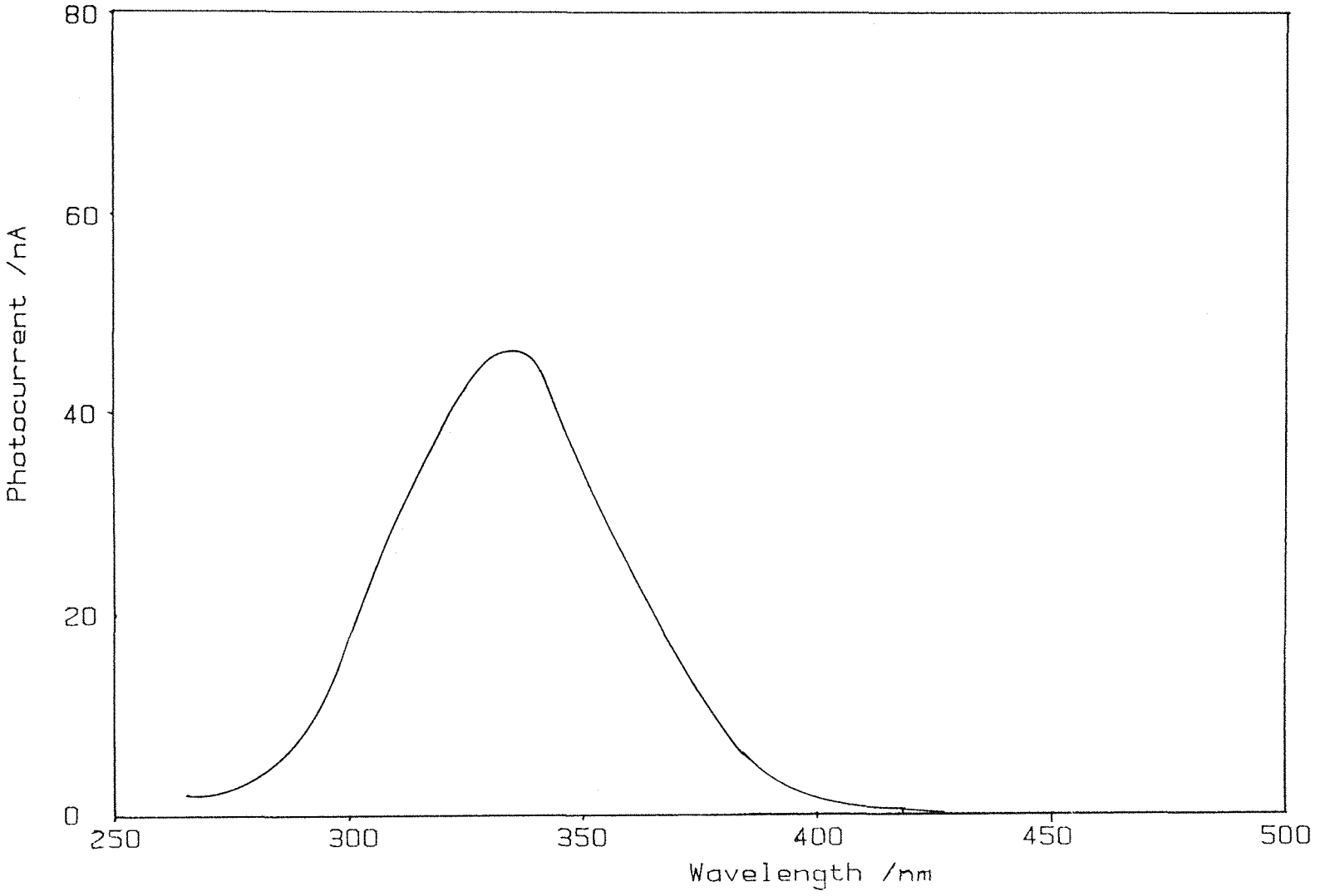

Fig. 4.14 Uncorrected photocurrent spectrum from an anodic oxide film on titanium held at its formation voltage of 3.0 V vs Hg/Hg_2SO_4. The film was grown at 100 mVs^{-1}, in 3 mol dm^{-3} H_2SO_4 at room temperature. Slit width = 7.5 nm.

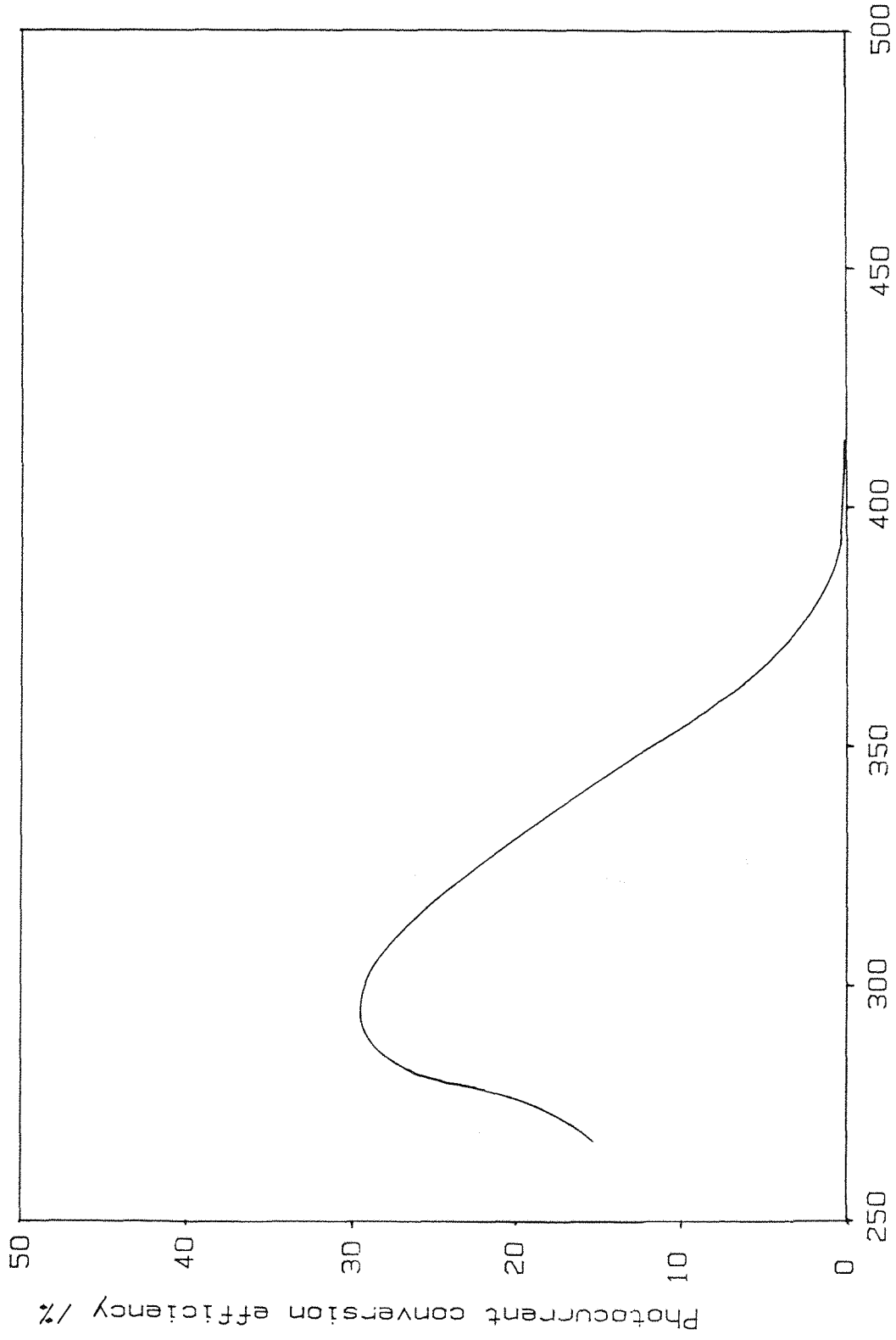

Fig. 4.15 Corrected photocurrent spectrum obtained from figure 4.14 after calibration of the incident light by a RCA 935 photodiode.

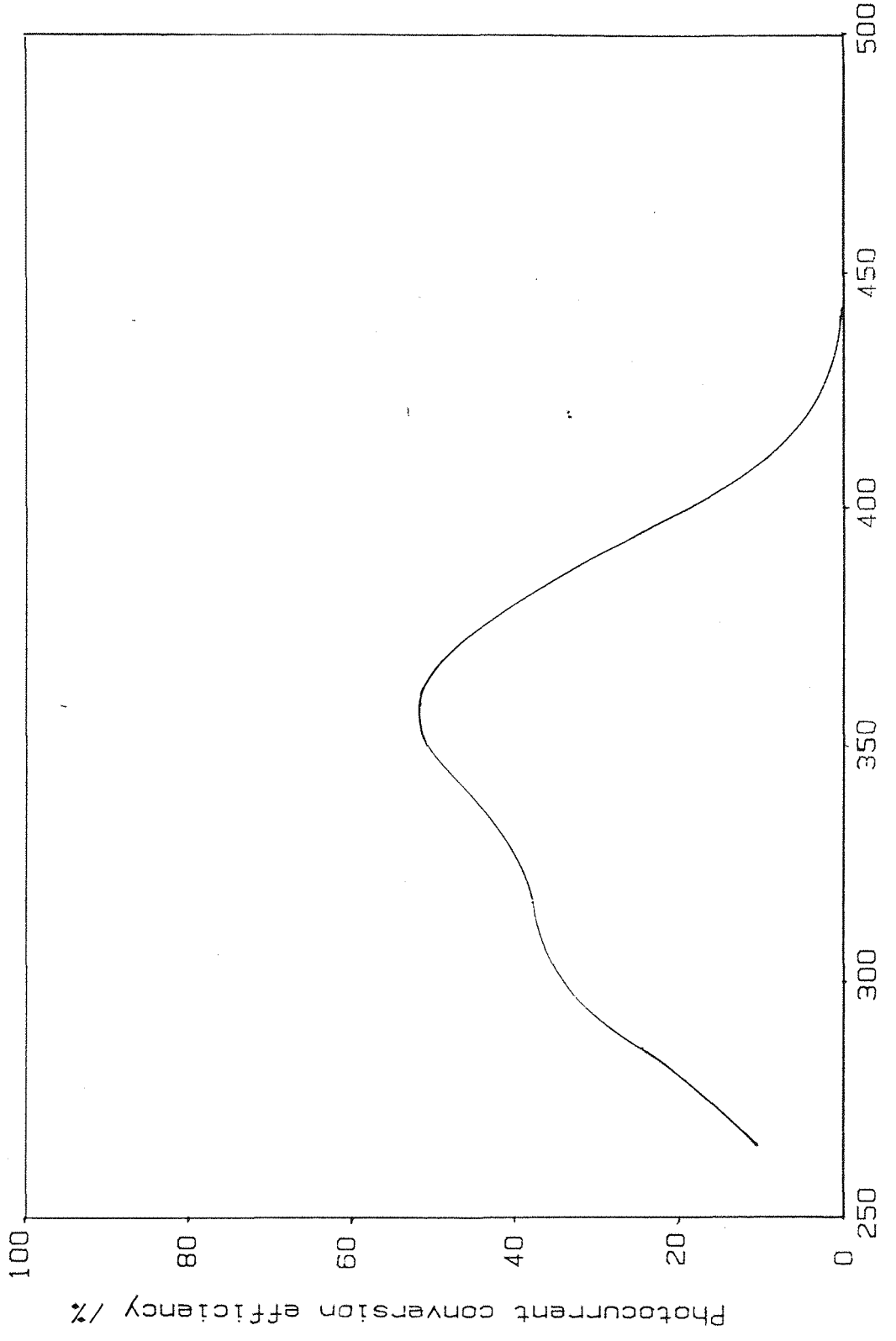

Fig. 4.16 Corrected photocurrent spectrum obtained from a rutile single crystal, held at a potential of 3.0 V vs Hg/Hg_2SO_4.

The photocurrent-voltage curve was recorded for a titanium electrode during oxide growth and on subsequent cycles (Fig. 4.17). No photocurrent was observed during growth until a potential of about +0.1 V vs Hg/Hg_2SO_4 was reached; at this point a film of approximately 2.5 nm should already be present on the electrode surface. Possible explanations for the absence of photocurrent are firstly that very thin films may have a different energy band structure from the bulk oxide, and secondly there may be a 'dead zone' close to the metal/oxide interface in which holes are quenched by electrons tunnelling from the metal. As the probability of tunnelling decreases exponentially with distance, this latter effect should fall off as the film thickness increases, which may explain the 's' shaped initial rise in the photocurrent. Heusler and Yun (20) have shown that tunnelling through oxide films dominated carrier transfer up to about 3.0 nm, although this thickness can be increased if a convenient energy level is available halfway through the film to act as an intermediate state for resonance tunnelling (21).

The photocurrent on the reverse potential cycle also displays a pronounced 's' shape, which could be attributed to the existence of surface states that act as recombination sites (22,23).

The photocurrent-potential relationship of a rutile crystal was also recorded (Fig. 4.18). In this case, the photocurrent showed a rapid transition from zero to a constant value, suggesting a much lower concentration of recombination sites.

In the absence of recombination, the potential at which the photocurrent falls to zero will be close to the semiconductor's flat band potential. From figures 4.17 and 4.18 the flat band potential for a film formed to 3.0 V vs Hg/Hg_2SO_4 was estimated to be -0.6 V, while that for rutile, in the same electrolyte, was -0.45 V vs Hg/Hg_2SO_4. As the extent of surface recombination is unknown, the photocurrent onset potentials can only be taken as limiting values of the flat band potentials. They are however, in good agreement with the values found by impedance techniques (Section 4.3) for the oxide films and with literature values for rutile (24).

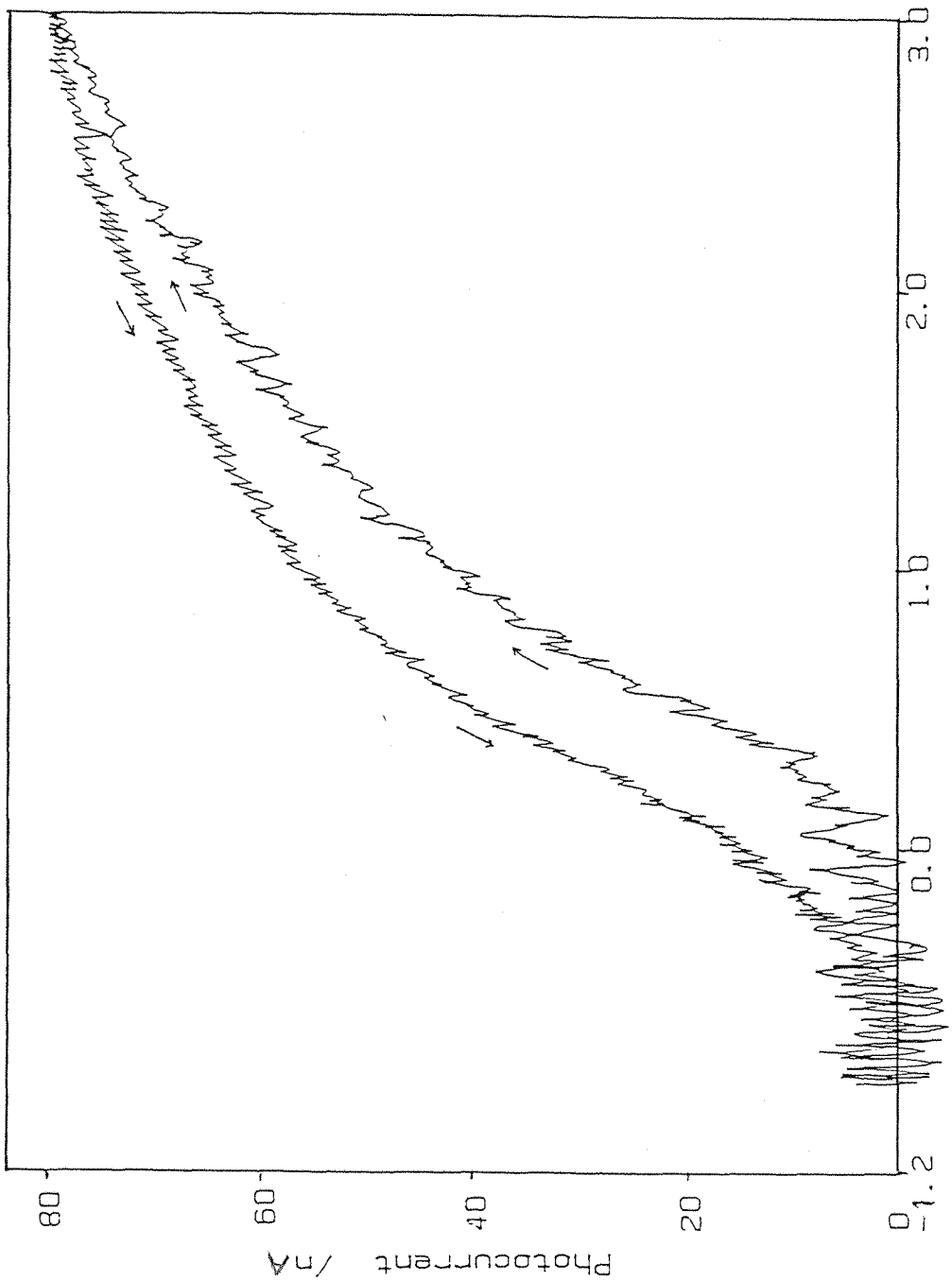

Fig. 4.17 Photocurrent-potential response of a titanium oxide film during both the growth and the reverse potential cycles. Scan rate 10 mVs^{-1} in 3 mol dm^{-3} H_2SO_4, at room temperature. Wavelength 310 nm with a slit width of 7.5 nm.

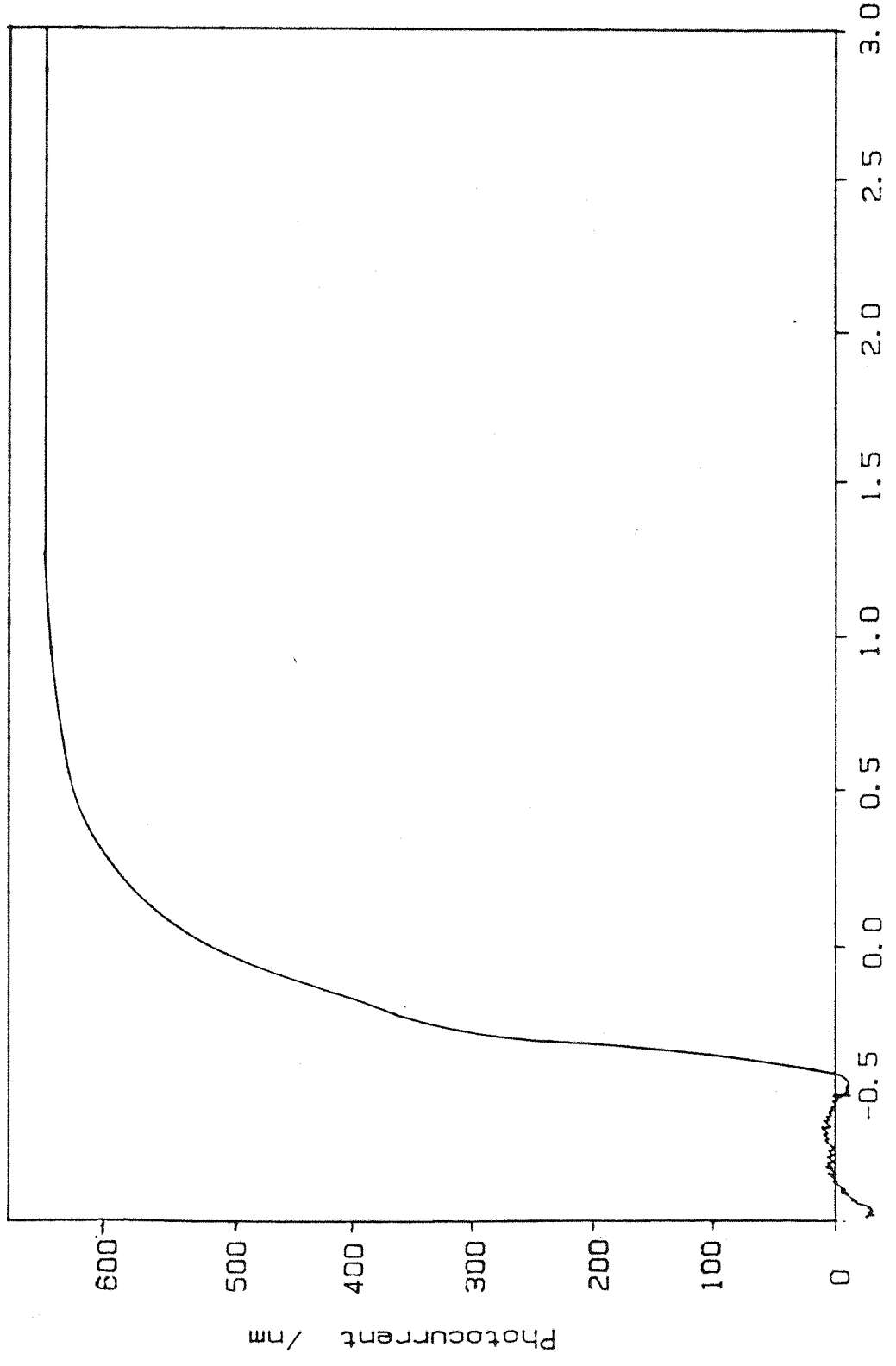

Fig. 4.18 Photocurrent-potential response of a rutile single crystal. Scan rate 10 mVs^{-1}. Wavelength 310 nm with a slit width of 10 nm.

4.4.3 Estimation of $\alpha(\lambda)$ for TiO_2 films

The capacitance of an anodic oxide film was recorded during its growth and on the reverse potential cycle, with a forward sweep rate of 1 mVs^{-1} for the first cycle, and then 10 mVs^{-1} for subsequent cycles. The photocurrent-voltage response of this film was then recorded for a range of wavelengths between 250 and 390 nm. Finally, the capacitance-voltage curve of the film was recorded again to make sure that no changes had occurred to the film.

The capacitance during film growth was used to construct a reciprocal capacitance plot (Fig. 4.8b), from which a value for εr^2 of 134 and a film thickness, L_f of 14.2xr nm were obtained. If a surface roughness of 1.5 is assumed, the value of ε is 60 and of L_f 9.5 nm.

The relationship between photocurrent and space-charge capacitance was shown in section 2.3.6 to be given by

$$\alpha\varepsilon\varepsilon_o r/C_{max} = Ln[\{ -(A-B-\Phi) + \sqrt{(A-B-\Phi)^2 + 4AB}\ \}/2B]$$

$$= Ln(\Lambda) \qquad 2.70$$

where

$$A = (1 - R_{12}) \qquad 2.65$$

$$B = (1 - R_{12})R_{23}\ e^{-2\alpha L_f} \qquad 2.66$$

For perpendicular radiation, the reflection coefficient at an interface between two virtually non-absorbing media is given by

$$R_{12} = \frac{(n_1 - n_2)^2}{(n_1 + n_2)^2} \qquad 4.4$$

This equation applies to a good approximation at the oxide/electrolyte interface, with n_1 being the refractive index of the electrolyte and n_2 that of the oxide.

At the oxide/metal interface on the other hand, account must be taken of the high extinction coefficient of the metal, K_3, so the reflection coefficient now becomes,

$$R_{23} = \frac{(n_2 - n_3)^2 + K_3^2}{(n_2 + n_3)^2 + K_3^2} \qquad 4.5$$

By assuming a constant value for n_1 of 1.34, and using values for n_2 extrapolated from the data of Holland (25) for evaporatied anatase films, and values for n_3 and K_3 from Johnson et al. (26), R_{12} and R_{23} were calculated for wavelengths in the region of 250-390 nm and are displayed in table 4.6.

The values calculated for R_{12} and R_{23} were inserted into equations 2.65 and 2.66, in order to obtain values for A and B. However, equation 2.66 shows that B is dependent on the absorption coefficient, through the term $e^{-2\alpha L_f}$, so that initial values for α were taken from the data of Memming et al (27) for TiO_2 films prepared by chemical vapour phase deposition (CVD). This enabled plots of the reciprocal capacitance of the oxide film, obtained on the reverse potential sweep against Ln(Λ) to be constructed for various wavelengths (Fig. 4.19). The slope of these plots are equal to $\alpha\varepsilon\varepsilon_o r$, so improved values for α could be calculated and used in turn to calculate new values for B, and hence improved $^1/C_{sc}$ vs Ln(Λ) plots could be constructed. In this way, an iterative procedure was employed until stable values of α and B were obtained.

From figure 4.19 it can be seen that the values of Ln(Λ) at low potentials fell below the expected line. This was probably due to the reduction in photocurrent brought about by surface recombination (section 2.3.3.2).

The intercepts of the $^1/C_{sc}$ vs Ln(Λ) plots yielded the Helmholtz capacitance, which was found to be in the region of 40 $\mu F\ cm^{-2}$ for λ = 290-370. Outside this wavelength range, lower values were obtained, possibly due to the low photocurrents being measured. This suggests that the absorption coefficients determined outside this wavelength region should be treated with caution.

Table 4.6 Calculated values for the reflection coefficients of anodic oxide films on titanium.

λ/nm	n_2 (25)	n_3 (26)	k_3 (26)	R_{12}	R_{23}
250	3.55	1.26	1.84	0.204	0.325
260	3.48	1.26	1.97	0.197	0.331
270	3.42	1.27	2.09	0.191	0.342
280	3.36	1.31	2.21	0.185	0.340
290	3.30	1.38	2.33	0.178	0.336
300	3.24	1.44	2.45	0.172	0.331
310	3.17	1.49	2.56	0.165	0.333
320	3.11	1.55	2.67	0.158	0.333
330	3.05	1.60	2.73	0.152	0.329
340	2.98	1.69	2.80	0.144	0.321
350	2.93	1.78	2.86	0.138	0.313
360	2.89	1.85	2.89	0.134	0.306
370	2.84	1.91	2.91	0.129	0.299
380	2.80	1.97	2.93	0.124	0.295
390	2.75	2.04	2.95	0.119	0.288

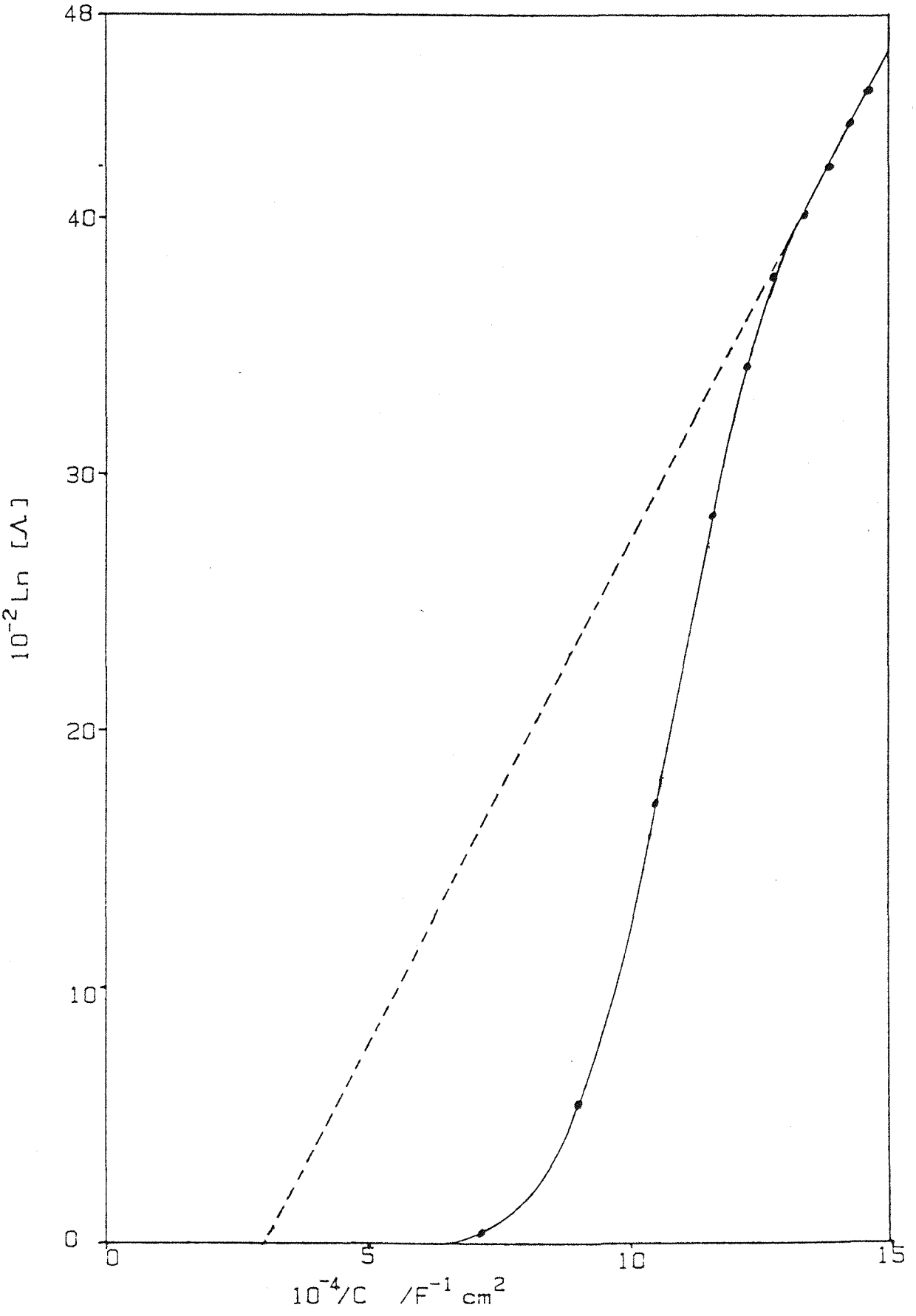

Fig. 4.19 Plot of LnA against the reciprocal of the space-charge capacitance for a titanium oxide film grown at 1 mVs^{-1} to a formation potential of 3.0 V vs Hg/Hg_2SO_4. Wavelength = 300 nm.

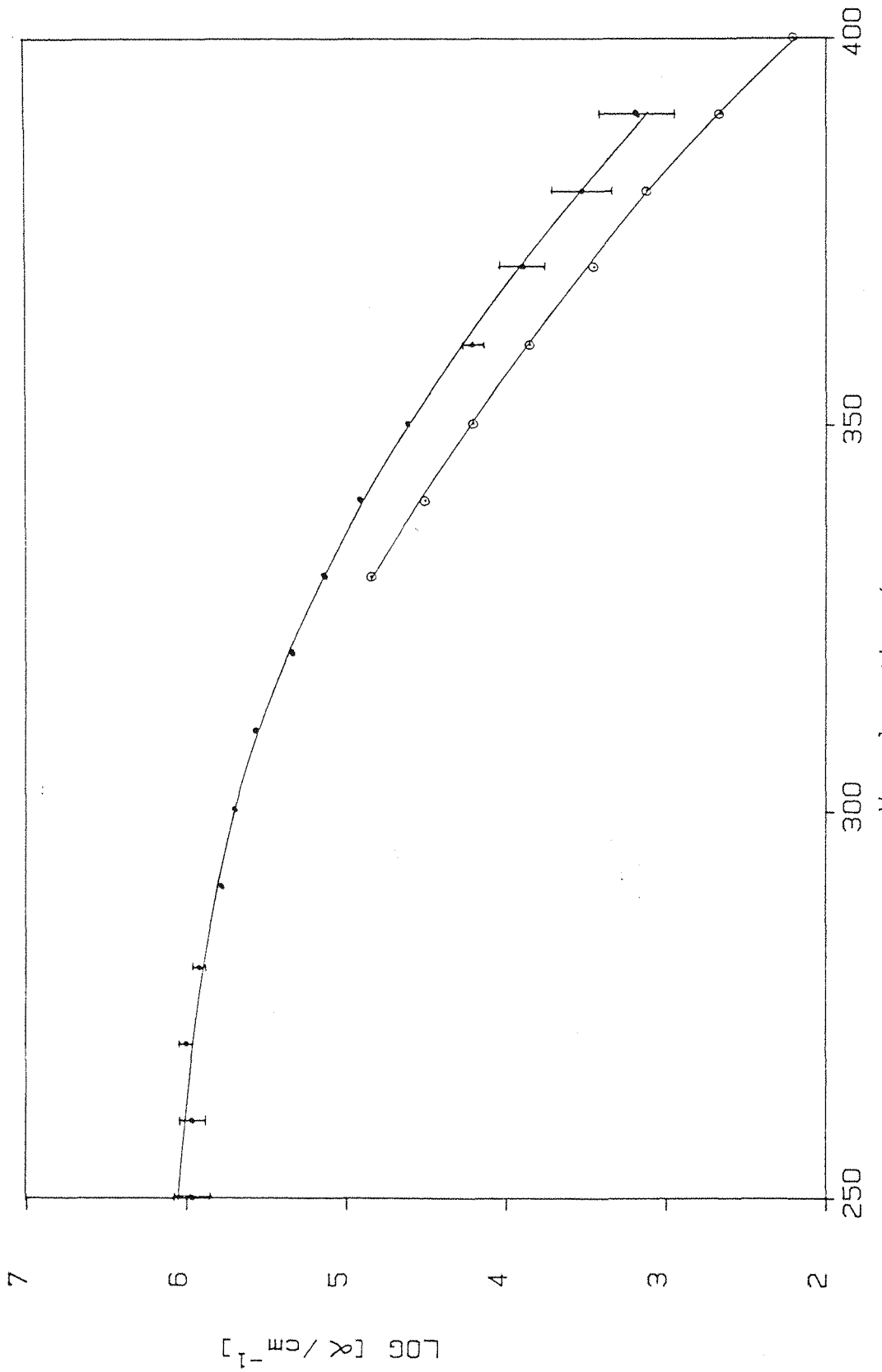

Fig. 4.20 Spectral dependence of the absorption coefficient of an anodic oxide film grown at 1 mVs^{-1} to a formation potential of 3.0 V vs Hg/Hg_2SO_4, •. Data for CVD film is also shown ⊙. (Memming et al. (27)).

Figure 4.20 shows the absorption coefficient spectrum obtained for the anodic oxide films, as well as Memming's (27) data for CVD films. It is clear that the two data sets correspond fairly closely at long wavelengths, but the analysis of photocurrent spectra also gives reliable absorption coefficients at short wavelengths where absorption measurements are no longer possible.

4.4.4 Effect of growth rate on the photocurrent-voltage response

Anodic oxide films were grown to a potential of 3.0 V vs Hg/Hg_2SO_4, at various sweep rates. The potential was held at the anodic limit for about 10 minutes until the measured photocurrent became stable, indicating the end of any significant film growth. The photocurrent-voltage response was then recorded at a reverse sweep rate of 10 mVs^{-1} for all the films.

The results obtained (Fig. 4.21) showed that the photocurrent fell steeply with potential on the reverse sweep for films grown at high sweep rates. By contrast, the photocurrent of films grown at low sweep rates fell away relatively slowly with potential on the reverse sweep until the flat band potential was approached, where the photocurrent dropped rapidly to zero. This behaviour is similar to that of the rutile single crystal, (Fig. 4.18) suggesting that slowly grown films are more crystalline and have fewer grain boundaries and imperfections to act as recombination centres, than their rapidly grown counterparts. All the films appeared to have flat band potentials in the region of -0.5 V to -0.6 V vs Hg/Hg_2SO_4.

The size of the photocurrent is related to the Schottky length, L_s, which in turn is related to the reciprocal of the space charge capacitance, (Equ. 2.39). Inspection of figure 4.9, shows that the slope of the Mott-Schottky plots in the high potential region increases as the growth rate of the films increases. This agrees with the observed trend in the photocurrent results, although the growth rate dependence of the capcitance data is much less than that of the photocurrent results.

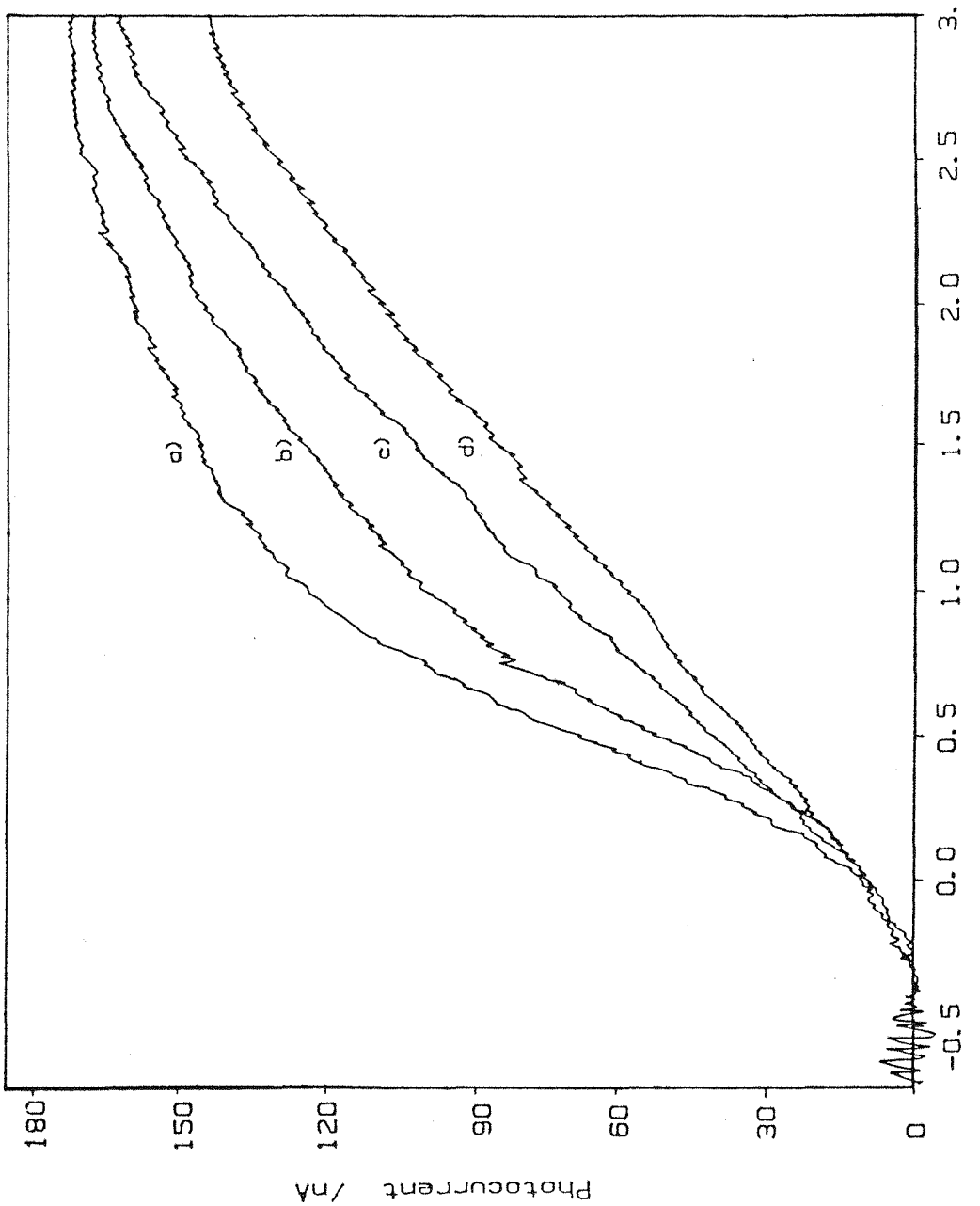

Fig. 4.21 Photocurrent-potential curves for titanium oxide films grown at various scan rates to 3.0V vs Hg/Hg_2SO_4 in 3 mol dm^{-3} H_2SO_4 at room temperature. All curves recorded on the reverse potential scan of $10mVs^{-1}$. Wavelength 310 nm, slits 10 nm. Growth rates were a) 1 mVs^{-1}, b) 10 mVs^{-1}, c) 100 mVs^{-1} and d) 1 Vs^{-1}.

4.4.5 Temperature dependence of the photocurrent.

The effect of formation temperature on the photocurrent response of anodic oxide films was investigated. Figures 4.22 and 4.23 show the effect on the reverse potential scan, at 10 mVs^{-1}, of films which were grown at 1 mVs^{-1} and 1 Vs^{-1} respectivley. Clearly the photocurrent increases with increasing temperature, with plots of the anodic limits photocurrent against temperature (Fig. 4.24) showing a 35% and 38% rise in the photocurrent between the temperatures of 298K and 338K respectively. In section 4.2.3, a 30% increase in plateau current of the cyclic voltammograms was found for the same temperature variation. It is therefore clear that the increase in photocurrent is due to the formation of thicker films at the elevated temperature.

The general shape of the photocurrent-potential curves of films grown at 1 mVs^{-1} did not alter with changes in temperature, which suggests the crystal structure is unchanged. In the case of the films grown at 1 Vs^{-1}, an increase in temperature results in photocurrents that are less potential dependent near the formation potential, suggesting a decrease in the density of surface states (22,23) or an increase in the crystallinity of the films.

The shape of the photocurrent-voltage response of a film grown at 1 Vs^{-1} at room temperature and heated subsequently to 60°C, was almost identical to that of a similar film which had been grown at that temperature. This result shows that the structure of the room temperature film changed as the temperature was increased. The process is evidently irreversible since the photocurrent-voltage behaviour did not revert back to its original form at room temperature.

4.5 Open-circuit and Reformation Experiments.

4.5.1 Potential-time curves

After growth, the anodic oxide films were switched to open-circuit and their potentials were monitored. Four distinct regions in the potential-time curves were observed; (Fig. 4.25):

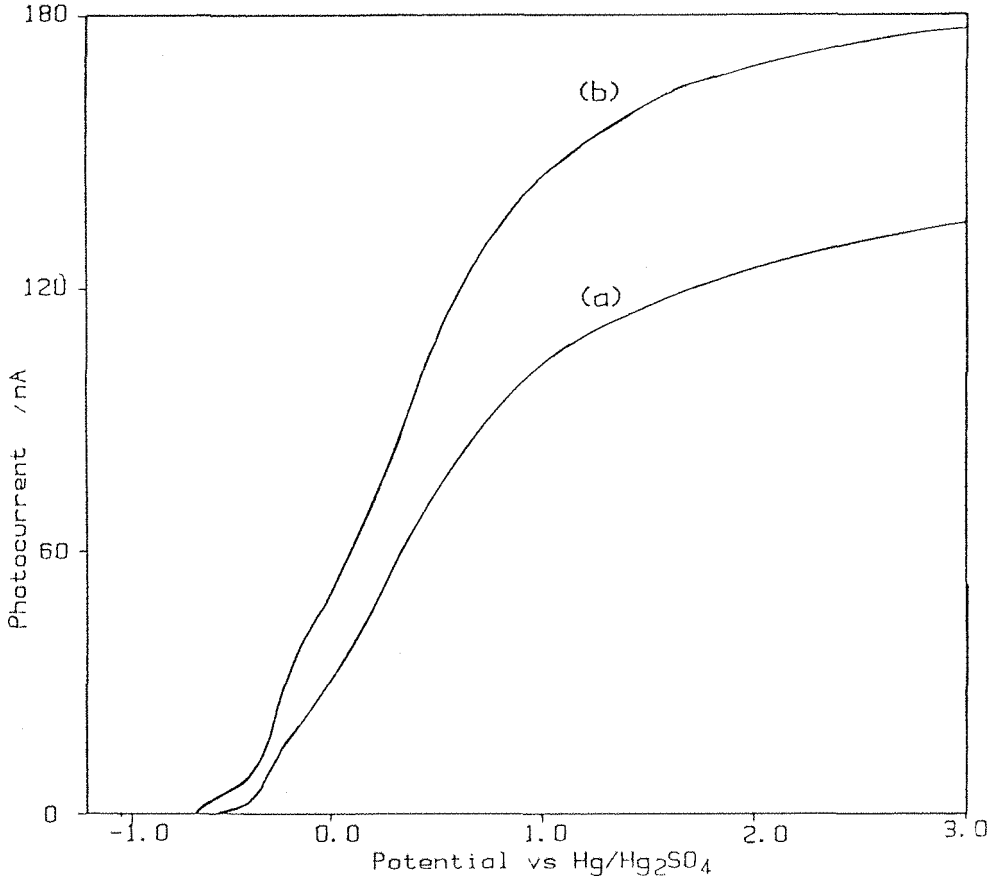

Fig. 4.22 Dependence of the shape of the photocurrent-potential curve, during the reverse potential scan, on temperature, for a titanium oxide film grown at 1 mVs^{-1}. 310 nm. Curve a) 20°C. curve b) 60°C.

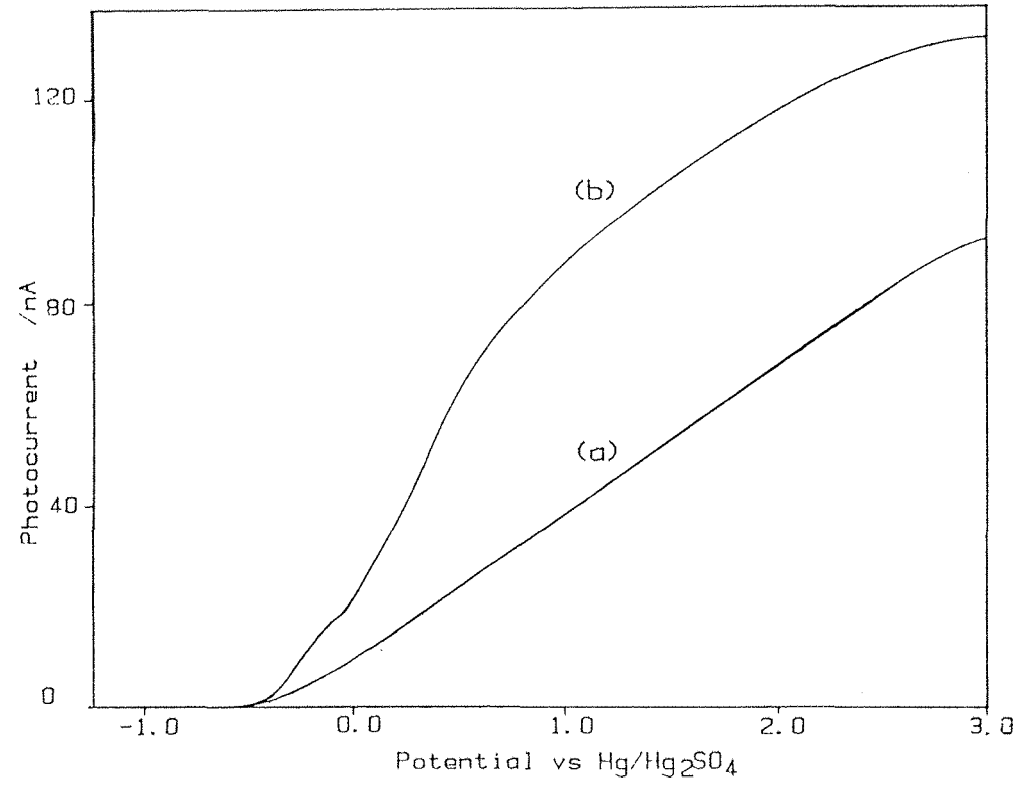

Fig. 4.23 Dependence of the shape of the photocurrent-potential curve during the reverse potential scan on temperature for a titanium oxide film grown at 1 Vs^{-1}. 310 nm. Curve a) 20°C, curve b) 60°C.

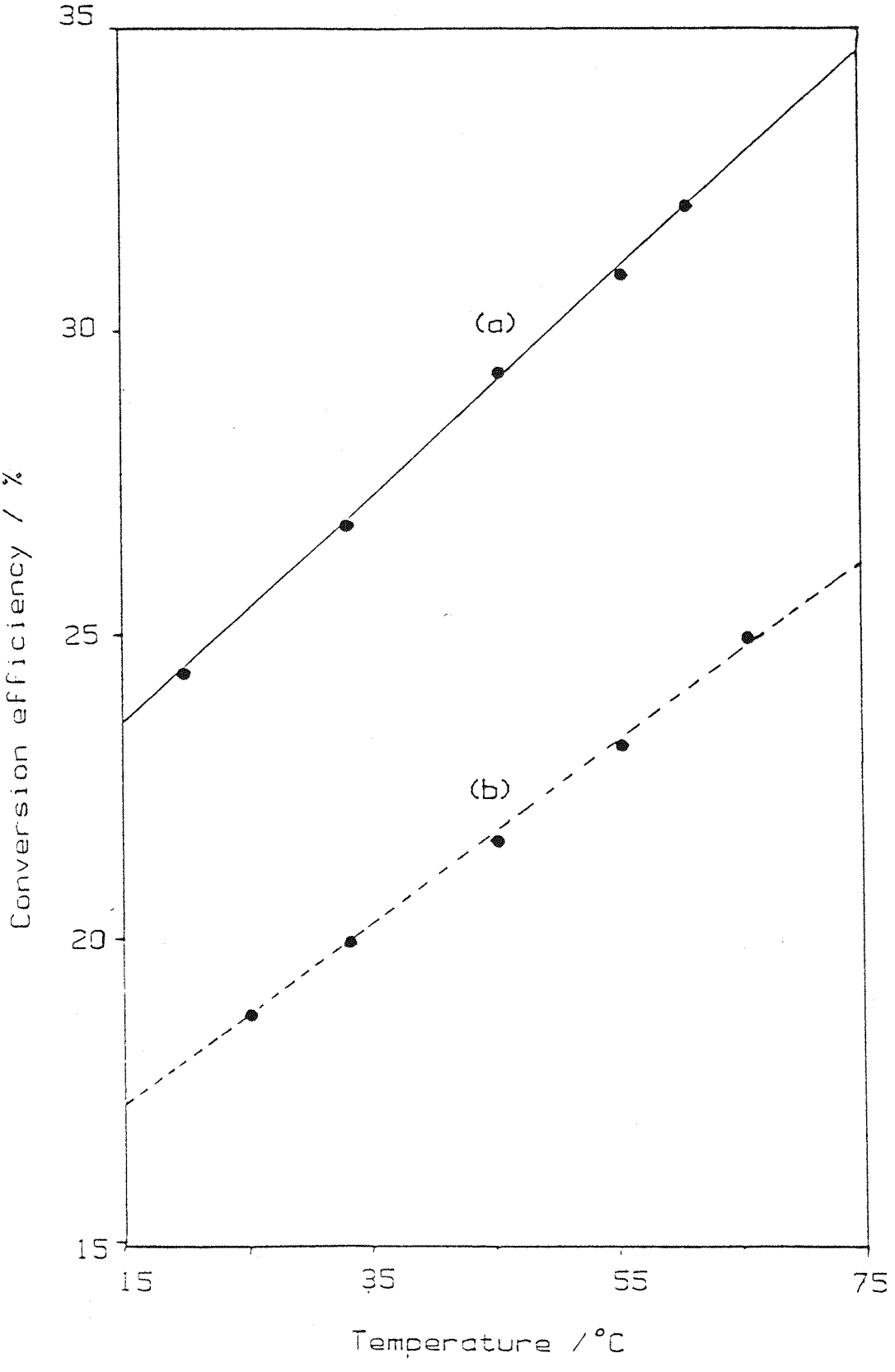

Fig. 4.24 Plots of photocurrent conversion efficiency against temperature for titanium oxide films grown at a) 1 mVs^{-1} and b) 1 Vs^{-1} to 3.0 V vs Hg/Hg_2SO_4 in 3 mol dm^{-3} H_2SO_4. Photocurrents measured at the formation potential. Wavelength 310 nm.

i) a rapid fall from the films formation potential,

ii) a slower decay in the open-circuit potential of the electrode,

iii) a step due to the breakdown of the film,

iv) a steady potential corresponding to the dissolution of Ti^{3+}.

The slope of the step, region (iii), was found to depend on the H_2SO_4 concentration in the electrolyte (cf. Fig. 4.25 and 4.26), with figure 4.27 yielding a relationship of 35 $mVs^{-1}/mol\ dm^{-3}$. A possible explanation of this dependence, is that the final catastrophic breakdown occurs when a small part of bare titanium metal is exposed to the acid; the resulting Ti^{3+} dissolution, the rate of which has been previously shown to be pH dependent (28), then breaks up or undermines the remaining film. Removal of the oxide film was demonstrated by running a 2nd cyclic voltammogram which showed that oxide growth started immediately at the 'Flade' potential. The currents in this second voltammogram were larger than those in the one obtained during the original growth of the film, indicating an increase in the electrode area had occurred during Ti^{3+} dissolution.

The effects of various different growth conditions, on the time taken for the oxide film to reach the final breakdown region (iii), were investigated by reformation experiments in which the oxide film was regrown under linear sweep conditions.

4.5.2 Reformation experiments

Anodic oxide films were grown by potential sweep and then left at open-circuit for a period of time, τ. Before region (iii) in figure 4.25 was reached, the electrode was switched back to potential control and the cyclic voltammogram was repeated. The resultant potential-time profile of the electrode is shown in figure 4.28.

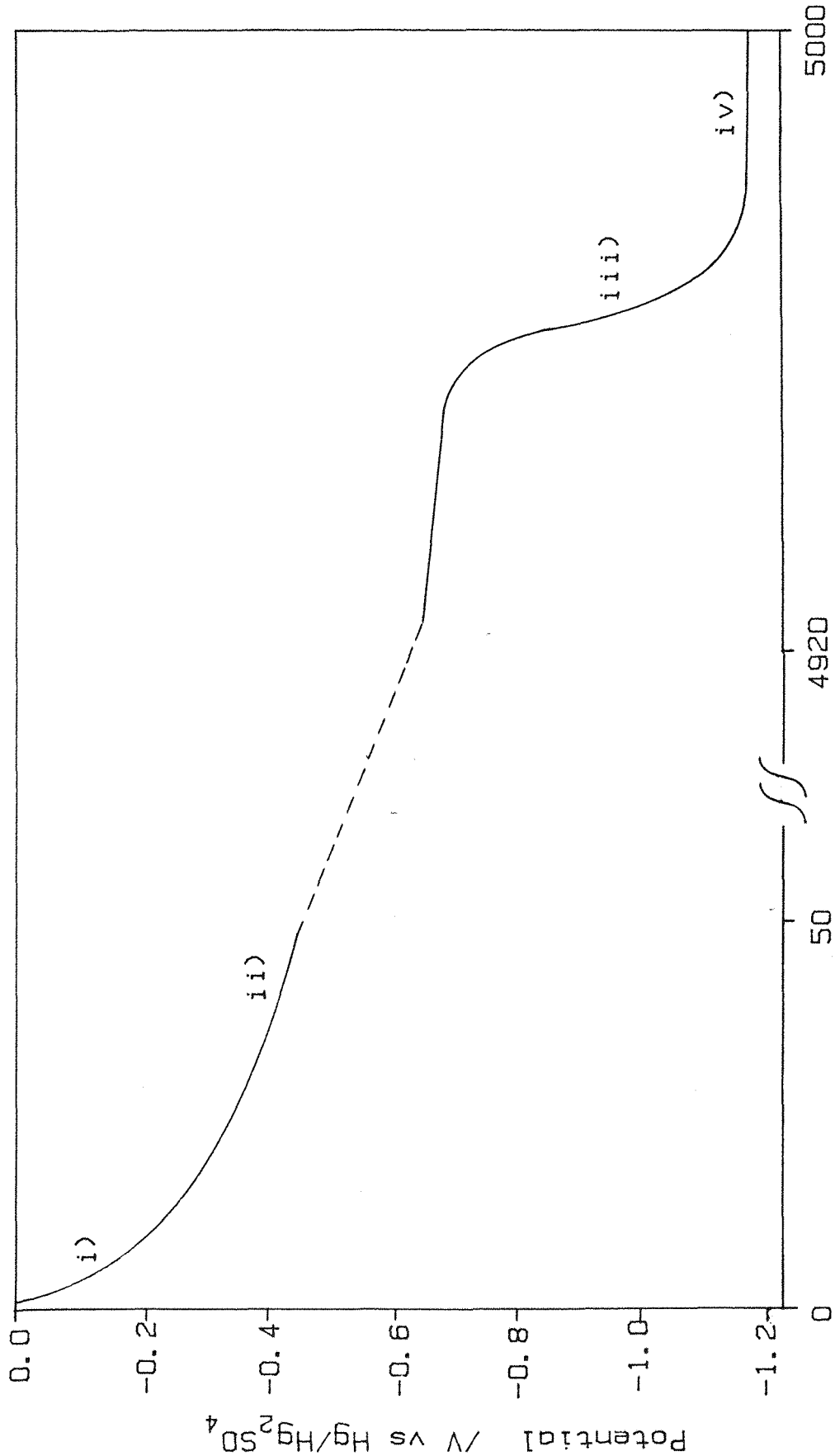

Fig. 4.25 Typical open-circuit potential vs time response for a titanium oxide film in 3 mol dm^{-3} H_2SO_4 at 65°C. Film originally grown at 100 mVs^{-1} to 3.0 V vs Hg/Hg_2SO_4.

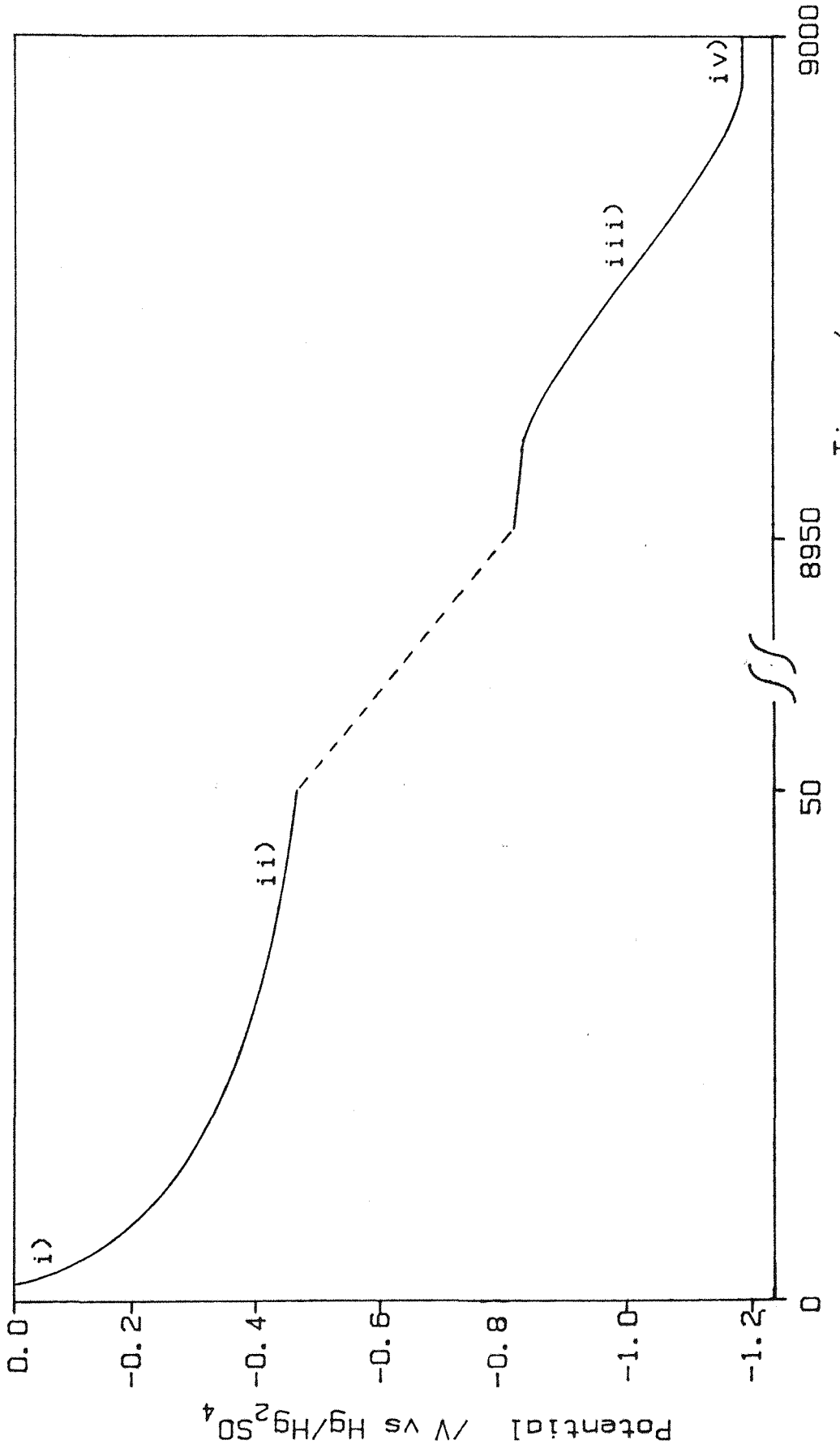

Fig. 4.26 Typical open-circuit potential vs time response for a titanium oxide film in 0.5 mol dm^{-3} H_2SO_4 at 65°C. Film grown originally at 100 mVs^{-1} to 3.0 V vs. Hg/Hg_2SO_4.

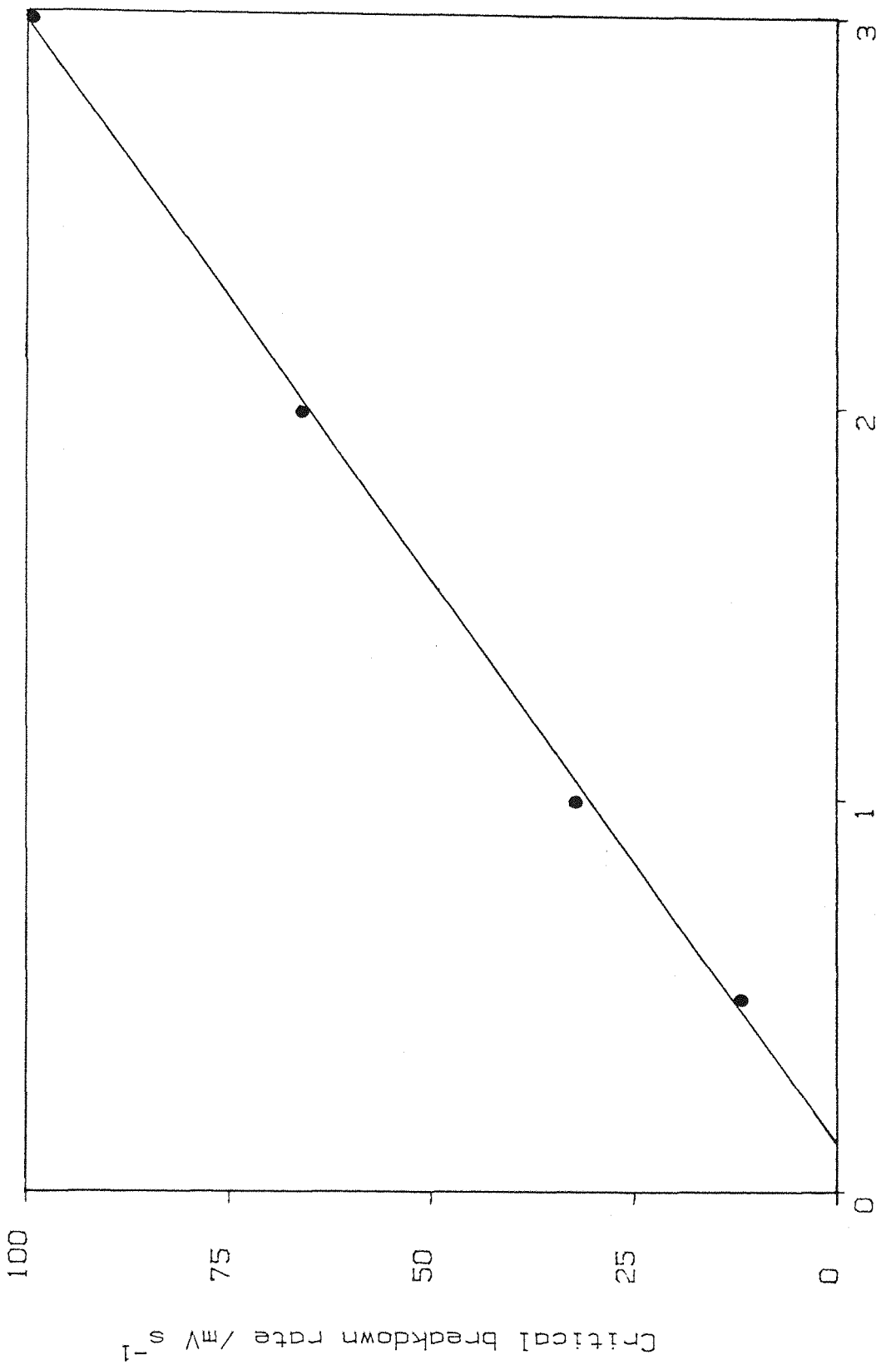

Fig. 4.27 Plot of the critical breakdown rate (slope of region (iii) in figures 4.26 and 4.27) against the concentration of sulphuric acid in which the oxide films were left at open-circuit. 65°C.

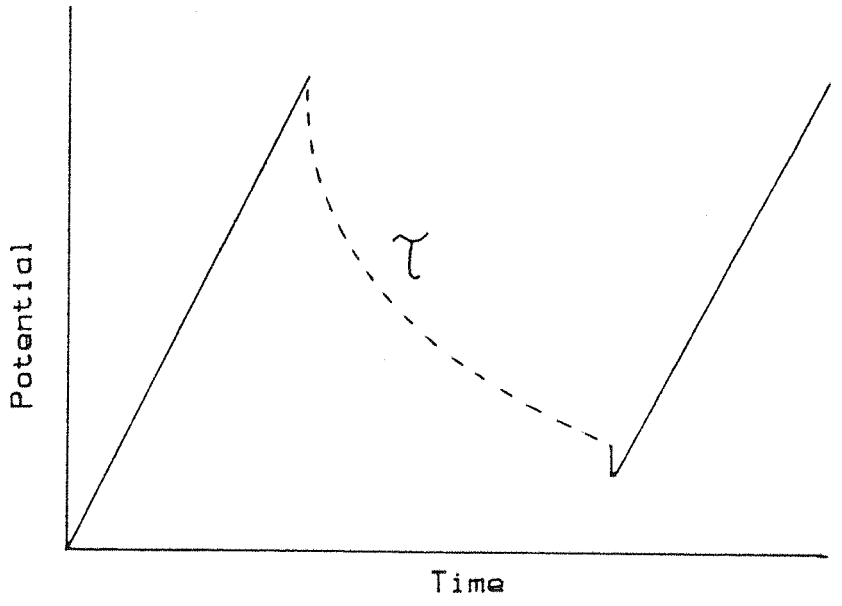

Fig. 4.28 Potential-time profile applied to the titanium electrodes during reformation experiments. Dashed line reprsents time at open-circuit.

A typical cyclic voltammogram resulting from this profile is shown in figure 4.29. Here curve b is obtained on the second potential sweep, and it is clear that there is a reformation charge required to repair the film to its original state. The need for this charge could be due to one fo the following possibilities;

a) film dissolution

$$TiO_{2(s)} \xrightarrow{4H^+} Ti^{4+}_{(aq)} + 2H_2O \text{ (Thinning)} \qquad 4.6$$

b) disproportionation at the metal/oxide interface, by either

i) $$3TiO_{2(s)} + Ti_{(s)} \longrightarrow 2Ti_2O_{3(s)} \qquad 4.7$$

or

ii) $$TiO_{2(s)} + Ti_{(s)} \longrightarrow 2TiO_{(s)} \qquad 4.8$$

Since the plateau current of the second potential scan (Fig. 4.29 curve b) is approximately the same size as that for the first (Fig. 4.29 curve a), it is likely that the reformation process is

$$Ti \longrightarrow TiO_2 + 4e^- \qquad 4.8$$

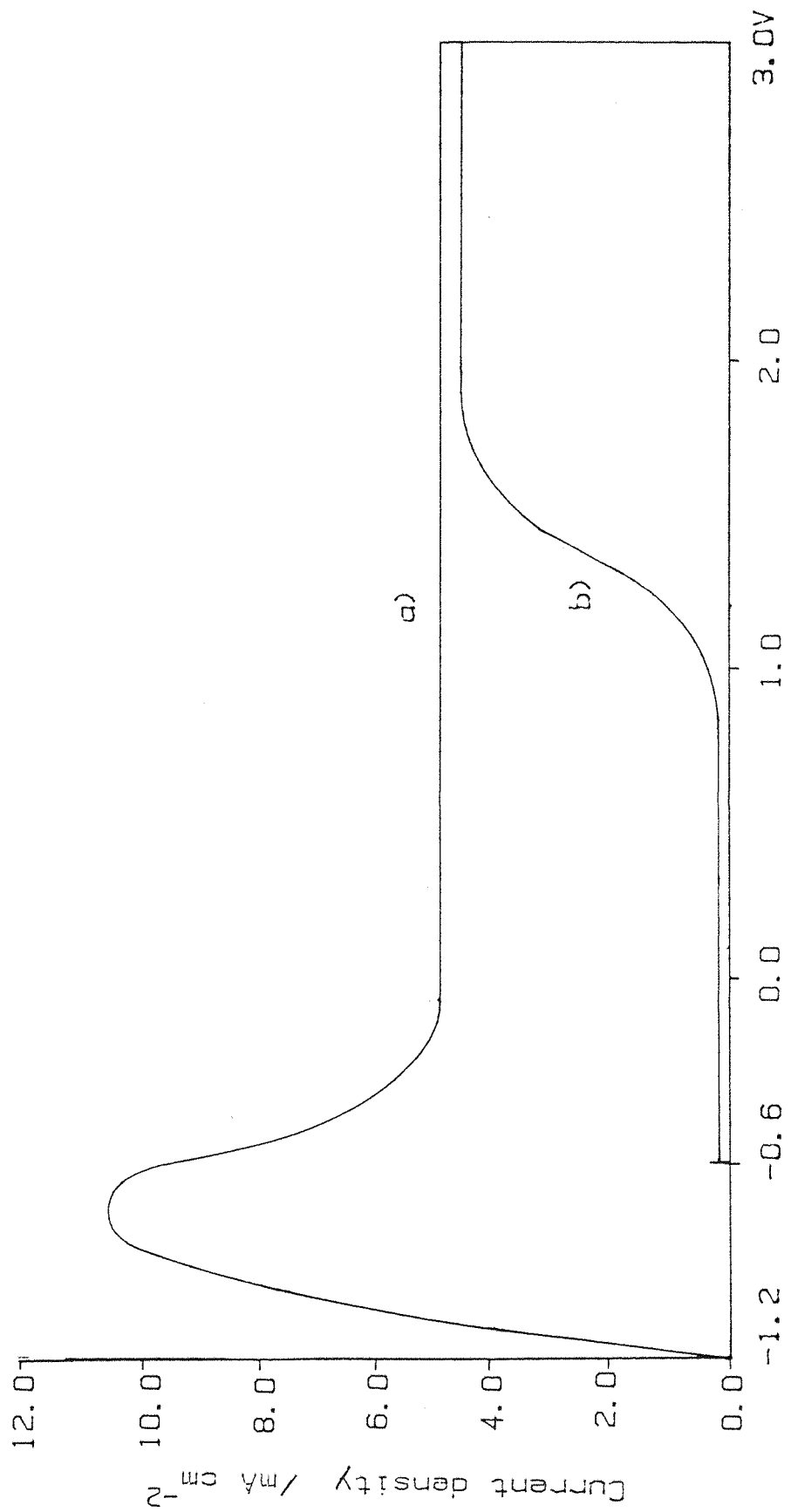

Fig. 4.29 Typical voltammogram obtained from a reformation experiment carried out on a titanium electrode in 3 mol dm^{-3} H_2SO_4 at 45°C. Scan rate = 1 Vs^{-1}, time at open-circuit = 6 x 10^3 s.

which in turn suggests that mechanism a), film dissolution, was occuring while the film was at open-circuit.

Pitting of the oxide film is considered unlikely, as the reformation current rises smoothly suggesting that the thinning of the film occurs non-preferentially over the whole surface.

By varying the time that the oxide films were left at open-circuit, it was possible to construct plots of reformation charges vs time (Fig. 4.30). These plots were found to be reasonably linear, suggesting that the oxide films thinned at a constant rate.

When an anodic oxide film is held at its growth potential, it should continue to grow in accordance with the inverse log law (section 2.1.2). However, any charge passed while the potential is being held constant will not contribute to the area under the cyclic voltammogram. Therefore, any such growth that occurs will not be detected in this series of experiments. This explains why the plot shown in figure 4.30 does not pass through the origin, but instead has an intercept on the ordinate axis which represents the charge needed to reform this additional oxide growth. To reduce this value, the potentiostat was switched off as soon as the anodic potential limit was reached on the initial cyclic voltammograms, for all subsequent experiments. Attempts to use an electronic integrator to obtain values for this additional formation charge were unsuccessful because currents due to additional processes, in particular oxygen evolution, were also integrated.

During the time the oxide films are at open-circuit, their potential is predominantly in the region -0.15 to -0.65 V vs Hg/Hg_2SO_4 ($E^{\ominus}_{TiO^{2+}/Ti^{3+}}$ = -0.54 V vs Hg/Hg_2SO_4 (29)). The open-circuit potential startedto fall rapidly when the critical breakdown of the film was approached, but if the potentiostat was switched in at this point and a cyclic voltammogram recorded, it was observed that the average film thickness was still 1.0 - 1.2 nm with only the foot of the reformation curve in an active potential region (-0.7 V - -0.8 V vs Hg/Hg_2SO_4).

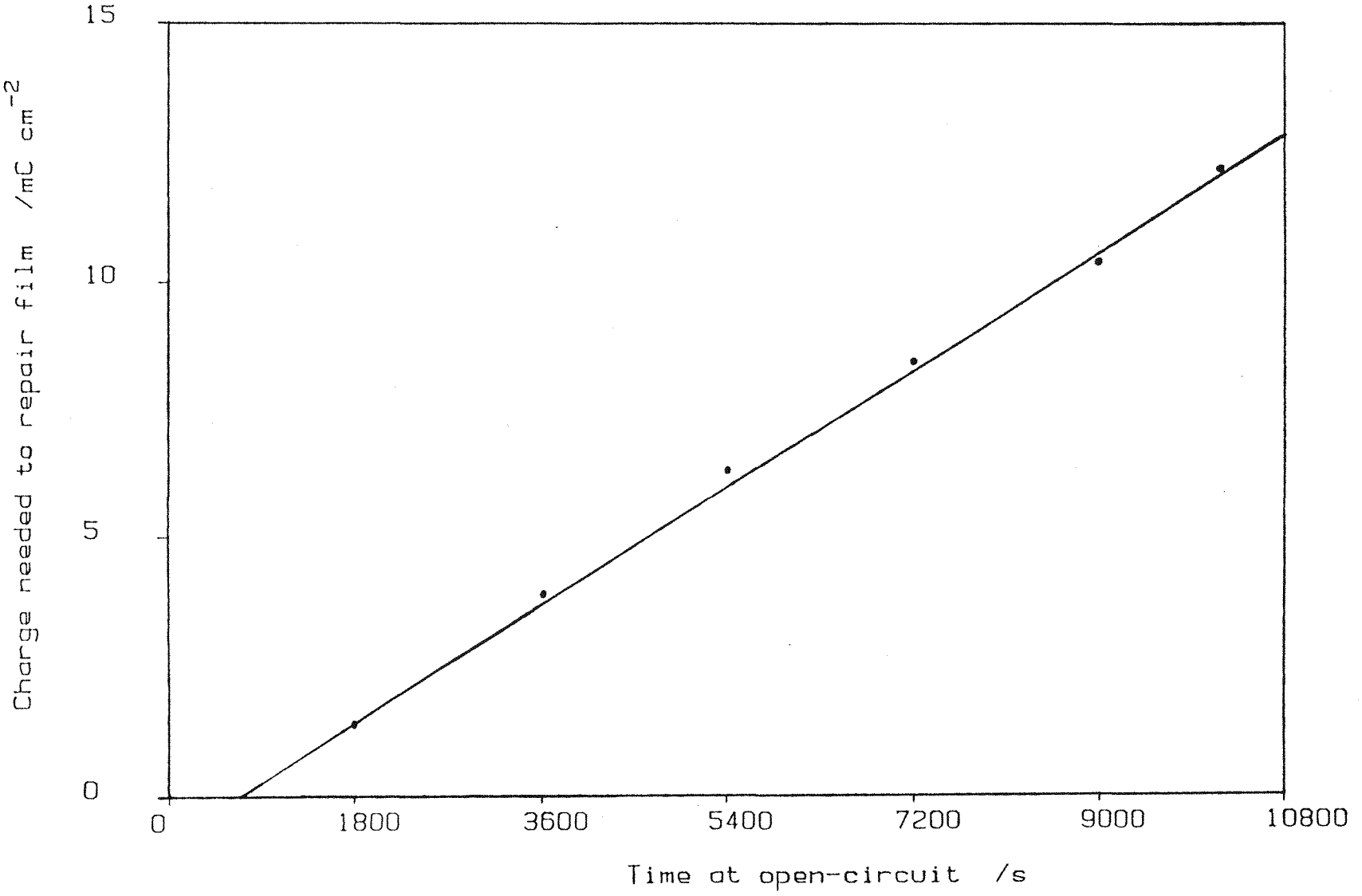

Fig. 4.30 Plot of the charge needed to repair the oxide film against the time spent at open-circuit. All films were grown at 1 Vs^{-1} in 3 mol dm^{-3} H_2SO_4 to 2.0 V vs Hg/Hg_2SO_4, at 45°C, and left under these conditions for their duration at open-circuit.

This suggests that only a small part of the bare titanium metal needs to be exposed to the acid, to cause rapid attack of the metal.

An Arrhenius plot (Fig. 4.31) was constructed from the slopes of a series of reformation charge vs time plots, for films grown at 1 Vs^{-1} in 3 mol dm^{-3} H_2SO_4, over the temperature range 25°C to 65°C. An activation energy of 63 kJ mol^{-1} was determined, along with a pre-exponential factor of 2.9 x 10^4 Cs^{-1} cm^{-2}.

The effect of varying the initial film thickness on open-circuit thinning rate was investigated. Table 4.7 summarises the results obtained, and it shows clearly that the rate of thinning of oxide films grown at 1 Vs^{-1} in 3 mol dm^{-3} H_2SO_4 at 45°C is independent of the initial film thicknesses for starting values greater than 4 nm. A similar result was observed by Gurina et al. (30) for the cathodic dissolution of TiO_2 films in acidic peroxide solutions.

The dissolution rate of the oxide was observed to increase as the critical breakdown region of the film was approached. Since this region appears to begin when there is still approximately 1.2 nm of the film still intact, it was not posisble to determine a linear thinning rate for films with initial film thickness less than 3.0 nm before this critical region was entered.

Table 4.7 Thinning rate of film grown to various anodic limits at 1 Vs^{-1} in 3 mol dm^{-3} H_2SO_4 at 45°C.

Anodic limit (V vs Hg/Hg_2SO_4)	Initial thickness/nm (Assuming A.R = 2.5 nmV^{-1})	Thinning rate (μC $cm^{-2}s^{-1}$)
0.0	2.40	Rapid breakdown
0.5	3.65	1.20
1.0	4.90	1.16
1.5	6.15	1.26
2.0	7.40	1.26
2.5	8.65	1.24
3.0	9.90	1.14

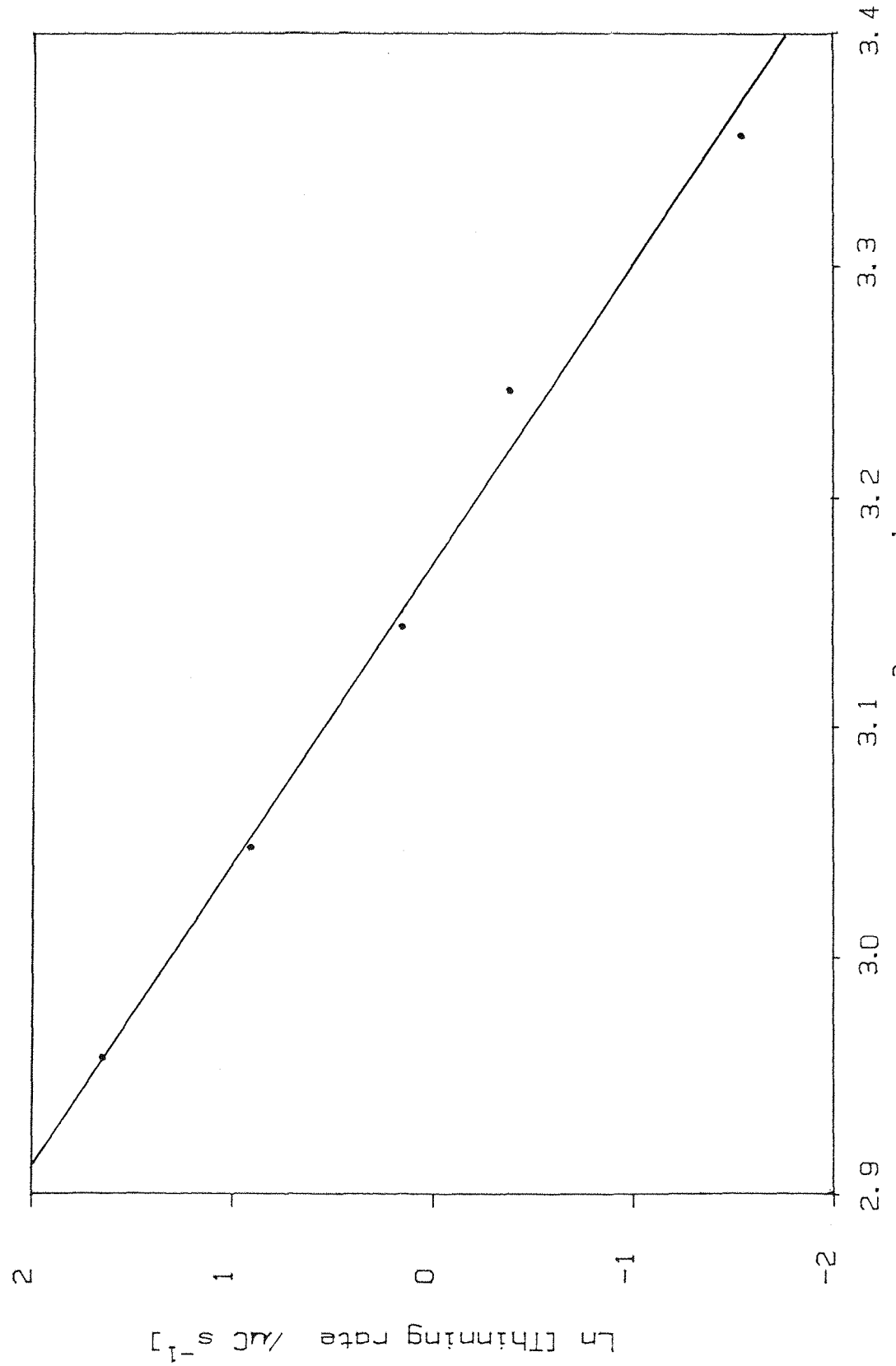

Fig. 4.31 An Arrhenius plot showing the temperature dependence of the thinning rate of titanium oxide in 3 mol dm^{-3} H_2SO_4. All films were grown at 1 Vs^{-1} to 2.0 V vs Hg/Hg_2SO_4.

The results presented so far in this section have mainly been for anodic oxide films grown at high sweep rates (1 Vs^{-1}). If this rate is reduced, the reformation cyclic voltammogram is observed to change, (cf. Fig. 4.29 and 4.32), with the reformation plateau current being lower than the original growth plateau current level. A possible explanation for this result is that because the slowly grown films thin at a much slower rate than their rapidly formed counterparts, they remain at open-circuit for a longer period of time. This may allow a change in structure to occur, leading to a reduction in the size of either the free energy of activation of oxide growth, $\overrightarrow{\Delta G}^{\neq}$, or the half-jump distance, a.

The fall in the plateau current could alternatively be interpreted as evidence for the occurrence of a disproportionation reaction at the metal/oxide interface, as this would require less charge to restore the film back to its original state, for example

$$Ti(o) \xrightarrow{-4e^-} Ti(iv) \qquad \text{(Growth)} \qquad 4.9$$

$$Ti(o) + 3Ti(iv) \longrightarrow 4Ti(iii) \qquad \text{(Disproportionation)} \qquad 4.10$$

$$Ti(iii) \xrightarrow{-e^-} Ti(iv) \qquad \text{(Reformation)} \qquad 4.11$$

Despite the effect on the reformation plateau currents, plots of reformation charge vs time at open-circuit could still be constructed for films grown at slow sweep rates. Table 4.8 summarises the effect of the initial growth rate of the anodic oxide films on their thinning rates at open-circuit. Figure 4.33 shows that the dependence on growth rate of the thinning rate, k_b, can be represented by the empirical relationship

$$k_b \propto \nu^{0.3} \qquad 4.12$$

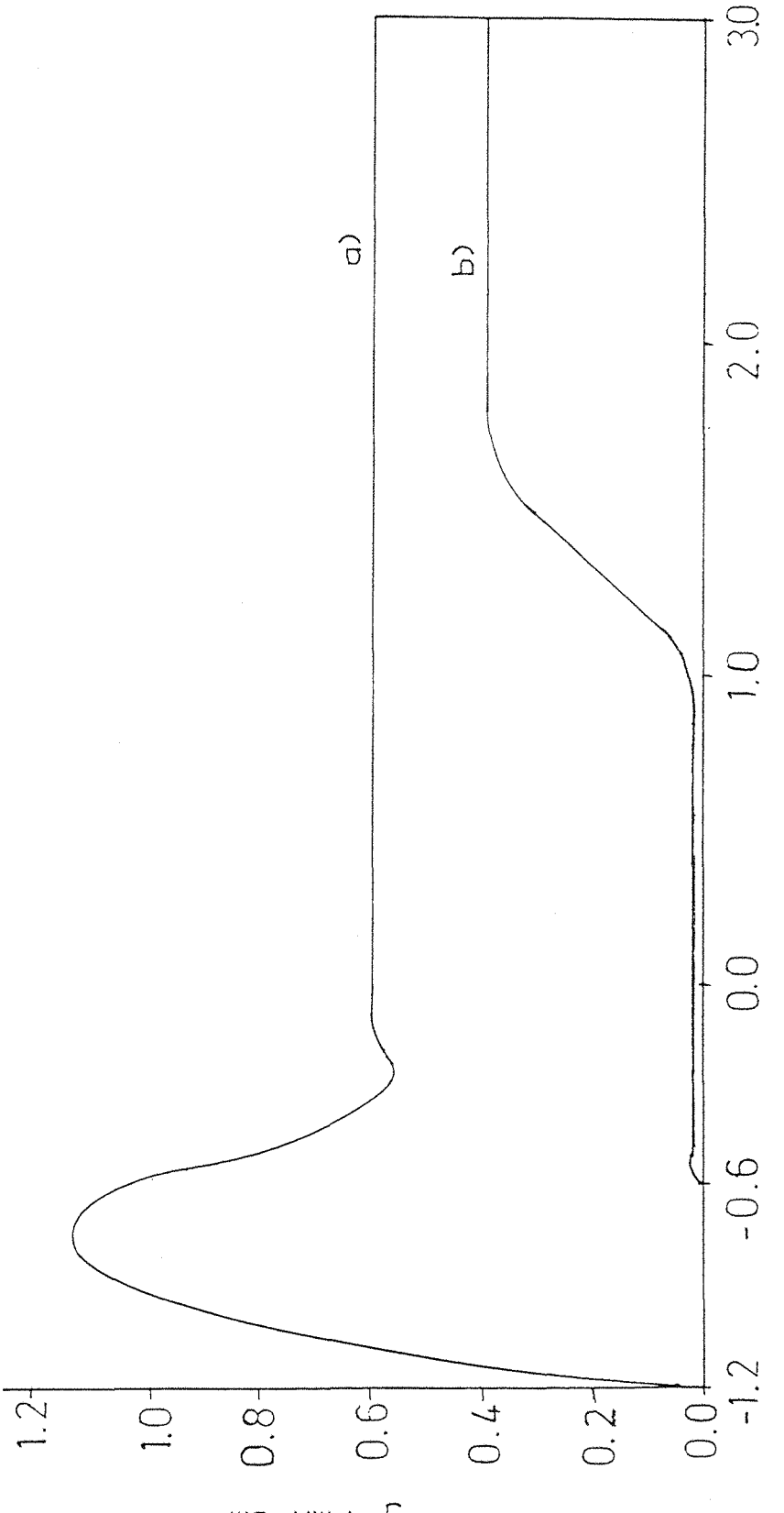

Fig. 4.32 Typical voltammogram obtained from a reformation experiment in which the film was originally grown at 100 m Vs^{-1} to 3.0 V vs Hg/Hg_2SO_4 in 3 mol dm^{-3} H_2SO_4 at 45°C. $\tau = 8.4 \times 10^3$s.

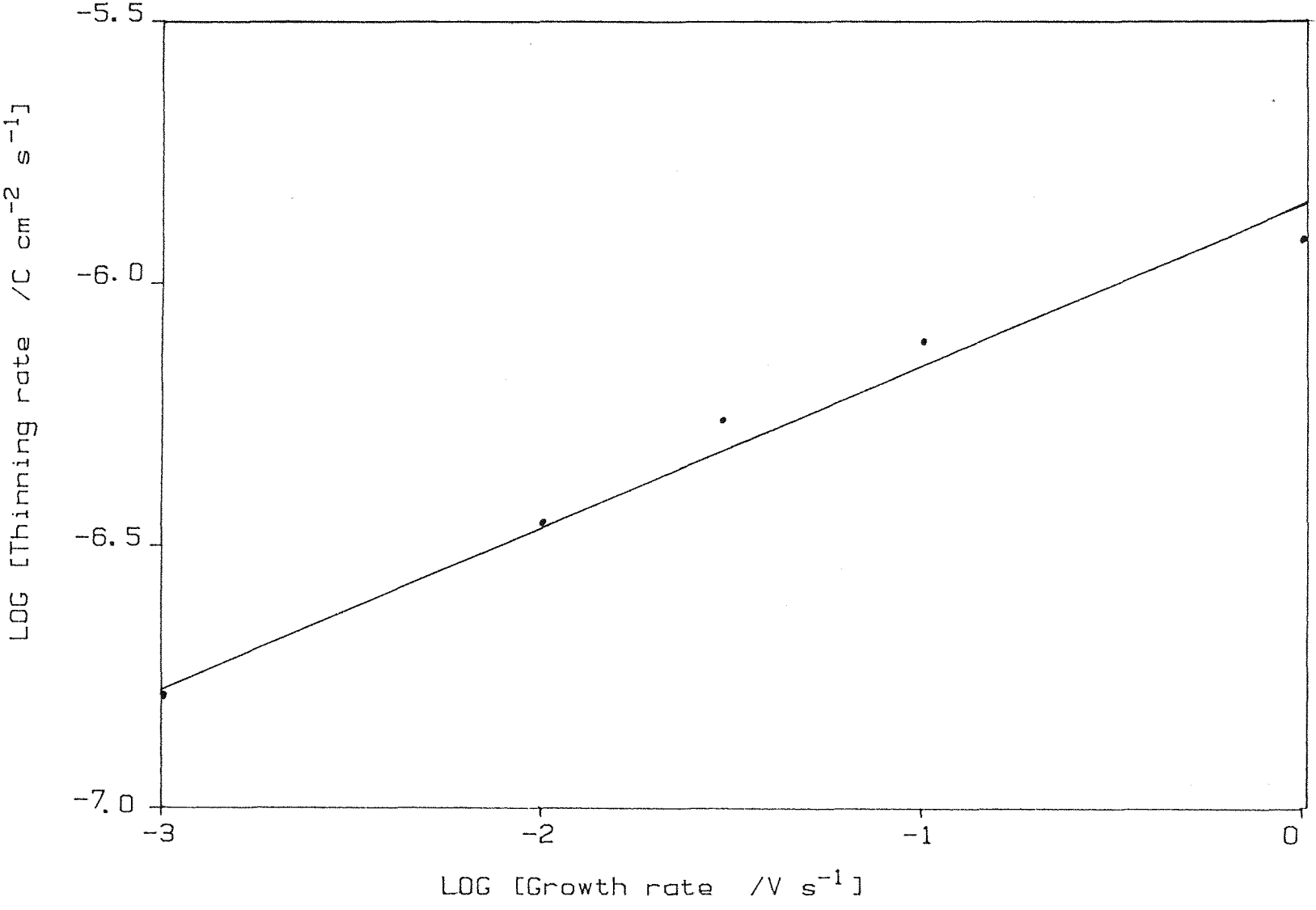

Fig. 4.33 Plot of Log (thinning rate) against Log (growth rate) for titanium oxide films in 3 mol dm^{-3} H_2SO_4 at 45°C.

Table 4.8 Growth rate dependence of the open-circuit thinning rate, for films grown in 3 mol dm^{-3} H_2SO_4 to 2.0 V vs Hg/Hg_2SO_4 at 45°C.

Growth rate/Vs^{-1}	Open-circuit thinning rate/$\mu C\ s^{-1}\ cm^{-2}$
1.0	1.24
0.1	0.78
0.03	0.55
0.01	0.35
0.001	0.15

The effect on the thinning rate of changing the media in which the oxide films were left at open-circuit was investigated by growing a series of identical oxide films at 1 Vs^{-1} in 3 mol dm^{-3} H_2SO_4 at room temperature. The anodised electrode was then placed in different media at 45°C for a set period of time before being reformed in the sulphuric acid again. The reformation charges needed to repair the films are given in table 4.9.

If the breakdown mechanism of the anodic oxide films involves primarily the metal/oxide interface, changing the open-circuit media should have little influence on its rate. However, table 4.9 indicates clearly a strong dependence of the open-circuit thinning rate on the composition at the oxide/solution interface, suggesting that this is where the breakdown mechanism occurs. If the oxide films are simply dissolving, then table 4.9 could be seen as a table of the solubility of TiO_2 in the various solutions. It is also apparent that the anion of the open-circuit solutions plays an important role in the thinning of the oxide films, as solutions of similar pH have quite different thinning rates (cf. 3 mol dm^{-3} HCl and 3 mol dm^{-3} $HClO_4$).

Table 4.9 Effect on the thinning rate of varying the open-circuit media for films grown at 1 Vs^{-1} to 2.0 V vs Hg/Hg_2SO_4 in 3 mol dm^{-3} H_2SO_4 at room temperature.

Open-circuit media at 45°C	Reformation charge/open-circuit time $\mu C\ cm^{-2}\ s^{-1}$
1 mol dm^{-3} KOH + 1 mol dm^{-3} H_2O_2	1.53
3 " " H_3PO_4	1.53
1 " " KOH	1.51
3 " " H_2SO_4	1.15
3 " " HCl	1.01
1 " " H_2SO_4	0.95
3 " " H_2SO_4+0.01 mol dm^{-3} $K_2C_2O_4$	0.79
1 " " $H_2C_2O_4$	0.74
1 " " H_2SO_4+ 1 mol dm^{-3} $NaHSO_4$	0.66
3 " " H_2SO_4+0.1 mol dm^{-3} $K_2C_2O_4$	0.57
3 " " $HClO_4$	0.54
0.25 " " H_2SO_4	0.48
0.05 " " $H_2C_2O_4$	0.43
1 " " H_2SO_4+1 mol dm^{-3} K_2SO_4	0.16
0.02 " " H_2SO_4	0.12
0.02 " " H_2SO_4+0.04 mol dm^{-3} K_2SO_4	0.08
1 " " $K_2C_2O_4$	0.038
1 " " $c(OH)(COOH)(CH_2.COOH)_2$	0.005

It was noted in section 4.2 that on the 2nd cycle of a voltammogram the growth field may become large enough to allow further oxide growth to occur as the anodic potential limit is approached, even though no thinning of the film formed on the first cycle had occurred. In addition, photocurrent experiments (section 4.4.5) indicated that the anodic oxide films can undergo an irreversible structural change on heating. Therefore two blank reformation experiments were carried out, in which the oxide films were placed in a nitrogen atmosphere at 45°C for periods of 2½ and 5 hours. In each case a reformation charge of 0.05 mC cm^{-2} was measured. As this value was independent of the time spent at open-circuit it was assumed that no degradation of the films was occurring in the nitrogen atmosphere, and that the charge measured was solely due to additional oxide growth. The thinning rates shown in table 4.9 have therefore been corrected to take account of this extra charge.

4.5.3 Galvanostatic breakdown of oxide films

It was found that the time, τ_b taken for an oxide film to breakdown was reduced when a small cathodic current ($\sim$ 5 μA cm^{-2}) was applied to the electrode instead of switching it to open-circuit. A possible explanation for this result is as follows:

Under open-circuit conditions the oxide film dissolves according to the reaction

$$TiO_{2(s)} \xrightarrow{4H^+} Ti^{4+}_{(aq)} + 2H_2O \qquad 4.5$$

If there is a critical film thickness, $L_{f(crit)}$, below which catastrophic breakdown of the film occurs, then the dissolution rate, k_b, can be expressed as

$$L_{f(int)} - L_{f(crit)} = \int_0^{\tau_o} k_b \, dt \qquad 4.14$$

$$\Delta L_{f(crit)} = k_b \tau_o \qquad 4.15$$

assuming k_b is not a function of time, and where τ_o is the open-circuit

breakdown time and $L_{f(int)}$ is the initial film thickness, expressed as the charge needed to origianlly form it.

If the applied cathodic current is assumed to reduce the dioxide at the oxide/electrolyte interface, then the resultant soluble Ti(iii) will rapidly dissolve;

$$TiO_{2(s)} + e^- \xrightarrow{H^+} \tfrac{1}{2} Ti_2O_{3(s)} + \tfrac{1}{2}H_2O \qquad 4.16$$

$$\tfrac{1}{2}Ti_2O_{3(s)} + 3H^+ \longrightarrow Ti^{3+}_{(aq)} + {}^{3}/_{2}H_2O \qquad 4.17$$

Equation 4.16 shows that this mechanism requires only a quarter of the charge originally needed to grow the film, in order to totally reduce it. Therefore equation 4.14 converts into

$$\Delta L_{f(crit)} = k_b \tau' + 4j_{ext} \tau' \qquad 4.18$$

Thus

$$j_{ext} = \frac{\Delta L_{f(crit)}}{4\tau'} - \frac{k_b}{4} \qquad 4.19$$

So a plot of j_{ext} vs ${}^{1}/_{\tau'}$ should be a straight line with a slope of $\frac{\Delta L_{f(crit)}}{4}$ and an intercept of $\frac{k_b}{4}$.

Plots of this nature were constructed for films of various thickness grown at 100 mVs^{-1} in 3 mol dm^{-3} H_2SO_4 at 65°C, and they are shown in figure 4.34. Although the resultant plots were indeed linear, the thicker films gave rise to positive intercepts. Since these correspond to negative values for k_b it is clear that the interpretation is inadequate.

The intercepts of the two thinnest films yielded a value for k_b of approximately 3.2 $\mu C\ cm^{-2}s^{-1}$, which is about the value that would be expected from reformation experiments (section 4.5.2). The positive intercepts of the thicker films can be explained if not all the external current contributes towards the reduction of the oxide film,

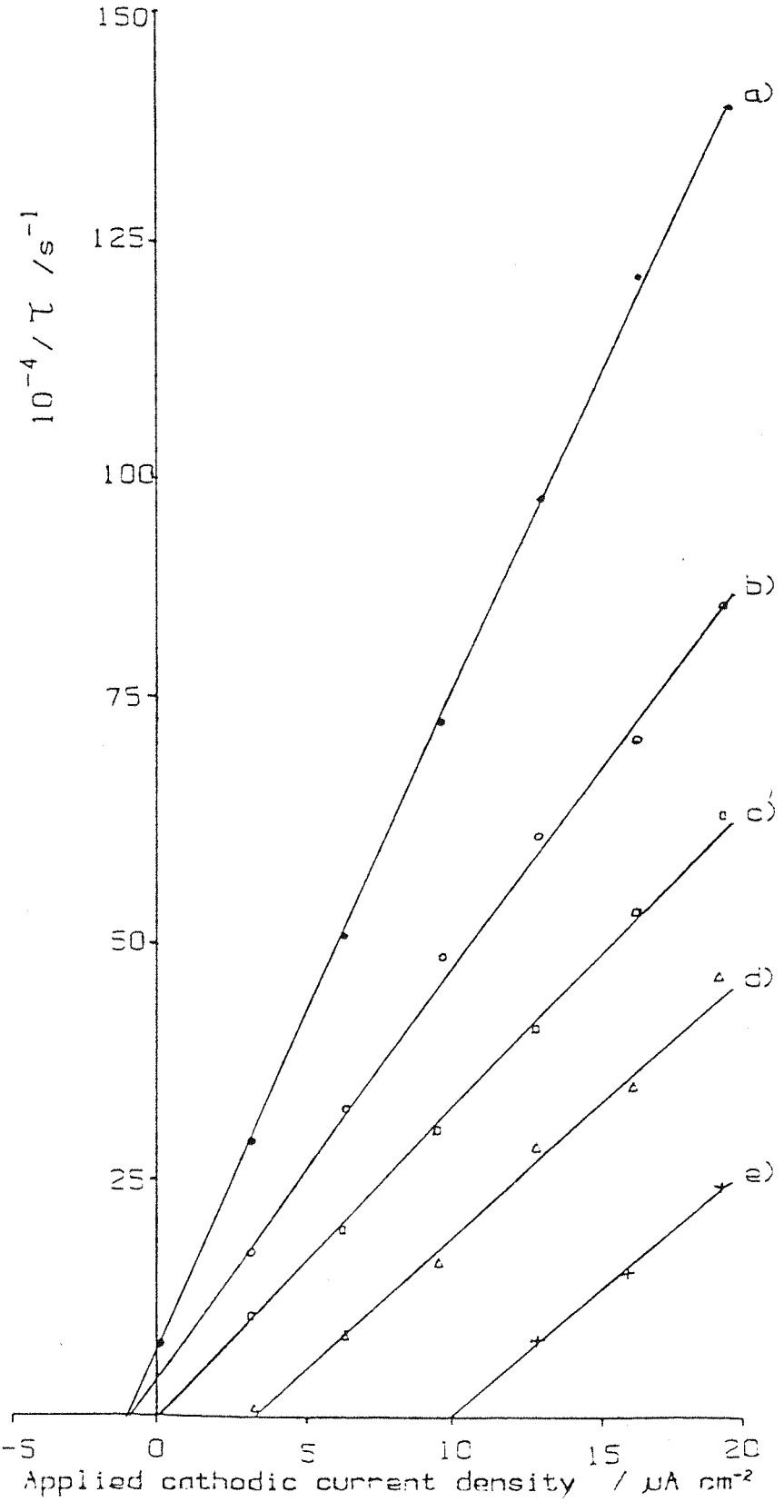

Fig. 4.34 Plot of the reciprocal of the open-circuit passive-active transition time against applied cathodic current, for titanium oxide films grown at 100 mVs^{-1} to a) 0.0V, b) 0.5V, c) 1.0V, d) 1.5V, and e) 2.0V vs Hg/Hg_2SO_4 in 3 mol dm^{-3} at 65°C.

but is used up instead in side reactions such as hydrogen evolution or the reduction of Ti(iv) ions already in solution.

From figure 4.4 a value for the anodising ratio of 6.9 $mC\ V^{-1}$ was determined for films grown at 100 mVs^{-1} in 3 mol dm^{-3} H_2SO_4 at 65°C. This value should therefore be the slope of a plot of $\Delta L_{f(crit)}$, obtained from figure 4.35, against the anodic potential limit of film growth, and the intercept of such a plot should yield a value for $L_{f(crit)}$.

$$\Delta L_{f(crit)} = L_{f(int)} - L_{f(crit)} \qquad 4.20$$

Figure 4.35 shows that a plot of $\Delta L_{f(crit)}$ vs potential limit is in fact curved, although a dashed line of the predicted slope has been drawn through the first three points on the graph. The intercept of this dashed line is at -0.75 V vs Hg/Hg_2SO_4. Assuming that growth started at the Flade potential (-0.96 V vs Hg/Hg_2SO_4) a value for $L_{f(crit)}$ of 1.45 mC cm^{-2} is obtained. This converts to 0.8 nm if the film is assumed to have the same density as anatase (3.84 of cm^{-3}(9)). $L_{f(crit)}$ is in fact a measure of the average film thickness at the critical breakdown point. However, the oxide film is unlikely to thin at a constant rate over the whole surface. Therefore if the critical breakdown occurs when only part of the film has thinned to the true critical thickness (which may correspond to the exposure of the bare metal), the average film thickness, $L_{f(crit)}$, at this point in time can be expected to increase as the initial film thickness increases. This could explain the curvature seen in figure 4.35.

Evidence that the cathodic current reduced the oxide film at the oxide/electrolyte interface rather than at the metal/oxide interface came from ellipsometry, (section 4.6). This showed that the oxide film thinned in the same way when a cathodic current was passed through it as when it was left under normal open-circuit conditions.

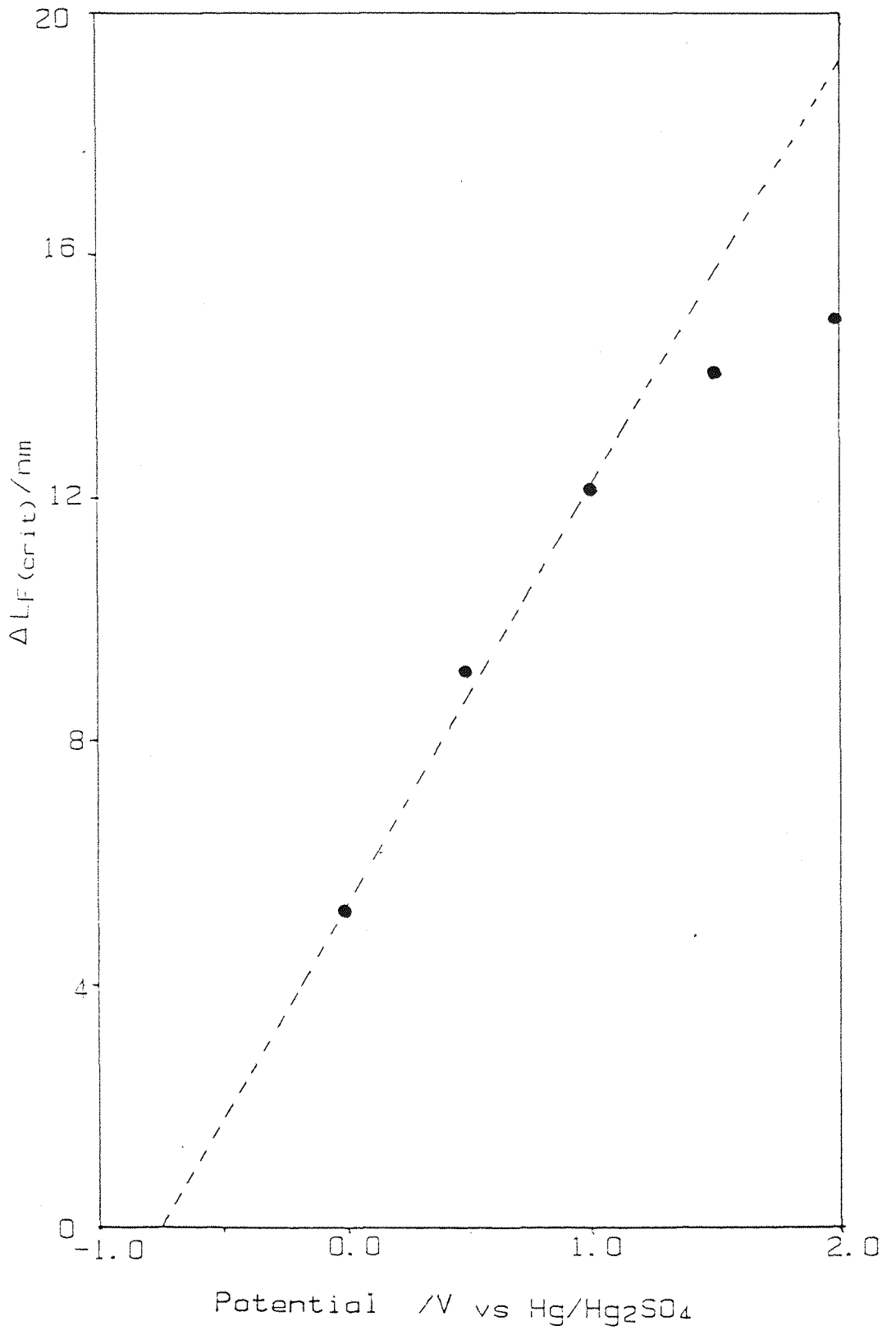

Fig. 4.35 Plot of $\Delta L_{f(crit)}$ obtained from figure 4.34, against formation potential. The dashed line represents the result expected if $L_{f(crit)}$ is assumed to be a constant.

4.6 Elipsometry

The growth of anodic oxide films on titanium was followed by ellipsometry, using the 632.8 nm line of a helium-neon laser. A computer program (31) was used to generate a theoretical fit for the results obtained, from which optical constants were determined for the titanium metal substrate to be in the range of n_s = 2.4-3.0 and k_s = 3.0-3.3, and for the anodic oxide film n_{ox} = 2.0-2.4 and k_{ox} = 0. The wide scatter in the values determined for the optical constants was attributed to the difficulty in obtaining a reproducible initial surface. The published literature values for the optical constants of anodic oxide films on titanium also vary widely and the above results are well within the range of values quoted (12,26,32-36).

Holland (25) has given values of the refractive indices of evaporated anatase (n = 2.33) and rutile (n = 2.65) films and the low values of n_{ox} obtained for the anodic oxide films therefore suggest that they resemble the anatase form of the dioxide.

Figure 4.36 shows a typical delta-psi plot obtained for a 6.0 V film grown at 100 mVs^{-1} in 3 mol dm^{-3} H_2SO_4. Also shown in the figure is the best fit computer generated curve using n_s = 2.98, k_s = 3.23 and n_{ox} = 2.2, from which an anodising ratio of 2.3 nm V^{-1} was obtained. This theoretical curve can be extended to show that an "egg" shape curve would have resulted if the film thickness had been allowed to increase without bound, with each lap of the "egg" corresponding to approximately 150 nm of film growth (Fig. 4.37). It is interesting to note that if a value of n_{ox} = 2.4 had been chosen a "broken egg" shape curve would have resulted (Fig. 4.38).

When the electrode was held at the anodic potential limit, the delta-psi plot was found to curve slightly towards the origin, and on open-circuiting, the plot tracked back along a curve parallel to the growth curve, suggesting that the oxide film was thinning (Fig. 4.39). This behaviour was also observed if a cathodic current was passed through the oxide although now the delta-psi plot changed at a faster

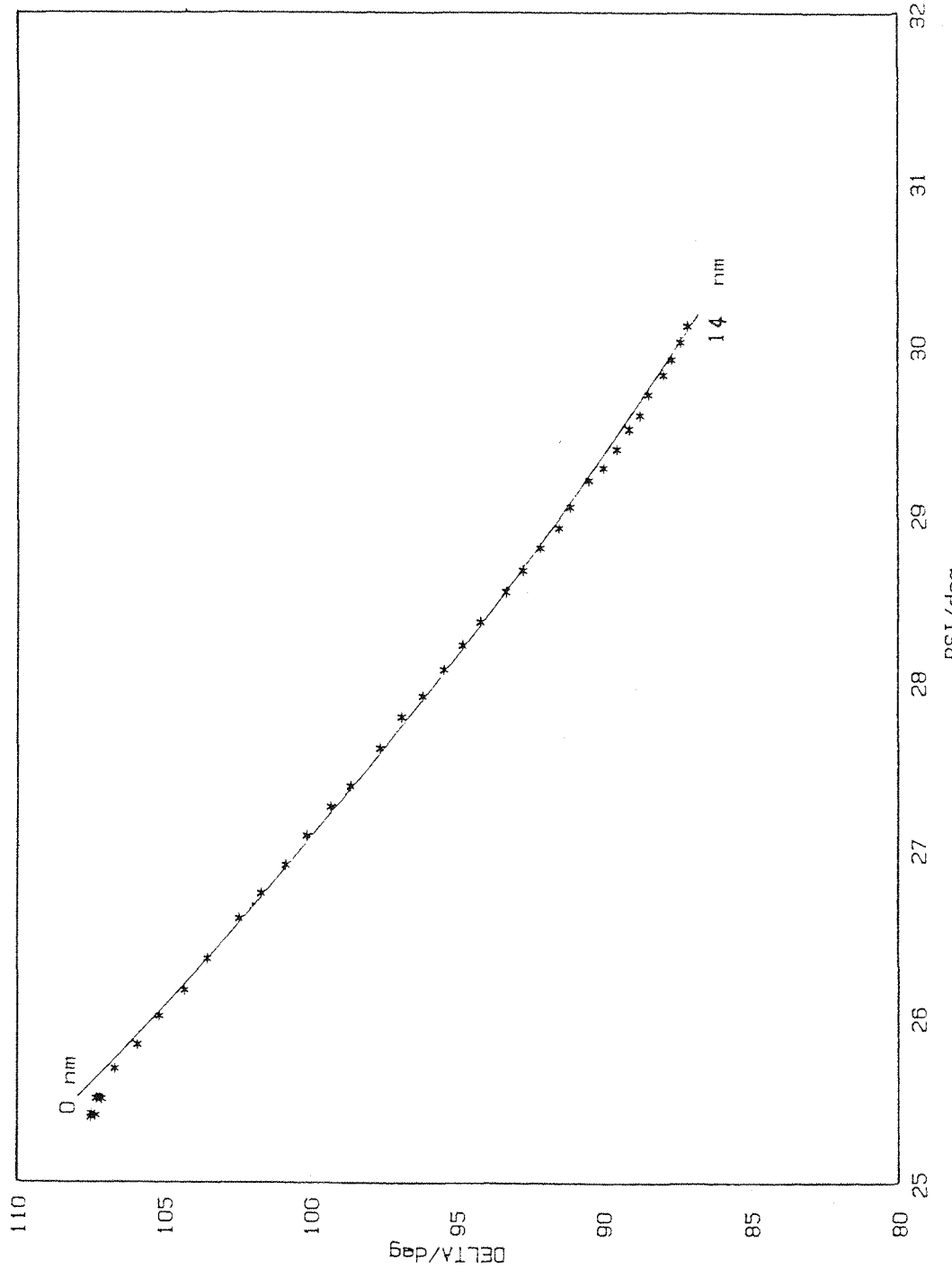

Fig. 4.36 Typical delta-psi plot obtained on growing an anodic oxide film on titanium at 5.0 V vs Hg/Hg_2SO_4 at 100 mVs^{-1} in 3 M H_2SO_4. * represents experimental points and the solid line is a theoretical curve generated using values of n_s = 2.98, k_s = 3.23, n_{ox} = 2.2, k_{ox} = 0 and a theoretical film thickness going from 0 to 14 nm.

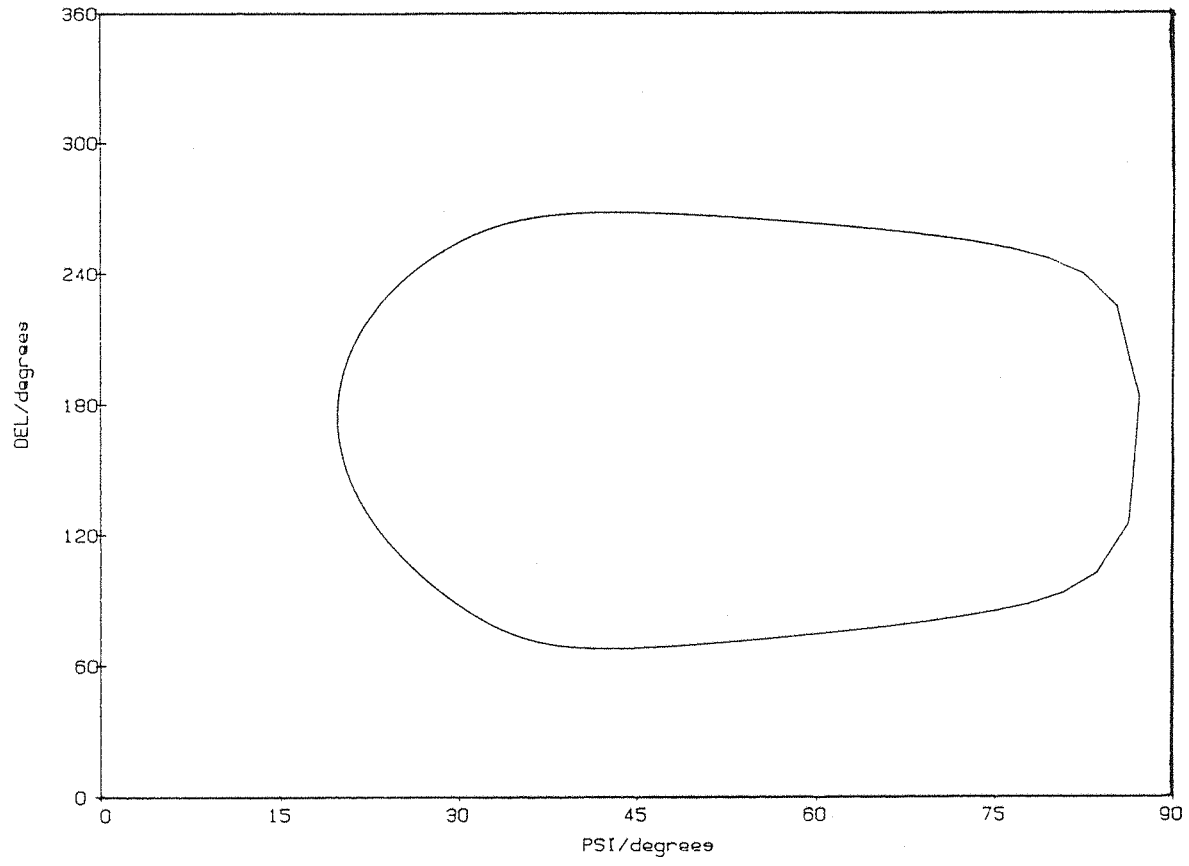

Fig. 4.37 Theoretical delta-psi plot for the case where the film thickness is allowed to increase without bound. $n_s = 2.98$, $k_s = 3.23$, $n_{ox} = 2.2$, $k_{ox} = 0$.

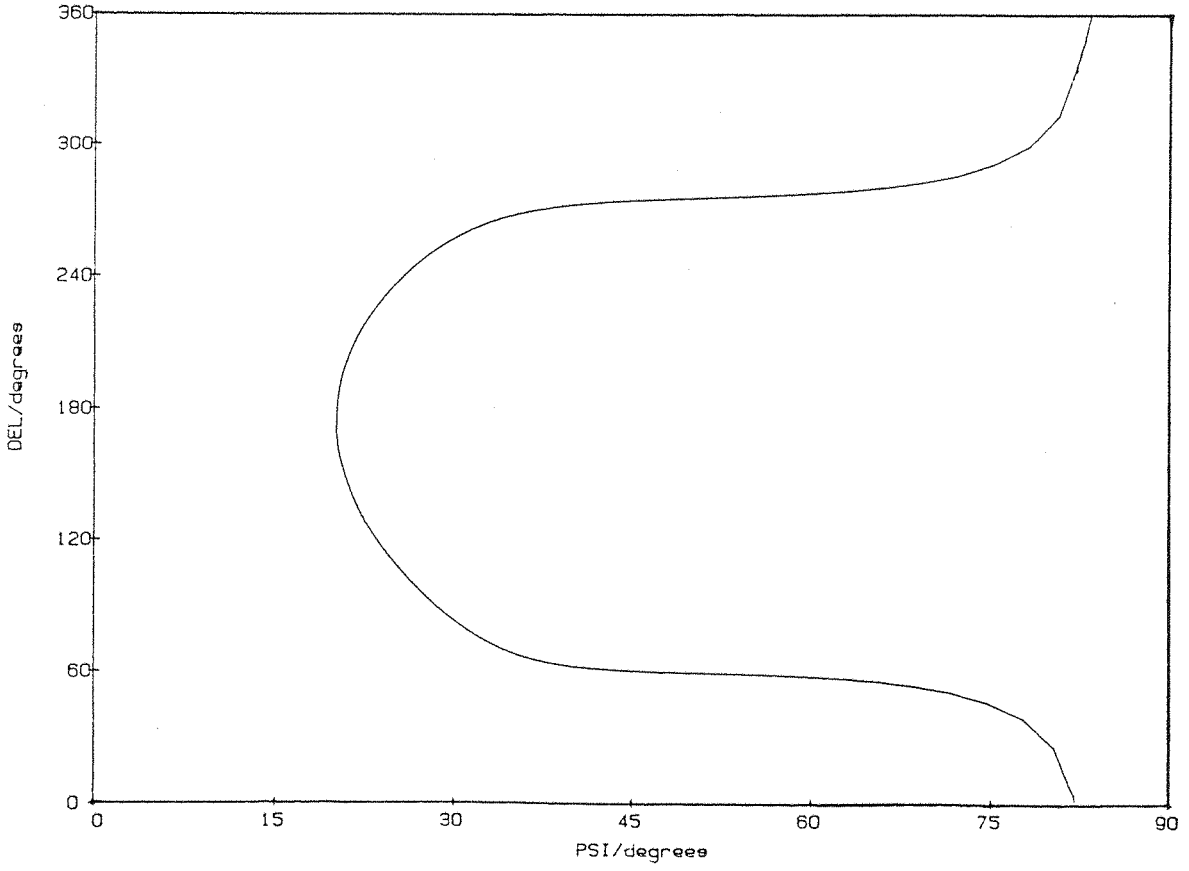

Fig. 4.38 Theoretical delta-psi plot, with conditions the same as figure 4.35, except now $n_{ox} = 2.4$.

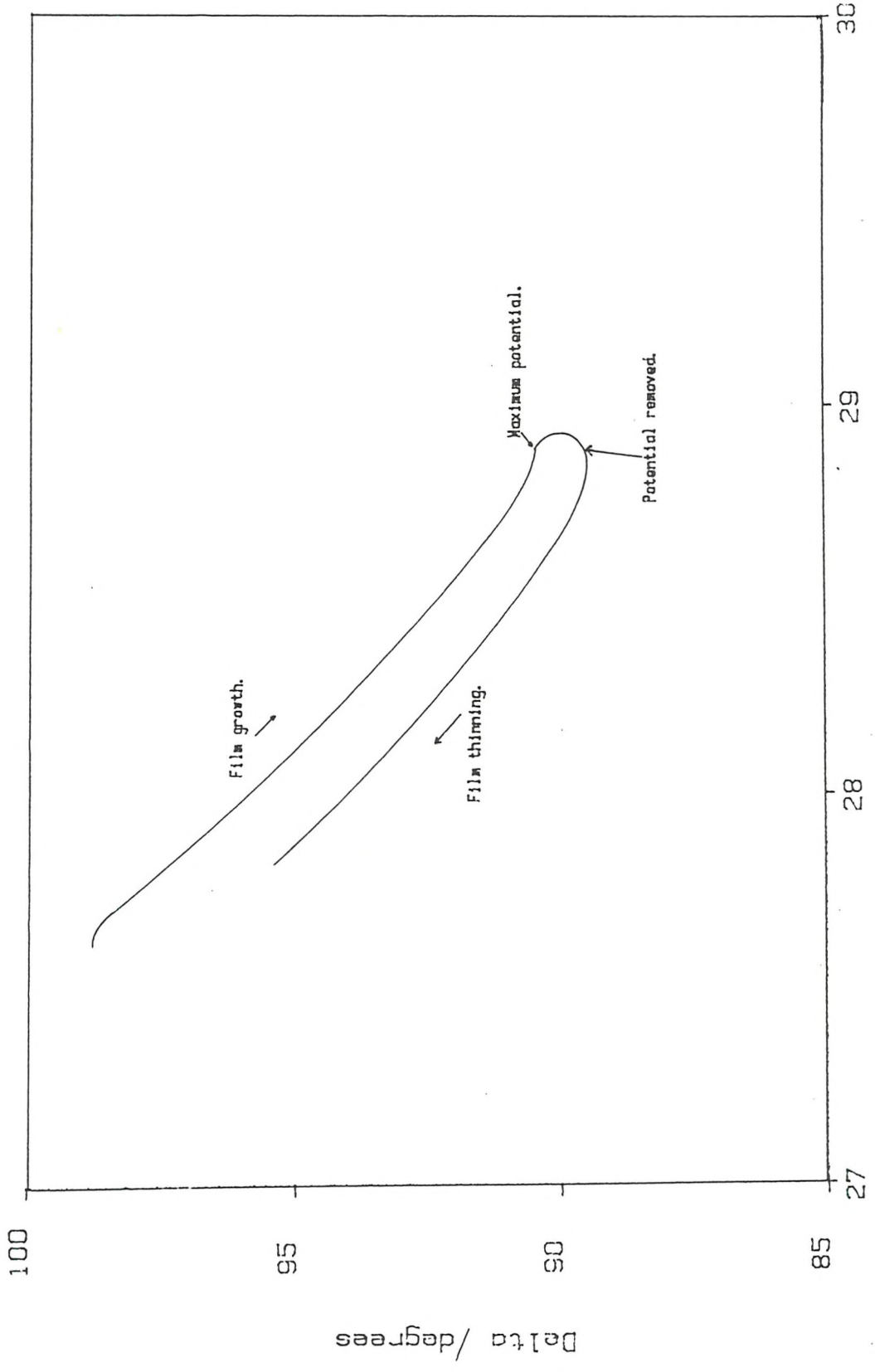

Fig. 4.39 Typical delta-psi plot obtained from following the growth and open-circuit behaviour of a 5.0 nm film grown at 100 mVs^{-1} in 3 mol dm^{-3}.

rate. This suggests that the film behaves in a similar way under these two conditions (section 4.5.3). Unfortunately it was not possible to follow the open-circuit behaviour of the anodic oxide films all the way to the critical breakdown region, as hydrogen evolution and surface roughness resulted in signal deterioration.

A computer calculation of the reverse curve showed that the optical constants of the oxide film remained constant, whereas change had occurred in the substrate's optical constants. This change is most probably due to the formation of a suboxide layer between the metal and the dioxide film. Figure 4.40 shows the results of a series of computer calculations based on a four layer model for a 10 nm top film with various thicknesses for the bottom film. It can be seen that only a very thin film (0.5 nm) is required to cause a shift in the delta-psi plot, and that this shift increases with the thickness of the sub-oxide layer. Unforutnately, the shift was not very sensitive to the optical constants of the suboxide layer, so that ellipsometry could not be used to identify the stoichiometry of this layer.

Figure 4.41 shows the delta-psi response obtained when the potential-time curve shown in figure 4.42 is applied to a titanium electrode;

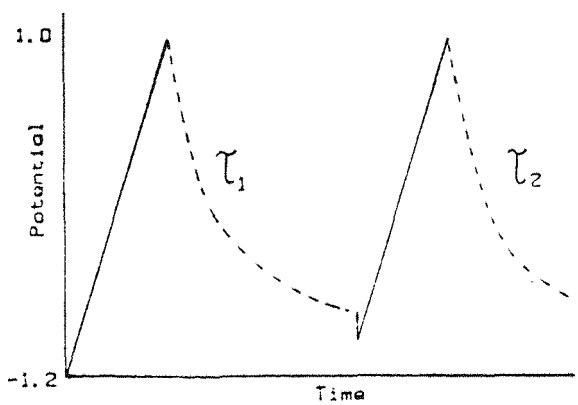

Fig. 4.42 Potential-time profile used to obtain figure 4.41. Dashed lines refer to times at open-circuit.

It can be seen that when the potential is applied for the second time (region c), the delta-psi plot almost exactly retraces the open-circuit curve (curve b), which suggests that the suboxide layer remains intact during the film's reformation. This suggests that titanium ions can migrate freely through the suboxide, which is expected to be essentially metallic. On reaching the anodic potential limit for the second time,

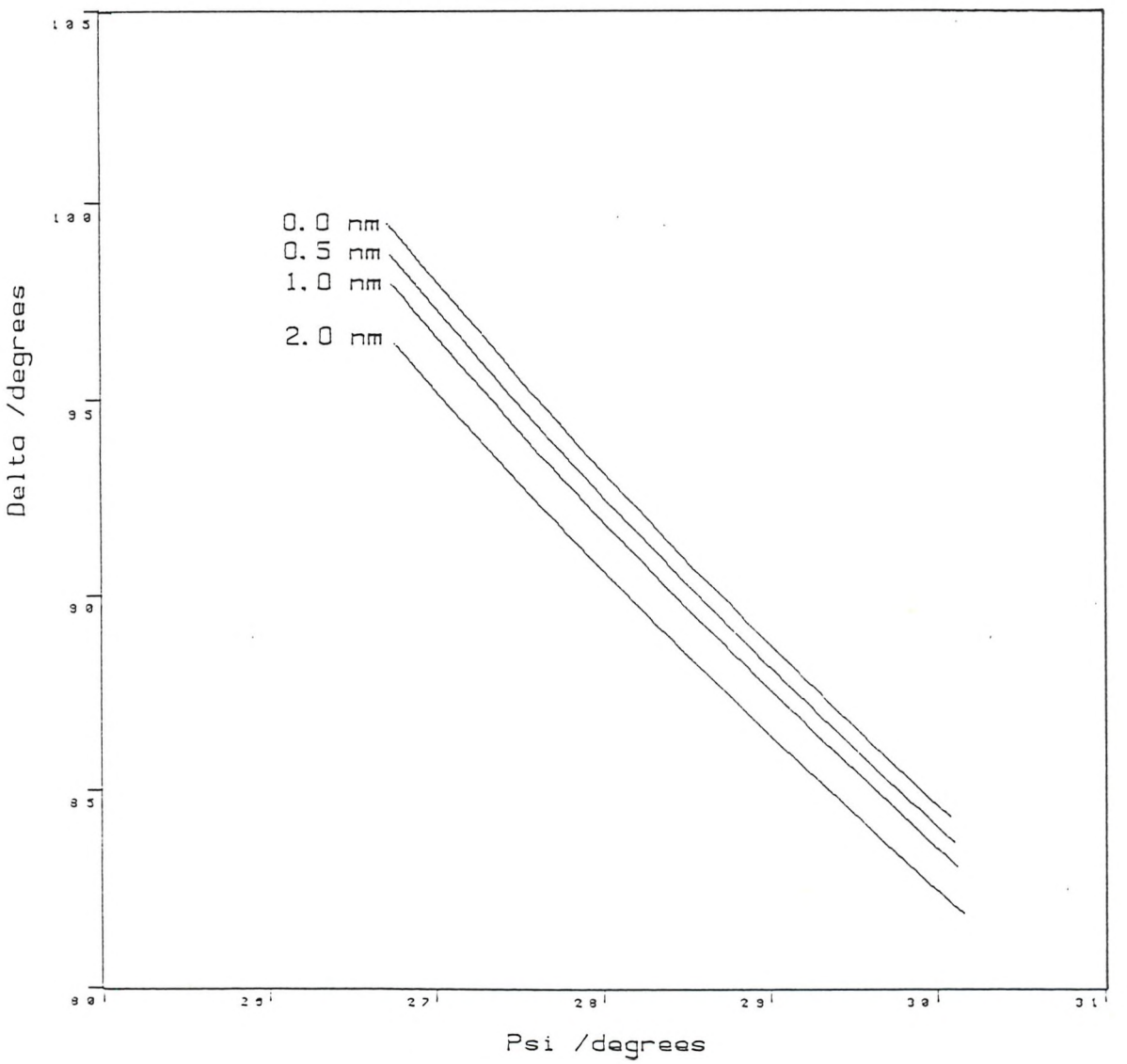

Fig. 4.40 Theoretical curves generated using a 4 layer model (31). The curves were calculated using values of n_s = 2.5, k_s = 3.0, n_1 = 2.3, k_1 = 0, n_2 = 2.4 and k_2 = 1.5 where the subscripts 1 and 2 refer to the top and bottom films respectively. The bottom film thickness was held at constant values of 0 nm, 0.5 nm, 1.0 nm and 2.0 nm, whilst the top film was allowed to grow from 0 nm to 10 nm in each case.

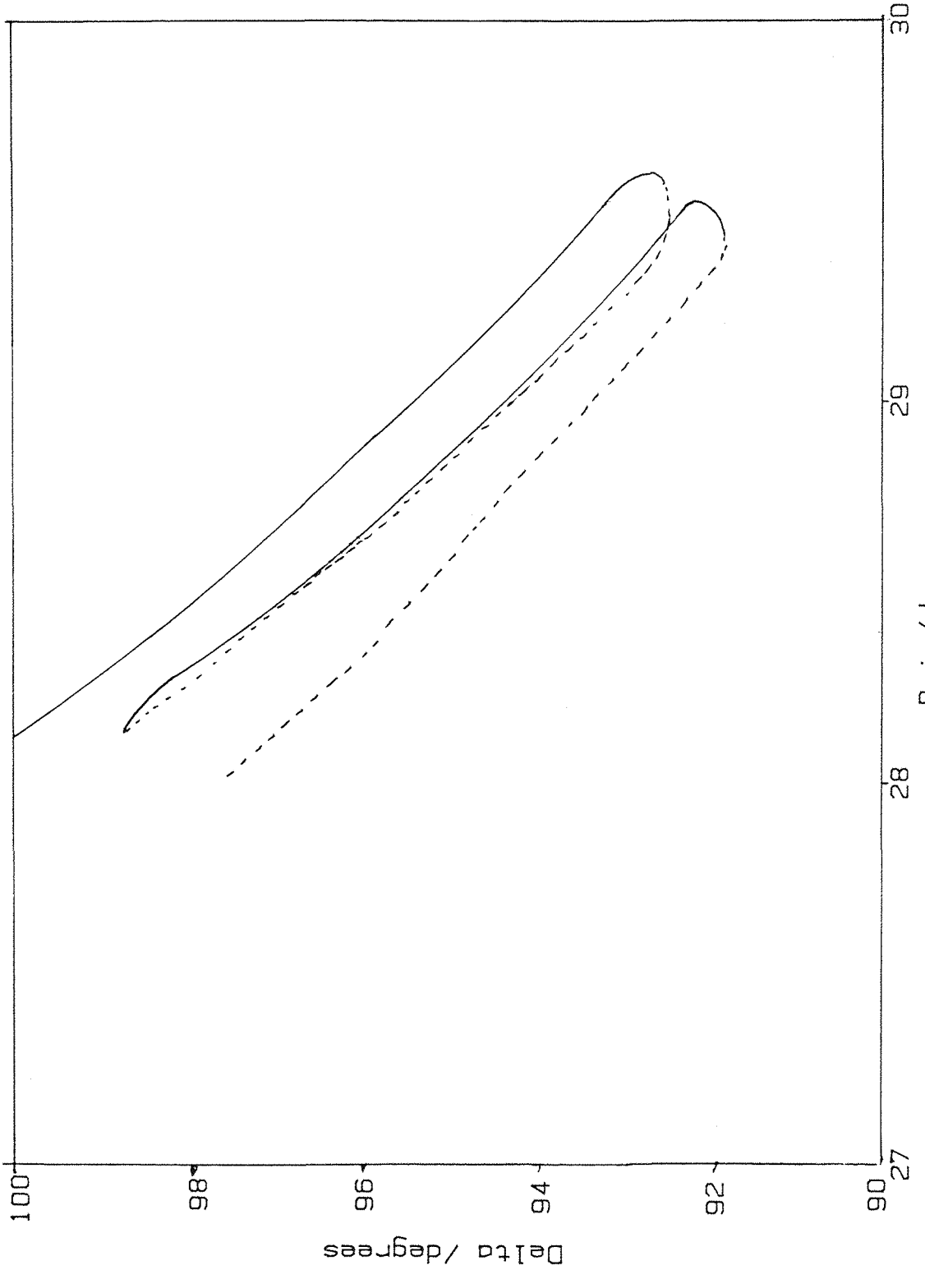

Fig. 4.41 Typical delta-psi plot obtained in response to application of the potential-time profile shown in figure 4.42 to a titanium electrode. Dashed lines represent open-circuit behaviur.

the delta-psi plot again curved towards the origin, indicating further growth of the suboxide layer.

The open-circuit delta and psi values for a film grown at 1 Vs^{-1} to 2.0 V vs Hg/Hg_2SO_4 in 3 mol dm^{-3} H_2SO_4 at room temperature were recorded over a period of 2.1 x 10^4 s, using a flow cell to overcome the problem of bubbles forming on the electrode's surface. This data was then used to calculate the film thickness as a function of the time at open-circuit. This resulted in a linear plot of L_f vs time with a slope of 1.9 x 10^{-11} cm s^{-1} (Fig. 4.43). A reformation experiment was carried out at the same time, and it was found that in bringing the oxide film back to 2.0 V vs Hg/Hg_2SO_4, 6.2 mC cm^{-2} of charge was passed (Fig. 4.44). This is equivalent to a thinning rate of 1.6 x 10^{-11} cm s^{-1}.

The discrepancy between the two thinning rates can be explained with reference to figure 4.45. This shows a plot of the film thickness measured by ellipsometry against potential during the original film growth. The line a-b represents a region of 0.8 nm of oxide growth which occurred after the anodic potential limit had been reached. The charge passed to grow this part of the oxide is not included in the area under the cyclic voltammogram, and it therefore represents a correction term to be added to the thinning rate calculated from the reformation experiment.

4.7 Open-circuit Impedance Measurements

The impedance of titanium oxide films at open-circuit has a frequency dependence which is similar to that seen under potential control (cf. Fig. 4.10 and Fig. 4.46). It had been hoped to combine impedance measurements with reformation experiments, so that plots of impedance against film thickness could be obtained but unfortunately, it was discovered that the impedance depended much more strongly on the open-circuit potential of the oxide than it did on the film thickness.

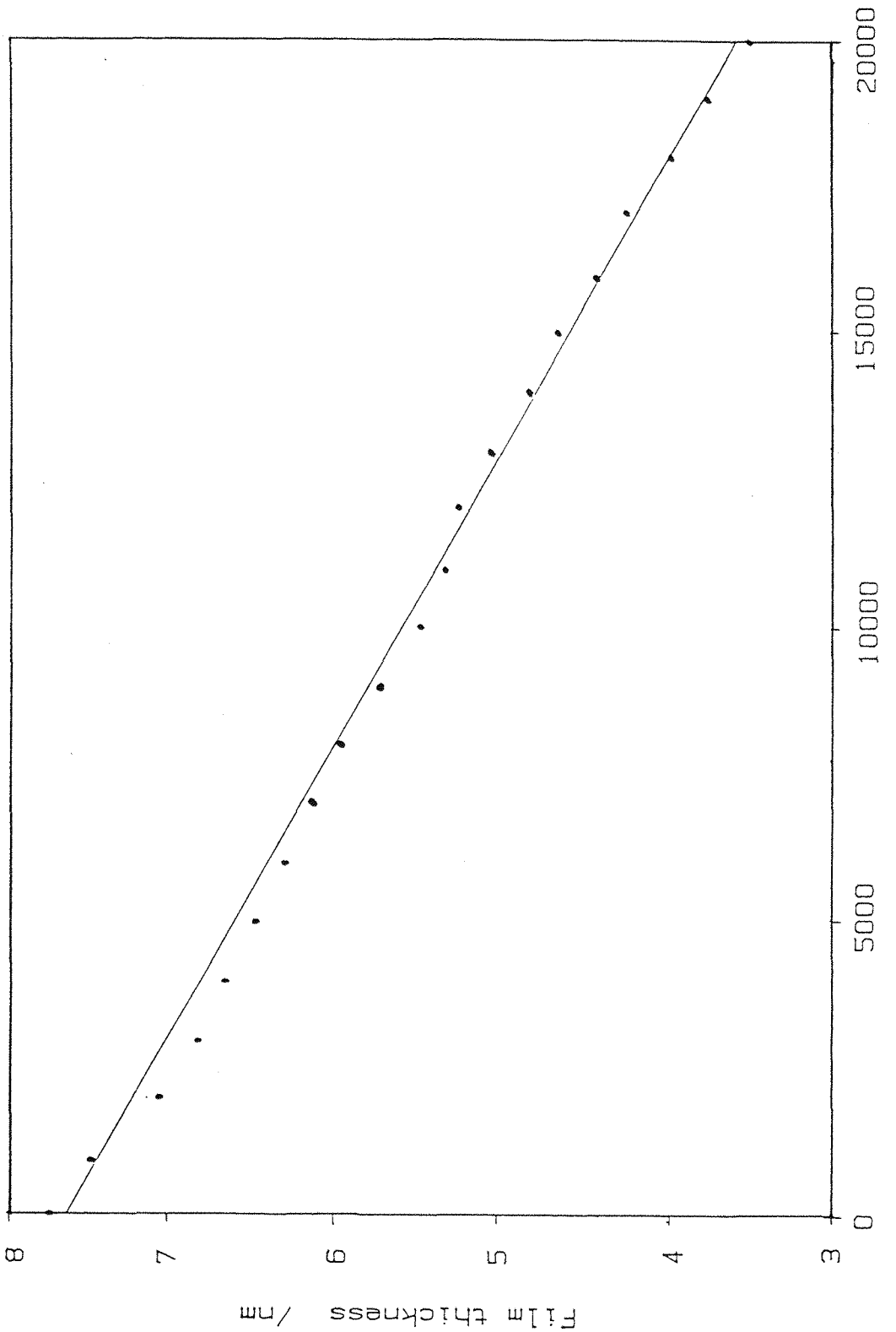

Fig. 4.43 Plot of film thickness, determined by ellipsometry, against time at open-circuit for a film which was originally grown at 1 vs^{-1} to 2.0 V vs Hg/Hg_2SO_4 in 3 mol dm^{-3} H_2SO_4 at room temperature. Open-circuit conditions were the same as the growth conditions.

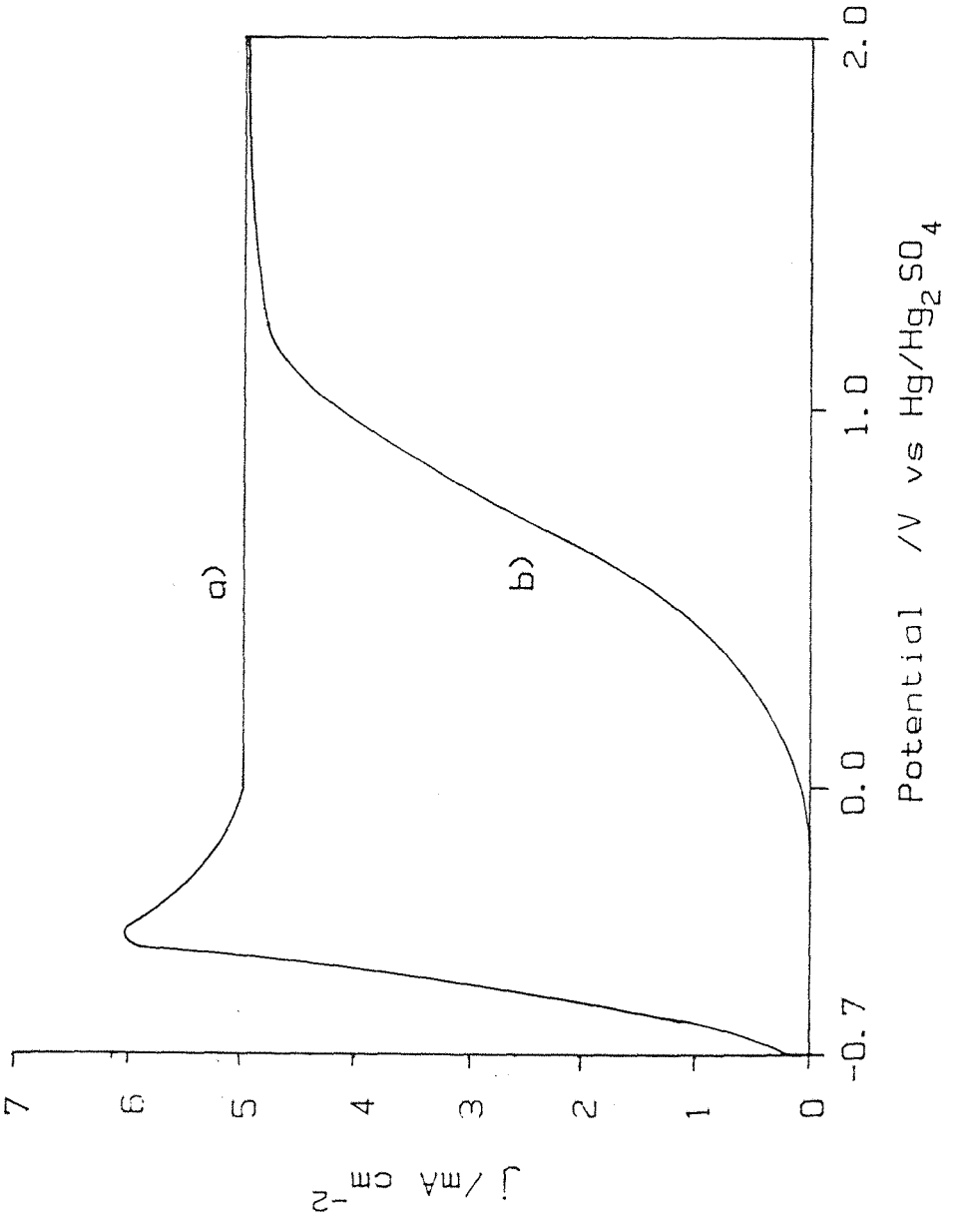

Fig. 4.44 Reformation voltammogram obtained from the same oxide film as figure 4.43.

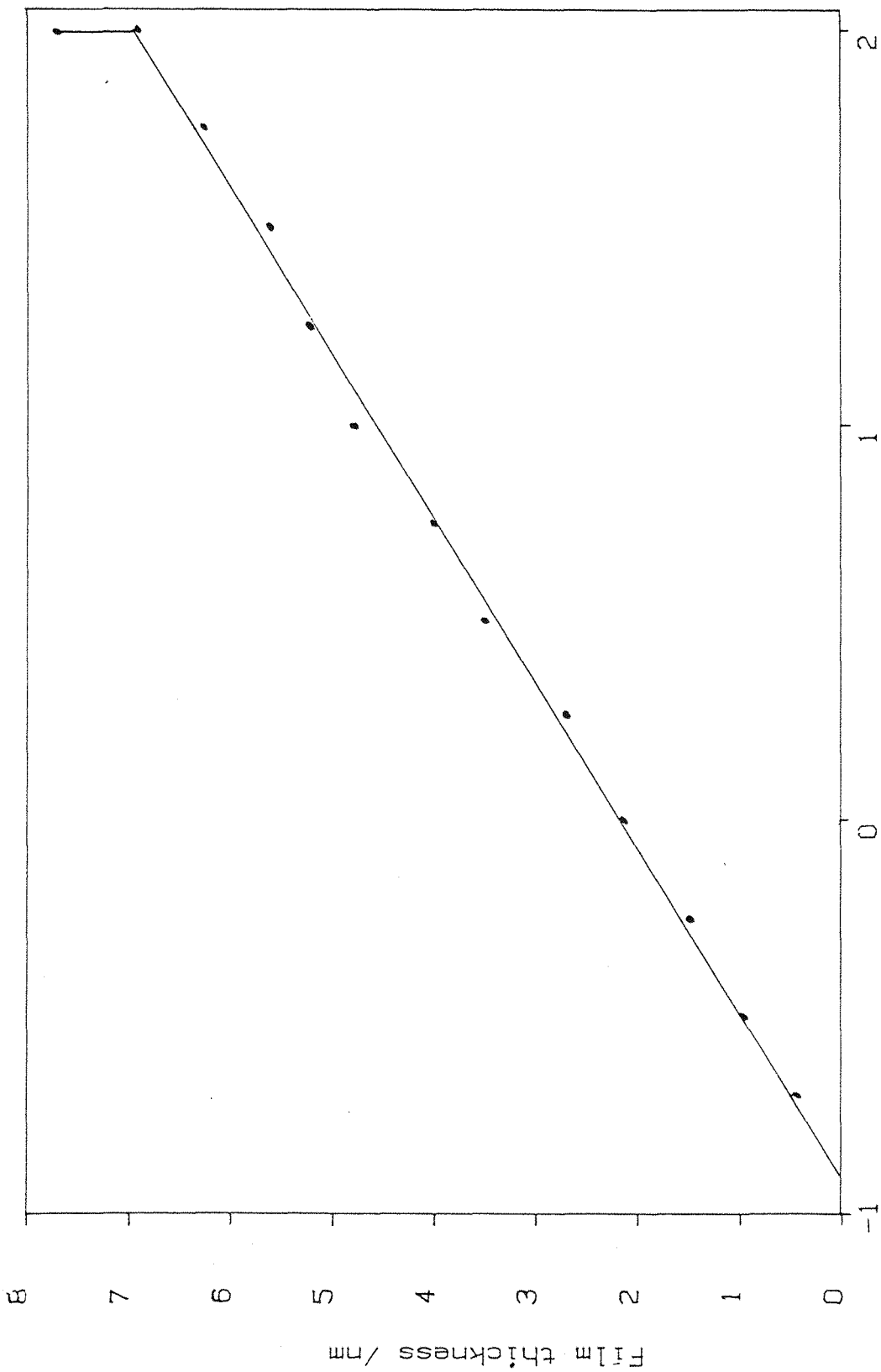

Fig. 4.45 Plot of the film thickness, determined by ellipsometry, against potential. Recorded during the growth of the oxide film used for figures 4.43 and 4.44.

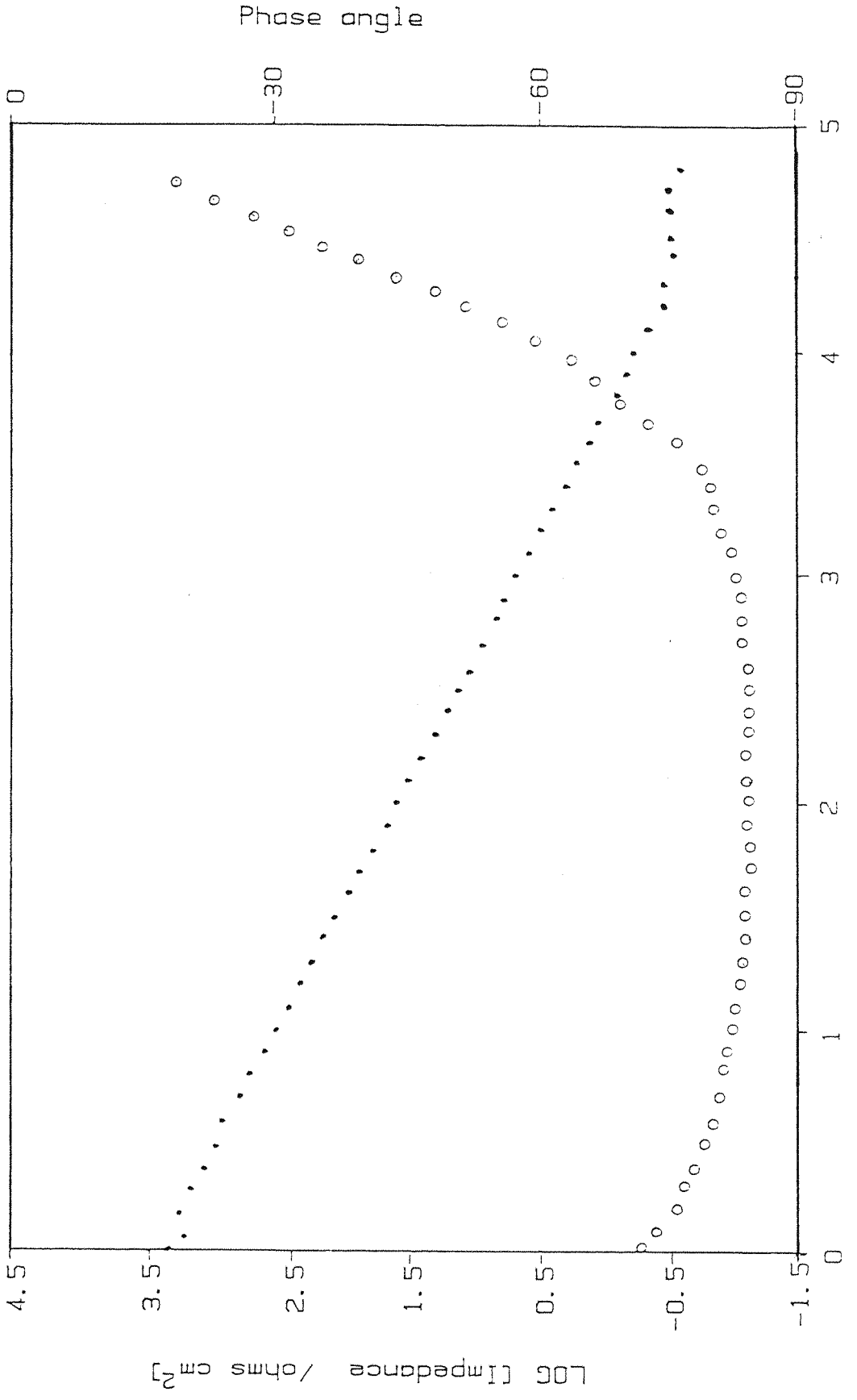

Fig. 4.46 Bode plot of Log (impedance), •, and phase angle, o, against Log (frequency), for a titanium oxide film originally grown at 10 mVs^{-1} to 0.0 V vs Hg/Hg_2SO_4 in 3 mol dm^{-3} at 45°C which had been under open-circuit conditions for 30 minutes.

The open-circuit potential of the anodic oxide films can be lowered by passing a small cathodic current through them. Therefore to demonstrate the strong potential dependence of the impedance, a cathodic current of 6.7 μA cm^{-2} was passed through an oxide film for 25 minutes. The film was then returned to normal open-circuit conditions for a further 25 minutes. Throughout this period the impedance of the film at 100 Hz was recorded. Figures 4.47 and 4.48 show the results obtained as a function of time and oxide potential respectively. Clearly the impedance recovers once the cathodic current is removed, but separate ellipsometry measurements showed that the oxide film should have thinned from about 7.5 nm to 3.0 nm during the course of such an experiment. From these observations it was concluded that the a.c. response of the oxide films was due to the space-charge layer rather than the whole film.

Pettinger et al. (10) showed that when the capacitance due to the Helmholtz layer, C_H, is significant the Mott-Schottky equation becomes

$$1/C^2_{meas} = \frac{2\Delta\phi}{e\varepsilon\varepsilon_o N_o r^2} + 1/C^2_H \qquad 4.21$$

If the oxide film is assumed to be behaving as a simple capacitor then the measured impedance, Z_{meas}, can be expressed as

$$Z_{meas} = 1/\omega C_{meas} \qquad 4.22$$

Hence equation 4.21 can be transformed into

$$Z^2_{meas} = \frac{2\Delta\phi}{e\varepsilon\varepsilon_o N_o \omega^2 r^2} + 1/\omega^2 C^2_H \qquad 4.23$$

Therefore it was possible to construct a "Mott-Schottky" plot from the open-circuit impedance data shown in figure 4.48 (Fig. 4.49). From the slope of this plot, using a value for εr^2 of 60, the donor density

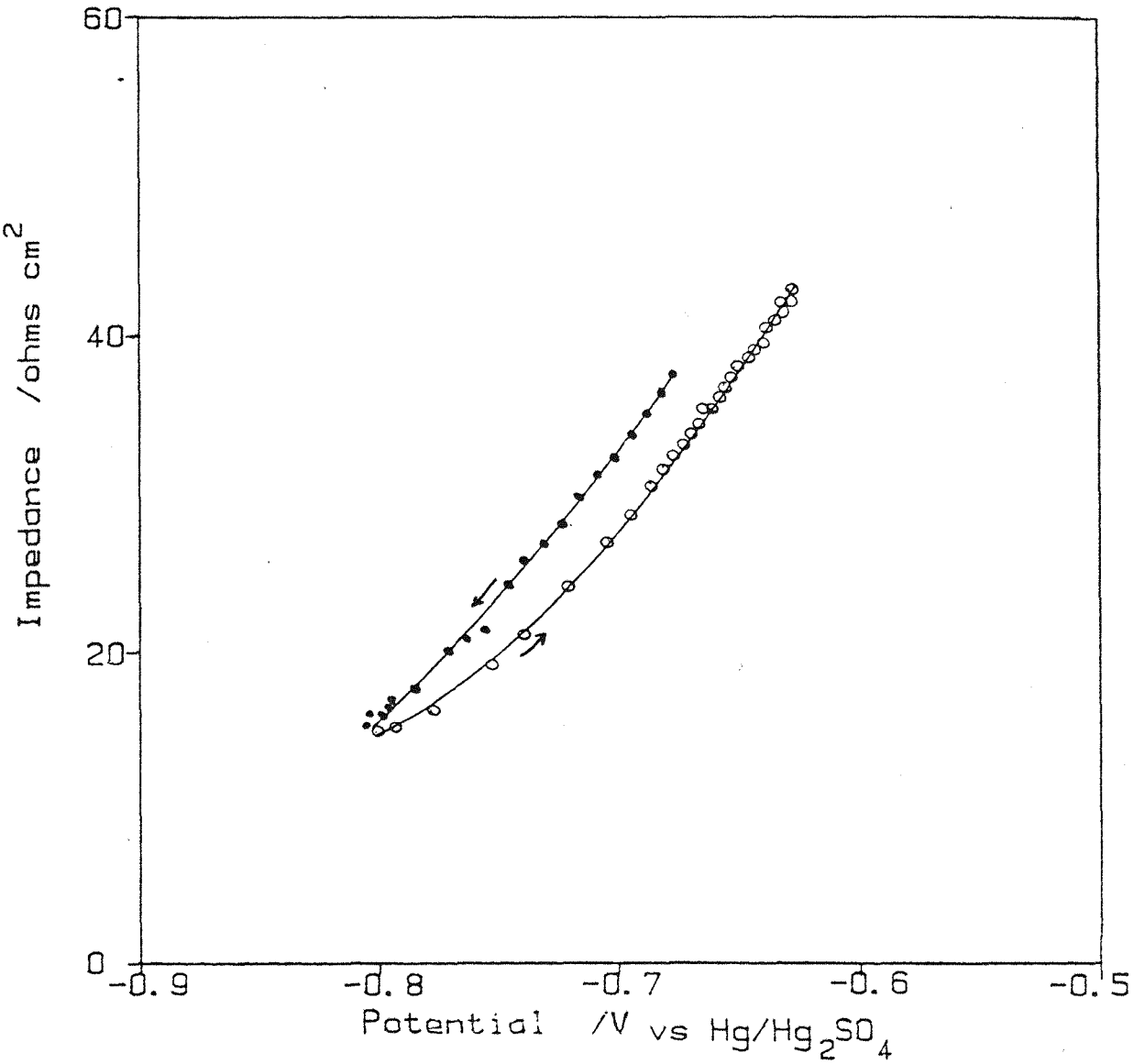

Fig. 4.48 Plot of impedance against electrode potential, obtained at the same time as figure 4.47. • indicates a measurement taken while the cathodic current was being applied, whilst o represents a measurement under true open-circuit conditions (100 Hz).

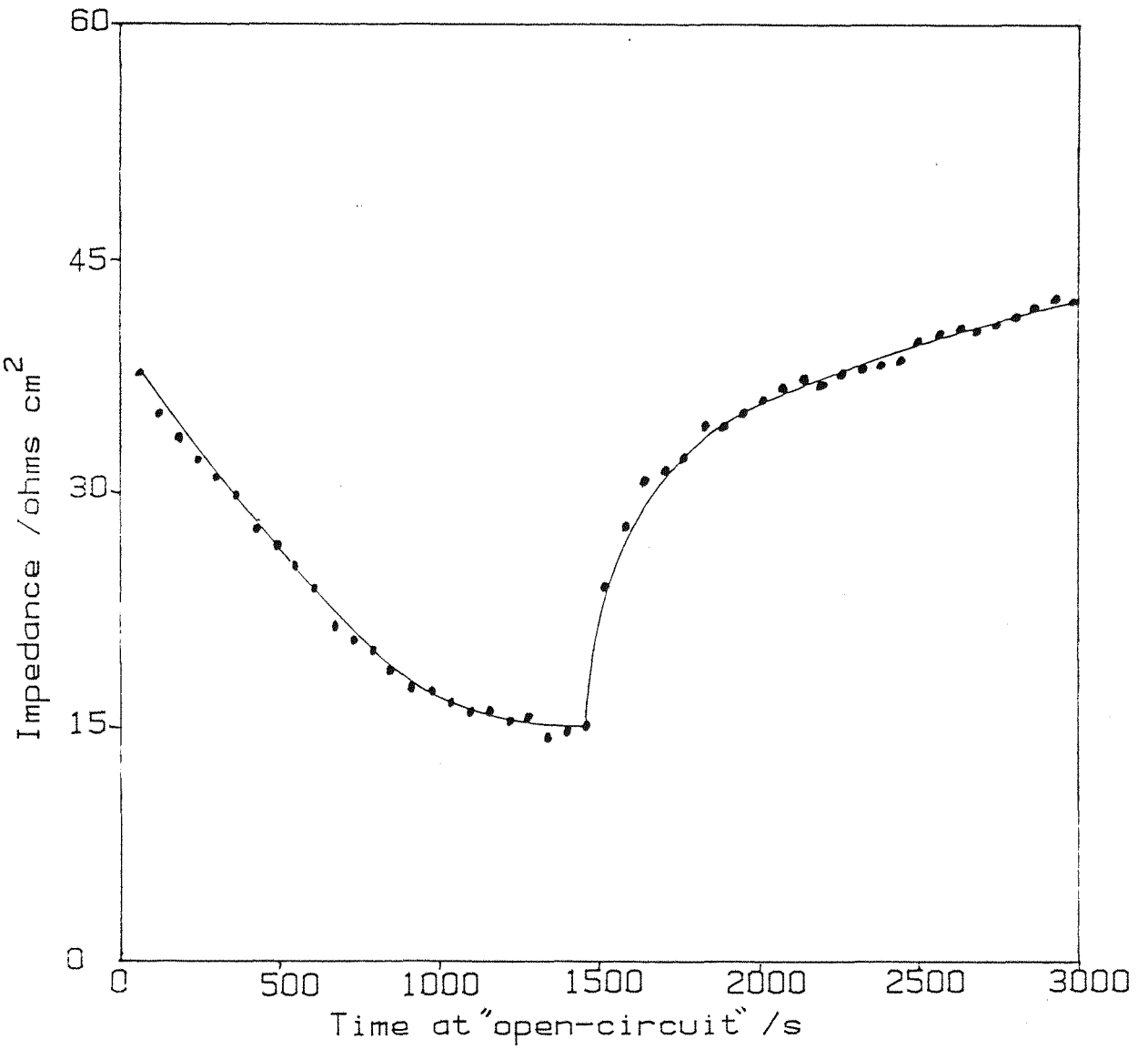

Fig. 4.47 Plot of the impedance of a titanium oxide film grown at 100 mVs^{-1} to 2.0 V vs Hg/Hg_2SO_4 in 3 mol dm^{-3} H_2SO_4 at room temperature against time under galvanostatic conditions (f = 100 Hz). For the first 1500 s a 6.7 μA cm^{-2} cathodic current was applied to the film, which had the effect of reducing the electrode's potential. The electrode was left subsequently at open-circuit.

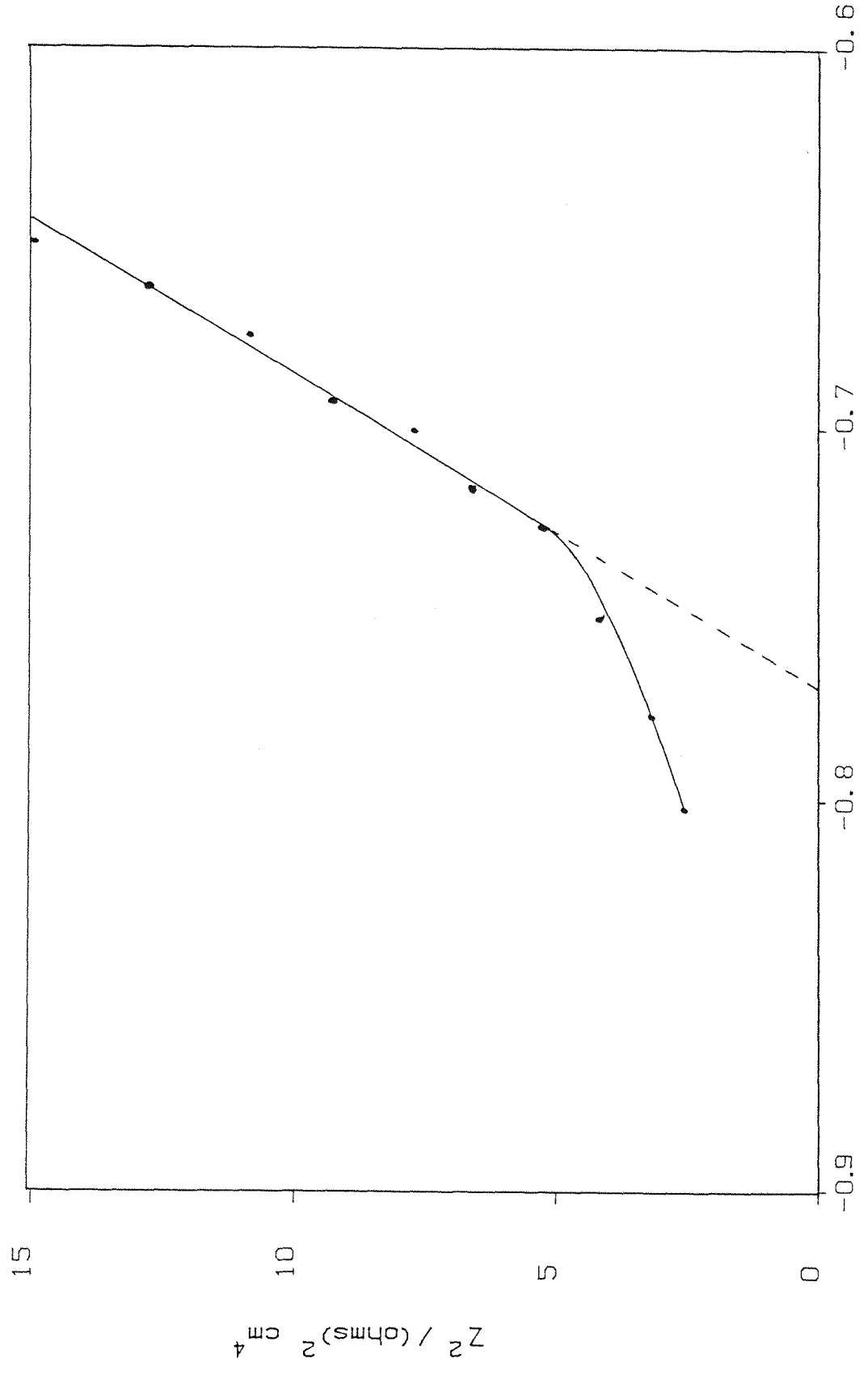

Fig. 4.49 Mott-Schottky plot, constructed from the true open-circuit data shown in figure 4.48 (100 Hz).

of the depletion region was calculated to be 5.7×10^{20} cm^{-3}. However, as this plot was constructed over a very small potential range, this value can only be taken as a rough estimate. The base of the plot is curved because $\Delta\phi$ is tending to zero, so that the measured impedance becomes dominated by the Helmholtz capacitance, which is potential independent.

Further evidence that the impedance of anodic oxide films at open-circuit is dominated by the space-charge region is shown in figure 4.50. This is a plot of the impedance of a film, which was grown at 1 Vs^{-1} to an anodic potential limit of 1.0 V vs Hg/Hg_2SO_4, which was held at a negative potential of -0.75 vs Hg/Hg_2SO_4 against the film thickness, calculated from a series of reformation experiments carried out simultaneously with the impedance measurements. It can be seen that the impedance remained virtually constant until the film had thinned to a thickness of about 3.0 nm, before falling rapidly as the film thickness decreased yet further. No data was produced for film thicknesses less than 0.75 nm, as this thickness was found to be relatively stable at the holding potential of -0.75 V vs Hg/Hg_2SO_4.

Harrison and Williams (37) have presented impedance data for thin anodic oxide films on titanium that were held at negative potentials. Plots of impedance against time were given that also showed an initial region of constant impedance before a rapid decrease. This was interpreted as being the nucleation and growth of patches of reduced oxide, as the authors believed that the film thickness was constant throughout their experiment. The present results show, however, that impedance is not a suitable technique for following the open-circuit behaviour of anodic oxide films on titanium which are in the region of 3.0 - 10.0 nm thick. This is due to the high donor densities that occur in these films, which produce a space charge region that dominates the impedance response. Ellipsometry and reformation experiments, on the other hand, give directly information about the thinning of the oxide film.

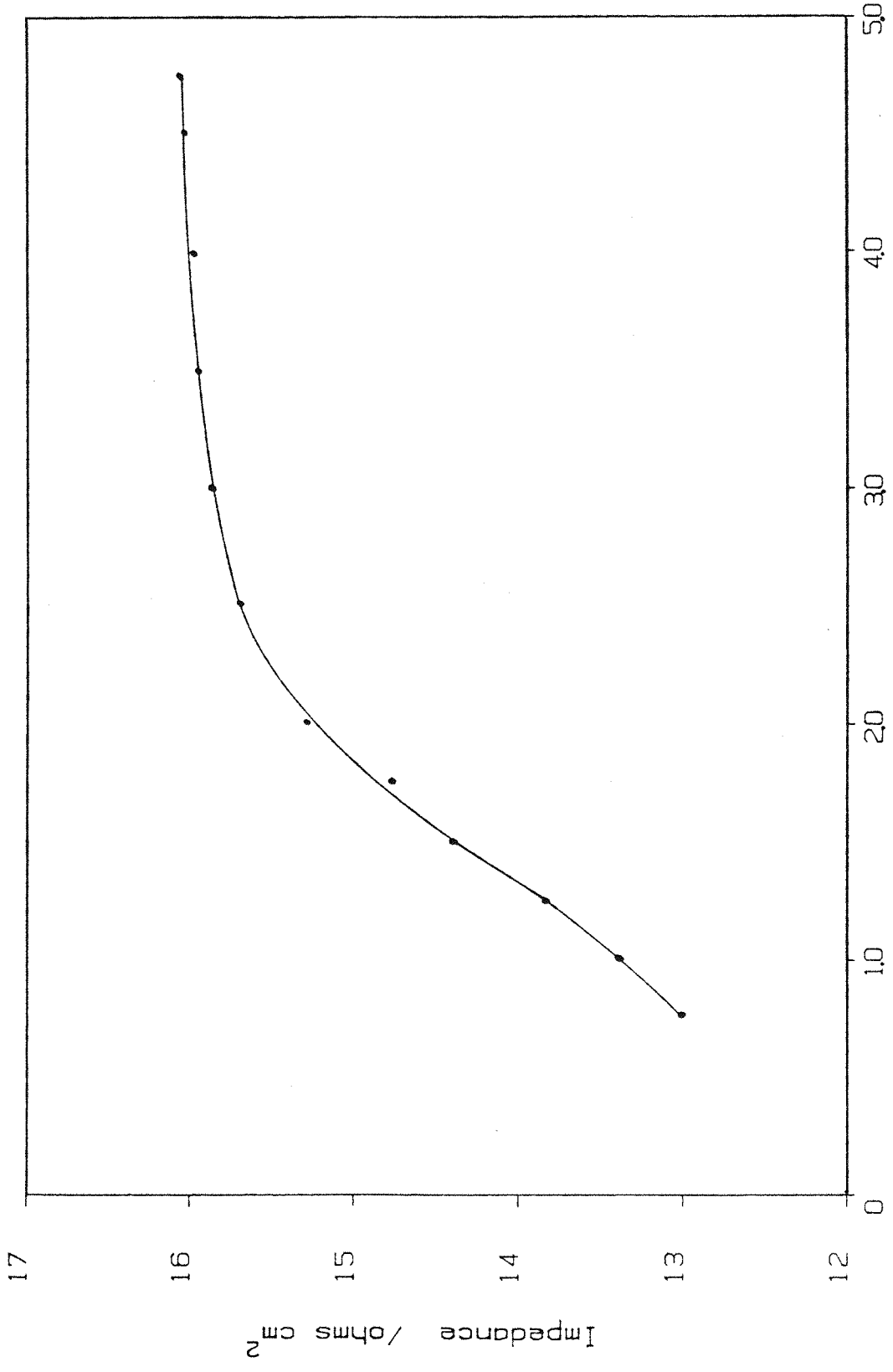

Fig. 4.50 Plot of impedance against film thickness for a titanium oxide film originally grown at 100 mVs^{-1} to 1.0 V vs Hg/Hg_2SO_4 in 3 mol dm^{-3} H_2SO_4 at room temperaure, and then held at -0.8 V. The film thickness was determined by a series of separate reformation experiments (100 Hz).

4.8 Modulated Electroreflectance

Modulated electrolyte electroreflectance (EER) spectra were obtained from an anodic oxide film grown to 3.0 V vs Hg/Hg_2SO_4 for both p and s polarised light (Fig. 4.51). There is a clear dependence of the EER spectra on the polarisation of the incident light, with the critical points moving to shorter wavelengths, when the polarisation is changed from s to p. The critical points of the two spectra are summarised in table 4.10.

Table 4.10 Critical points for EER spectra for an anodic oxide film grown to 3.0 V vs Hg/Hg_2SO_4 at 10 mVs^{-1}. 100 mV peak-peak modulation signal at 270 Hz. D.c. bias at anodic potential limit.

Polarisation	Low energy peak		High energy peak		Cross over
	Energy/eV	$10^{-3}\frac{\Delta R}{R}$	Energy/eV	$10^{-3}\frac{\Delta R}{R}$	Energy/eV
p	3.76	5.4	4.09	1.1	3.95
s	3.63	2.5	3.97	1.9	3.79

No spectral features were observed for wavelengths longer than 430 nm, and the spectra were found to be independent of the modulation frequency between 27 Hz and 2.7 kHz. The remaining experiments in this section were carried out using s-polarised light. This polarisation was chosen as it had the highest intensity.

The intensity of the $\frac{\Delta R}{R}$ signal was found to be linearly dependent on the size of the a.c. modulation, with figure 4.52 giving a value for $d\left(\frac{\Delta R}{R}\right)/dV_{ac}$ of 2.55×10^{-2} V^{-1} for the low energy peak at 342 nm.

The dependence of the EER spectrum on the d.c. bias potential is

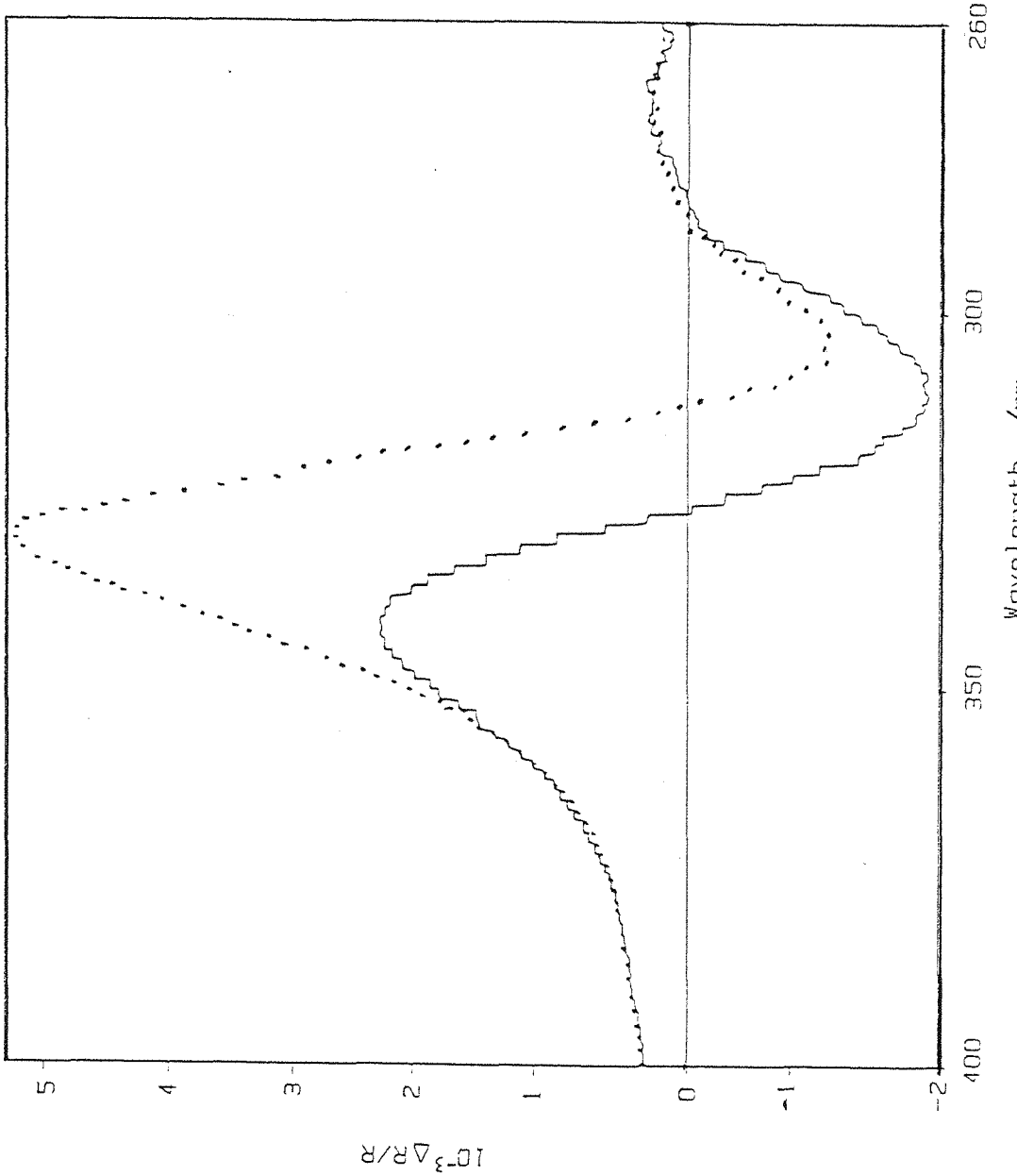

Fig. 4.51 Typical EER spectrum obtained from a titanium oxide film grown at 10 mVs^{-1} to 3.0 V vs Hg/Hg_2SO_4 in 3 mol dm^{-3} H_2SO_4 at room temperature. The measurement was obtained at the formation potential using a 100 mV peak to peak square wave perturbation at 270 Hz.
• p - polarized, —— s-polarized light.

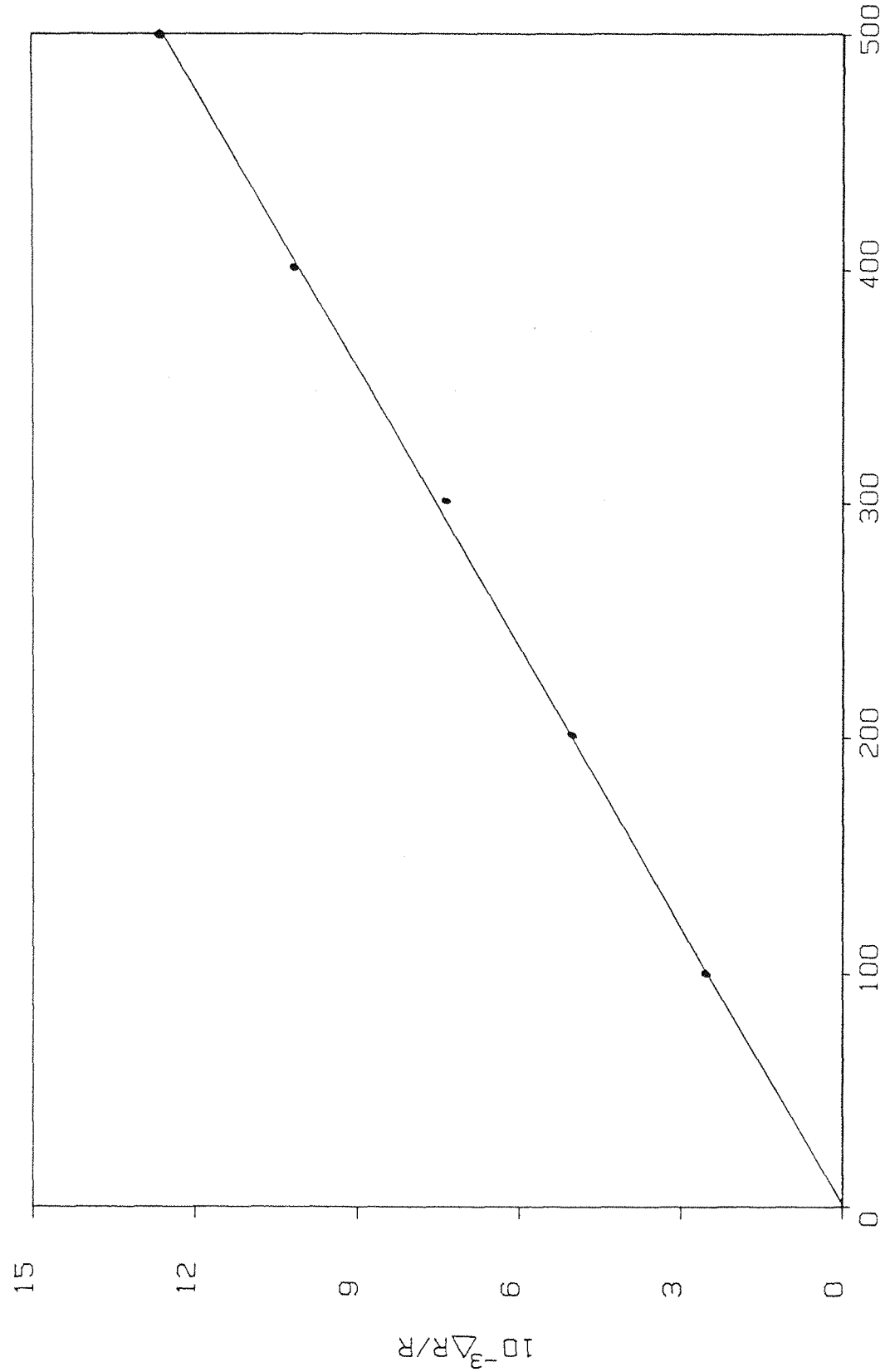

Fig. 4.52 Dependence of the $\Delta R/R$ signal, shown in figure 4.51, on the size of the a.c. peak-peak modulating potential. s-polarized light at 342 nm (270 Hz).

illustrated in figure 4.53. Although no significant change occurs in the position of the spectrum's critical points, the $\frac{\Delta R}{R}$ signal was observed to collapse as the d.c. bias was reduced. At a potential of -0.37 V vs Hg/Hg_2SO_4, the signal vanished entirely. On reducing the bias yet further, however, the spectrum was observed to reform, but it had now inverted.

Figure 4.54 shows the $\frac{\Delta R}{R}$ response obtained for a constant wavelength (342 nm) with the d.c. bias potential being reduced at 5 mVs^{-1}. The $\frac{\Delta R}{R}$ signal was found to depend on the square root of the d.c. bias for potentials greater than -0.37 V vs Hg/Hg_2SO_4. (Fig. 4.54b).

The effect on the EER spectra of changing the film thickness was investigated over a range of 5.0 to 22.5 nm (assuming A.R. = 2.5 nmV^{-1}). The results obtained are summarised in table 4.11. A dramatic change in the shape of the EER spectrum occurred when the film thickness was increased above 20 nm, with all three critical points moving to lower energy values (Fig. 4.55). This possibly indicates a change in the structure of the anodic oxide films.

Earlier electroreflectance measurements on rutile single crystals (38,39) showed no correlation with the results obtained above on anodic oxide films. Frova et al. (38) therefore suggested that the spectra obtained from films greater than 30 nm thick were dominated by electroabsorption effects (EA). The evidence put forward for this idea was that the authors observed no light modulation in the energy range where the absorption coefficient was greater than 5×10^5 cm^{-1} (approximately below 310 nm according to Fig. 4.20). This observation can also be made from the spectra obtained from the somewhat thinner films discussed in this thesis.

Bondeau et al. (40) have also suggested that interference effects should be considered when interpreting the EER spectra obtained from thin anodic oxide films.

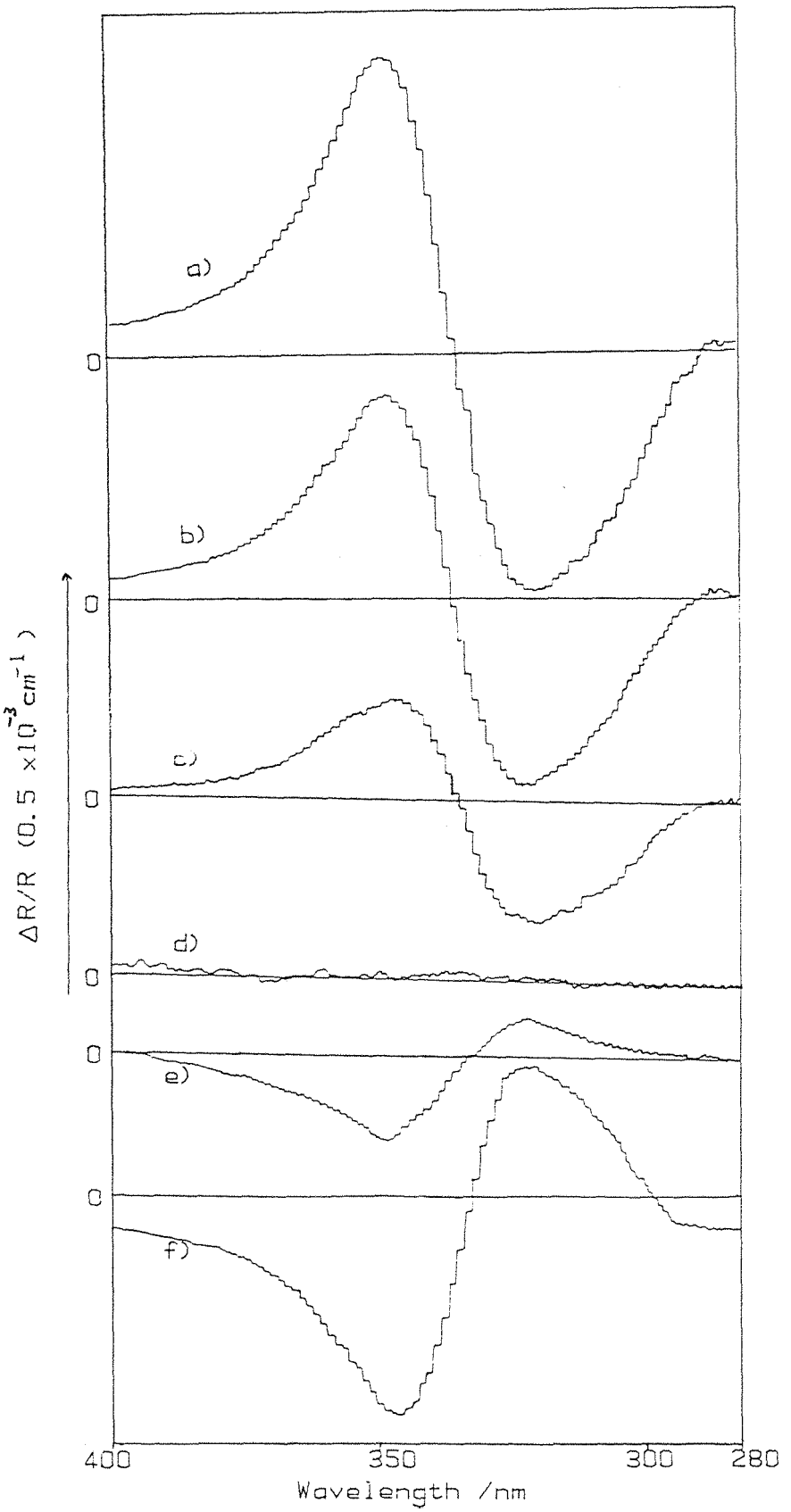

Fig. 4.53 Effect on the shape of the EER spectrum shown in figure 4.51 of reducing the d.c. bias to a) 3.0 V, b) 1.0 V, c) 0.0V, d) -0.37 V, 3) -0.4 V and f) -0.6 V vs Hg/Hg_2SO_4.

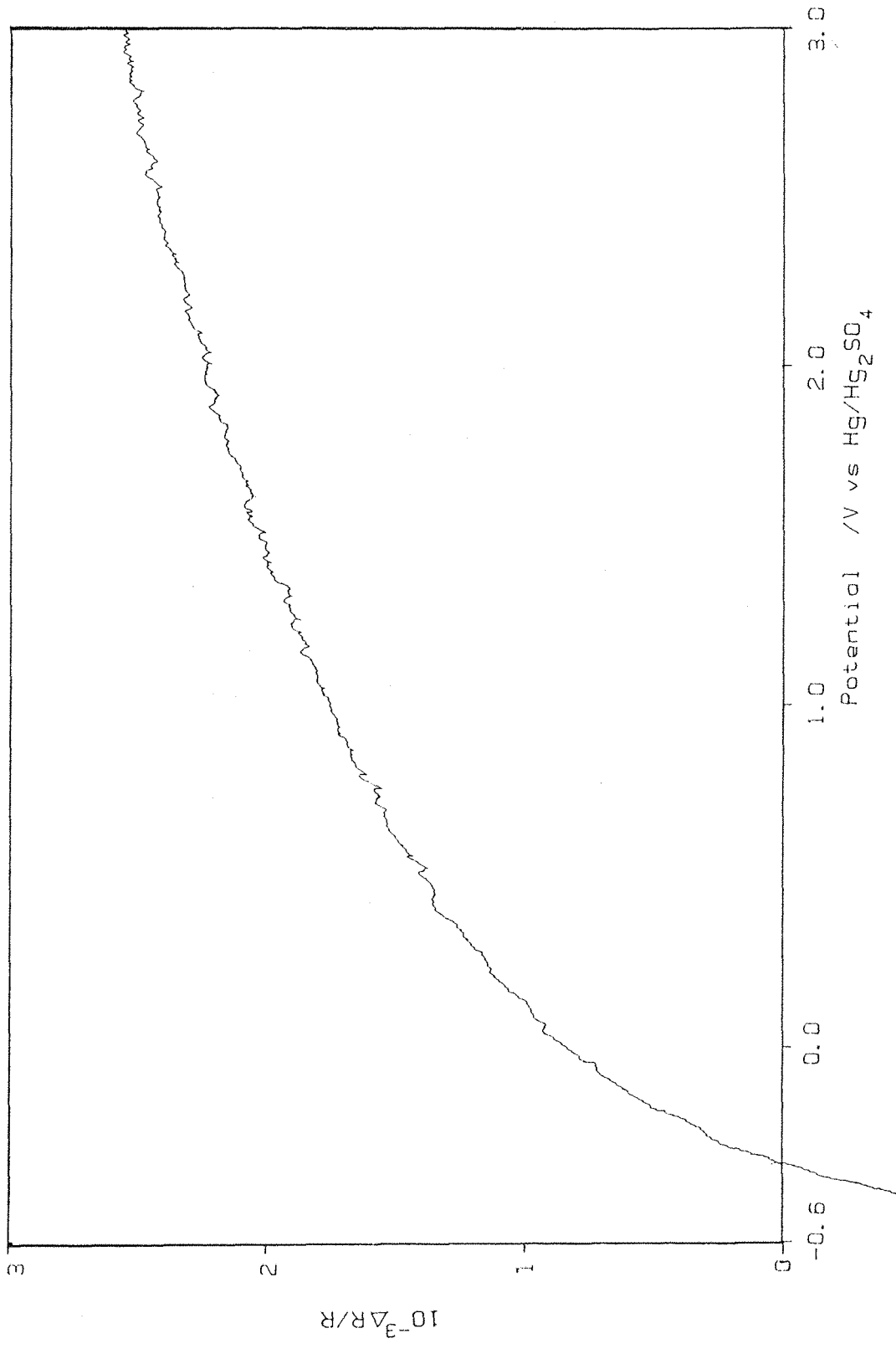

Fig. 4.54a Dependence of the $\Delta R/R$ signal on the d.c. bias potential, for a film originally grown at 10 mVs^{-1} to 3.0 V vs Hg/Hg_2SO_4 in 3 mol dm^{-3} H_2SO_4. The d.c. bias was reduced at a scan rate of 5 mVs . s-polarized light at 342 nm, and an a.c. peak-peak modulation signal of 100 mV at 270 Hz was used.

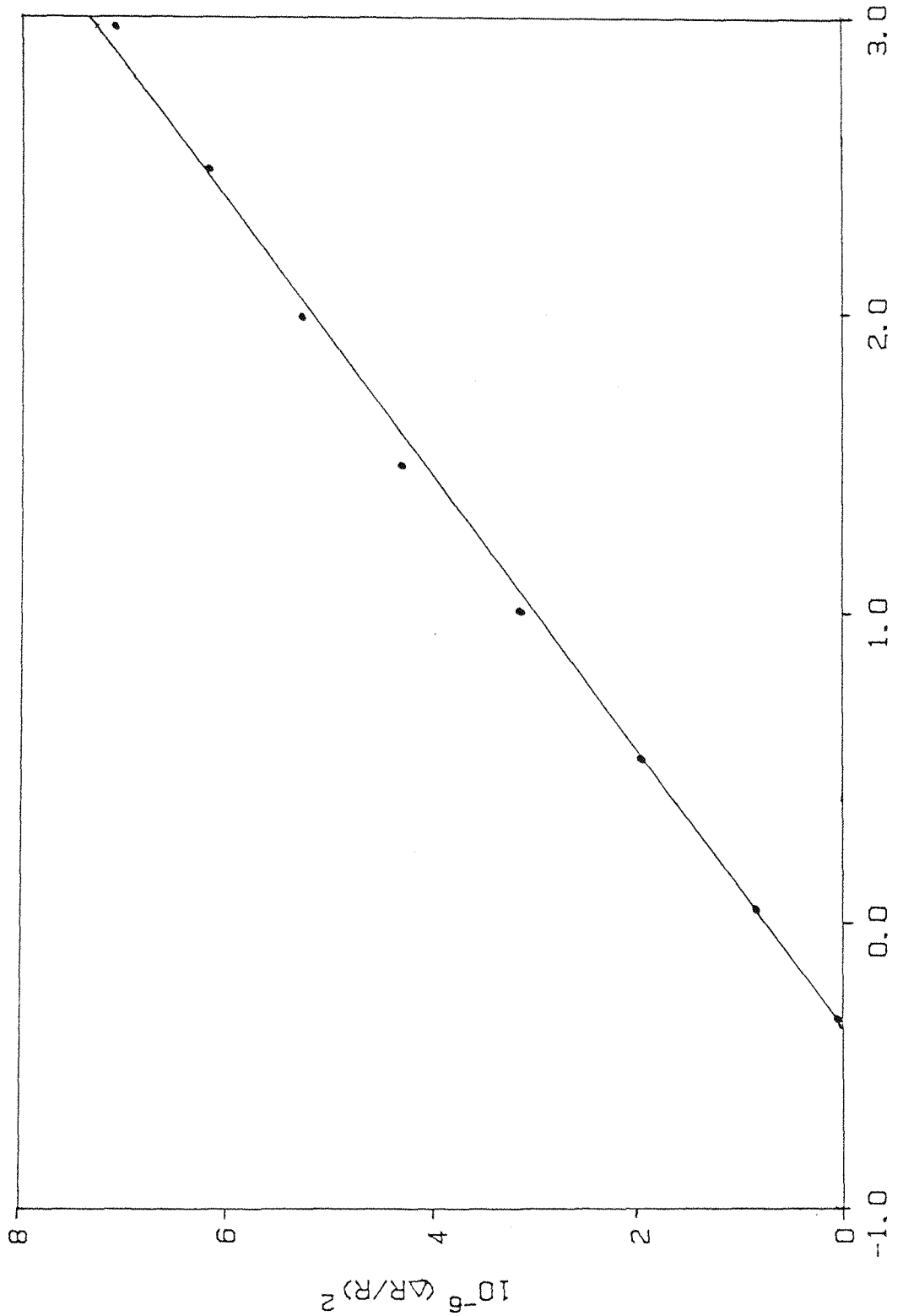

Fig. 4.54b Plot of $(\Delta R/R)^2$ against the d.c. bias potential from the curve obtained in figure 4.53.

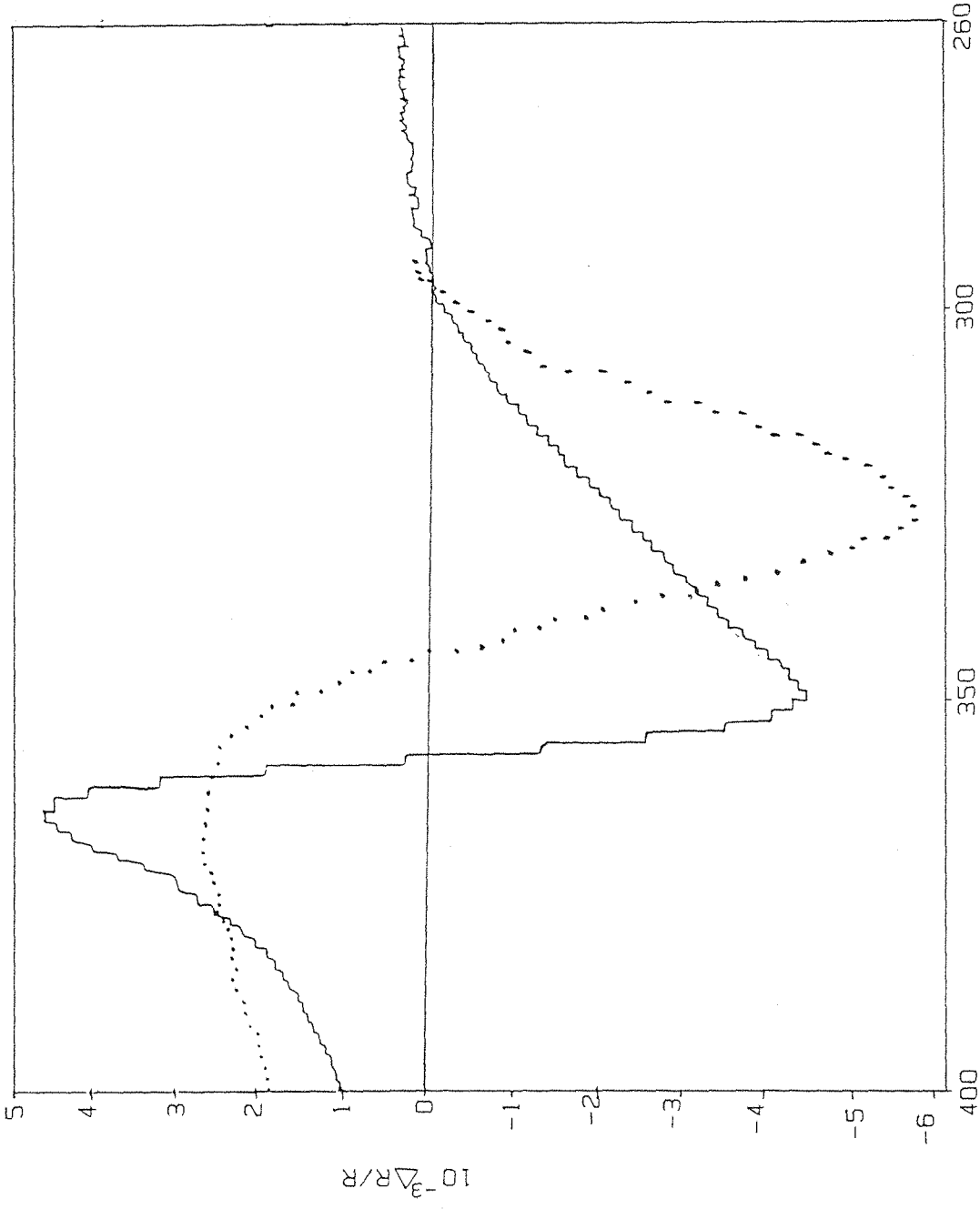

Fig. 4.55 EER spectrum obtained from a titanium oxide film grown to 7.0 V vs Hg/Hg_2SO_4. Measured at the formation potential, all other conditions being the same as for figure 4.51. • p-polarized, — s-polarized light.

Table 4.11 Effect of changing the film thickness on the critical points of the EER spectrum. All films grown at 10 mVs^{-1}. D.c. bias = anodic potential limit. A.c. modulation = 100 mV pk-pk at 270 Hz. An anodising ratio of 2.5 nm V^{-1} has been assumed.

Film thickness/nm	Polarisation of incident light	Low energy peak		High energy peak		Crossover
		Energy/eV	$10^{-3}\ \frac{\Delta R}{R}$	Energy/eV	$10^{-3}\ \frac{\Delta R}{R}$	Energy/eV
5.0	s	3.66	1.1	4.06	0.7	3.82
7.5	s	3.61	1.9	3.95	1.5	3.75
10.0	s	3.63	2.5	3.97	1.9	3.79
12.5	s	3.63	3.3	3.95	2.3	3.76
15.0	s	3.59	4.4	3.83	3.4	3.66
17.5	s	3.53	5.4	3.73	4.1	3.61
20.0	s	3.35	4.5	3.53	4.5	3.40
22.5	s	3.17	2.4	3.52	2.4	3.30
5.0	p	3.75	2.0	4.13	0.3	3.98
7.5	p	3.75	4.1	4.10	0.8	3.96
10.0	p	3.76	5.4	4.09	1.1	3.95
12.5	p	3.75	5.7	4.11	1.2	3.94
15.0	p	3.73	4.9	4.03	1.5	3.87
17.5	p	3.64	1.8	3.91	1.9	3.70
20.0	p	-	1.3	3.82	2.9	3.59
22.5	p	-	0.8	3.73	1.6	3.41

A full interpretation of the EER spectra obtained from thin anodic films would therefore be very complicated, and so this technique cannot yet provide the structure information which can be obtained from photocurrent spectroscopy and ellipsometry.

4.9 Hydrogen Penetration of Titanium Electrodes

After prolonged use at high temperature in strong acids, changes in the cyclic voltammograms of the titanium electrodes were observed (Fig. 4.56). The most noticeable change was the appearance of additional peaks, which on the second cycle resembled a redox couple centred around the hydrogen evolution reaction (-0.64 V vs Hg/Hg_2SO_4).

Similar peaks had been observed previously by Francis (41), who concluded that oxidation and reduction of hydrogen in some form of association with the titanium metal was the most likely cause of their existence. The hydrogen was believed to enter the metal during dissolution, the mechanism of which had earlier been reported as being (42)

$$Ti_{(s)} \rightleftharpoons Ti^{2+} + 2e^-$$

$$Ti^{2+}_{(ads)} + H^+ \longrightarrow Ti^{3+}_{(aq)} + H_{(ads)}$$

$$H_{(ads)} \rightleftharpoons H^+_{(aq)} + e^-$$

Indeed Francis (41) showed that new titanium electrodes developed the 'hydrogen redox couple' when left under conditions of open-circuit dissolution for long periods of time (> 3 hours).

To investigate this phenomenon further, the tip of an 'old' electrode was cut off and placed in a secondary ion mass spectrometer (SIMS). The results obtained were then compared to those of a 'new' titanium surface. (The SIMS spectrometer was operated by P. Chalker, at AERE Harwell).

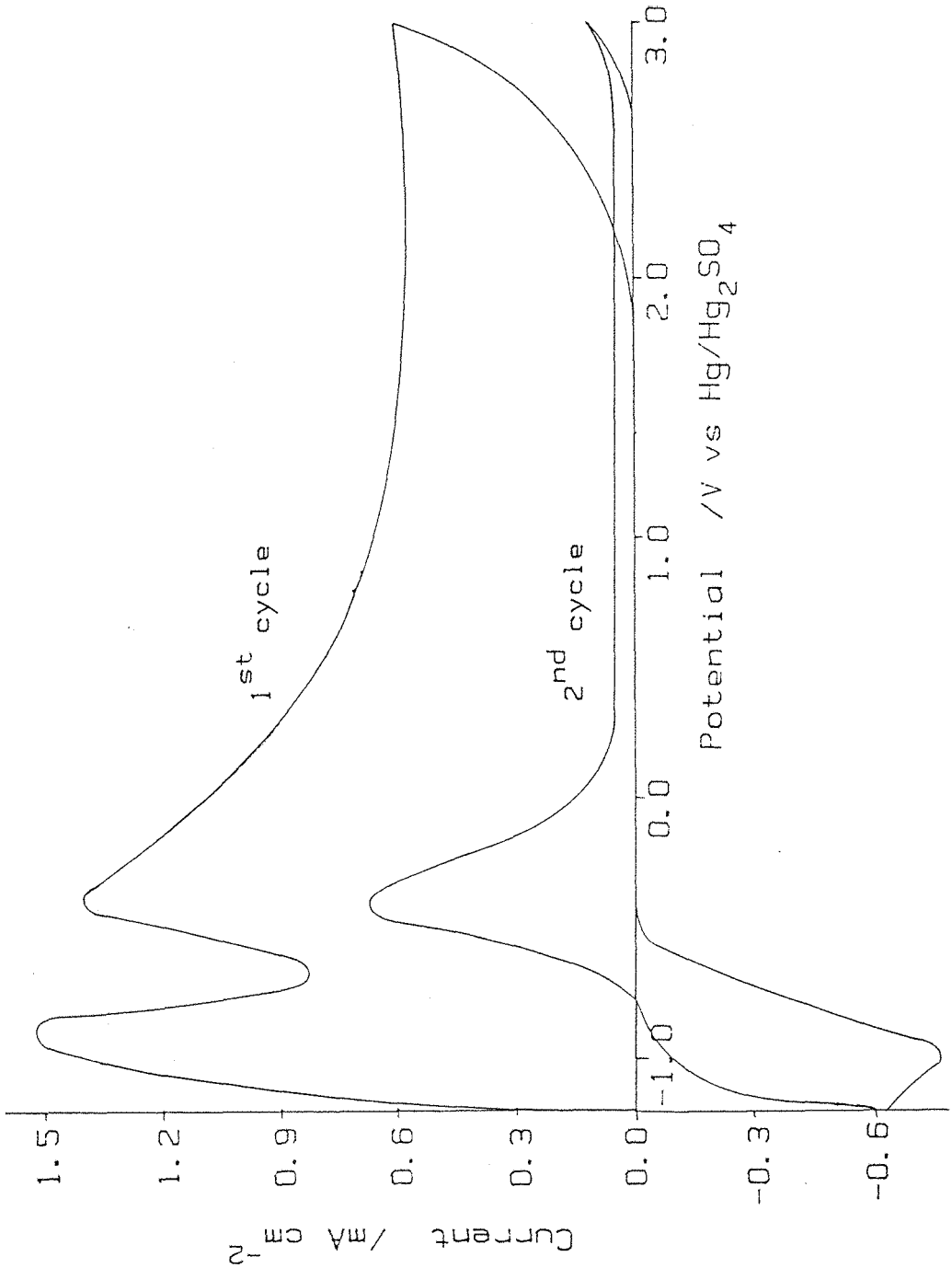

Fig. 4.56 Typical cyclic voltammogram of an 'old' titanium electrode showing additional 'redox couple'. Scan rate = 100 mVs^{-1} in 3 mol dm^{-3} H_2SO_4 at room temperature.

The mass spectra obtained from the two samples were virtually identical (cf. Figs. 4.57 and 4.58), with C, Na, Mg, Al and Si in addition to a wide range of titanium clusters being detected. The presence of Al and Si was attributed to the polishing procedure. No hydrogen is recorded in these figures due to a calibration problem. However, by tuning the spectrometer for hydrogen it was possible to obtain depth profiles in both the samples.

The 'new' titanium sample showed a virtually homogeneous hydrogen concentration in the metal after a couple of hundred nanometres had been penetrated (Fig. 4.59). However, this concentration was very close to the background level for hydrogen in the spectrometer, indicating that no hydrogen was present in the bulk of the 'new' titantium sample.

The depth profile for the 'old' titanium electrode (Fig. 4.60) on the other hand, showed a large increase in the hydrogen concentration compared with the 'new' sample. This concentration was observed to decrease as the metal was penetrated, although even at a depth of 5 μm the hydrogen count was still way above the background level.

The spectrometer used for these experiments had an imaging capacity, and this was used to look at the grain structure in the two samples. In the 'old' sample an H^+ image (Fig. 4.61a) showed the hydrogen rich regions as bright needle-like structures. In addition O^+ (Fig. 4.61b) and Ti^+ (Fig. 4.61c) micrographs of the 'old' sample showed a resolvable grain structure. Conversely, the Ti^+ image of the 'new' sample appeared to be comparatively structureless (Fig. 4.62a) and an H^+ image (Fig. 4.62b) indicated a near homogeneous distribution of hydrogen species across the 'new' samples surface, which is consistent with a hydrogen concentration close to the spectrometer's background level.

In order to examine the crystallinity of the two samples in greater detail, they were transferred to a scanning electron microscope. Grain sizes of up to 100 μm were observed on both of the samples.

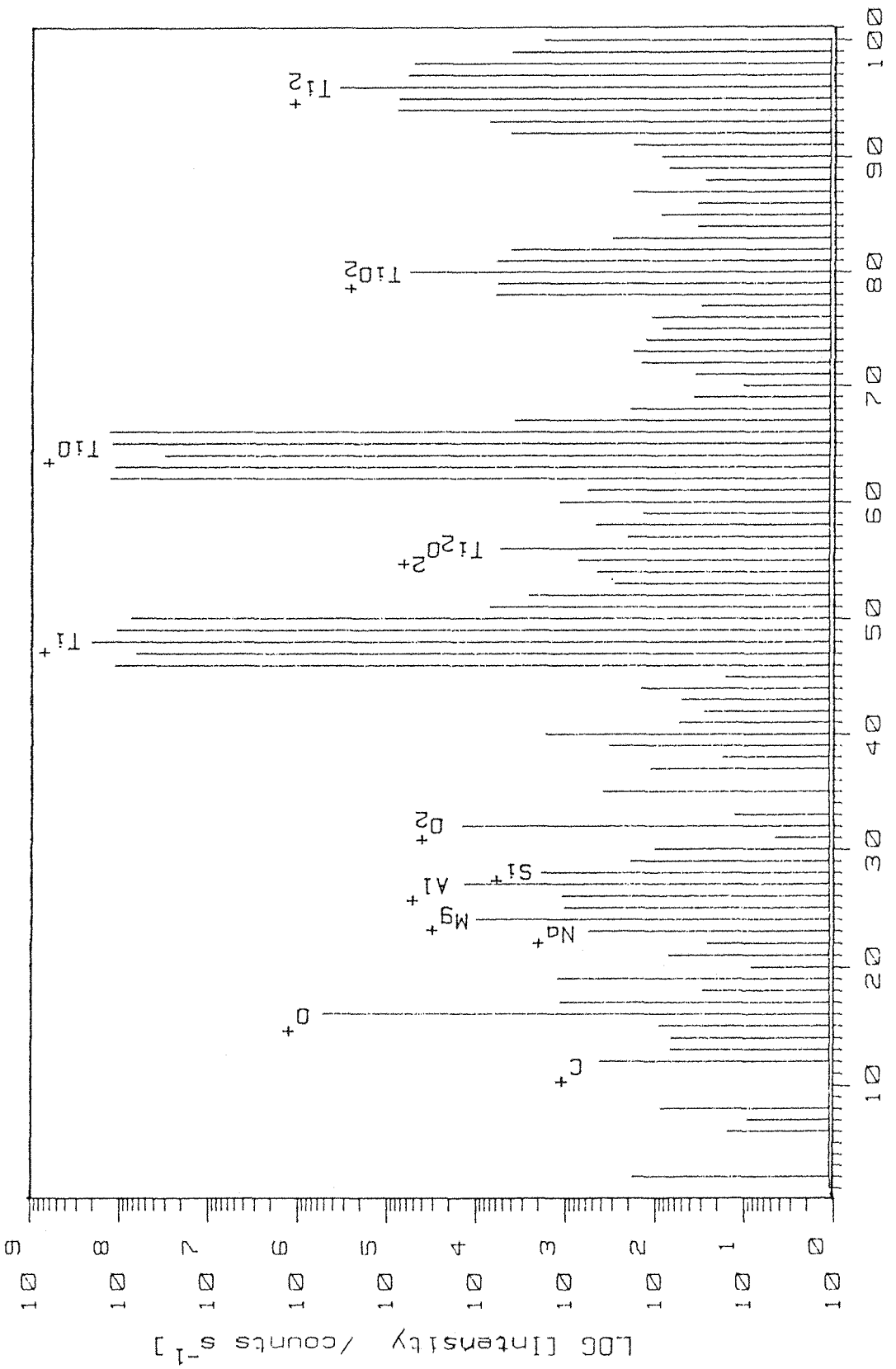

Fig. 5.47 S.I.M.S. Mass spectrum obtained from 'old' titanium electrode, using an O_2^+ primary ion beam, 15 kV energy, recording the positive secondary ions.

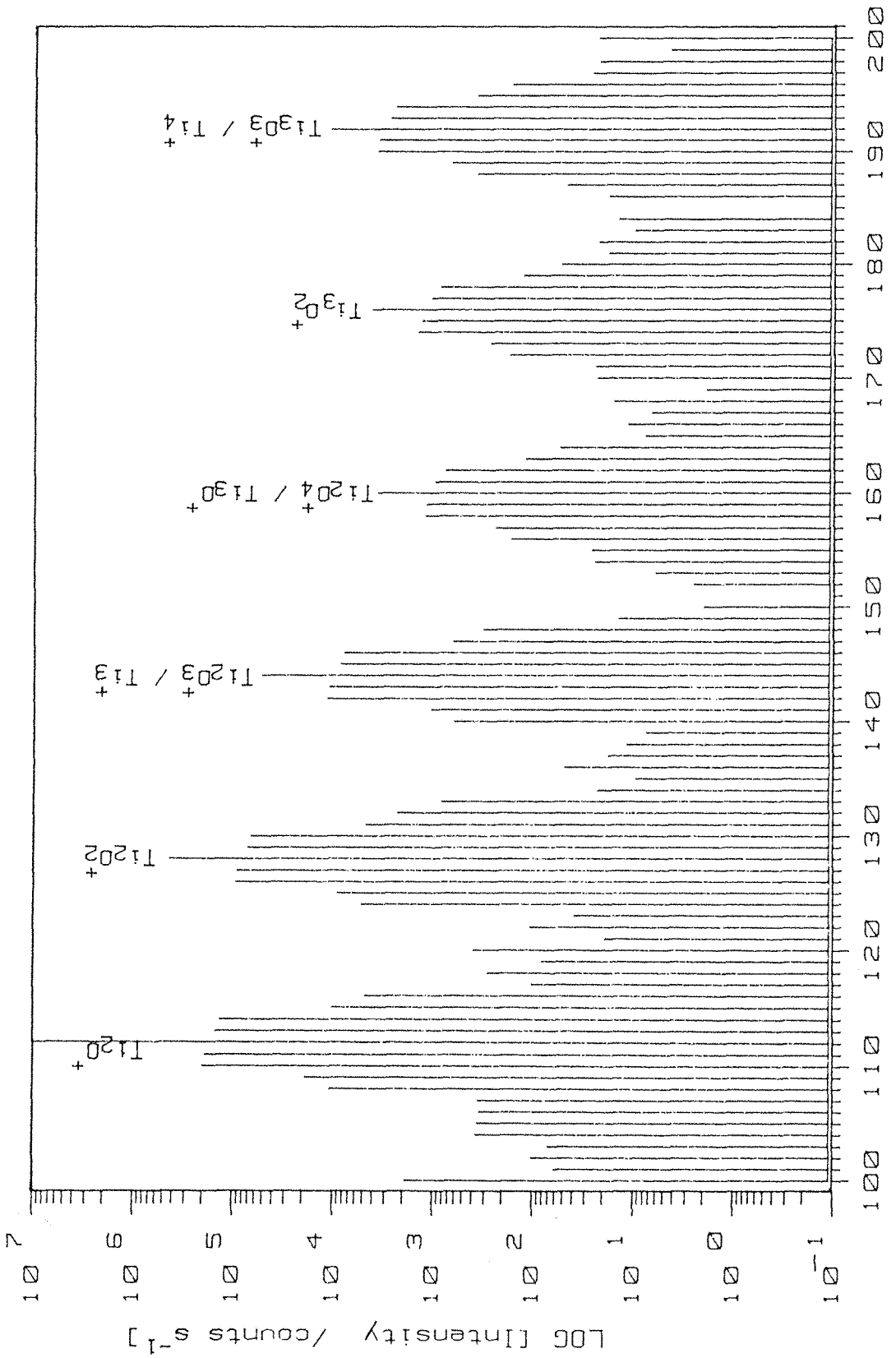

Fig. 4.47 (continued)

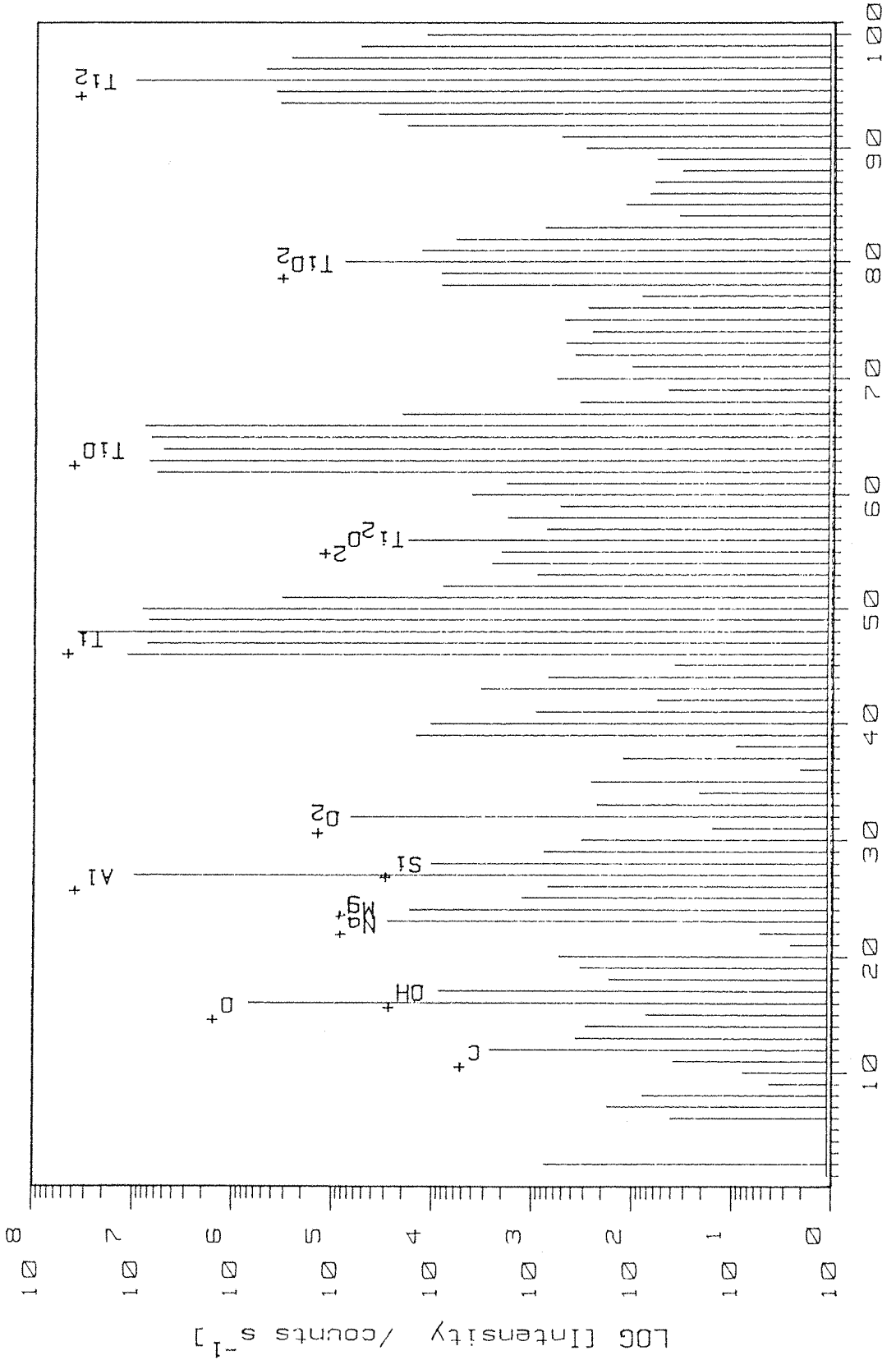

Fig. 4.58 S.I.M.S. Mass spectrum obtained from a 'new' titanium sample, using a O_2^+ primary ion beam, 15 kV energy, recording the positive secondary ions.

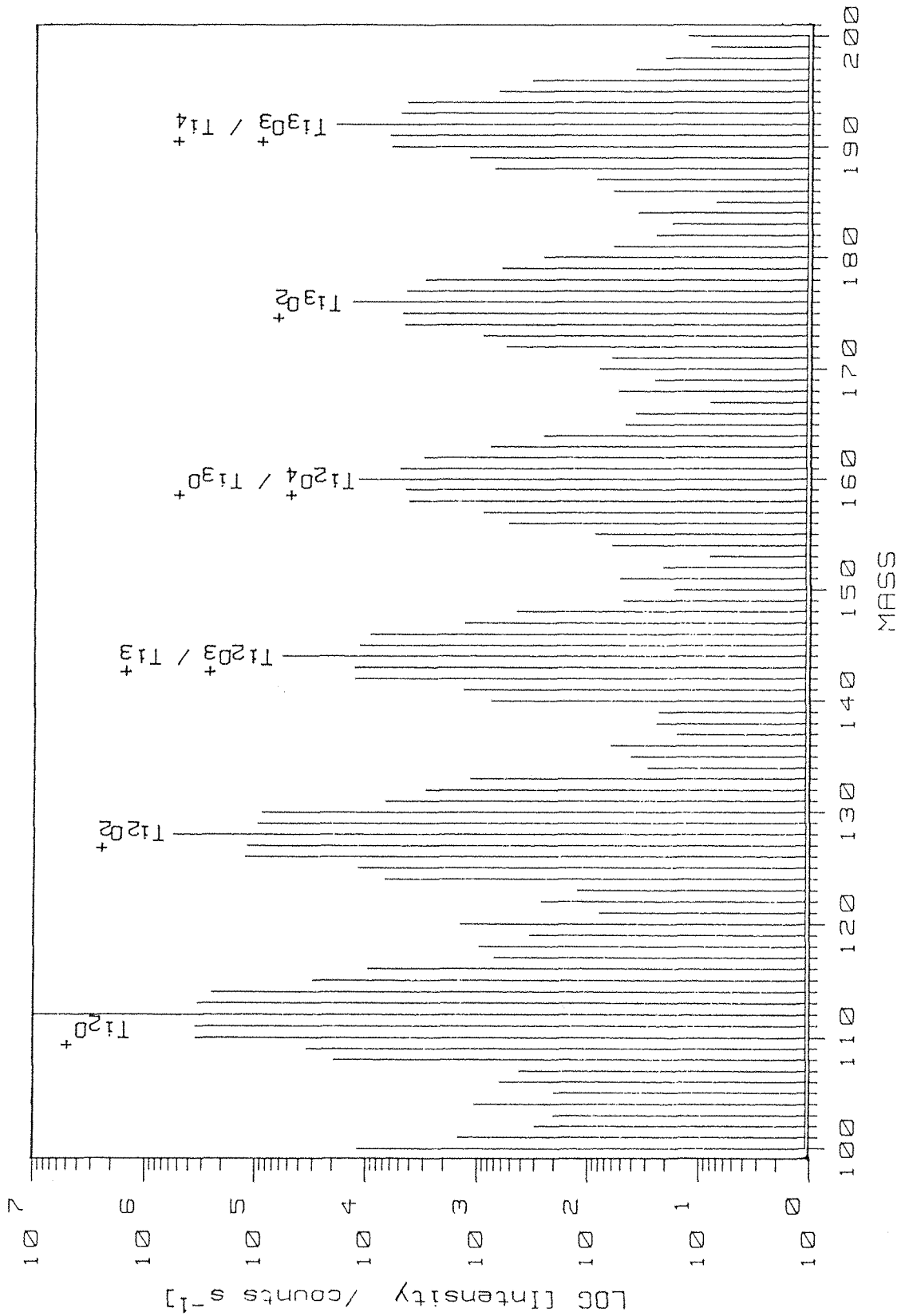

Figure 4.58 (continued)

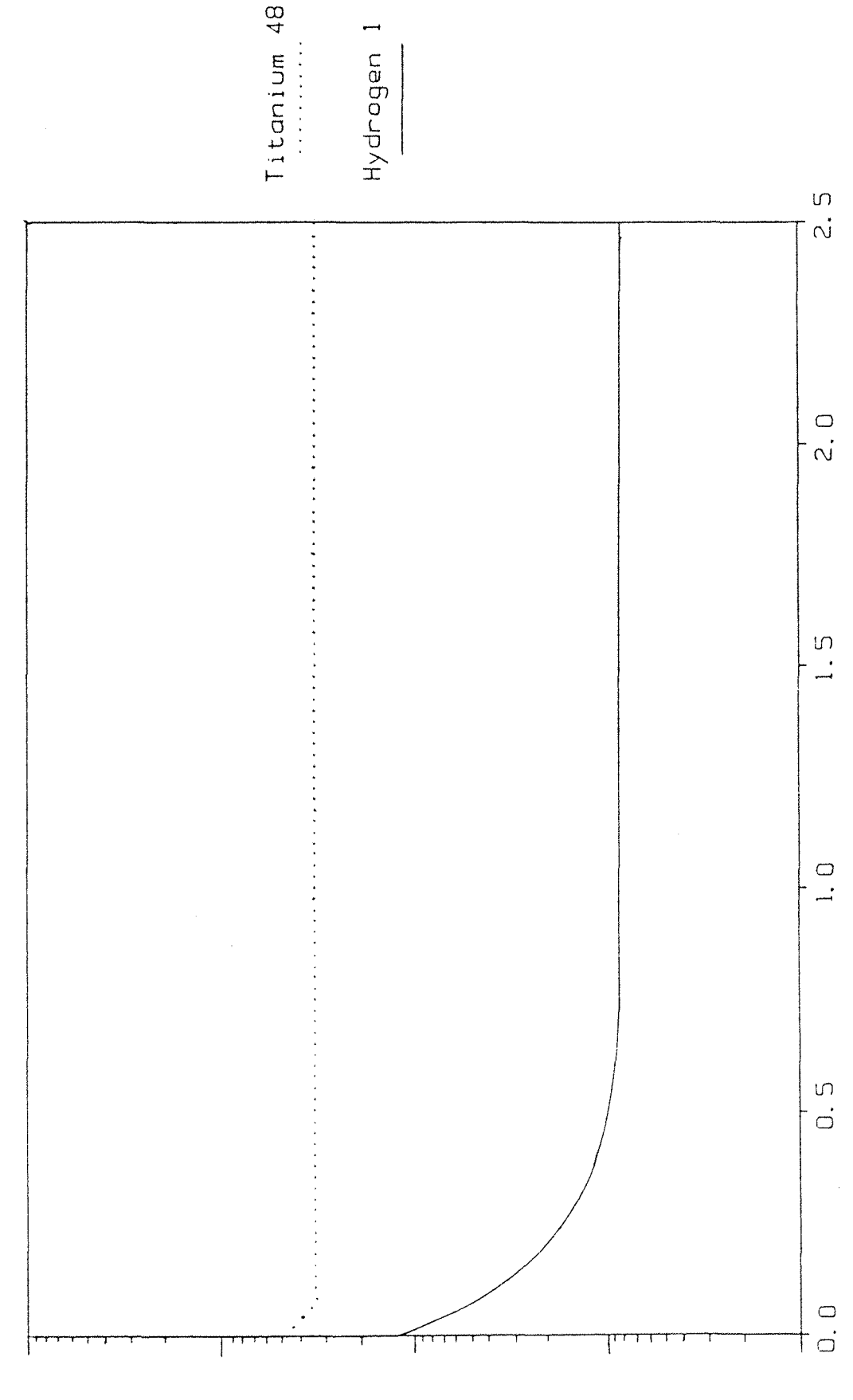

Fig. 4.59 S.I.M.S. depth profile of a 'new' titanium sample.

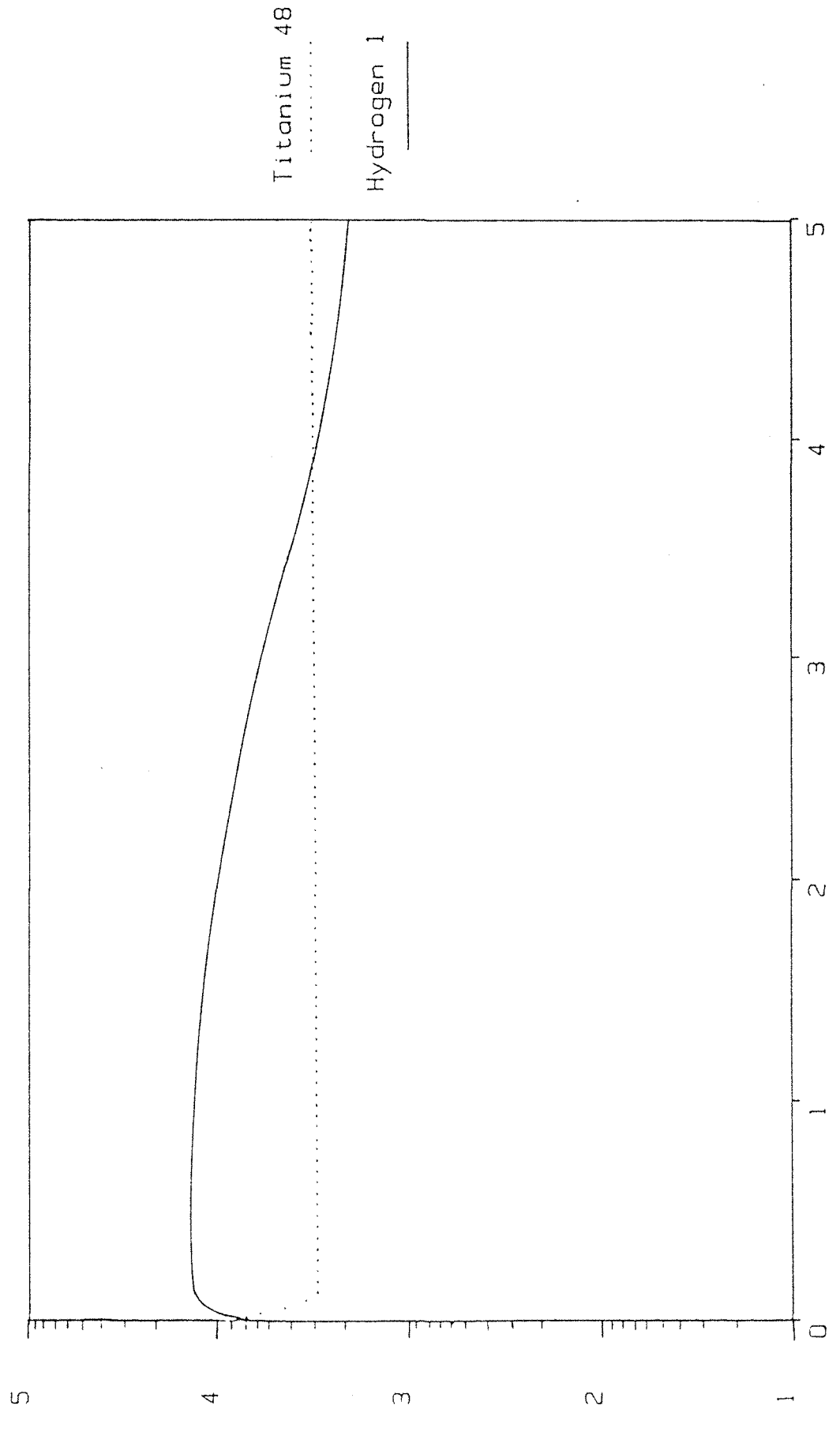

Fig. 4.60 S.I.M.S. depth profile of an 'old' titanium electrode.

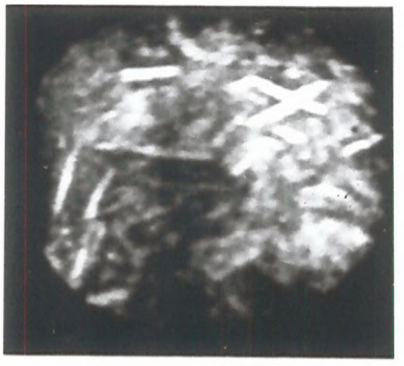

(a) H^+ image

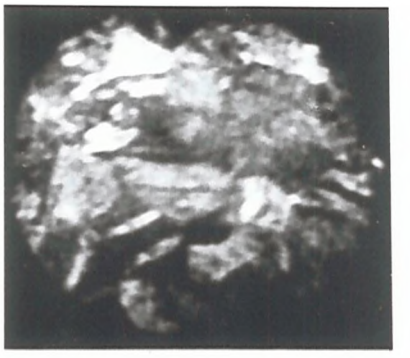

(b) O^+ image

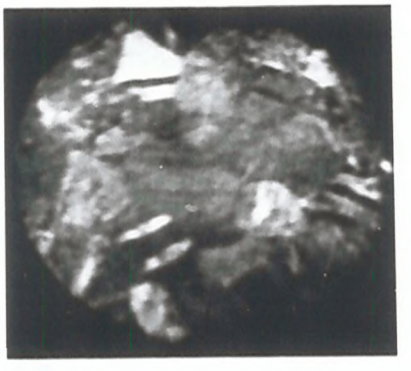

(c) Ti^+ image

Fig. 4.61 Cation images of the surface of an "old" titanium electrode, using the imaging capability of the IMS-3F spectrometer.

(a) Ti^+ image (b) H^+ image

Fig 4.62 Cation images of the surface of a "new" titanium electrode

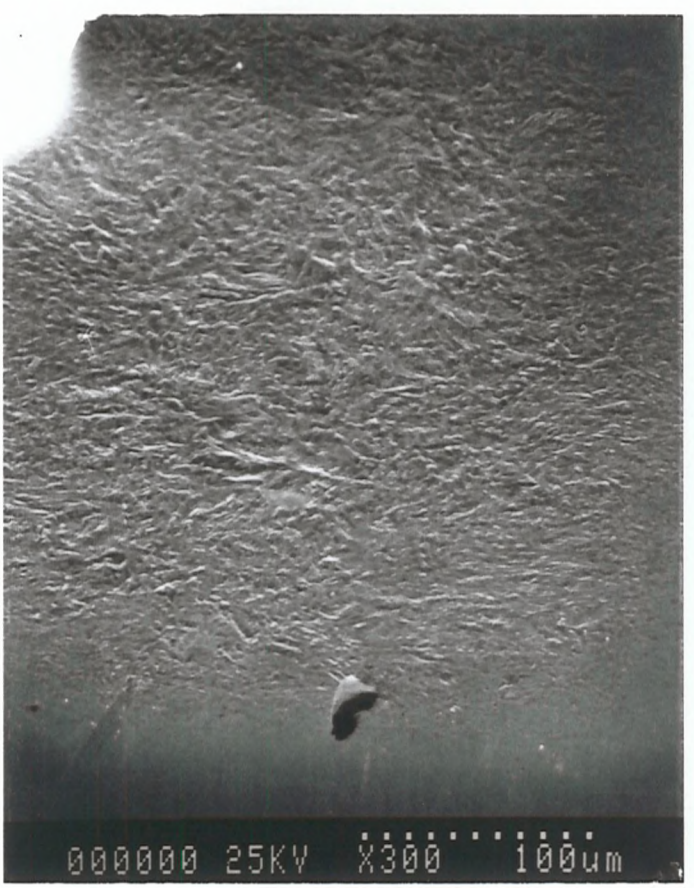

Fig. 4.64 SEM photograph of the surface of a "new" titanium sample showing litte grain structure

A clear grain structure was observed on the 'old' specimen (Fig. 4.63a), which on closer examination appeared to be platelets (Fig. 4.63b), consistent with the formation of titanium hydride plates. In contrast, the 'new' sample indicated a rougher surface without the characteristic grain structure seen in the 'old' electrode (Fig. 4.64).

In conclusion, it is clear that prolonged use of titanium in strong acid conditions results in the irreversible incorporation of hydrogen atoms deep into the structure of the metal. This results in a change in the grain structure of the metal, and possibly the formation of titanium hydride.

(a)

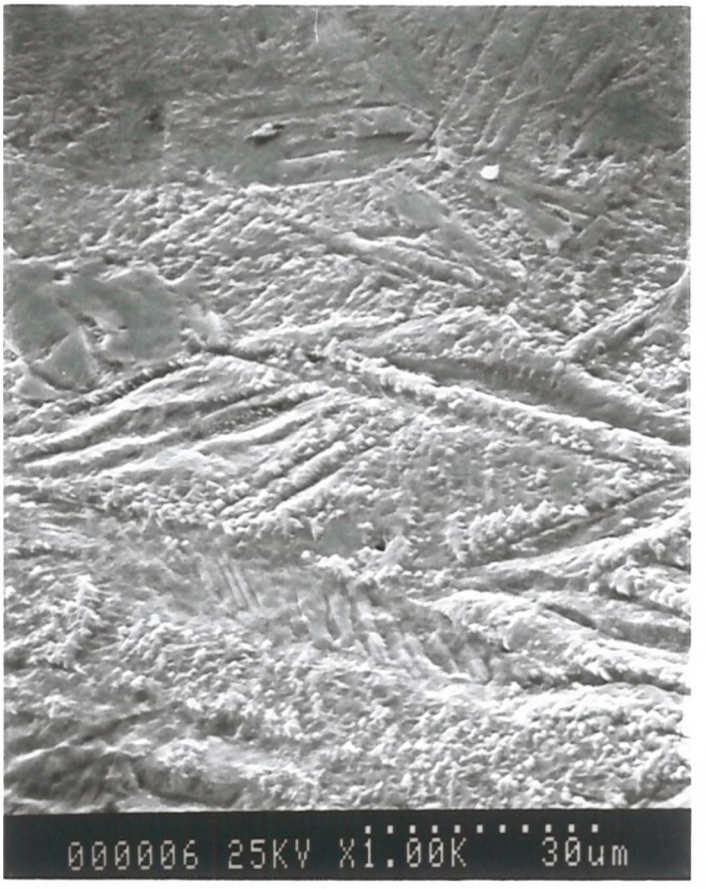

(b)

Fig. 4.63 SEM photographs of the surface of "old" titanium electrode, indicating a platlet structure.

References

1. PETRENKO, A.T. ; RUSS, J. Phys. Chem. 36, (1962), 815.
2. KICHIGIN, V.I., KAVARDAKOV, N.I. & KUZNETSOV, V.V.; Sov. Electrochem. 18 (1982) 940.
3. KELLY, E.J. & BRONSTEIN, H.R.; J. Electrochem. Soc. 131, (1984) 2232.
4. TRASATTI, S.; J. Electroanal. Chem. 39 (1972) 163.
5. KELLY, E.J. in "Modern Aspects of Electrochemistry" Vol. 14, Bockris, J. O'M.,Conway, B.E. and White, R.E. (Eds.), Ch. 5. Plenum Press, New York (1982).
6. WILLIAMS, D.E. & WRIGHT, G.A.; Electrochim. Acta. 21 (1976) 1009.
7. ALLARD, K.D., AHRENS, M. & HEUSLER, K.E.; Werkst. & Korrosion, 26 (1975) 694.
8. BLONDEAU, G., FROELICHER, M., FROMENT, M. & HUGOT-LE GOFF, A.; J. Microsc. Spectrosc. Electron. 2 (1977) 27.
10. PETTINGER, B., SCHOPPEL, H.R., YOKOYAMA, T. & GERISCHER, H.; Ber. Bunsenges. Phys. Chem. 78 (1974) 1024.
11. DI QUARTO, G., GERISCHER, H. &' DOBLHOFER, K.; Electrochim. Acta. 23 (1978) 195.
12. YANIV, M., LASER, D. & GOTTESFELD, S.; J. Electrochem. Soc. 125 (1978) 358.
13. DYER, C.K. & LEACH, J.S.L.; Electrochim. Acta. 23, (1978) 1387.
14. YOUNG. L. "Anodic Oxide Films", Academic Press, London, (1961).
15. MADOU, M., CARDON, F. & GOMES, W.P.; J. Electrochem. Soc. 124 81977) 1623.
16. SCHOOMAN, J., VOS, K. & BLASSE, G.; J. Electrochem. Soc. 127 (1980) 324.
17. MYAMLIN, V.A. & PLESKOV, Y.G.; "Electrochemicstry of semiconductors", Plenum Press, New York (1967).
18. LI, J.,PETER, L.M. & POTTER, R.; J. Appl. Electrochem. 14 (1983) 495.
19. LASER, D. & GOTTESFELD, S.; J. Electrochem Soc. 126 (1978) 475.
20. HEUSLER, K.E. & YUN, K.S.; Electrochim. Acta. 27 (1977) 977.
21. SCHMICKLER, W. & ULSTRUP, J.; Chem. Phys. 19 (1977) 217.

22. PETER, L.M., LI, J. & PEAT, R.; J. Electroanal. Chem. 165 (1984) 29.

23. MORRISON, S. R.; "Electrochemistry at Semiconductor and Oxidised Metal Electrodes", Plenum Press, New York (1980).

25. HOLLAND, L., "Vacuum Deposition of Thin Films", Chapman and Hall, London (1963).

26. JOHNSON, P.B. & CHRISTY, R.W.; Phys. Rev. B. 9 (1974) 5056.

27. MEMMING, R., MOLLERS, F. & ROLLE, H.J.; J. Electrochem. Soc. 121 (1974) 1160.

28. PETERS, J.M. & MYERS, J.R.; Corrosion, 23 (1967) 326.

29. POURBAIX, M., SCHMETS, J. & VAN MUYLDER, J.; "Atlas of Electrochemical Equilibria", Edited by Pourbaix, M, Pergamon Press, Oxford (1966).

30. GURINA, T.V. & ANASHKIN, R.D.; Sov. Electrochem. 15 (1979) 197.

31. See, for example, McCRACKIN, F.L.; "A Fortran Progam for Analysis of Ellipsometer Measurements", Natl. Bur. Stand., Tech. Note 479, U.S. Govt. Printing Office, Washington D.C., (1969).

32. PETER, L.M. & McALEER, J.F.; J. Electrochem. Soc. 129 (1982) 1252.

33. DYER, C.K. & LEACH, J.S.L.; J. Electrochem. Soc., 125 (1978) 1032.

34. BLONDEAU, G., FROELICHER, M., FROMENT, M. & HUGOT-LE GOFF, A.; Thin Solid Films, 38 (1976) 261.

35. DE PAULI, C.P., GIORDANA, M.G. & ZERBINO, J.O.; Electrochim. Acta. 28 (1983) 1781.

36. OHTSUKA, T., MASUDA, M. & SATO, N.; J. Electrochem. Soc. 132 (1985) 787.

37. HARRISON, J.A. & WILLIAMS, D.E.; Electrochim. Acta, 27 (1982). 891.

38. FROVA, A., BODDY, P.J. & CHEN, Y.S.; Phys. Rev. 157 (1967) 700.

39. VOS, K. & KRUSEMEYER, H.J.; J. Phys. C: Solid State Phys. 10 (1977), 3893.

40. BLONDEAU, G., FROELICHER, M., JOVANCICEVIC, G. & HUGOT LE-GOFF, A.; Surf. Sci. 80 (1979) 151.

41. FRANCIS, K.F.; University of Southamtpon, M.Sc. Thsis (1982).

42. ARMSTRONG, R.D., HARRISON, J.A., THIRSK, H.R. & WHITFIELD, R.; J. Electrochem. Soc. 117, (1970) 1003.

CHAPTER 5

SUMMARY AND CONCLUSIONS

5.1 New information on the breakdown of TiO_2 films

Ellipsometry and reformation experiments have shown clearly that the process which leads to the catastrophic open-circuit breakdown of the anodic oxide filmsis chemical dissolution:

$$TiO_{2(s)} \xrightarrow{4H^+} Ti(IV)_{aq} + 2H_2O \qquad 5.1$$

This process was found to occur at a uniform rate, which in turn was observed to increase with increasing growth rate and temperature. In addition, the open-circuit dissolution rate was found to be dependent on the nature and concentration of both the cation and the anion in the open-circuit solution.

The open-circuit breakdown was observed to occur when there was still an average film thickness of about 1.0 nm left on the electrode surface, although some patches of the bare metal may have been exposed to the acid electrolyte.

Application of small cathodic currents was found to increase the rate of anodic oxide dissolution, probably by reducing the dioxide at the oxide/electrolyte interface.

$$TiO_2 + e^- \xrightarrow{H^+} \tfrac{1}{2} Ti_2O_3 + \tfrac{1}{2} H_2O \qquad 5.2$$

$$\tfrac{1}{2} Ti_2O_3 + 3H^+ \longrightarrow Ti^{3+}_{(aq)} + {}^{3}/_{2}\, H_2O \qquad 5.3$$

However, it was observed that not all the applied current went towards reduction of the dioxide film, as much of it may be lost in side reactions such as hydrogen evolution.

Prolonged use of titanium in acidic environments was found to lead to the metal being penetrated by hydrogen, and SIMS showed that this penetration occurred to a depth of several microns. SEM photographs also indicated a change in the grain structure of the

aged metal, which may have been the result of the formation of TiH_2.

5.2 New information on the properties of TiO_2 films

Photocurrent spectroscopy indicated that the indirect bandgap of the anodic oxide films found on titanium was approximately 3.1 eV. This is between the bandgaps of rutile (3.0 eV) and anatase (3.2 eV). However, ellipsometry revealed optical constants for the anodic oxide films that suggested that they resemble the anatase form of TiO_2.

The growth rate dependence of the open-circuit dissolution rate was believed to be due to a change in the cyrstallinity of the oxide films. Recombination effects result in photocurrent spectroscopy being very sensitive the crystal structure, and this technique revealed that the crystallinity of the anodic oxide films increased when the growth rate was decreased or the temperature was increased. These results show that the increased stability of films grown at low sweep rates is associated with the formation of a more perfect polycrystalline oxide which dissolves more slowly at open-circuit.

From the impedance measurements the permittivity of the oxide films was found to be frequency dependent, with $\tan\delta$ being constant between 10 Hz and 10 kHz. This is typical for valve metal anodic oxides and is usually explained in terms of dielectric relaxation phenomena. Mott-Schottky plots obtained from the titanium anodic oxide films were found to be curved, indicating a spatial distribution of donors. This observation was explained by assuming the donors to be titanium ions, which, as travelling to the oxide/electrolyte interface during growth, became trapped in interstitial sites when the growth field was reduced.

The spectral dependence of the absorption coefficient of the thin anodic oxide films formed on titanium was obtained by combining photocurrent and capacitance measurements for the wavelength range 250 - 400 nm.

Ellipsometry measurements indicated that a thin suboxide layer forms between the metal and the dioxide when the growth potential is reduced. However, identification of this layer by ellipsometry was not possible due to a lack of sensitivity. It was hoped to identify this suboxide layer using angle resolved Auger electron spectroscopy on anodic oxide films grown on evaporated titanium films, but unfortunately there was not enough time to complete these experiments.

5.3 The effect of the Helmholtz layer on anodic oxide film growth

During the growth of thin anodic oxide films, the potential drop across the Helmholtz layer is a significant proportion of the total potential drop across the electrode/electrolyte interface. Theoretical charge-time transients showed that the Helmholtz layer will cause the growth of thin anodic oxide films on valve metals to deviate from the inverse log law. This deviation arises because the Helmholtz layer acts as if it were an initial film thickness of $\varepsilon_{ox}L_H/\varepsilon_H$. However, in practice it would be necessary to measure over several decades of time in order to observe the effects of the Helmholtz layer.

The effect of the Helmholtz layer on cyclic voltammetry experiments is that it should again be equivalent to an initial film thickness of $\varepsilon_{ox}L_H/\varepsilon_H$ Therefore the onset potential should be shifted in the anodic direction, but the size of the plateau current should be uneffected. In practice the detection of these effects is complicated by the uncertainty concerning the equilibrium potential at which film growth becomes thermodynamically feasible.

APPENDICES

Appendix 1 A.C. Theory

A sinusoidal voltage may be expressed in the form,

$$E = \Delta E \sin(\omega t) \qquad A.1.1$$

where ΔE is the maximum amplitude and ω is the angular frequency ($2\pi f$). The resulting sinusoidal current in a linear circuit will have an identical frequency, but a different amplitude and phase, depending on the kind of electric components involved in the circuit. This current can be represented by

$$i = \Delta i \sin(\omega t + \theta) \qquad A.1.2$$

where θ is the phase difference, which can be positive leading the voltage, or negative, lagging the voltage.

If the sinusoidal voltage is applied across an ordinary resistor, R, then Ohm's law will apply;

$$i = E/R = \frac{\Delta E}{R} \sin(\omega t) \qquad A.1.3$$

As there is no phase shift in this equation, θ is zero, (Fig. A.1.1.)

The basic relationship for a capacitor is,

$$q = CE \qquad A.1.4$$

where q is the charge on the plates, C is the capacitance and E is the potential across the plates. The current is thus obtained by differentiation,

$$i = \frac{dq}{dt} = C\frac{dE}{dt} \qquad A.1.5$$

So for a sinusoidal applied voltage

$$i = \omega C \Delta E \cos(\omega t)$$

$$= \omega C \Delta E \sin(\omega t + \pi/2) \qquad \text{A.1.6}$$

Hence application of a sinusoidal voltage to a capacitor will give rise to a sinusoidal current which has the same angular frequency as the perturbing voltage, but $\pi/2$ out of phase with it (Fig. A.1.2)

The impedance, Z, of an electrical component is defined by Ohm's law

$$E = iZ \qquad \text{A.1.7}$$

For sinusoidal signals this can be defined as having a magnitude given by

$$|Z| = \frac{\Delta E}{\Delta i} \qquad \text{A.1.8}$$

and a phase angle, θ, corresponding to the phase difference between the current and the voltage. Thus impedance becomes a vector quantity and can be represented on an Argand diagram (Fig. A.1.3), with polar coordinates $|Z|e^{j\theta}$ or cartesian coordinates

$$Z_{real} = |Z| \cos\theta \qquad \text{A.1.9}$$

$$Z_{imag} = |Z| j \sin\theta \qquad \text{A.1.10}$$

where $j = \sqrt{-1}$. The impedance is thus redefined as a complex number,

$$Z = Z_{real} + Z_{imag} \qquad \text{A.1.11}$$

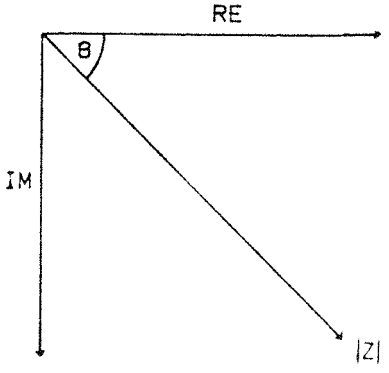

$$|Z| = \sqrt{RE^2 + Im^2}$$

$$\theta = \tan^{-1}\left(\frac{Im}{RE}\right)$$

Fig. A.1.3 Representation of the impedance of an electrical component as a vector on an Argand diagram.

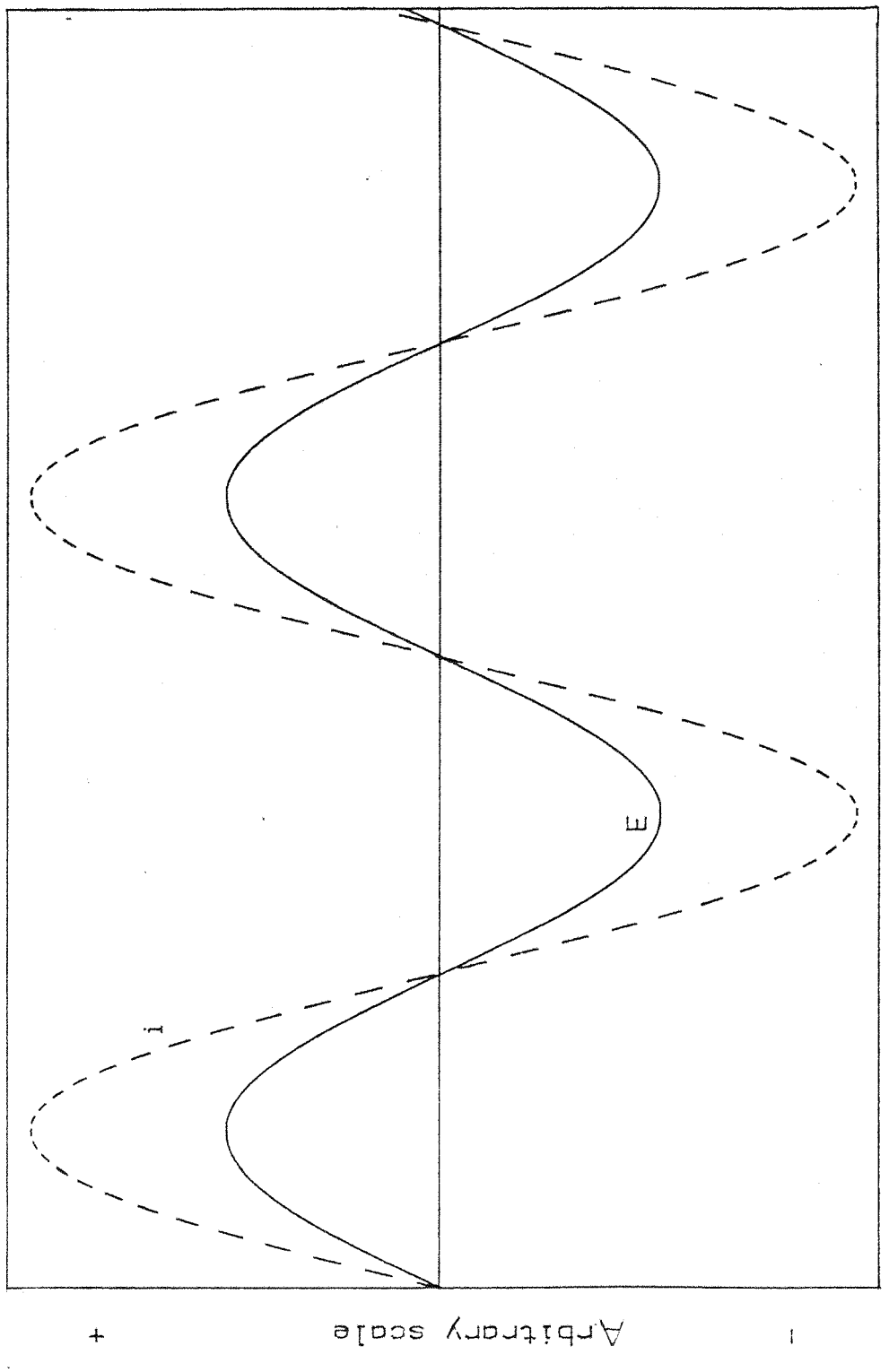

Fig. A.1.1 Relationship between sinusoidal current and voltages in a purely resistive circuit where the phase angle is zero.

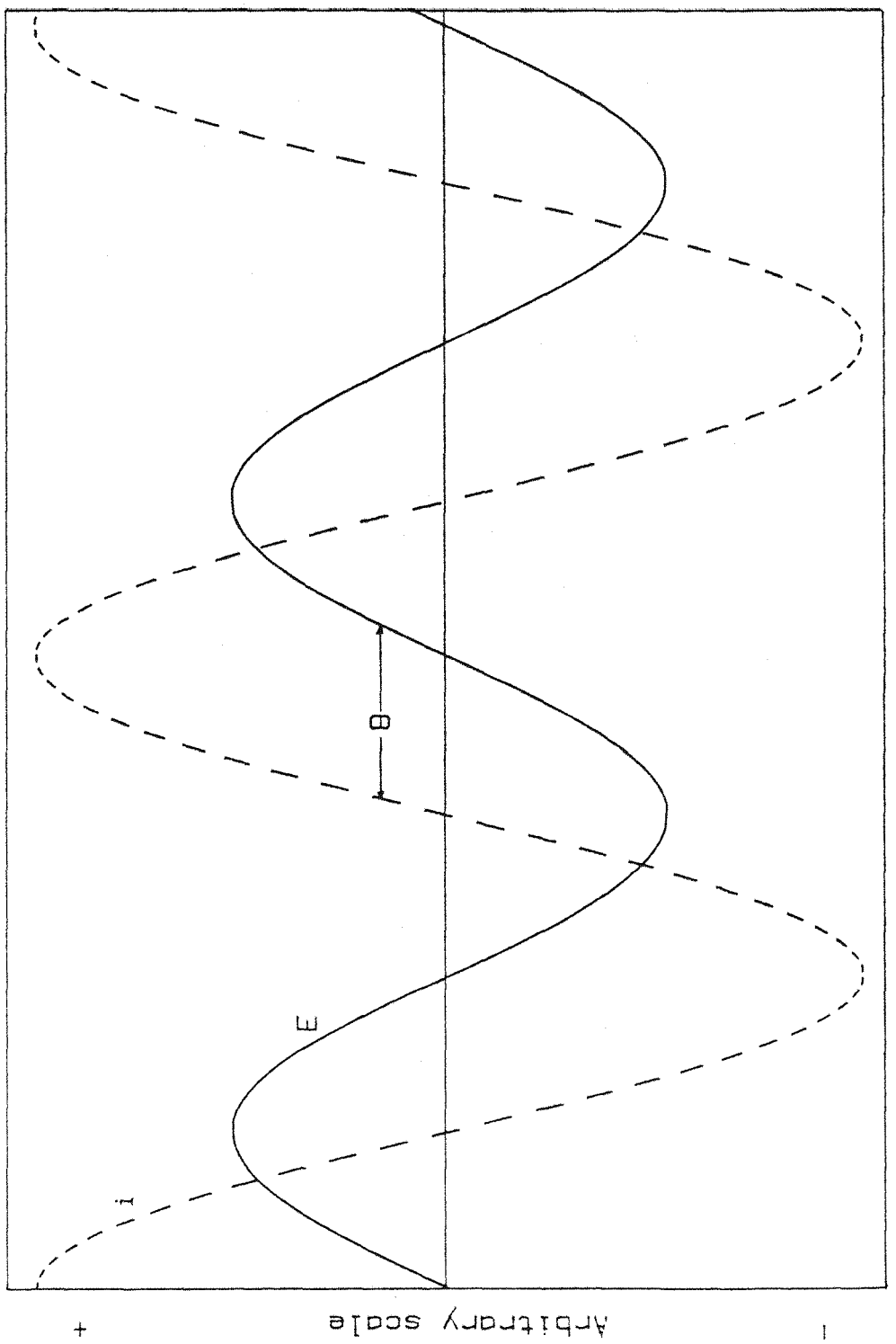

Fig. A.1.2 Relationship between sinusoidal current and voltage across a pure capacitor where the phase angle is 90°.

It is easy to show, from equation A.1.3, A.1.9 and A.1.10 that the impedance of a resistor is simply equal to its resistance, R, and from equation A.1.6 that the impedance of the capacitor is given by the reciprocal of the product of its capacitance multiplied by the angular frequency, $^{-j}/_{\omega C}$. The negative sign is due to the practice of measuring the voltage with respect to the current.

The impedance for a many component electrical circuit can be analysed by applying the following rules:

1. Kirckhoff's laws of network analysis must be obeyed(1);
   a) the total current through a parallel connection, is the sum of all the individual currents driven through each part of the connection by the applied voltage. That is to say that the sum of the currents at any node must be zero.

   b) the total voltage required to drive a current through a series connection is the sum of the voltages needed to drive that current through the individual elements of the connection. Thus, the algebraic sum of the potential differences around any closed part of a network is zero, this being a consequence of the law of conservation of energy.

2. Ohm's law must be obeyed;

$$E = iZ. \qquad \text{A.1.2}$$

3. Components in series add their impedances directly

$$Z = Z_1 + Z_2 + Z_3 \ldots + Z_n \qquad \text{A.1.3}$$

4. Parallel components add their impedances reciprocally,

$$^{1}/_{Z} = {}^{1}/_{Z_1} + {}^{1}/_{Z_2} + {}^{1}/_{Z_3} \ldots + {}^{1}/_{Z_n} \qquad \text{A.1.4}$$

Appendix 2

Mathematical treatment of the impedance of oxide films

In the case where the counter electrode and double layer impedance are negligible compared to that of the oxide film, the following simple equivalent circuit may be used,

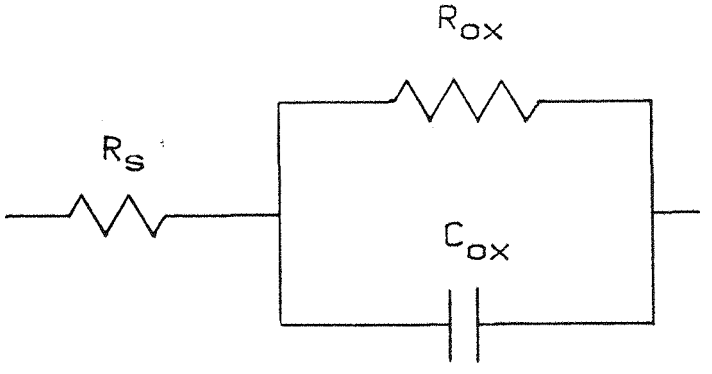

Fig. A.2.1 Representation of the equivalent circuit for an oxide film.

where R_s is the solution resistance and R_{ox} and C_{ox} are the leakage resistance and the capacitance of the semiconductor film respectively.

The impedance of the parallel part of the circuit, Z_1' is given by

$$1/Z' = 1/R_{ox} + j\,\omega C_{ox} \qquad \text{A.2.1}$$

$$Z' = R_{ox}/(1 + jR_{ox}\omega C_{ox}) \qquad \text{A.2.2}$$

Multiplication by the complex conjugate gives

$$Z' = \frac{R_{ox}}{(1 + R_{ox}^2\omega^2 C_{ox}^2)} - \frac{jR_{ox}^2 C_{ox}}{(1 + R_{ox}^2\omega^2 C_{ox}^2)} \qquad \text{A.2.3.}$$

$$= Z'_{real} + Z'_{imag}$$

and after including the solution resistance, the following is obtained,

$$Z_{real} = R_s + Z'_{real} \qquad A.2.4$$

$$Z_{imag} = Z'_{imag} \qquad A.2.5$$

The frequency response analyser gives results for both the real, RE, and the imaginary, IM, parts of the impedance. R_{ox} and C_{ox} can be calculated from this data in the following way;

$$RE = R_s + \frac{R_{ox}}{(1 + R_{ox}^2 \omega^2 C_{ox}^2)} \qquad A.2.6$$

$$IM = \frac{-jR_{ox}^2 \omega C_{ox}}{(1 + R_{ox}^2 \omega^2 C_{ox}^2)} \qquad A.2.7$$

Eauation A.2.6. can be rearranged in two ways,

$$\frac{R_{ox}}{(RE - R_s)} = 1 + R_{ox}^2 \omega^2 C_{ox}^2 \qquad A.2.8$$

$$\frac{(R_{ox} - (RE - R_s))}{(RE - R_s)} = R_{ox}^2 \omega^2 C_{ox}^2 \qquad A.2.9$$

Substitution of A.2.8 into A.2.7 and squaring the resultant equation gives rise to

$$IM^2 = R_{ox}^2 \omega^2 C_{ox}^2 (RE - R_s)^2 \qquad A.2.10$$

insertion of A.2.10 into A.2.8 gives,

$$IM^2 = (RE - R_s)(R_{ox} - (RE - R_s)) \qquad A.2.11$$

Rearrangement gives

$$R_{ox} = \frac{(IM^2 + (RE - R_s)^2)}{(RE - R_s)} \qquad A.2.12$$

After placing A.2.12 into A.2.9 and taking the square root,

$$\frac{IM}{(RE-R_s)} = \frac{\omega C_{ox} (IM^2 + (RE-R_s)^2)}{(Re - R_s)} \qquad A.2.13$$

this expression can be rearranged to give

$$C_{ox} = \frac{IM}{(IM^2 + (RE-R_s)^2)\omega} \qquad A.2.14$$

Values for R_{ox} and C_{ox} can be calculated by using equations A.2.13 and A. 2.14, together with a value for R_s obtained from the high frequency results where $RE = R_s$.

Appendix 3 Second Rank Tensors (2)

A scalar can be defined as a zero rank tensor and a vector as a first rank tensor. Second rank tensors are square arrays (3 x 3 if in three-dimensional space) that tranform upon rotation according to,

$$A'^{ij} = \sum_{kl} \frac{\partial x'_i}{\partial x_k} \frac{\partial x'_i}{\partial x_l} A^{kl} \qquad \text{contravariant} \qquad \text{A.3.1}$$

$$B'^{i}_{j} = \sum_{kl} \frac{\partial x'_i}{\partial x_k} \frac{\partial x'_i}{\partial x_j} B^{k}_{l} \qquad \text{mixed} \qquad \text{A.3.2}$$

$$C'_{ij} = \sum_{kl} \frac{\partial x_k}{\partial' x_i} \frac{\partial x_l}{\partial x'_j} C_{kl} \qquad \text{covariant} \qquad \text{A.3.3.}$$

where unprimed variables refer to the original system, primed variables to the new rotated system, superscripts to components of a contravariant vector and subscripts to components of a covariant vector.

In cartesian coordinates,

$$\frac{\partial x_j}{\partial x'_i} = \frac{\partial x'_i}{\partial x_j} \qquad \text{A.3.4}$$

so there is no difference between contravariant and covariant transformations, but for other coordinate systems the distinction between them is usually real and must be observed.

Appendix 4 Kramers-Kronig analysis (3)

The Kramers-Kronig dispersion relations between the real and imaginary parts of the refractive index of a dispersive media can be derived by considering either

i) the dependence of the phase and amplitude of the polarization or the displacement upon the electric field, E, when this is a function of t

$$E = E_o e^{i\omega t} \qquad \text{A.4.1}$$

or

ii) the dependence of the phase and amplitude of the scattered upon the corresponding quantities of the incident wave.

The relationships are integral equations and may be expressed in the form of

$$n(\omega) - 1 = {}^{1}/_{\pi} \int_{-\infty}^{\infty} P \frac{n\alpha}{\omega'(\omega'-\omega)} \, d\omega' \qquad \text{A.4.2}$$

and

$$\frac{n\alpha c}{\omega} = {}^{1}/_{\pi} \int_{-\infty}^{\infty} P \frac{n(\omega') - 1}{\omega' - \omega} \, d\omega' \qquad \text{A.4.3}$$

where c is the velocity of light, ω' is used instead of ω to indicate which parts should be integrated and P denotes that the Cauchy principle part must be taken

$$P \int_{0}^{\infty} \equiv \lim_{a \to \infty} \left(\int_{0}^{\omega-a} + \int_{\omega+a}^{\infty} \right) \qquad \text{A.4.4}$$

The Kramers-Kronig relationships are in fact purely mathematical ones which can be obtained from the properties of continuous function of a complex variable, they have thus been used to describe other systems, outside optics, such as electrochemical impedance (4).

Appendix 5

A flow diagram for the computer program used to control the frequency analyser (FRA) in impedance experiments is shown below:

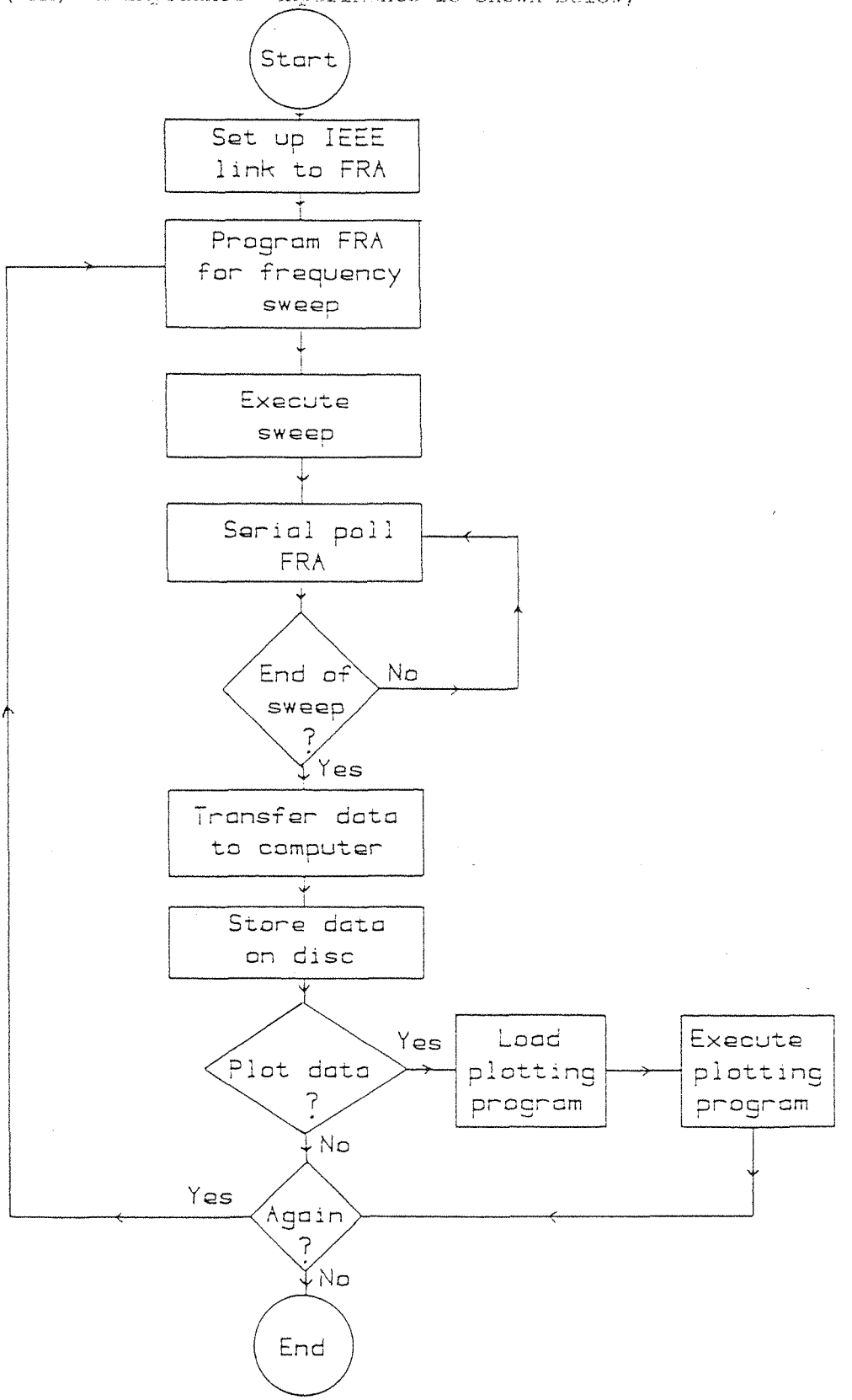

References

1. BROPHY, J.J.; "Basic Electronics for Scientists", 4th ed., McGraw-Hill, Tokyo, 1983.
2. ARFKEN, G.; "Mathematical Methods for Physicists", 2nd ed. Academic Press, New York, 1970.
3. STERN, F.; Solid State Phys. 15 (1963) 299.
4. CARDON, F.; DUTOIT, E.C., GOMES, W.P. & van MEIRHAEGE, R.L.; Electrochim. Acta. 21 (1976) 39.

List of Symbols

Symbol	Definition
A	Geometric area.
A	$(1 - R_{12})$
A.R.	Anodising ratio.
a	Half-jump distance for a barrier at the metal/oxide interface.
B	$(1 - R_{12})R_{23}$ Exp $[-2\alpha Lf]$.
b	Half-jump distance for a barrier within the bulk oxide.
C_{dl}	Capacitance of the double layer.
C_{ox}	Capacitance of the oxide film.
C_{geo}	Geometric capacitance of the oxide film.
C_{sc}	Space-charge capacitance of the oxide film.
c	Velocity of light in a vacuum (plane wave).
$E^{\ominus}$	Standard potential.
E_{tot}	Total field across the electrode.
E_{ox}	Field across oxide film.
E_H	Field across the Helmholtz layer.
$\underline{E}_s$	Electic vector for s-polarized light.
$\underline{E}_p$	Electric vector for p-polarized light.
E	Energy of an electron.
$\mathbf{E}_F$	Fermi energy level.
$\mathbf{E}_C$	Energy level of the bottom of the conduction band.
$\mathbf{E}_V$	Energy level of the top of the valence band.
$\mathbf{E}_{gap}$	Energy of the indirect bandgap.
ΔE	Maximum amplitude of a sinusoidal voltage.
e	Modulus of the electronic charge.
F	Faraday's constant.
f	Fraction of donors which are ionised in the bulk of the semiconductor.
$\Delta G^{\neq}$	Activation energy.
g(E)	Density of states.
H_o	Hamiltonian of an electron.
H'	Perturbation in the Hamiltonian of an electron.

Symbol	Definition
h	Plank's constant.
$\hbar$	$h/2\pi$
I_o	Intensity of incident light.
I_t	Intensity of transmitted light.
I_a	Intensity of light absorbed.
I_x	Intensity of light at the point x.
IM	Image component of the electrodes impedance.
i	Current or $\sqrt{-1}$.
i_o	Exchange current.
i_{pc}	Photocurrent from an oxide film.
i_{pd}	Photocurrent from a photodiode.
J_x	flux of the ions x through the oxide.
j	Current density or $\sqrt{-1}$.
j_o	Exchange current density.
k_b	Dissolution rate of the oxide film.
k_ω	Rate constant for the injection of holes from the semiconductor into the electrolyte.
k	Boltzmann's constant.
k	Extinction coefficient.
L_f	Thickness of the oxide.
$L_{f(crit)}$	Critical film thickness of the oxide film before open-circuit passive-active transition.
L_H	Width of the Helmholtz layer.
L_S	Schottky length.
m	Effective mass of an electron.
N	Surface density of ions available to cross a potential barrier.
N_D	Donor density in a semiconductor.
N_s	Density of ionised donors at low potentials.
N_t	Density of ionised donors at high potentials.
N_x	Density of donors at the point x.
N_C	Density of states in the conduction band.
N_V	Density of states in the valence band.
n	Refractive index.
$\hat{n}$	Complex refractive index, $\hat{n} = n - ik$.

Symbol	Definition
O	Concentration of oxidised species.
P	Momentum of an electron.
P_{O_2}	Partial press of oxygen.
P_L	Power of radiation incident on the electrode surface.
p	Parallel polarized light.
Q	Charge on a capacitor.
q	Charge passed.
RE	Real component of the electrodes impedance.
R_{ij}	Coefficient of reflection at the surface i/j for normal incident radiation.
r_{ij}	Fresnel amplitude reflection coefficient at the surface i/j.
$\hat{R}$	Overall complex reflection coefficient.
r	Roughness factor.
s	Perpendicular polarized light.
T	Absolute temperature.
t	Time.
V_{tot}	Total potential drop across the electrode.
V_{ox}	Potential drop across the oxide film.
V_H	Potential drop across the Helmholtz layer.
V_m	Molar volume of the oxide.
Y	$-e\Delta\phi/kT$.
Z	Impedance.
Ze	Charge on a migrating ion.
$\alpha(\lambda)$	Absorption coefficient for the media for a given wavelength, λ .
β	Zea/kT.
β_ω	Phase change produced by a single crossing of the film by the wave.
γ	$b/_a$
Δ	Phase difference between the p and s components of an elliptically polarized wave.
δ	Loss angle.
δ_x	Phase of oscillation of a wave relative to a reference.

Symbol	Definition
ε_o	Permittivity of free space.
ε_{ox}	Relative permittivity of the oxide.
ε_H	Relative permittivity of the Helmholz layer.
ε_1	Real part of the complex permittivity of the oxide.
ε_2	Imaginary component of the complex permittivity of the oxide.
ε'	Real part of the optical-frequency dielectric constant.
ε''	Imaginary component of the optical-frequency dielectric constant.
Φ	Photocurrent conversion efficiency.
θ	Phase angle.
Λ	$\frac{-(A - B - \phi) + \sqrt{(A - B - \phi)^2 + 4AB}}{2B}$
λ	Wavelength.
$\bar{\mu}_x$	Electrochemical potential of x.
ν	Potential scan rate.
ρ	$\hat{R}_p/\hat{R}_s$.
τ	Time electrode spends at open-circuit.
τ_b	Time taken for an oxide film to breakdown.
ψ	Arc tan of the ratio of the p component to the s component of an elliptically polarized wave.
$\Delta\phi$	Potential across the depletion layer.
$e\Delta\phi$	Band bending arising from the space-charge.
ω	Angular fequency.